From trapped bulk-acoustic-wave cavities to optomechanics

Kevin Rosenziveig

UBFC
UNIVERSITÉ
BOURGOGNE FRANCHE-COMTÉ

UNIVERSITÉ DE FRANCHE-COMTÉ

THÈSE DE DOCTORAT DE L'ÉTABLISSEMENT UNIVERSITÉ BOURGOGNE FRANCHE-COMTÉ

PRÉPARÉE À L'UNIVERSITÉ DE FRANCHE-COMTÉ

École doctorale n°37
Sciences Pour l'Ingénieur et Microtechniques

Doctorat d'Optique et Photonique

par

KEVIN ROSENZIVEIG

From Trapped Bulk Acoustic Waves Cavities to Optomechanics

Des Cavités à Ondes Acoustiques jusqu'à l'Optomécanique

Thèse présentée et soutenue à Besançon, le 14 Décembre 2021

Composition du Jury :

M. TESSIER GILLES	Professeur, Sorbonne-Université, Institut de la Vision, Paris	Président
M. LLOPIS OLIVIER	Directeur de Recherche CNRS, LAAS, Toulouse	Rapporteur
M. BELLON LUDOVIC	Chargé de Recherche CNRS, HDR, ENS Lyon	Rapporteur
M. PASSILLY NICOLAS	Chargé de Recherche CNRS, FEMTO-ST, Besançon	Co-directeur de thèse
M. COHADON PIERRE-FRANÇOIS	Maître de Conférence, HDR, ENS Paris, LKB	Co-directeur de thèse
M. GALLIOU SERGE	Professeur, ENSMM, FEMTO-ST, Besançon	Directeur de thèse

école doctorale **sciences pour l'ingénieur et microtechniques**

Title: From Trapped Bulk Acoustic Waves Cavities to Optomechanics

Keywords: Optomechanics, Quartz Crystal Resonator, Acoustics, Fabry-Perot Cavity

Abstract:

This PhD work continues and reinforces recent investigations on bulk acoustic wave resonators at cryogenic temperature (typically 4 Kelvins). In such operating conditions their unique properties open up new applications in different fields, from ultra-stable oscillators to hybrid quantum systems. For all these areas of research, new low-loss devices can play a game changing role. This work, which is oriented towards optomechanics, explores the possibilities of light-based actuation of an acoustical cavity with the horizon of building a cryogenic oscillator with such a cavity. Without loss of generality, the selected cavity is a quartz crystal resonator, adapted to the usage requirements with cryogenic environment. The first part of this thesis focuses on the theoretical and experimental study of optical Fabry-Perot cavities with absorptive mirrors, most notably with a novel method to extract the index of refraction of thin metallic films based on their particular properties when used in an optical cavity, i.e. a broadened Full Width at Half Maximum with respect to the non-absorptive case, as well as a frequency shift between the transmitted and the reflected peaks. In the second part, an analysis is performed on different means of mechanical actuation by light, i.e. by the photothermal force, the radiation pressure force and the electrostrictive force. An experimental study of the former demonstrates in particular the feasability of photothermal actuation at frequencies exceeding some Megahertz. The conclusion opens gives way to some perspectives, and specifically about other geometries which may potentially optimize the optomechanical coupling.

Titre : Des Cavités à Ondes Acoustiques jusqu'à l'Optomécanique

Mots-clés : Optomécanique, Résonateur à Quartz, Oscillateur, Acoustique, Cavité Fabry-Perot

Résumé :

Ce travail de thèse est destiné à poursuivre et renforcer les travaux démarrés récemment sur le comportement des résonateurs acoustiques à onde de volume piégée à basses températures (typiquement 4 Kelvins). Dans ces conditions de fonctionnement, leur propriété unique ouvre en effet des perspectives d'applications nouvelles dans différents domaines, depuis les oscillateurs ultra-stables jusqu'aux systèmes quantiques hybrides. Dans toutes ces thématiques de recherche, ces cavités à faibles pertes peuvent jouer un rôle déterminant. Ce travail orienté vers l'optomécanique explore les possibilités d'excitation d'une cavité acoustique par la lumière, avec pour horizon la conception d'un oscillateur cryogénique avec une telle cavité. Sans perdre en généralité, la cavité choisie est un résonateur à quartz adapté aux conditions d'utilisation cryogéniques. La première partie de cette thèse se concentre donc naturellement sur l'étude théorique et expérimentale des cavités optiques Fabry-Perot à miroirs absorbants métalliques, avec notamment une nouvelle méthode pour extraire l'indice de refraction des couches fines metalliques grâce à leurs propriétés particulières lors d'un utilisation en cavité optique, i.e. une largeur à mi-hauteur élargie par rapport au cas non-absorbant, ainsi qu'un décalage en fréquence entre les pics transmis et réfléchis. La deuxième partie analyse divers mécanismes d'excitation mécanique par la lumière, tels que l'excitation photothermique, la pression de radiation et la force électrostrictive. Une étude expérimentale démontre en particulier la faisabilité de l'excitation photothermique à des fréquences supérieures au MHz. La conclusion ouvre sur des perspectives, en particulier d'autres géometries optimisant potentiellement le couplage optomécanique.

UBFC UNIVERSITÉ BOURGOGNE FRANCHE-COMTÉ

Université Bourgogne Franche-Comté
32, avenue de l'Observatoire
25000 Besançon, France

À mon maître, Daisaku Ikeda
我が師匠、池田大作先生へ

REMERCIEMENTS

Je remercie en premier lieu Serge Galliou, mon encadrant de thèse qui m'a accompagné pendant ces années de doctorat. Il a toujours démontré une grande curiosité à l'égard de beaucoup de sujets de physique, parfois connexes à mon travail, qui ont été une source d'intérêt pour moi également. Il a su poser certains problèmes simplement, permettant au néophyte que j'étais d'appréhender plusieurs aspects du travail auxquels je n'étais pas familier. Je le remercie donc pour son accompagnement et son engagement quotidien pour la réalisation de ce travail de doctorat. Sa disponibilité a été une source d'inspiration pour moi, malgré tous ses engagements parallèles. Merci beaucoup de m'avoir accompagné jusqu'au bout de ce travail.

Je remercie également Nicolas Passilly, qui a su me donner des conseils parfois précieux à des moments où ils étaient nécessaires, et en particulier la pertinence de ses remarques pour m'obliger à réfléchir en profondeur à mon travail m'ont permis d'arriver à l'idée de publier un article, et d'améliorer sensiblement la qualité de mon travail. Merci également pour sa disponibilité.

Je remercie aussi Pierre-François Cohadon, qui m'a donné des conseils avisés sur l'optomécanique et m'a permis de profiter de son expérience sur le sujet.

Je remercie les membres du jury, qui ont accepté de prendre leur temps pour évaluer mon travail et se sont déplacés pour venir assister à ma soutenance. Vos remarques intéressantes et votre opinion ont participé à me rendre satisfait d'avoir effectué ce travail.

Je remercie également les institutions qui ont rendu ce travail de doctorat possible, en particulier le Labex FIRST-TF, l'Equipex, EUR-EIPHI-BFC et la Région Bourgogne Franche-Comté. Je remercie également l'ENSMM qui héberge le département Temps-Fréquence de l'institut FEMTO-ST.

Je remercie toutes les personnes du laboratoire qui ont rendues ce travail possible, et en particulier Philippe Abbé qui a conçu et bricolé beaucoup d'éléments qui font le squelette de ce travail de doctorat; Valérie Soumann, qui a fait des dépôts à tire-larigot pour pouvoir les tester, en accord avec mes demandes incessantes pour lui fournir du travail; Roberta Tittarelli pour ses excellents conseils sur les développements mathématiques d'équations d'ondes perturbées, et ses références concernant ce sujet ainsi que son temps accordé; Vincent Laude et Jean-Charles Beugnot pour leurs conseils et leur aide sur les questions de Brillouin et leur temps; Benoît Dubois pour son aide précieuse avec toutes les questions autour de Python; Remo Giust pour son aide concernant les Fabry-perot absorbantes et son temps accordé; Nicolas Martin pour ses conseils concernant les dépôts métalliques; Xavier Vacheret pour son aide pour les fabrications de quartz.

Je tiens également à remercier toutes les personnes qui travaillent au département Temps-Fréquence et qui ont aidé de près ou de loin mon travail, avec notamment Damien, Émile, Clément, Jacques, Marion, Jean-Michel, Gwennaël, Virginie, Yann, Ausrine, Samuel, Joël, Fabrice, Pierre-Yves, Bernard, Enrico, Thomas, Yannick, Valérie, Gilles. Une pensée spéciale pour Jean-Jacques, qui nous a quitté et dont la bonne

humeur chronique me revient parfois encore en tête quand je passe au TF.

Merci également infiniment à Fabienne et Sarah pour leur aide régulière au cours de ces années, aussi bien pour des questions de secrétariat que pour les commandes et autres joyeuseries administratives...

Une mention particulière pour mes collègues de bureau, Cricri Podcast qui a tout entendu et tout vu dans ses podcasts; et Dadou la Panique, qui n'a "pas l'temps, pas l'temps!". Ces années de doctorat n'auraient clairement pas été les mêmes sans vous.

Une mention particulière pour Jérémy aussi, qui a initié ce travail avec Serge avant que j'arrive et qui vogue désormais vers d'autres aventures optomécaniques.

Enfin, merci à tous les doctorants et toutes les doctorantes du département TF et d'ailleurs, qui ont rendu ces années de doctorat plus intéressantes et qui ont permis que le quotidien y soit plus amusant. Une pensée particulière pour le Tonton Falzon (chercheur!), qui "est là, non?".

Merci infiniment également à mes amis hors du laboratoire qui m'ont apporté leur soutien moral et scientifique sur certains sujets, et en particulier merci à Guesereseg et SisiosowaSAsh.

Sans l'aspect scientifique cette fois mais toujours en dehors du labo, merci beaucoup aux membres d'Exirium Brass pour le soutien moral et les bons moments musicaux.

Un immense merci également à mes amis dans la foi, qui ont eu un rôle de soutien plus qu'important. Merci en tout particulier à Toshi, grâce à qui j'ai pu commencer ce doctorat, et qui a été présent dans les moments de doute.

Merci immense à mes amis de toujours qui ont été présents tout au long de cette aventure et qui ont été un soutien récurrent: merci à Rourou, Soniak, Madame Soso, Betti, Raph, Paulito et Dr. Alex. Une pensée spéciale pour Dr. Alex justement, grâce à qui les graines qui ont germé en l'idée du doctorat ont pu apparaître dans ma vie.

Merci infiniment à mes parents, grâce à qui j'ai pu arriver jusqu'au bout de ce travail et merci pour leur soutien incessant. Merci également aux membres des Rosen Five, i.e. Mickew, Yo, Xia et Grid pour leur intérêt et leur soutien moral.

Enfin, cette section serait largement incomplète sans remercier Juliana. Tu as été beaucoup de choses pendant ces années et tu as amené beaucoup de joie et d'espoir à travers ces saisons. Ton nom rime merveilleusement bien avec chacun des moments qui composent ces années de doctorat, et pour cela, merci, merci, merci, merci.

ACKNOWLEDGEMENT

I thank first of all Serge Galliou, my thesis supervisor who accompanied me during these years of PhD. He always showed a great curiosity towards many physics subjects, sometimes related to my work, which were a source of interest for me too. He knew how to pose certain problems simply, allowing the neophyte that I was to apprehend several aspects of the work with which I was not familiar. I would like to thank him for his support and his daily commitment to the realization of this doctoral work. His availability has been a source of inspiration for me, despite all his parallel commitments. Thank you very much for having accompanied me until the end of this work.

I also thank Nicolas Passilly, who knew how to give me sometimes precious advices at moments when they were necessary, and in particular the relevance of his remarks to force me to think deeply about my work allowed me to arrive at the idea of publishing an article, and to improve significantly the quality of my work. Thanks also for his availability.

I also thank Pierre-François Cohadon, who gave me good advice on optomechanics and allowed me to benefit from his experience on the subject.

I thank the members of the jury, who accepted to take their time to evaluate my work and came to attend my defense. Your interesting remarks and your opinion have contributed to my satisfaction in having done this work.

I also thank the institutions that made this PhD work possible, in particular the Labex FIRST-TF, the Equipex, EUR-EIPHI-BFC and the Region Bourgogne Franche-Comté. I also wish to thank the ENSMM, which is host to the Time-Frequency department of the FEMTO-ST institute.

I thank all the people of the laboratory who made this work possible, and in particular Philippe Abbé who designed and tinkered with many of the elements that make up the skeleton of this PhD work; Valérie Soumann, who has made a lot of depositions in order to test them, in agreement with my incessant requests to provide her with work; Roberta Tittarelli for her excellent advice on the mathematical developments of perturbed wave equations, and her references concerning this subject as well as her time; Vincent Laude and Jean-Charles Beugnot for their advice and help on Brillouin questions and their time; Benoît Dubois for his precious help with all the questions about Python; Remo Giust for his help with absorbing Fabry-perot and his time; Nicolas Martin for his advices concerning the metallic deposits; Xavier Vacheret for his help with the quartz fabrications.

I would also like to thank all the people working in the Time-Frequency department who helped me in some way, especially Damien, Émile, Clément, Jacques, Marion, Jean-Michel, Gwennaël, Virginie, Yann, Ausrine, Samuel, Joël, Fabrice, Pierre-Yves, Bernard, Enrico, Thomas, Yannick, Valérie, Gilles. A special thought for Jean-Jacques, who left us and whose chronic good mood still comes back to my mind when I go to the TF.

Many thanks also to Fabienne and Sarah for their regular help during these years, as well for secretarial questions as for orders and other administrative joys.

A special mention to my office colleagues, Cricri Podcast who has heard and seen everything in her podcasts; and Dadou la Panique, who has "no time, no time! These years of PhD would clearly not have been the same without you.

A special mention to Jérémy too, who initiated this work with Serge before I arrived and who is now sailing to other optomechanical adventures.

Finally, thanks to all the PhD students in the TF department and elsewhere, who made these years of PhD more interesting and fun. A special thought for Uncle Falzon (researcher!), who "is here, isn't he?

Thanks also to my friends outside the lab who gave me moral and scientific support on some subjects, and in particular thanks to Guesereseg and SisiosowaSAsh.

Without the scientific aspect this time but still outside the lab, many thanks to the members of Exirium Brass for the moral support and the good musical moments.

A huge thank you also to my friends in faith, who had a more than important support role. A special thanks to Toshi, thanks to whom I was able to start this doctorate, and who was present in moments of doubt.

Huge thanks to my friends who have always been present throughout this adventure and who have been a recurrent support: thanks to Rourou, Soniak, Madame Soso, Betti, Raph, Paulito and Dr. Alex. A special thought for Dr. Alex indeed, thanks to whom the seeds that blossomed into the idea of the doctorate could appear in my life.

Many thanks to my parents, thanks to whom I was able to finish this work and thanks for their unceasing support. Thanks also to the members of the Rosen Five, i.e. Mickew, Yo, Xia and Grid for their interest and moral support.

Finally, this section would be largely incomplete without thanking Juliana. You have been many things over the years and have brought much joy and hope throughout all these seasons. Your name rhymes beautifully with each of the moments that make up these doctoral years, and for that, thank you, thank you, thank you, thank you.

CONTENTS

General Introduction

Time keeping is of primary importance in everyday's life, for applications ranging from GNSS (Global Navigation Satellite System) navigation to fundamental physics experiments [Bushev et al., 2019]. This task is generally performed through transforming a signal at a precise frequency to a time. The reference frequency can be provided by two main families of devices: bulk-material based clocks and atomic-based clocks.

Within the bulk-based clocks, quartz is a material which is widely used because of its price and availability, as well as its piezoelectric properties which allows to actuate the crystals in a direct way. It displays good performances at providing a stable frequency source thanks to its good mechanical properties, with some bare quartz crystal providing fractional frequency stabilities of about 10^{-9} at 1 s integration time. Several architectures even allow to improve this figure through compensating the unstabilities originating from environmental sources that must be well-controlled (e.g. vibrations, temperature fluctuations), for example with the OCXO (Oven Controlled Crystal Oscillator) that can achieve fractional frequency stabilities down to 10^{-13} at 1 s.

It has been shown in some previous work in our team that the mechanical quality factor Q can display values as high as some 10^9 for the very best quartz [Galliou et al., 2013] at cryogenic temperature. Because the Q factor is related to the ultimately reachable fractional frequency stability, this allows to expect figures improvements by a factor 1000 with respect to a typically good quartz resonator at room temperature, with a floor of the fractional frequency stability as low as 10^{-16}.

The idea to use such high quality quartz resonators at cryogenic temperatures in order to build an ultrastable oscillator stems from this observation. The typical piezoelectric excitation scheme, however, can bring noise to the measurement and in particular in a cryocooler environment (through e.g. spatially variable thermal noise) which can limit this ultimate stability. In this context, the need for an alternative actuation scheme arises. An optomechanical actuation is therefore considered, which consists in mechanically actuating the quartz through an optical input, typically a laser [Kharel et al., 2019] [Rakich et al., 2010]. By doing so, one avoids the aforementioned noises while also allowing non-piezoelectric materials to be used as frequency references if they display good mechanical properties (e.g. sapphire [Bourhill et al., 2015]).

While one may consider at first glance dielectric super mirrors in order to maximize the light coupling by turning the quartz crystal resonator into a Fabry-Perot cavity, literature shows that these coatings dampen the mechanical qualities of the resonator, limiting it to some 10^6 in most common solutions such as Ta_2O_5 [Galliou et al., 2016a]-based coatings. Metallic thin films coatings also induce damping, although it has been shown that they limit the mechanical qualities less than their dielectric counterpart [Galliou et al., 2016a]. Furthermore, the quartz crystal resonators are routinely coated with metallic layers providing electrical contacts, and because such metallic layers also constitute mirrors [Echániz et al., 2014], they might readily constitute devices that can be optomechanically actuated. The aim of this thesis is then to evaluate the potential of

metallic coatings for the generation of an optomechanically actuated oscillator, and investigate in this framework their properties to target their optimization. The thesis manuscript is therefore structured as follows:

- Chapter 1 gives an overview of the state of the art for time-references and a reminder of some basic descriptive framework for oscillators. The reasons behind our interest for the quartz crystal resonator is specified in more details, as well as some background concerning the expected improvements for the stability brought by our device. The reasons for the preference towards an optomechanical actuation are also discussed.

- Chapter 2 gives a quick reminder concerning some quartz crystal formalities, as well as a few equations of continuum physics formalism that are useful to analyze the situation for optomechanical actuation.

- Chapter 3 focuses on the study of the optical characteristics of the common quartz crystal resonator used as a Fabry-Perot cavity. This is in the aim of asserting whether these resonators can answer the requirements of optomechanical actuation, which are established in chapter 4. The first emphasis is put on the theoretical developments of the Fabry-Perot cavities, for the ideal cavity as well as for the absorptive mirrors cavity. Some specific characteristics are shown for the latter, such as an increased FWHM (Full Width at Half Maximum) of the transmitted peak, an asymmetry of the reflected peak as well as a frequency shift Δf between the reflected and the transmitted peaks. An experimental study is also led, with a measurement campaign of several different layers of different thicknesses and of different materials, allowing to establish that silver is the best candidate for obtaining the highest possible reflectivity among common metals (chromium, gold, silver). Several properties are measured, both at room temperature and 4 K. This measurement campaign also allows to feed a numerical method that we designed to obtain the refractive index, starting from the knowledge of the FWHM and the peaks' frequency shift Δf. Such knowledge is usually very method-dependent (as well as process-dependent) and is not widely found for cryogenic temperatures.

- Chapter 4's primary concern is to analyze several light-induced forces as the potential actuation sources for mechanical actuation, and in particular in the case of quartz crystal resonators coated with thin metallic films. The first force to be discussed is the photothermal force, for which a simplified 1D theoretical framework is developed through continuum mechanics. Some experimental results are then exposed, demonstrating the possibility to actuate the quartz crystal resonator with metallic thin films through this method at 5 MHz, both at room temperature and cryogenic temperature, as well as with or without optical resonance with the optical cavity formed by the thin films. The second force to be discussed is the radiation pressure force, with a brief reminder of the Hamiltonian framework from literature as well as an application to the case at hand with our quartz resonators. Lastly, the electrostrictive force and the subsequent Brillouin scattering interaction is analyzed with a similar continuum mechanics framework as mentioned above. A numerical application of the expected results of the optomechanical forces (i.e. radiation pressure and electrostriction) for the quartz resonator coated with metallic thin films is given, raising the requirement of other possible geometries for the resonators.

- Chapter 5 provides a conclusion to this work, as well as a perspective regarding other geometries for the quartz crystal resonators' mirrors, i.e. with combinations of metallic thin films and dielectric supermirrors, either deposited directly onto the resonator or suspended in front of it. A comparison of the different possibilities is briefly discussed.

1

STATE OF THE ART

This chapter aims to provide the general background for this thesis, regarding time keeping and basic concepts regarding oscillators as well as an outlook on the state of the art of some frequency sources. We then introduce the reasons why this work can be of interest towards the conception of an ultrastable cryogenic clock.

1.1/ GENERAL MOTIVATION

1.1.1/ TIME AND FREQUENCY METROLOGY, APPLICATIONS

There are countless devices in today's world using time references for their basic functioning: let us just mention a few devices such as cellphones, clocks, computer, GNSS, and in several industries too, such as spatial industry, military industry. Some applications require extreme efforts in time-keeping, such as e.g. fundamental physics experiments (see [McGrew et al., 2018]).

Time metrology, the precise measure of time, is in fact often reduced to counting periods of oscillations or the related frequency. The frequency of a resonator is electronically measured and conveniently transformed into a time.

Several tools exist for evaluating how "precise" the time is, and different kind of references for time have been invented (see a detailed description in [Vallet, 2018], chapter 2). The vernacular concept of "precision" in fact includes several different concepts, one being the accuracy of the time (is the device's "one second" actually our world reference's "one true second"), and another one being the instability of the time (unrelated to whether the device's "one second" is in fact a real second, does it keep on beating the same "one second" as time passes?).

Throughout this thesis work, the main focus will be drawn onto the concept of instability. Some devices may naturally have a better short-term stability (such as quartz crystal for example), and some others may have a better long-term stability (such as atomic reference clocks for example). However, only by making a hybrid system can a device get a good short-term and long-term stability (see for example the diverse hydrogen masers devices commercially available).

1.1.2/ OSCILLATORS, PHYSICS ABOUT IT

1.1.2.1/ BASICS, PHASE FLUCTUATIONS

In the simplest approach to resonance with the mechanical pendulum, it is well known that any object that resonates, and in this case the pendulum, will eventually stop to oscillate because of the natural losses, e.g. friction. In a general fashion, when devices entering in resonance which we will call resonators are left alone, the system losses (engineering losses, intrinsic losses, etc) eventually dampens the resonance. This is why an oscillator is needed in order to forcefully prevent the resonance from stopping. The term oscillator designates the ensemble of the resonator with its accompanying components to maintain the oscillation (see for example [Riehle, 2004], section 2.2).

Taking a general picture for oscillator, the required elements for an oscillator to function are the resonator (through the resonance frequency, it is possible to extract a time), an amplifier (that will coherently provide the energy lost by the resonator during its vibration cycles) and the power source for the amplifier. In a familiar mechanical pendulum, the resonator is the mechanical arm, the amplifier is the set of gears and the energy source is generally either a human intervention to load the springs or an electrical power supplier. In a typical quartz wrist watch, the resonator is a resonating quartz tuning fork, the amplifier is an electronic amplifier and the power source a battery.

A simplified scheme of such an electronic oscillator is shown in Fig. 1.1, with a resonator and an amplifier. The amplifier's transfer function is noted as A in Fig. 1.1b. The res-

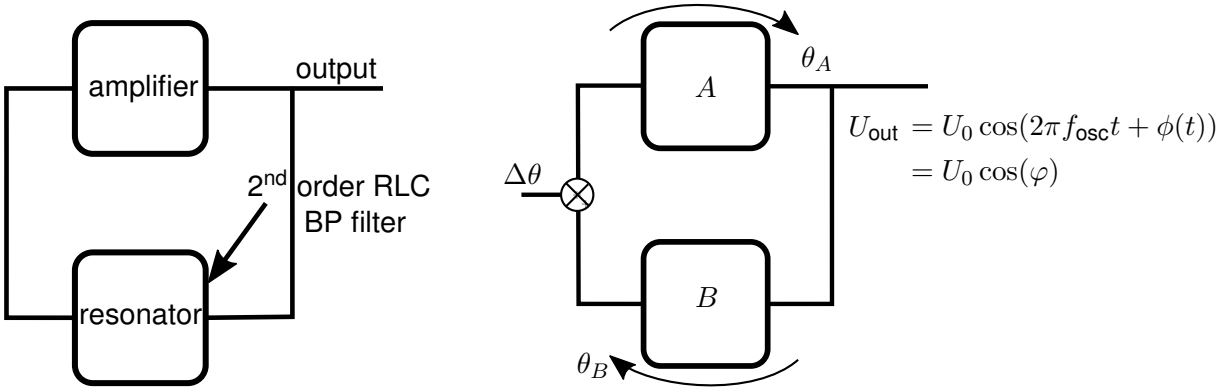

(a) Simplified scheme (b) Mathematical representation

Figure 1.1: *1.1a Simple scheme of an oscillator and 1.1b mathematical representation of this oscillator. A and B, respectively the amplifier's gain and the resonator's gain, are a priori complex and impart a phase on the signal. The phase fluctuations inside the loop are noted here $\Delta\theta$ and come from other sources than the amplifier and resonator, whereas the output voltage $U_{out} = U_0 \cos(2\pi f_{osc} t + \phi(t))$, where U_0 is considered a constant and $\phi(t)$ are the phase fluctuations outside the loop. f_{osc} is the oscillating frequency, which, because of the phase response of the amplifier, might be different from f_0, the resonance frequency of the resonator.*

onator, which we denoted as B, can be e.g. a quartz crystal resonator. It is possible to accurately represent its electrical behavior around resonance with an electronic 2nd order RLC system with a parasitic capacitance C_0, with typical order of magnitude of 3 pF-5 pF

(see Fig. 1.2)[1]. The resonator then acts as a band-pass filter (see Fig. 1.3).

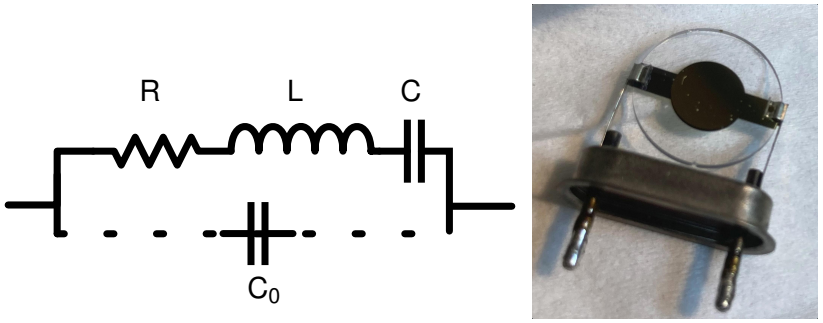

(a) RLC (near-resonance) equivalent circuit (b) Quartz picture

Figure 1.2: *A second order RLC circuit (Fig. 1.2a), representing an electronic equivalent circuit of the quartz crystal resonator close to a resonance frequency when excited by piezoelectric means, with a parasitic C_0 capacitance due to electrodes (typical order of magnitude of* 3 pF-10 pF*), deposited in order to apply the exciting electric field, as seeable on Fig. 1.2b (see Fig. 1.5 for a sketch of these electrodes).*

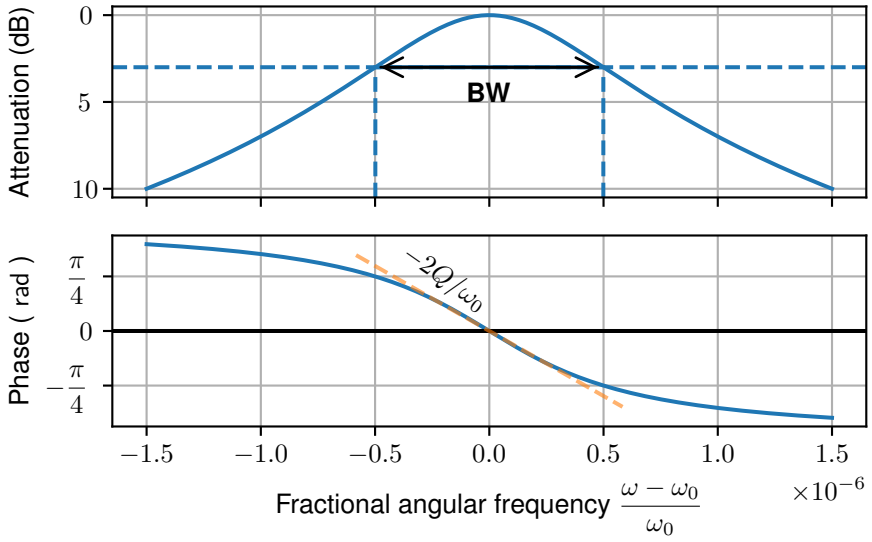

Figure 1.3: *Bode diagram of the admittance (i.e. the inverse of the impedance), representing the frequency response of the equivalent circuit for the quartz resonator around resonance. Here, losses are normalized to* 0 dB *at resonance and the parasitic capacitance C_0 (see Fig. 1.2) is neglected . It is typically the response of a band-pass filter, whose bandwidth is $\Delta f = f_0/Q$. The bandwidth is also visible on the attenuation plot and is denoted as **BW**, and the phase-frequency slope at resonance is also drawn on the phase diagram (see Eq. 1.7). Here, some common experimental values of a "good" quartz crystal resonator are taken for the plot: $\omega_0 = 10$ MHz, $Q = 10^6$, $R = 100\,\Omega$.*

The so-called Barkhausen conditions are conditions given for a loop in a steady state

[1]Note near resonance, the resonator mainly acts as a RLC system, whereas far from resonance, it essentially acts as its parasitic capacitance C_0.

(see for example [Riehle, 2004] p.31):

$$|B||A| = 1 (\geq 1) \tag{1.1a}$$

$$\arg A(\omega) + \arg B(\omega) = 0 \ [2\pi] \tag{1.1b}$$

The first condition Eq. 1.1a means that the amplification needs to counterbalance the losses in the resonator. Oscillations typically start from noise, provided that $|B||A| > 1$ when the oscillator is turned on. Once the oscillations take place, $|B||A| = 1$ is met because of the nonlinearities. The second condition Eq. 1.1b describes the phase condition that needs to exist between both functions.These conditions are usually validated around a resonance frequency of the resonator $f_0 = \frac{1}{t_0} = \frac{\omega_0}{2\pi}$. From this last statement, it is possible to conclude as well that, if the resonator and the amplificator are operating correctly and the resonance of the system is achieved, then the phase fluctuations from one element should compensate the phase fluctuations of the other:

$$\Delta\theta_A = -\Delta\theta_B \tag{1.2}$$

Related to the transfer function of the resonator, its impedance can be written (neglecting the parasitic capacitance C_0):

$$Z = R + j\left[L\omega - \frac{1}{C\omega}\right] \tag{1.3}$$

where $\omega = 2\pi f$ is the angular frequency. Let us remind that the quality factor, in such an RLC circuit, is related to the R, L and C characteristics in the following way:

$$Q = \frac{\text{Energy stored}}{\text{Energy dissipated during } t_0} = \frac{f_0}{\text{BW}} = \frac{L\omega_0}{R} = \frac{1}{RC\omega_0}, \tag{1.4}$$

where $\omega_0 = 2\pi f_0 = 2\pi/T_0$ is the resonance angular frequency. It is therefore possible to rewrite the impedance of Eq. 1.3 in terms of the mismatch with the resonance frequency:

$$Z = R + jR\left[\frac{L\omega_0}{R}\frac{\omega}{\omega_0} - \frac{1}{CR\omega_0}\frac{\omega_0}{\omega}\right]$$

$$Z = R + jRQ\left[\frac{\omega}{\omega_0} - \frac{\omega_0}{\omega}\right] \tag{1.5a}$$

$$Z \approx R + 2jRQ\frac{\Delta\omega}{\omega_0} \qquad \text{with } \omega = \omega_0 + \Delta\omega, \text{ and } \Delta\omega \ll \omega_0 \tag{1.5b}$$

Note from this last Eq. 1.5b that when exactly at resonance (i.e. $\omega = \omega_0$ and $\Delta\omega = 0$), the impedance becomes purely real and resistive. If the parasitic capacitance C_0 were to be taken into account, it would introduce a slight shift in the series resonance frequency and would generate an antiresonance, a few tens of Hz apart typically.

By writing the argument of this last expression in Eq. 1.5b:

$$\text{Arg}\, Z = \arctan^{-1}\left(\frac{\text{Im}(Z)}{\text{Re}(Z)}\right) \approx 2\frac{Q}{\omega_0}\Delta\omega \tag{1.6}$$

we can highlight, as a consequence, that the transfer function of the resonator $B(\omega)$ related to the impedance Z exhibit a frequency-phase relationship close to the resonance frequency ω_0 (see Fig. 1.3 for a visual representation of this relationship):

$$\Delta f = -\frac{f_0}{2Q}\Delta\theta_B \tag{1.7}$$

The phase changes for B can come either from $\Delta\theta_A$ (as Eq. 1.2 implies) or by other phase noise sources inside the loop. This leads to a signal frequency change Δf, whose Power Spectral Density (PSD) is, inside the operation range of the loop (i.e. the BW of the resonator):

$$S_f(\nu) = \frac{f_0^2}{4Q^2} S_\theta(\nu) \tag{1.8}$$

1.1.2.2/ PSD OF THE PHASE FLUCTUATIONS

Very often, for commodity reasons, the PSD of the frequency fluctuations is measured indirectly: a phase-meter bench at the output of the loop permits to retrieve the PSD of the phase fluctuations $S_\varphi(\nu)$, related to the PSD of the frequency fluctuations $S_f(\nu)$ through:

$$S_f(\nu) = \nu^2 S_\varphi(\nu) \quad \text{because} \quad f(t) = \frac{1}{2\pi}\frac{\mathrm{d}\varphi}{\mathrm{d}t} \tag{1.9}$$

Phase fluctuations inside the loop get therefore translated into frequency fluctuations with the resonator, in the way described with Eq. 1.7. It is therefore possible to write the following relation between the phase fluctuations inside and outside the loop, distinguishing between the case where the Fourier frequency of the fluctuation is included in the resonator's bandwidth (i.e. $\nu < f_L = f_0/2Q$, the Leeson frequency):

$$\begin{aligned} S_\varphi^{\text{in}}(\nu) &= \frac{1}{\nu^2} S_f(\nu) \\ &= \frac{1}{\nu^2}\left(\frac{f_0}{2Q_L}\right)^2 S_\theta(\nu) \end{aligned} \tag{1.10a}$$

and outside the bandwidth (i.e. $\nu > f_L$, see Fig. 1.4.):

$$S_\varphi^{\text{out}}(\nu) = S_\theta(\nu) \tag{1.10b}$$

where we used Q_L the loaded quality factor (i.e. of the resonator inside the loop), which differs from the unloaded quality factor Q of the resonator alone. The total output power spectral density of the phase fluctuations is therefore written

$$S_\varphi^{\text{out}}(\nu) = \left(1 + \frac{f_0^2}{4Q_L^2}\frac{1}{\nu^2}\right) S_\theta(\nu) \tag{1.11}$$

which is known as the Leeson model.

Following empirical observations, the typical Power Spectral Density (PSD) of the phase fluctuations for an amplifier such as A on Fig. 1.1a (or coming from an extra noise source) can be modeled by a frequency-power development (See for example [Rubiola, 2009] p30):

$$S_\theta(\nu) = a\nu^{-1} + b\nu^0 \tag{1.12}$$

where the ν^0 component is proportional to the temperature of the system. By injecting in Eq. 1.11 the expression for a typical phase fluctuations of Eq. 1.12, it is possible to obtain the general trend represented in Fig. 1.4.

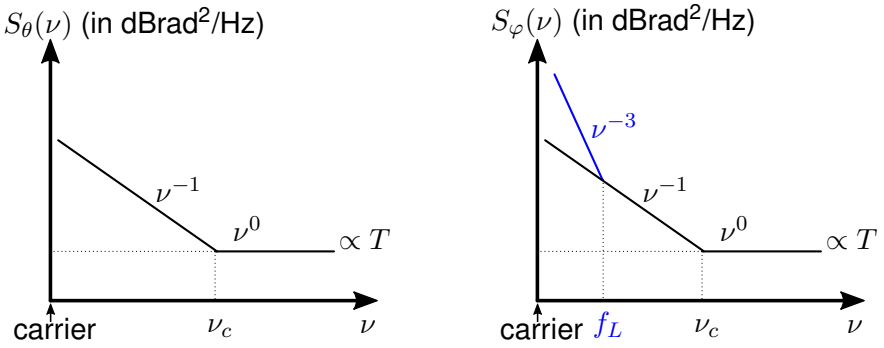

(a) Ideal case (open loop) (b) Leeson model (closed loop)

Figure 1.4: *Typical Power Spectral Density (PSD) in an open loop (Fig. 1.4a) and at the output of a closed loop with the Leeson model (Fig. 1.4b), with a term proportional to ν^{-1} and another term proportional to ν^0 (i.e. constant). ν_c is the corner frequency, at which the ν^{-1} noise starts to be under the ν^0 term. The latter term is proportional to the temperature T. In the Leeson model, there is furthermore a part, inside the bandwidth, where the ν^{-1} noise is converted and superseded by the ν^{-3} noise, created by the closed loop. The latter noise level is proportional to $1/Q^2$, see Eq. 1.10a. Note that in the case drawn here, $\nu_c > f_L = f_0/2Q$ the Leeson frequency, as is typically the case for quartz oscillators, but the opposite might be true, in which case there would also be a ν^{-2} noise, created from the ν^0 according to Eq. 1.10a.*

1.2/ STATE OF THE ART FOR FREQUENCY SOURCES

It is possible to classify the time-keeping references systems into two main families: bulk-material based clocks and atomic-based clocks. We shall briefly present examples of the former kind, then present some instances of the latter.

Time-keeping and sensors applications [2] include time reference in cellphones, oscilloscopes, CPUs, aerospatial industry, military industry.

The two main types of bulk-material based clocks are the Bulk Acoustic Waves (BAW) devices, and Surface Acoustic Waves (SAW) devices.

SAW devices primarily serve as filters [Ohsato et al., 2012] [Wall et al., 2015] and sensors [Fachberger et al., 2004] [Almirall et al., 2019], but can also be used as high quality resonator too (see [Zhang et al., 2017]), for frequencies typically greater than a few hundred MHz up to a few GHz.

BAW frequency sources include many piezoelectric materials, among which, quartz crystal resonators are of primary importance. Beyond the fact that synthetic crystals are relatively cheap, there are several reasons for their predominent role: as they are piezoelectric, they are rather simple to actuate. Furthermore, they have low losses and can even have extremely low losses, which is generally interesting for minimizing frequency instability (see section 1.3.1). The instability may have different origins, sometimes intrinsic or sometimes caused by engineering or environment related phenomena (see section 1.3.1 for a lengthier discussion about these phenomena). In a familiar pendulum clock,

[2] They are essentially related through the fact that e.g. a device which is fairly insensitive, frequency-wise, to temperature fluctuations will be a good metrological device, whereas the opposite situation results in a good sensor for temperature through monitoring the frequency.

for example, a change in temperature might influence the arm's length and hence is beating period. This is the reason why temperature fluctuations have to be taken accounted for, both through its stabilization but also through finding a turning point in the frequency-temperature curve (see chapter 2).

Quartz resonators can be used with different crystalline cuts in order to compensate for different kinds of effects (e.g. stress compensation, temperature compensation), i.e. render the device as insensitive as possible to the given parameter. It can also be used in the opposite regime, to be very sensitive to a certain parameter for creating sensors (e.g. Quartz Crystal Microbalance). The quartz resonator market reaches several billion of US dollars (see for example the market report, available online, by Mordor Intelligence), amounting to billions of units sold every year. They vary in frequency, from a few kHz to a few hundred of MHz for BAW devices. They also vary in frequency stability. Several types of packagings are built around the resonator, and, as mentioned earlier, they usually act on the frequency-temperature relationship of the resonator in order to improve its frequency stability through temperature stabilization at a turning point of the frequency-temperature curve.

The simple quartz crystal oscillator (XO) without any specific processing is the most common time reference unit, which, under the best conditions, can have an Allan deviation of about 10^{-9} at 1 s (see for example [Riehle, 2004]). Another widely used unit where the output frequency is corrected according to the ambient temperature is the Temperature Compensated Crystal Oscillator (TCXO). Some devices can be shrinked down to MEMS size, typically less than a mm^3, with stability performances Allan deviation exceeding a few 10^{-11} at 1 s (see [Kubena et al., 2018]). Let us mention as well the Oven Controlled Crystal Oscillator (OCXO), which is used for the best performances in terms of frequency stability with quartz resonators. It consists of the crystal and its accompanying temperature control elements to be put in an oven set at the turning point of the frequency-temperature curve of the crystal. The crystal cut is selected so that the turning point is greater than the maximum operating temperature of the environment (typically 80 °C). Such an OCXO, however, is power consuming and is rather big with a typical size greater than $200\,\mathrm{cm}^3$. The phase noise performances of such OCXO can reach $-170\,\mathrm{dBc\,Hz}^{-1}$ at 100 MHz (see [Sakamoto et al., 2008]), and the Allan deviation can be better than some 10^{-13} at 1 s (see [Hudson et al., 2019]). Companies providing quartz devices include AR electronique and Rakon.

Other piezoelectric materials used include the popular Lead Zirconate Titanate (PZT) family of materials, that can also be used for resonators, as well as aluminium nitrate AlN [Löbl et al., 2001] [Pulskamp et al., 2011].

There also are other ways of obtaining frequency references which do not use a mechanical resonance of the device. For example, Sapphire is used for that purpose, in particular for its dielectric properties (although it also has very good acoustical properties, see for example [Driscoll et al., 1992], see section 1.3.2)). It is used e.g. as the heart of a commercial Cryogenic Sapphire Oscillator (CSO) clocks built here by FEMTO Engineering, which uses electromagnetic whispering gallery modes. They display very good stability performances, with Allan deviation of some 10^{-16} at 1 s (see for example [Giordano et al., 2016] [Grop et al., 2010]) and moreover, they are certified to have Allan deviations lower than 3×10^{-15} for integration times ranging from 1 s to 10 000 s. Their competitors, Cryoclock, have similar though slightly lower performances (see their respective datasheet on their respective websites: Uliss and CryoClock).

Let us also mention the existence of some other ways to obtain time-references, such as Spintronics, i.e. the manipulation of electronic spin, is also of interest for reference signal generation (see for example [Prokopenko et al., 2011]) or optoelectronics oscillators (OEO) which typically relies on a laser and a Mach-Zehnder Modulator (see for example [Lelievre et al., 2017] or the OEWAVES company products).

The other main kind of time reference which does not directly rely on the mechanical or dielectric properties of materials is atomic and ionic clocks (see [Audoin et al., 2001]). Generally speaking, an atomic (ionic) clock uses the frequency of the electromagnetic radiation associated with the energy transition between two levels of an atom (ion). There was historically a development mainly of microwave-range transitions (several hundreds of MHz) in this type of clocks, whereas today's technology tends more to the optical frequency range (hundreds of THz).

The current definition of the second relies on a microwave-frequency atomic clock. Indeed, since the 13$^{\text{th}}$ Conférence Générale des Poids et Mesures (CGPM) in 1967, "The second is the duration of 9 192 631 770 periods of the radiation corresponding to the transition between the two hyperfine levels of the ground state of the caesium 133 atom" (see the Bureau International des Poids et Mesures (BIPM) official website, and [McCarthy et al., 2009] for a description of the definition and the role of a second). The very best performances for long term stability, as of today, are achieved with optical-frequencies atomic clocks with orders of magnitude for Allan deviation floor of about 10^{-18} (see for example [Nakamura et al., 2020])

Some effort is also made towards miniaturizing atomic clocks, while keeping fair performances: Coherent Population Trapping (CPT) used on a miniature atomic clock has demonstrated performances of Allan deviation of 7.5×10^{-11} at 1 s and better than 2×10^{-11} at 1 day (see [Vicarini et al., 2019], SA.45s chip-scale atomic clock by Microsemi or MMAC by Syrlinks).

Among all these devices, we now turn to the reasons behind the choice to investigate some particular quartz crystal throughout this thesis.

1.3/ INTEREST OF OUR DEVICE

Some of the quartz resonators precedently investigated here in our team have displayed extremely high mechanical quality factors Q at cryogenic temperature, for the uncommon extensional (breathing) A-mode (see [Galliou et al., 2013]), as high as several billion for the very best ones. In fact, as this section highlights, this is the reason why they are of such interest and why we consider the option of a metallized quartz crystal resonator at the heart of an ultrastable clock (section 1.3.1). We subsequently show that the choice of studying an optomechanical coupling arises very naturally (section 1.3.2). Finally, we show some examples for which very high Q devices such as those mentioned earlier may help with fundamental physics (section 1.3.3).

1.3.1/ $1/Q^4$ AND $f_0/2Q$

A typical quartz resonator used in many devices is a plano-convex disc (in order to trap the energy), coated with a metallic layer in order to actuate it piezoelectrically. Very

commonly, it is coated with a few nanometers of chromium (as it better adheres to the quartz than the subsequent gold layer) and about 100 nm-200 nm of gold (see Fig. 1.5).

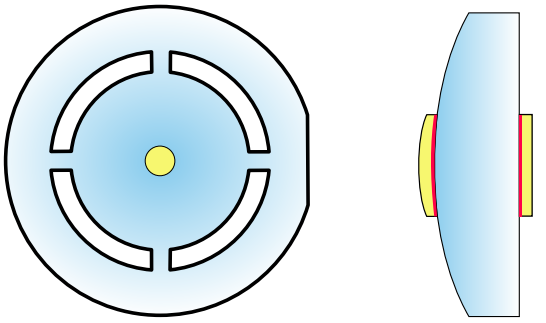

(a) Face view (b) Side view

Figure 1.5: *Typical plano-convex quartz crystal resonator used in many devices. Very commonly coated with a few nanometers of chromium (represented in red on Fig. 1.5b) on the quartz, in order for the* 100 nm-200 nm *layer of gold to better adhere on the whole structure. Note the plane on the front view on the right, which is typically made in order to keep track of a particular crystalline axis (commonly the* y *axis). Note that the size of the electrodes on the side view is greatly exagerated with respect to both the front view and the quartz size for visual clarity.*

Generally speaking, the Q factor is related to mechanical losses (they are proportional to $1/Q$) in the medium from diverse origins, which are influencing the total (unloaded) Q through the following relation (see for example [Bon, 2018], p30, and [Schröter, 2008] throughout):

$$\frac{1}{Q} = \sum_i \frac{1}{Q_i} = \frac{1}{Q_{\text{phonon-phonon}}} + \frac{1}{Q_{\text{thermoelastic}}} + \frac{1}{Q_{\text{scattering}}} + \frac{1}{Q_{\text{holders}}} + \frac{1}{Q_{\text{TLS}}} + \cdots \quad (1.13)$$

Q being linked with the losses of the system. The losses, in turn, can be linked with either intrinsic losses phenomena, that is, physical phenomena or with engineering phenomena[3]. As an illustration of the engineering losses, see Fig. 1.6 focusing on the geometrical design linked with the mechanical clamping losses as well as the on-quartz electrodes ddeposition losses; see Fig. 1.7 for some experimental data regarding losses of some of the resonators from Fig. 1.6, attributed by the authors to both the clamping and the coating influence (see [Galliou et al., 2016b])

It follows that the Q factor should have an influence on the general trend of the phase noise. Indeed, an empirical study of the power spectral density of the fractional frequency fluctuations at 1 s for different devices available from litterature has been made by Gagnepain (see Frequency Standards and Metrology [De Marchi, 1989], p. 151), as shown in Fig. 1.8a. It clearly displays a general tendency of the PSD to be proportional to $1/Q^4$. This means that following this general trend, taking naively the $6/Q^4$ dependency would

[3]The physical phenomena can include e.g. phonon-phonon interactions, thermoelastic interactions linked with the acoustical wave creating thermal gradients, scattering losses on the quartz' surface etc whereas the engineering phenomena include e.g. the device holders losses, the Two Level System (TLS) lossed linked with impurities in the quartz that may be engineered to migrate on the side of the crystal with an intense electric field, making use of Top High Quality quartz which limits the impurities and defects and is obtained with the first growth from a natural quartz germ.

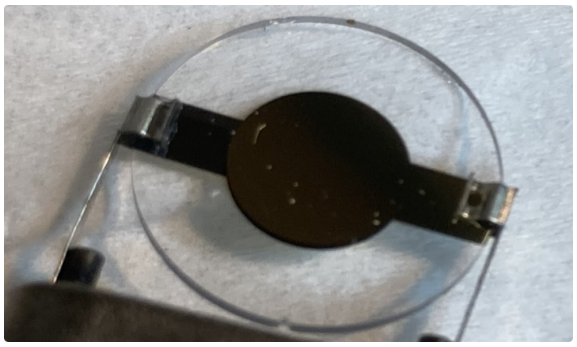

(a) Simple quartz

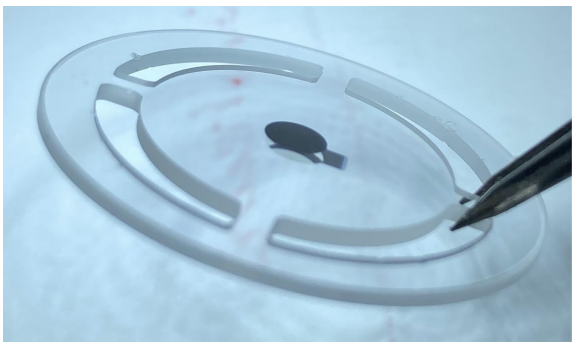

(b) QAS quartz

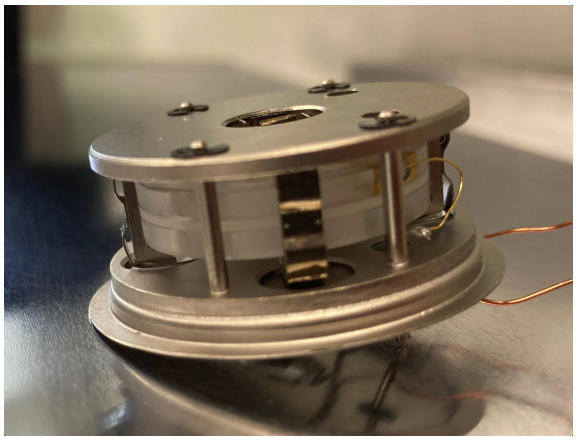

(c) BVA quartz

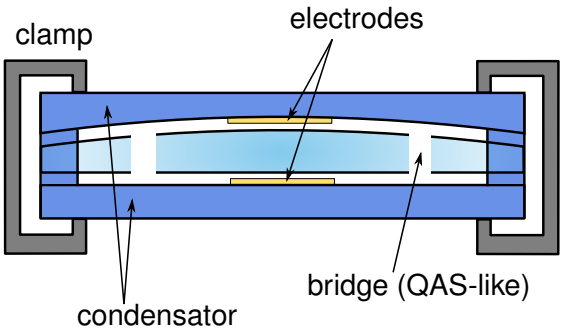

(d) BVA schematics

Figure 1.6: *An illustration of the different efforts to minimize the engineering losses. On Fig. 1.6a, a quartz is simply coated with rather big metallic electrodes and is suspended in the same fashion as a flag would be. On Fig. 1.6b, a Quartz Auto-Suspendu (QAS, "self-hanged quartz") is presented; the bridges permit to minimize the losses of energy of the acoustical mode, as the oscillations are better confined in the middle part. On Fig. 1.6c, a Boîter à Vieillissement Amélioré (BVA, "casing with improved aging") is presented. It presents the double advantage of conserving the same decoupling of the central vibrating part from the holding part like in Fig. 1.6b, but it also takes the electrodes off the quartz to coat the so-called condensators instead, which are two quartz pieces cut in the same crystallin cut as the resonator and which permit approaching the electrodes close to the resonator without directly coating it, see scheme on Fig. 1.6d*

lead for a $Q = 1 \times 10^9$ resonator to a PSD of the fractional frequency fluctuations at 1 Hz of $S_y(1\,\mathrm{Hz}) \approx 9 \times 10^{-36}\,\mathrm{dBrad^2\,Hz^{-1}}$ (see Fig. 1.8b). This would correspond to an Allan deviation floor of $\sigma_y(1\,\mathrm{s}) \approx 3.5 \times 10^{-18}$!

In addition to this effect, an unrelated improvement is also at stake. Indeed, as Eq. 1.10a indicates, the ν^{-3} noise is proportional to $1/Q^2$. Furthermore, the Leeson frequency $f_0/2Q$ that marks the change of the ν^{-3} noise to the ν^{-1} noise (in the phase fluctuations PSD) is smaller if Q is bigger. Under the assumption that the ν^{-1} noise would not differ between the room temperature where most quartz crystals are operated and the cryogenic temperature (around 4 K) at which the quartz resonators from [Galliou et al., 2013] need to be operated, an improvement in the $S_y(\nu < f_0/2Q)$ figure is to be expected. In-

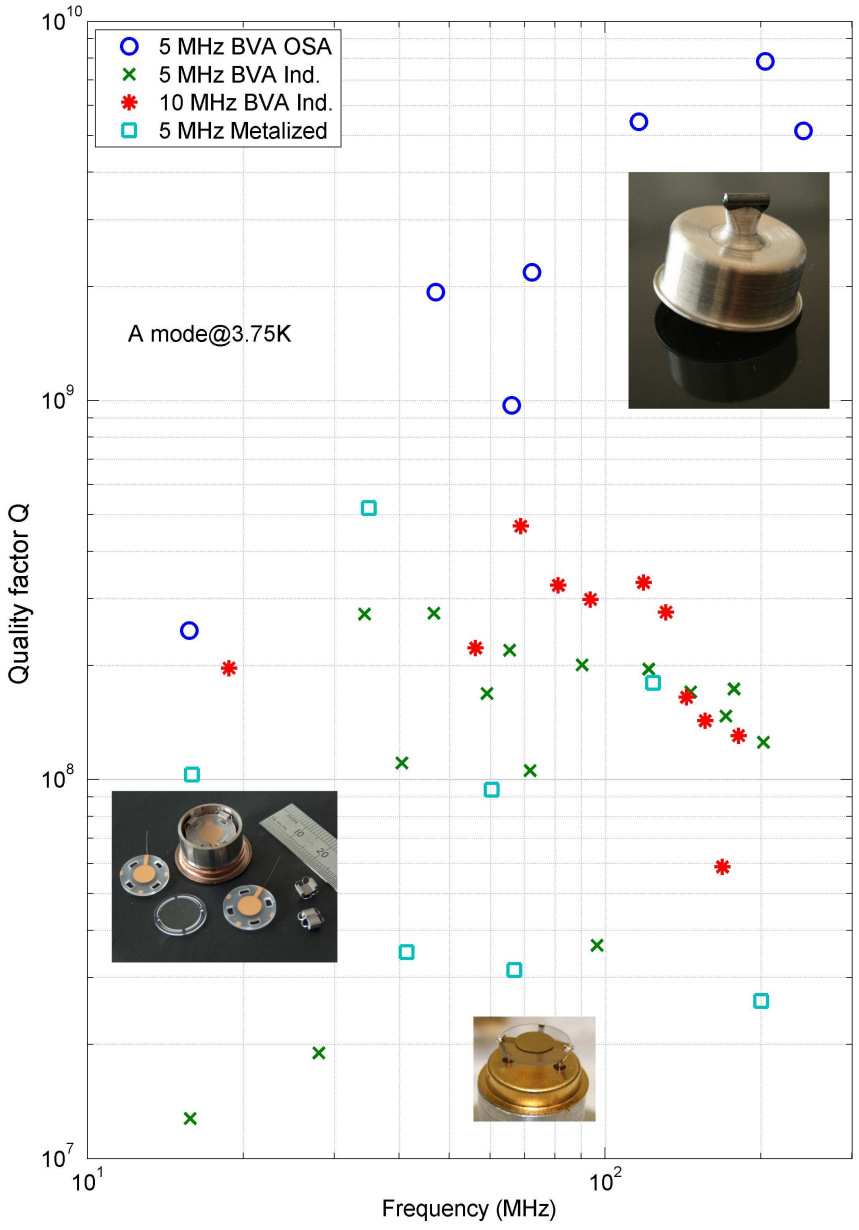

Figure 1.7: *Mechanical quality factor Q, plotted against the mechanical resonance frequency for several quartz crystal resonators. BVA stands for "Boîter à Vieillissement Amélioré" (see Fig. 1.6c), whereas OSA and BVA Industry are quartz resonator providers. The figure is taken from [Galliou et al., 2016b]. It shows that the losses (hence the quality factors) depend on whether the quartz is coated, and whether some work is done on decoupling the resonating part of the crystal from the clamping etc (see Fig. 1.6 for visual details about this point).*

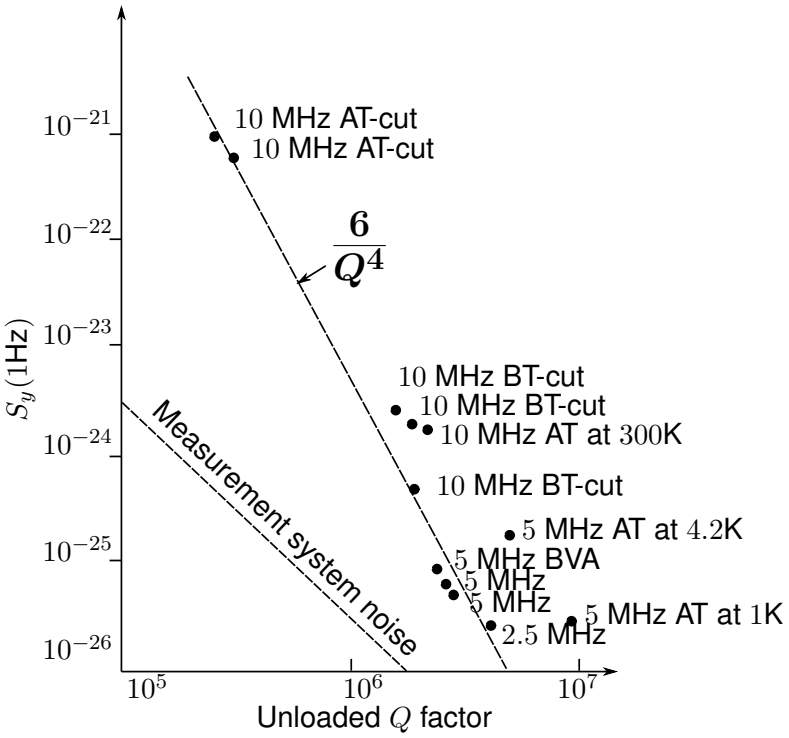

(a) Gagnepain

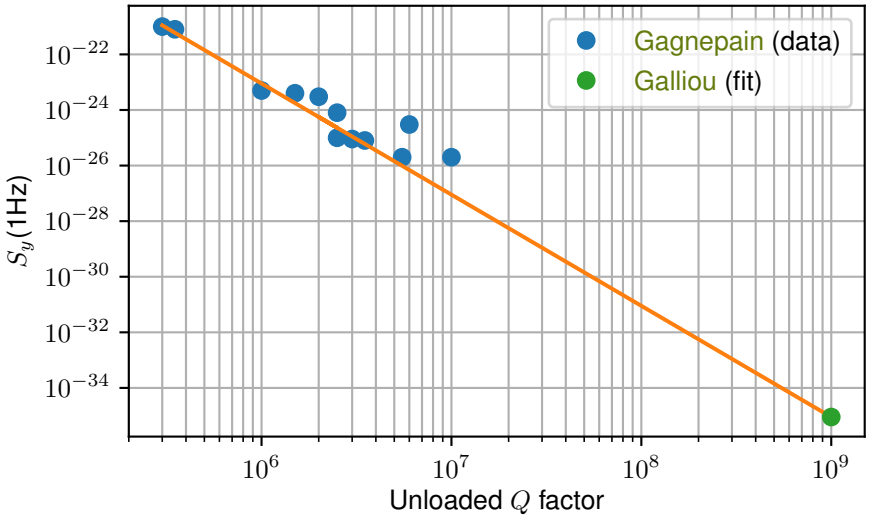

(b) Fit

Figure 1.8: *1.8a Graph taken from Gagnepain (see Frequency Standards and Metrology [De Marchi, 1989], p. 151), with experimental points from litterature of the time. Shows the general tendency of the power spectral density of the fractional frequency fluctuations to go as* $\frac{1}{Q^4}$*, with* Q *the quality factor of the resonator. 1.8b Fit of the same points, along with a* $Q = 1 \times 10^9$ *at cryogenic temperature device from [Galliou et al., 2013].*

deed, on Fig. 1.9, the Leeson frequency where the ν^{-1} and the ν^{-3} curves of the $S_\varphi(\nu)$

cross permits to establish the following relation between the coefficients for each slope:

$$a_{-3}f_L^{-3} = a_{-1}f_L^{-1} \tag{1.14}$$

Additionally, the PSD for the relative frequency fluctuations are related to the PSD of the phase fluctuations through:

$$S_y(\nu) = \frac{\nu^2}{f_0^2}S_\varphi(f) \tag{1.15}$$

On the other hand, the floor of the Allan variance for the relative frequency fluctuations is located in the area of the frequency flicker noise (i.e. the ν^{-1} slope on a $S_y(\nu)$ plot and ν^{-3} slope on a S_φ plot). It is formally written:

$$\sigma^2_{y\,\text{floor}} = 2\ln 2 S_y(f = 1\,\text{Hz}) \tag{1.16}$$

In order to express in a more specific form this last Eq. 1.16, let us rewrite Eq. 1.15 in the area of the frequency flicker noise, hence replacing S_φ in Eq. 1.15 by its value in the frequency flicker noise area (corresponding to the ν^{-3} slope) and making use of the relation in Eq. 1.14 for a_{-3}:

$$S_y(\nu \approx \nu_{\text{flicker}}) = \frac{\nu^2}{f_0^2}a_{-3}\nu^{-3} = \frac{a_{-1}f_L^2}{f_0^2}\nu^{-1} \tag{1.17}$$

Which permits to obtain from Eqs. 1.16 and 1.17 and by replacing the Leeson frequency by its value $f_L = f_0/2Q$ the Allan deviation floor:

$$\sigma_{y\,\text{floor}} = \sqrt{\frac{\ln 2}{2}a_{-1}} \times \frac{1}{Q} \tag{1.18}$$

By using this last Eq. 1.18 and the bibliography listed in section 1.2, with good quartz crystal resonators with accompanying packaging having typical $Q \approx 10^6$ (at room temperature) that amount to an Allan deviation floor of $\sigma_{y\,\text{floor}} \approx 10^{-13}$, it is reasonable to expect that with a device with a very high $Q \approx 10^9$ as mentioned in the begining of this section (three orders of magnitude higher Q), a typical Allan deviation floor of $\sigma_{y\,\text{floor}} \approx 10^{-16}$ (three orders of magnitude lower according to Eq. 1.18) can ideally be expected, provided the resonator environement is ideally controlled (e.g. vibrations, temperature fluctuations). This is what is shown on Fig. 1.9.

1.3.2/ Advantages of Optomechanical Actuation

As mentioned, because quartz is piezoelectric, it is most commonly actuated with an electric field, taking advantage of its piezoelectrical properties. Even some non-piezoelectric materials are sometimes stratified with some piezoelectric material in order to actuate them, creating a so-called High-overtone Bulk Acoustic Resonator (HBAR) (see for example [Ballandras et al., 2012] and [Baron et al., 2013]). There are, however, other possibilities that call for attention in actuating quartz resonators, such as thermal actuation (see [Dieulesaint et al., 1974] [Dieulesaint et al., 1989] [Dieulesaint et al., 1986]) and optomechanical actuation (see e.g. [Renninger et al., 2018]). The latter will be extensively discussed in this thesis, presenting a lengthier state of the art specifically for optomechanical interactions in section 4.2.1, and presenting in current section 1.3.2 its comparative

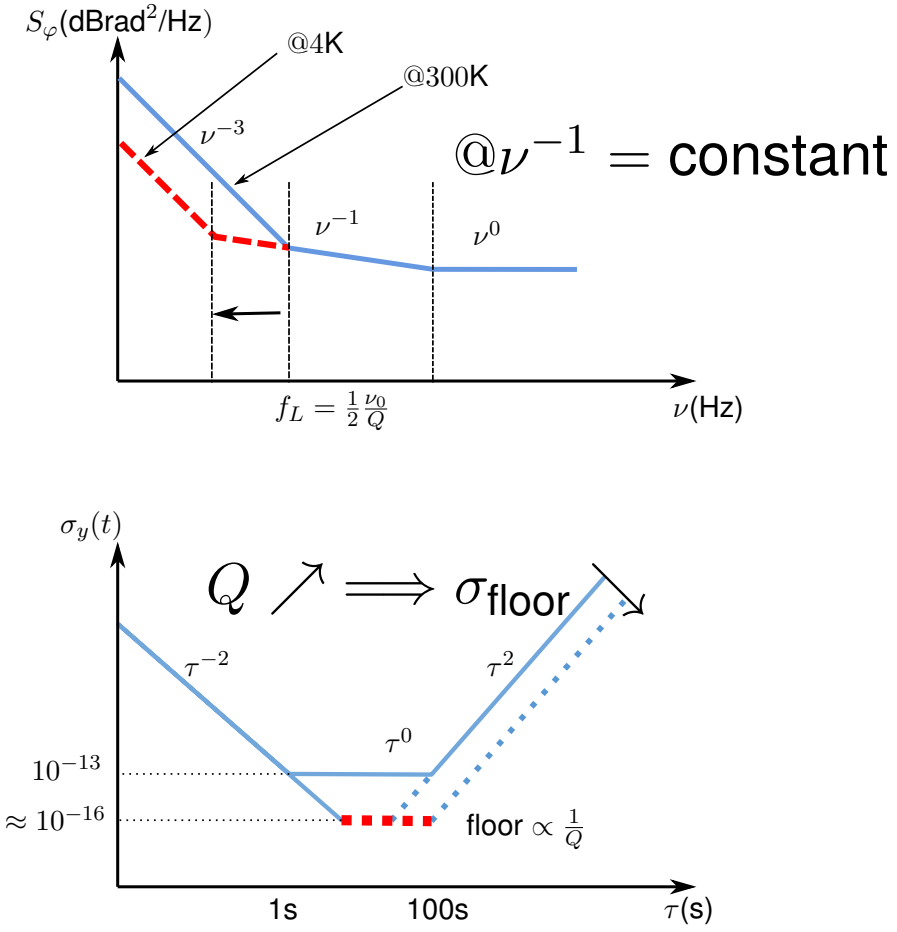

Figure 1.9: *Scheme of possible improvements for the Allan variance. See main text at the end of section 1.3.1 for details of the orders of magnitude.*

advantages with respect to piezoelectric actuation for plano-convex quartz crystal resonators.

The metallic electrodes typically deposited on quartz crystal resonators (see Fig. 1.5) readily constitute mirrors as well, especially since most metals in the near infrared are rather reflective (see for example [Echániz et al., 2014]). As such, it is only natural to investigate the possibility of using these electrodes as mirrors in order to achieve a Fabry-Perot cavity (see part 3), having in mind that this allows increasing the light intensity within the cavity, hence possibly increasing the total force exerted by wavepackets with any of the optical forces exerted (see part 4). A naive scheme of such optomechanical coupling is presented in Fig. 1.10 for conceptual understanding.

There are two main advantages to actuate the quartz resonator with the help of an optomechanical coupling, instead of using typical piezoelectrical properties of the quartz.

The first and most immediate one is the fact that cables going down the cryogenerator to electrically actuate the quartz are no longer required, therefore saving the technological efforts of stabilizing the signal through the small temperature (hence length and phase) variations, generally with a Pound scheme [Pound, 1946] (see for example [Grop et al., 2010], section 3.2.2). Indeed, considering a simplified model of only thermal fluctuations affecting the length of the wires (and hence the phase of the signal), con-

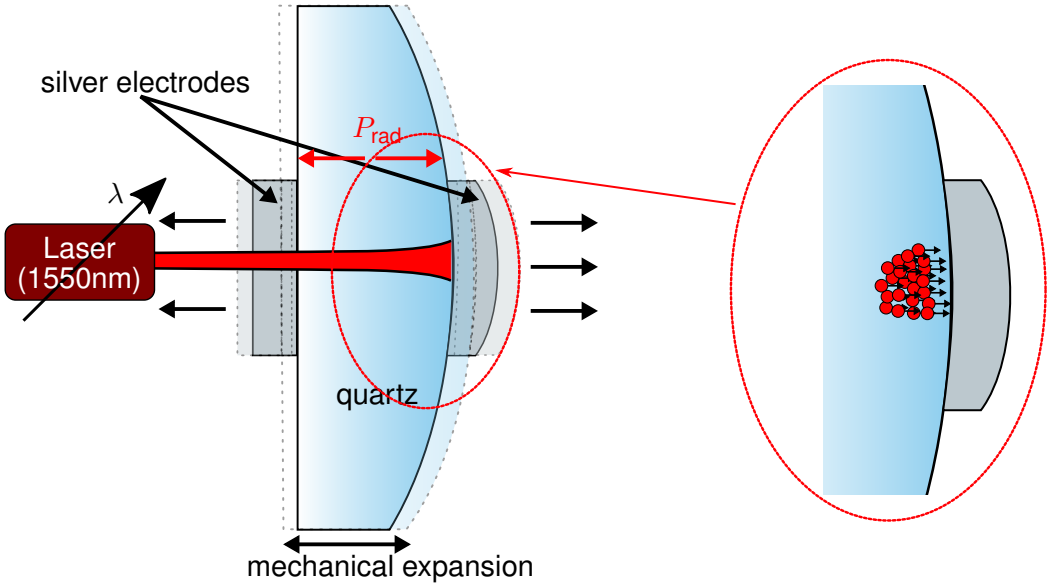

Figure 1.10: *Naive scheme of optomechanical coupling with radiation pressure. The incident light onto the quartz crystal resonator is amplified inside it, provided that the electrodes, constituting here mirrors, are at the right distance from one another with respect to the incoming wavelength (making it a Fabry-Perot cavity, see section 3.1). The pressure exerted by each individual wavepacket is therefore amplified and theoretically allows, under certain conditions discussed in part 4, the quartz crystal resonator to enter into mechanical resonance. Note that the size of the electrodes are greatly exagerated for visual clarity.*

sidering a cable length of approximately $L_0 = 3\,\mathrm{m}$, a loaded Q factor of approximately $Q = 5 \times 10^8$ (half ot the best expected factors), a 50 MHz signal yielding a wavelength of $\lambda = c/\nu = 5.99\,\mathrm{m}$, and taking the thermal expansion coefficient of the cable to be $\alpha_{\mathrm{Cu}} = 1.7 \times 10^{-5}\,\mathrm{K}^{-1}$, we get a phase fluctuation along the cable of:

$$\frac{\Delta\nu/\nu_0}{\Delta T} = \frac{2\pi L_0}{Q_L \lambda_0}\alpha_{\mathrm{Cu}} \approx 1.06 \times 10^{-13}\,\mathrm{K}^{-1} \tag{1.19}$$

which could indeed limit the expected instability of the quartz crystal resonator. Furthermore, the Radio-Frequency (RF) Pound to stabilize these cable length fluctuations implies using a circulator (the optical equivalent is a polarized beam-splitter cube). Although they are easily available commercially for frequencies in the GHz range, they become much more scarce under some hundred MHz. This therefore makes this correction rather arduous in the aimed range of frequencies for our device (in the 5 MHz-100 MHz range, see [Galliou et al., 2013]).

The second advantage, which is conceptually more important, is that it permits to consider actuation of non-piezoelectric material with the help of optomechanics. Some materials that show rather promising mechanical properties could therefore be investigated with this method, such as sapphire (Corundum, Al_2O_3) (see [Uchiyama et al., 1999], [Rowan et al., 2000], [Wang et al., 2010] or more recently [Bourhill et al., 2015]), silicon (see [Nawrodt et al., 2008], [Nietzsche et al., 2006] or [Schröter, 2008]) or calcium fluoride (see [Schröter, 2008]).

1.3.3/ FUNDAMENTAL PHYSICS

The very high quality factors previously reported in section 1.3.1 permits some fundamental physics applications.

As an example, [Bushev et al., 2019] has shown that very high quality factor Q permits to have a better numerical insight on upper bounds for quantum gravity's corrections to existing theory, therefore allowing finer testing for theory than previously reported.

Also directed towards a fundamental physics theory limits, a paper by [Lo et al., 2016] shows that using a high Q quartz crystal resonator has also helped improving by 1-3 orders of magnitude previous bounds to Lorentz symmetry breaking. In fact, both these last articles even have a perspective for further improvements using even higher Q in cryogenic temperatures (in the same way this thesis work is expecting an improvement of stability for metrological applications based on the improvement of the mechanical quality factor Q, see previous section 1.3.1).

Another possible use for high Q quartz resonators is presented by [Kotler et al., 2017], and consists in trapping an ion or an electron close to the quartz to couple the charged particle's motion to the quartz (because of its piezoelectricity) in order to transfer its quantum properties for Quantum Information Processing (QIP) applications.

In this introduction, we have seen the basics of oscillators and some relations about these systems. We also have seen a brief state state of the art of these oscillators of different nature, e.g. acoustical, dielectric, atomic. Within the group of acoustical resonators-based oscillators, quartz resonators have a particular status as their use is widely spread. They have been shown, under certain circumstances, to display exceptional quality factors which allow for very good performances in terms of fractional frequency instability. This allows to expect Allan deviation floor in the order of some $10^{-}16$. It is necessary to lead an experimental measurement to assess more accurately the integration time range within which these performances are realistically achievable. This goes beyond the scope of this thesis work.

We also have shown that a cableless actuation is preferable, through e.g. an optomechanical actuation. To this end, the immediate presence of a Fabry-Perot cavity within the quartz crystal resonator, due to its metalic electrodes, is an advantage. It therefore calls for a careful study of the optical properties of these optical cavities (see chapter 3) before assessing their use for optomechanical actuation (see chapter 4).

2

GENERAL REMINDERS

This chapter contains several short reminders and basic equations regarding the quartz' cuts and continuum mechanics' basic equations. A short description of the design of the quartz resonators we use is also given.

2.1/ QUARTZ CUT

2.1.1/ CUT FORMALISM

Because quartz is anisotropic with trigonal symmetry 32, it can be cut along different directions of its crystalline structure to obtain different properties. There exists several IEEE (Institute of Electrical and Electronics Engineers) standards to define the piezoelectric properties and the crystalline cuts, where the main difference is the sign convention for the piezoelectric constants.

Throughout this thesis, we will adopt the convention from [IEEE, 1987]. Several cuts are shown in Fig. 2.1. The cuts are defined with the help of two main angles, φ and θ. When both angles are 0, the cut is a Y cut i.e. perpendicular to the Y axis (see Fig. 2.1b).

1. The first angle φ is the angle of rotation around the Z axis, thus defining new axes X' and Y' ($Z' = Z$). Note that $0 < \varphi < 30°$.
2. The second angle θ is the angle of rotation around the X' axis, thus defining new axes Y'' and Z'' ($X'' = X'$). Note that $-90° < \theta < 90°$.

Several cuts angles and main characteristics are listed in Table 2.2.

2.1.2/ ROTATED CUT TENSORIAL CHARACTERISTICS

Mechanical and electrical characteristics of the quartz can be expressed through tensorial formalism, which, due to quartz symmetry, can be broken to matricial writing. These characteristics are, for example, the dielectric tensor ϵ_{ij}, piezoelectric contants e_{ijk} and mechanical stiffness C_{ijkl}. Useful quartz characteristics are explicitely and numerically given in Annex A, and consist, throughout this thesis, of three type of tensors: second, third and fourth order. Because of the crystal symmetry, it is convenient to use the Voigt notation convention, summed up in table 2.1: With this notation, the tensors have the

i,j	1	2	3
1	1	6	5
2		2	4
3			3

Table 2.1: *Voigt notation formalism.* $i,j=1,2,3$ *and so that the combination of* ij *is reported at the intersection of the correspond row and column. For example,* $i=1$ *and* $j=3$ *gives the corresponding Voigt notation* 5*. The table is only filled on the upper half, as it is symmetrical.*

following form:

$$\epsilon_{ij} = \begin{pmatrix} \epsilon_1 & 0 & 0 \\ 0 & \epsilon_1 & 0 \\ 0 & 0 & \epsilon_3 \end{pmatrix} \tag{2.1a}$$

$$e_{ijk} = \begin{pmatrix} e_1 & -e_1 & 0 & e_4 & 0 & 0 \\ 0 & 0 & 0 & 0 & -e_4 & -e_1 \\ 0 & 0 & 0 & 0 & 0 & 0 \end{pmatrix} \tag{2.1b}$$

$$C_{ijkl} = \begin{pmatrix} C_{11} & C_{12} & C_{13} & C_{14} & 0 & 0 \\ C_{12} & C_{11} & C_{13} & -C_{14} & 0 & 0 \\ C_{13} & C_{13} & C_{33} & 0 & 0 & 0 \\ C_{14} & -C_{14} & 0 & C_{44} & 0 & 0 \\ 0 & 0 & 0 & 0 & C_{14} & \frac{C_{11}-C_{12}}{2} \end{pmatrix} \tag{2.1c}$$

By default, these characteristics are expressed in the non-rotated Y cut. However, choosing another cut requires to rotate the characteristics. The way to do such a rotation is exposed in [Auld, 1973] p.74 or in [Bon, 2018] p.57. Taking the angles as before, we define the 3×3 matrix:

$$a_{ij} = \begin{pmatrix} \cos(\varphi) & \sin(\varphi) & 0 \\ -\cos(\theta)\sin(\varphi) & \cos(\theta)\cos(\varphi) & \sin(\theta) \\ \sin(\theta)\sin(\varphi) & -\sin(\theta)\cos(\varphi) & \cos(\theta) \end{pmatrix} \tag{2.2}$$

As well as the 6×6 matrix:

$$M = \left(\begin{array}{ccc|ccc} a_{11}^2 & a_{12}^2 & a_{13}^2 & 2a_{12}a_{13} & 2a_{11}a_{13} & 2a_{11}a_{12} \\ a_{21}^2 & a_{22}^2 & a_{23}^2 & 2a_{22}a_{23} & 2a_{21}a_{23} & 2a_{21}a_{22} \\ a_{31}^2 & a_{32}^2 & a_{33}^2 & 2a_{32}a_{33} & 2a_{31}a_{33} & 2a_{31}a_{32} \\ \hline a_{21}a_{31} & a_{22}a_{32} & a_{23}a_{33} & a_{22}a_{33}+a_{23}a_{32} & a_{23}a_{31}+a_{21}a_{33} & a_{21}a_{32}+a_{22}a_{31} \\ a_{31}a_{11} & a_{32}a_{12} & a_{33}a_{13} & a_{32}a_{13}+a_{33}a_{12} & a_{33}a_{11}+a_{31}a_{13} & a_{31}a_{12}+a_{32}a_{11} \\ a_{11}a_{21} & a_{12}a_{22} & a_{13}a_{23} & a_{12}a_{23}+a_{13}a_{22} & a_{13}a_{21}+a_{11}a_{23} & a_{11}a_{22}+a_{12}a_{21} \end{array}\right) \tag{2.3}$$

where a_{ij} designates the corresponding matrix element from Eq. 2.2. Note that an emphasis has been put on the pattern of the matrix by adding lines to divide it into four parts.

With these matrices, we can now write the way to rotating the matrix notation of the

Cut	θ	φ	Main interest
AT	35°	0°	TC at room temperature
BT	−49°	0°	TC at room temperature
SC	33.88°	22.4°	Stress Compensated - TC at room temperature and has a weak stress-frequency effect
IT	34°	19°	TC at room temperature
LD	34°	27°	Low Defect - low sensitivity of the resonance frequency to exciting power
FC	34°	15°	Frequency Compensated - TC for a large temperature range
SBTC	−34.5°	16.3°	Low sensitivity of the B mode to pressure. C mode used as a pressure sensor
X+5	5°	30°	TC at 4 K (see [Bon, 2018])

Table 2.2: *Table summing up some common quartz cuts and their main characteristics, taken from [Bon, 2018]. TC stands for "Temperature Compensated". The angles are defined as in the IEEE standard [IEEE, 1987]. Note that the cuts angles are defined within a certain tolerance, generally within* 1°*, as one adapts the exact angle to the desired result (e.g. workig temperature).*

tensors defined in Eq. 2.1:

$$\epsilon'_{ij} = a\epsilon_{ij}a^T \tag{2.4a}$$
$$e'_{ijk} = ae_{ijk}M^T \tag{2.4b}$$
$$C'_{ijkl} = MC_{ijkl}M^T \tag{2.4c}$$

This is exactly what we do with a python routine in Annex A in order to obtain the SC-cut characteristics from the non-rotated Y-cut characteristics, with the proper angles φ and θ.

2.2/ QUARTZ DESIGN

Earlier development and ground work concerning optomechanical coupling in a quartz crystal resonator in our group come from [Bon, 2018]. Indeed, as we have seen in section 1.3.2, one of the reasons why optomechanical coupling is particularly adapted is for avoiding noise from the thermal expansion of the cables. However, to that end, it is important that also the quartz crystal resonator be as insensitive as possible to thermal fluctuations. The quartz resonator is a priori sensitive to temperature for any given resonance mode, so that when looking at the frequency vs temperature curve, minimizing this effect implies to be at a local minimum (with null derivative). This happens for certain modes, and specifically at certain angles in the quartz cut in its crystalline structure. For example, the thickness shear (C) mode is temperature-compensated for the 3rd overtone with an SC cut. See Table 2.2 for some quartz cut example with their main characteristic, and section 2.1 for a formal definition of the quartz cut and subsequent characteristics.

As shown in [Bon, 2018] (see Table 2.2), at cryogenic temperatures of around 4 K, a temperature-compensated cut was found for an X+5 quartz. Ultimately, this is therefore the cut we look to implement towards an ultrastable clock. However, production of (high

quality factors) quartz crystal is not a trivial task, so that as a first approach to light-induced mechanical oscilation (see part 4) we mostly use SC-cut quartz resonators which were commercially available from former company BVA industries.

The quartz crystal resonators we use throughout this thesis are typically with geometrical characteristics detailed in Fig. 2.2. As we shall see in section 3.1.3, these geometrical characteristics are compatible with optical use, and they also are compatible with energy trapping for mechanical resonance (see [Stevens et al., 1986]). Our theoretical approach to describe the dynamics of the quartz crystal throughout will mainly be based on continuum mechanics, for which some basic reminders and formulæ are given in the next section.

2.3/ MECHANICAL EQUATIONS

In continuum mechanics, it is possible to express the equations governing the dynamic of the solid in a tensorial form. Following the notation and conventions of Royer in [Royer et al., 2000a] chapter 3, we can write the fundamental Equation Of Motion (EOM):

$$\rho \frac{\mathrm{d}^2 u}{\mathrm{d}t^2} = \sum f_{vol} \tag{2.5}$$

where ρ is the material's mass density and f_{vol} and u are the volumic forces applied and the displacement at each point, respectively.

We can separate the forces acting on the material as an instrinsic reaction force, following the (small) deformation of any solid, and a force caused by the possible presence external fields. We write, with the usual Einstein convention of summation over repeated index and where every small-letter index is for each spatial direction (i.e. $i, j, k, l = 1, 2, 3$):

$$f_i^{in} = \frac{\mathrm{d}T_{ij}^{in}}{\mathrm{d}x_j} \tag{2.6}$$

$$T_{ij}^{in} = C_{ijkl} S_{kl} + \eta_{ijkl} \frac{\mathrm{d}S_{kl}}{\mathrm{d}t} \tag{2.7}$$

f_i^{in} is the intrinsic reaction volumic force, T_{ij}^{in} is the stress tensor following a material deformation (in the linear regime, with small deformations), x_j is the j^{th} spatial coordinate. Eq. 2.7 is Hooke's law with losses (see [Royer et al., 2000a] Eq. 4.62), C_{ijkl} and η_{ijkl} are the stiffness and viscosity tensor which apply to the strain S_{kl} and strain rate $\dot{S_{kl}}$.

As we shall see throughout this thesis, multiple external fields can be applied through different means and result in different reactions from within the solid. The main physical processes which give rise to different effects are thermal, mechanical and electrical (see [Nye, 1984], chapter 10). However, only some of the properties will be taken into account throughout this thesis at different times when they become sufficiently important to be included in the theoretical treatment.

Quartz crystal is not pyroelectric because of crystal symmetry (see [Nye, 1984], remark after Eq. 60 in chapter 10). This means that there is no primary relation effect between thermal and electrical field.

It is possible to follow energy conservation considerations in this piezoelectric thermoelasticity problem, in the absence of ultrafast-heating (see [Li et al., 2020]), and obtain all

the interesting first order terms for the mechanical field and the electric displacement field (omitting the pyroelectric terms in virtue of the preceding remark):

$$\begin{cases} T_{ij} = C_{ijkl}^{E,T} S_{kl} + \eta_{ijkl} \dfrac{\partial S_{kl}}{\partial t} - e_{kij}^{T} E_k + \beta_{ij}^{E} \theta & \text{(2.8a)} \\ D_i = e_{ijk}^{E} S_{jk} + \epsilon_{ij}^{S} E_j & \text{(2.8b)} \end{cases}$$

where θ is the temperature increment, $C_{ijkl}^{E,T}$ is the elastic tensor at constant electric and temperature field, e_{kij} is the piezoelectric tensor and β_{ij}^{E} is the stress-temperature at constant electric field [1] and ϵ_{ij}^{S} is the dielectric tensor at constant strain. The mechanical losses have been included in Eq. 2.8a.

Higher order effects can also be taken into account, which most notably include the radiation pressure and electrostrion (see section 4.2). These effects can be shown (see e.g. [Rakich et al., 2010]) to be respectively written, in addition to the previously given total stress:

$$T_{ij}^{es} = -\frac{\epsilon_0}{2} \epsilon_{ml} p_{lkij} \epsilon_{kn} E_m E_n \quad \text{(2.9a)}$$

$$T_{ij}^{rp} = D_i E_j - \frac{1}{2} D_i E_j \delta_{ij} + H_i B_j - \frac{1}{2} H_i B_j \delta_{ij} \quad \text{(2.9b)}$$

where D_i and E_i designate the electric displacement and electric field, H_i and B_i the magnetic fields ($H_i = \mu_{ik} B_k$ with μ_{ij} the magnetic permability), ϵ_{ij} the dielectric permittivity tensor, p_{ijkl} is the elasto-optic tensor and δ_{ij} is the kronecker delta. See more details in section 4.2.

[1] Note that the stress-temperature coefficients arise because the internal strain S_{ij}^{in} is related to the internal stress T_{ij} throuh the elastic coefficients. Therefore, upon writing $T_{ij} = T_{ij}^{\text{in}} = C_{ijkl}^{\text{in}} S_{ij}$, one writes that $T_{ij} = C_{ijkl}(S_{kl} - \alpha_{kl}\theta)$ with α_{kl} the thermal expansion coefficients. From this, we therefore write the stress-temperature coefficients as $\beta_{ij} = C_{ijkl}\alpha_{kl}$.

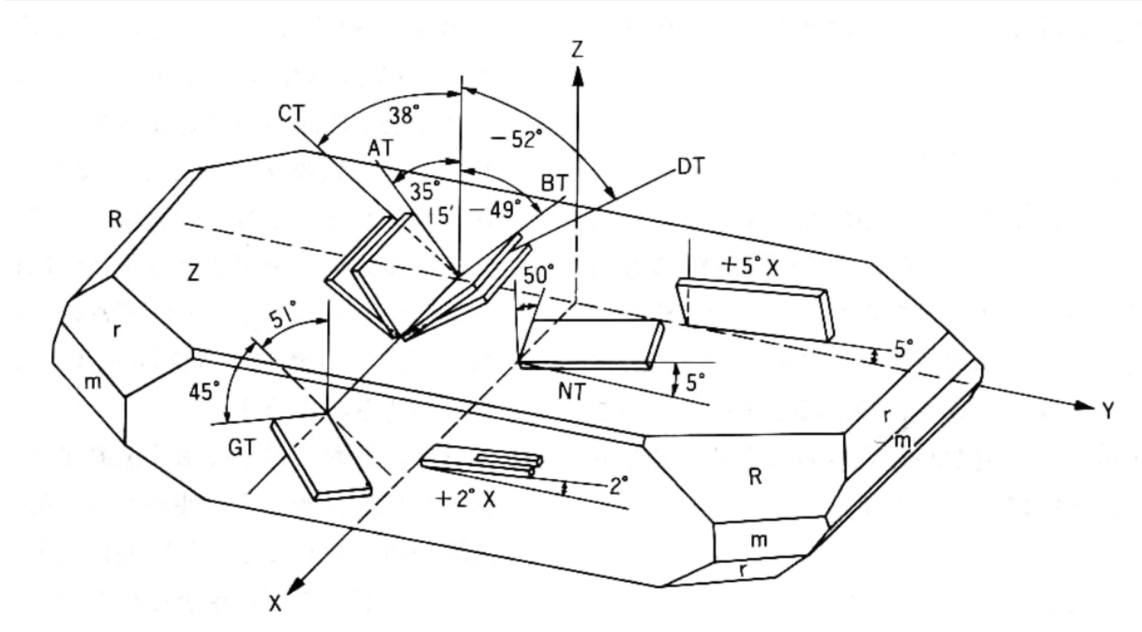

(a) Quartz cuts

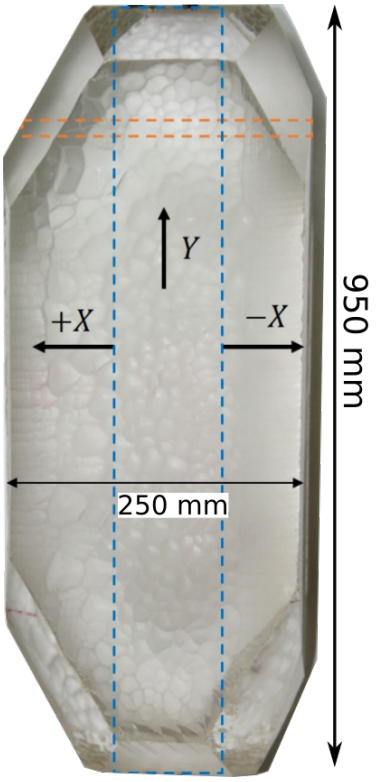

(b) Quartz crystal front view

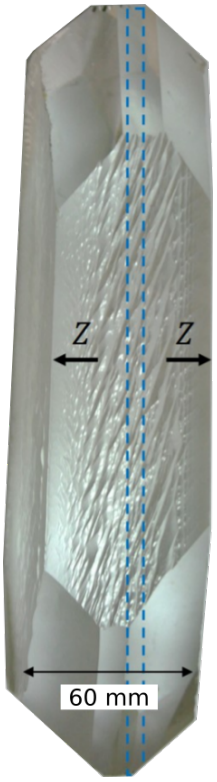

(c) Quartz crystal side view

Figure 2.1: *Quartz cuts, with IEEE 1949 standard on piezoelectricity for the angles (taken from [Bon, 2018]. Front view (Fig. 2.1b) and side view (Fig. 2.1c) of a synthetic quartz crystal, with crystallographic axes X, Y and Z, as well as crystal typical dimensions. The blue dotted line indicates the position of the initial quartz from which the crystal has grown, and the orange dotted line indicate a Y-cut.*

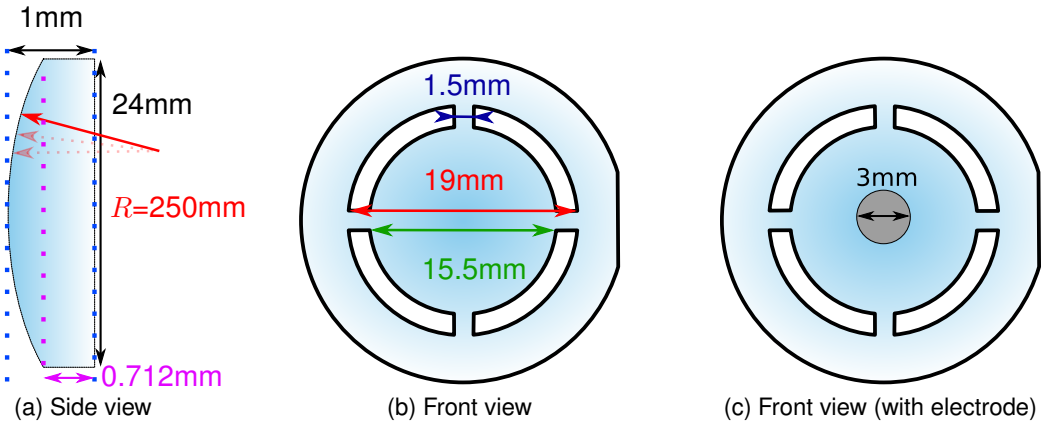

(a) Side view (b) Front view (c) Front view (with electrode)

Figure 2.2: *Side view and front view of the quartz, and its accompanying geometrical properties. R designates the radius of curvature of the convex side of the quartz.*

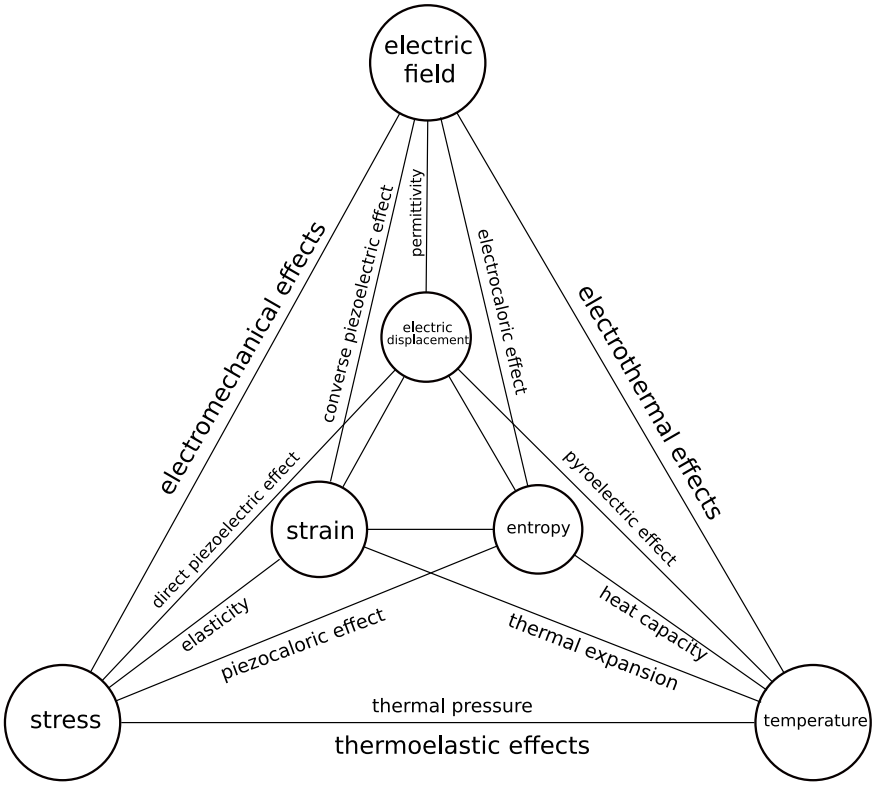

Figure 2.3: *All a priori possible mechanical, electrical and temperature-related effects affecting a solid, summed up in a graph, taken from [Nye, 1984] Fig. 10.1a.*

3

QUARTZ CRYSTAL RESONATOR USED AS AN OPTICAL CAVITY

In this chapter, we establish the basic descriptive framework for the quartz crystal resonator used as a Fabry-Perot optical cavity. To this end, we show the theoretical developments of both the ideal three-layers Fabry-Perot cavity and the absorptive mirrors cavity. We then proceed to an experimental study of these absorptive cavities, with a measurement campaign of the particular characteristics of the absorptive mirrors cavities with several depositions types and thicknesses. Finally, we give the description of a novel method to extract the refractive index from the deposited thin films.

3.1/ FABRY-PEROT CAVITY

3.1.1/ BIREFRINGENCE + MEASUREMENTS

Birefringence is defined as the property of a material to have a refractive index which depends on the incident light's polarization. Crystalline quartz is a birefringent material (see for example [Shields et al., 1956]). It is a trigonal-symmetric birefringent material with symmetry 32 around the optical axis z (see for example [Rosenbaum, 1988] part 2.5, [Royer et al., 2000a] vol.1 part 2.2.3 or the IEEE standard on piezoelectricity [IEEE, 1987]) , which leads to different values for the refractive index n and the dielectric tensor ϵ. Fig. 3.1 illustrates these differences depending on the angle θ between the x_3 vector of the quartz cut and the z axis of the crystalline frame.

The most general way to express the refractive index along a specific direction consists in writing that if $\hat{\mathbf{e}}$ is the direction along which the field of interests is polarized, then the refractive index for a non-magnetic material [1] is given by

$$n_d^2 = \sum_{i=1}^{i=3} \sum_{j=1}^{j=3} e_i e_j \epsilon_{ij} \tag{3.1}$$

with ϵ the relative dielectric tensor. In the case of the propagation direction being along the x_3 direction with an angle ψ from the Z-cut, the refractive index of the major axis yields (see Fig. 3.1):

$$n(\psi) = n_0 + \Delta n \sin^2(\psi) \tag{3.2}$$

[1] The most general expression for the refractive index is $n^2 = \sum_{i,j,k=1}^{3} e_i \epsilon_{ij} \mu_{jk} e_k$ where ϵ is the relative dielectric constant and μ the relative magnetic susceptibility constant.

where $\Delta n = n_e - n_0$. Throughout this thesis however, the more common situation will be a propagation along the x_2 axis and an angle θ (in the double rotated cut [2]) with respect to the non-rotated Y-cut, which permits to write that in this case, the refractive index yields:

$$n(\theta) = n_e - \Delta n \sin^2(\theta) \tag{3.3}$$

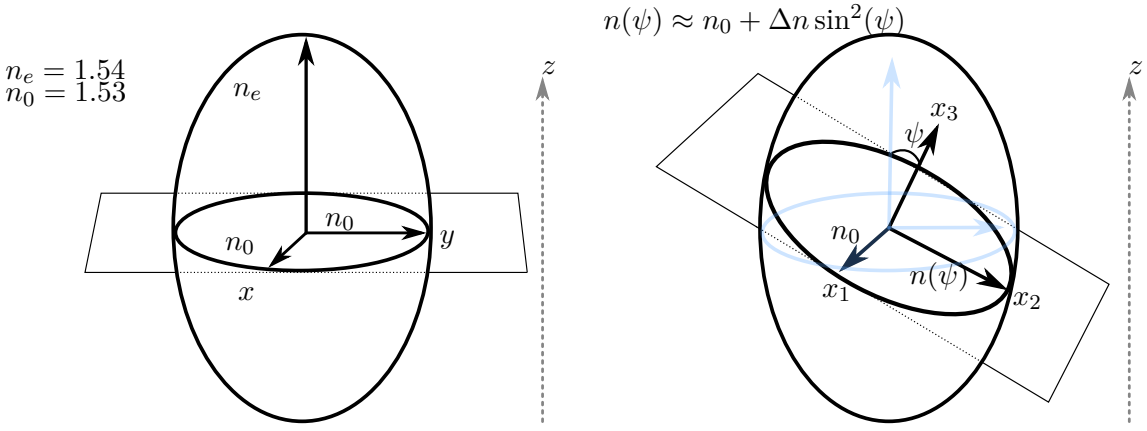

(a) Non-rotated cut

(b) Rotated cut

Figure 3.1: *Scheme of birefringence for quartz crystal with a beam propagating along x_3, with the ellipsoid of indices in the case of a non-rotated cut with respect to the crystalline axes in Fig. 3.1a and with an angle ψ (with respect to the z axis, for a rotation aroud the x axis) in Fig. 3.1b. In Fig. 3.1a, the cartesian axis of the crystal cut x_1, x_2, x_3 and the crystalline frame x, y, z coincide. In Fig. 3.1b, they do not coincide and the quartz-cut frame has been indicated in light blue. The indicated ordinary and extraordinary refractive index values $n_0 = 1.53$ and $n_e = 1.54$ are taken for optical wavelengths. See the most general formulation for the refractive index along any direction in Eq. 3.1. Note that the apparent anisotropy is greatly exagerated for visual clarity.*

This has, of course, extensive influence on a Fabry-Perot cavity. Indeed, following Eq. 3.1, the polarization will define whether a particular frequency will indeed resonate or not, as the refractive index influences the optical path and therefore the overall phase conditions along propagation for a specific wavepacket (see Eq. 3.17, the resonance frequency is a multiple of the Free Spectral Range (FSR) which depends on n the refractive index). In the following, a specific linear polarization along a particular (ordinary or extraordinary) axis will therefore be considered.

3.1.2/ THREE LAYERS PLANAR CAVITY

3.1.2.1/ WAVES AMPLITUDES

Let us start by consering a typical plano-plano Fabry-Perot cavity in an isotropic non-magnetic material without losses and with no alignment mismatch, as in Fig. 3.2. The

[2] Note that because the rotations are non-commutative and that the quartz cut are defined (see chapter 2) with a first rotation around Z by an angle φ and then around x_1' (the rotated x_1 vector) by an angle θ, the vector x_1' will always be in the initial equatorial plan and have an index n_0, and x_2'' (x_2 after the two rotations) will depend only on θ and not on φ for a given propagation direction along e.g. x_2.

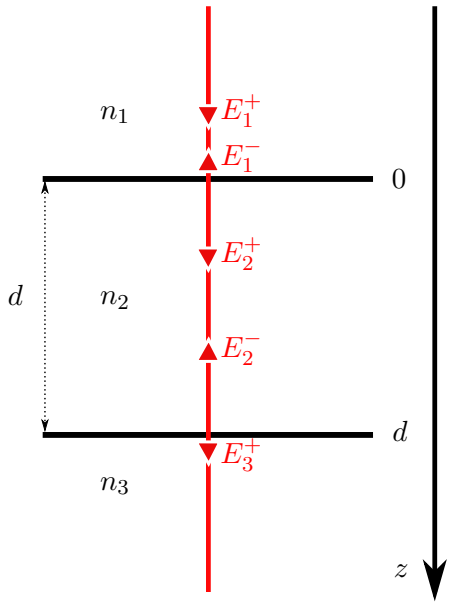

Figure 3.2: *Three layers optical cavity, with no entrance angle and therefore no misalignment. Each medium is represented by its refractive index n_i ($i = 1, 2, 3$). The two black lines represent the media interfaces, which are separated by a distance d.*

three media are therefore separated by two interfaces, and each medium is represented by its refractive index n. Let us represent the electric fields at each point by some co-propagating and counter-propagating plane wave:

$$E_i^+(z,t) = A_i e^{i(\omega t - kz)} \tag{3.4a}$$
$$E_i^-(z,t) = A_i e^{i(\omega t + kz)} \tag{3.4b}$$

where A_i is the amplitude of the i^{th} electric field, k the wavevector for the field and z its position along the z axis (see Fig. 3.2).

Omitting the time dependance in the following equations, the conditions of electric field conservation at the interfaces are written:

$$E_1^-(0) = r_{12}E_1^+(0) + t_{21}E_2^-(0) \tag{3.5a}$$
$$E_2^+(0) = t_{12}E_1^+(0) + r_{21}E_2^-(0) \tag{3.5b}$$
$$E_2^-(d) = r_{23}E_2^+(d) \tag{3.5c}$$
$$E_3^+(d) = t_{23}E_2^+(d) \tag{3.5d}$$

where where used the Fresnel coefficients:

$$r_{ij} = \frac{n_i - n_j}{n_i + n_j} \text{ the reflection coefficient} \tag{3.6a}$$
$$t_{ij} = \frac{2n_i}{n_i + n_j} \text{ the transmission coefficient} \tag{3.6b}$$

at the interface between media i and j. The so called Stokes Relations relate the reflection and transmission coefficient at an interface:

$$r_{12}^2 + t_{12}t_{21} = 1 \tag{3.7a}$$
$$r_{12} = -r_{21} \tag{3.7b}$$

Further developing and finding the expected amplitudes for the differents fields (see Fig. 3.2) requires to inject the field forms from Eqs. 3.4 in the boundary conditions equations in Eqs. 3.5:

$$A_1^- = r_{12}A_1^+ + t_{21}r_{23}e^{-2ikd}A_2^+ \tag{3.8a}$$
$$A_2^+ = t_{12}A_1^+ + r_{21}r_{23}e^{-2ikd}A_2^+ \tag{3.8b}$$
$$A_2^- e^{ikd} = r_{23}A_2^+ e^{-ikd} \tag{3.8c}$$
$$A_3^+ e^{-ikd} = t_{23}A_2^+ e^{-ikd} \tag{3.8d}$$

Solving this system after some straightforward calculation, by replacing and expressing each amplitude in function of A_1^+, the input field (which is supposed known), yields:

$$A_1^- = \left(r_{12} + \frac{t_{12}t_{21}r_{23}e^{-2ikd}}{1 - r_{21}r_{23}e^{-2ikd}}\right)A_1^+ \tag{3.9a}$$
$$A_2^+ = \left(\frac{t_{12}}{1 - r_{21}r_{23}e^{-2ikd}}\right)A_1^+ \tag{3.9b}$$
$$A_2^- = \left(\frac{t_{12}r_{23}e^{-2ikd}}{1 - r_{21}r_{23}e^{-2ikd}}\right)A_1^+ \tag{3.9c}$$
$$A_3^+ = \left(\frac{t_{12}t_{23}}{1 - r_{21}r_{23}e^{-2ikd}}\right)A_1^+ \tag{3.9d}$$

Now, in order to find the well known formulas for the Fabry-Perot cavity, let us consider the more specific case where the media 1 and 3 are equal. In this case, the coefficients reduce to $r \equiv r_{12} = -r_{21}$ and $t \equiv t_{12}$ and $t' \equiv t_{21}$. We can therefore rewrite Eqs. 3.9 with the use of the Stokes relations 3.7 and after a few simplifications the amplitudes can be written:

$$A_1^- = r\left(\frac{1 - e^{-2ikd}}{1 - r^2e^{-2ikd}}\right)A_1^+ \tag{3.10a}$$
$$A_2^+ = \left(\frac{t}{1 - r^2e^{-2ikd}}\right)A_1^+ \tag{3.10b}$$
$$A_2^- = \left(\frac{-tre^{-2ikd}}{1 - r^2e^{-2ikd}}\right)A_1^+ \tag{3.10c}$$
$$A_3^+ = \left(\frac{tt'}{1 - r^2e^{-2ikd}}\right)A_1^+ \tag{3.10d}$$

3.1.2.2/ TRANSMITTED INTENSITY

Taking the square of Eq. 3.10d , we can find the transmitted intensity through the Fabry-Perot cavity:

$$I_t(\lambda) \equiv I_3^+ = \left|A_3^+\right|^2 = \frac{T^2 I_1}{1 + R^2 - 2R\cos(2kd)} \tag{3.11}$$

or, in order to write it in the more common form, note that $tt' = \frac{1}{\frac{1}{tt'}}$ and using the fact that $\cos(2\alpha) = 1 - 2\sin^2(\alpha)$ during the calculation, the last equation 3.11 yields the so-called

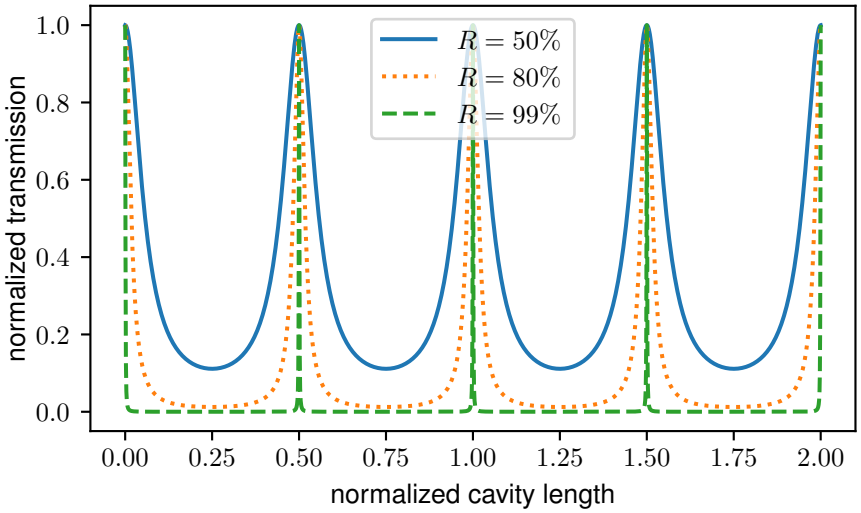

Figure 3.3: *Normalized transmitted intensity as a function of normalized distance $\bar{d}$ between the media interfaces, for different values R of reflection at each interface. Note that the reflectivity does not alter the maximum transmission peak, always equal to unity at resonance. In Eq. 3.13, $kd = \frac{2\pi}{\lambda_0} d$ so that here, the normalized cavity length is $\bar{d} = \frac{d}{\lambda_0}$.*

Airy peak form [3]:

$$I_t(\lambda) = \frac{I_1}{1 + m \sin^2(kd)} \tag{3.13}$$

where I_t (I_1) is the transmitted (incoming) intensity and

$$m = \frac{4R}{T^2}, \quad R = r^2, \quad T = tt' \tag{3.14}$$

Fig. 3.3 illustrates what happens to the transmission lines for different values of reflectivity $R = r^2$. We note the well known fact that increasing reflectivity sharpens the resonance peak, as well as it lowers the minimum of the transmission closer to 0 as R grows. In other words, the more reflective the mirrors, the lesser the light is able to pass through if the resonance condition is not met.

The transmission is maximum each time that the $\sin^2(kd)$ in Eq. 3.13 cancels out, that is, each time the resonance condition is filled:

$$kd = p \times \pi \tag{3.15}$$

with p any integer number. This bring the condition to resonance in terms of the wavelength:

$$\lambda = \frac{1}{p} \times 2nd \tag{3.16}$$

[3] Note that near resonance, i.e. when $d_0 = p \times \lambda/2$ (see Eq. 3.16), if we shift slightly the cavity's length (or, equivalently, the wavelength) so that $d = d_0 + \epsilon$ and if we notice that $kd_0 = 2\pi[2\pi]$, we can write the Airy peak in a Lorentzian form:

$$I_t^{\text{res}}(\lambda) = \frac{I_1}{1 + m\pi^2 \frac{\epsilon^2}{(\lambda/2)^2}} \tag{3.12}$$

Taking the dispersion relation $k = \frac{\omega}{c/n} = n \times \frac{\omega}{c} = n \times k_0$ with ω the angular frequency, n the refractive index, c_n the speed of light in the medium and c the speed of light in vacuum, we can write that the difference in frequency between two consecutive resonances, also called the FSR, is:

$$\begin{aligned} n\Delta\omega\frac{d}{c} &= \pi \\ \Delta\omega &= \pi\frac{c}{nd} \\ \mathrm{FSR} = \frac{\Delta\omega}{2\pi} &= \frac{c}{2nd} \end{aligned} \tag{3.17}$$

In the case where a 1 mm thick quartz cavity, selecting $n = 1.54$, the FSR is calculated to be

$$\mathrm{FSR}_{\mathrm{ideal}} \approx 97.33\,\mathrm{GHz} \tag{3.18}$$

A way of visualizing the resonance phenomenon in terms of phase is sketched in Fig. 3.4. A wavepacket's evolutions is drawn against time. Let us suppose that $n_2 < n_1$. At its arrival upon the interface, the wavepacket is partially reflected but acquires no specific phase from this reflection (if $n_2 < n_1$, then $r_{12} = r > 0$, see Eq. 3.19 for clarity.) We define the phase at this point as the reference, thus setting it to $\varphi_0 = 0$. The part which is transmitted also has the same phase. Along its path until the next interface in $z = d$, it acquires a phase φ_1. Upon reflection, $r_{21} < 0$ so that we write (using the same notations as in Fig. 3.2):

$$\begin{aligned} E_2^-(d) &= r_{21}E_2^+(d) \\ E_2^-(d) &= -r_{12}E_2^+(d) \\ E_2^-(d) &= re^{i\pi}E_2^+(d) \end{aligned} \tag{3.19}$$

From Eq. 3.19, we see that the wavepacket acquires a π phase when reflected on a higher refractive index medium. The phase of the leaked exiting wavepacket is therefore φ_1, whereas the reflected wavepacket has a phase $\varphi_1 + \pi$. Upon its return towards the entrance, it again acquires a φ_1 phase, now amounting to a total $2\varphi_1 + \pi$ upon arrival at the $2 \to 1$ interface. The leaked wavepacket now has a phase $2\varphi_1 + \pi$ and the reflected wavepacket a phase $2\varphi_1 + 2\pi$. More generally, the wavepacket that has done n round-trips inside the cavity leaks out of the first interface with a phase $2n\varphi_1 + \pi$ and out of the second interface with a phase $(2n + 1)\varphi_1$. Therefore, the wavepacket that was first reflected off the interface upon entrance is in phase opposition with the wavepacket that got reflected inside the cavity (and all the following) if $\varphi_1 = p \times \pi$, with p any natural number. On the other hand, the wavepackets that get transmitted through the second interface will all be in phase if the same condition is true.

3.1.2.3/ REFLECTED INTENSITY

In very much the same way as in the previous section 3.1.2.2, one could calculate the reflected intensity through taking the squared modulus of the reflected amplitude in Eq. 3.10a. However, considering that the medium is lossless, it follows that the energy conservation imposes at al time that $I_1^- + I_3^+ = I_1^+$. In other words, the incident inten-

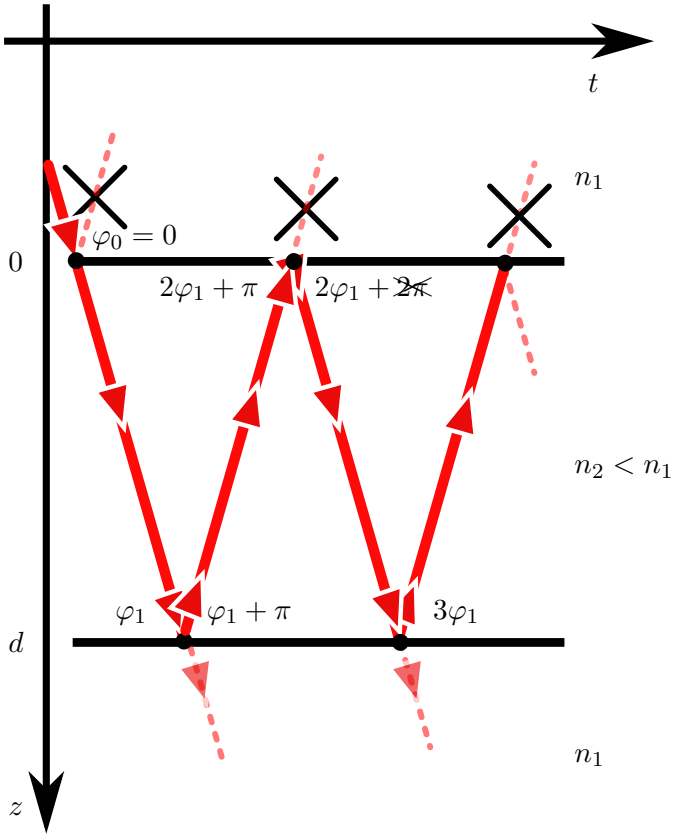

Figure 3.4: *Phase matching drawing in a three layers non-absorptive Fabry-Perot cavity. Let us stress that here, the evolution of a wavepacket evolving on the same straight line as in Fig. 3.2 is drawn against time, thus giving the false impression of a spatial propagation with an angle. The incident wavepacket gets partially reflected without an additional phase (we suppose $n_1 > n_2$ in this drawing), so that both the transmitted wavepacket and reflected wavepacket have a reference phase $\varphi_0 = 0$. Upon arrival on the next interface, the wavepacket now has a phase φ_1 and is transmitted with this phase, whereas it now acquires a π phaseshift upon reflection. It returns to its entrance point with a phase $2\varphi_1 + \pi$. The wavepacket that leaks from the first interface is therefore in phase opposition with the first reflected beam if $2\varphi_1 = p \times 2\pi$, with p being a natural number. All of the wavepackets leaking from the second interface, on the other hand, are in phase if the same condition is true.*

sity is split between the transmitted intensity and the reflected intensity in the stationnary regime [4].

Therefore, it is simpler to refer to the (normalized) reflected intensity as

$$I_r \equiv I_1^- = 1 - I_t \tag{3.20}$$

The maximum (minimum) of the transmission (reflection) obviously occur at the same frequency, as the conservation of energy dictates. See the illustration in Fig. 3.4.

[4] It is possible to verify that $I_1^- + I_3^+ = I_1^+$ by reminding the Stokes relation 3.7. It imposes that, by noting $T = tt'$ and $R = r^2$, the addition of the reflected and transmitted intensity numerator reads $(1-R)^2 + 2R - 2R\cos(2kd) = 1 + R^2 - 2R\cos(2kd)$, which is equal to the denominator of the both fractions, hence yielding 1.

3.1.2.4/ PEAK'S WIDTH

To be able to find the peak's width (either the transmitted or reflected peak), usually defined as the Full Width at Half Maximum (FWHM), it suffices to find for which frequencies the peak is at half its maximum. It is necessary to rewrite the transmitted intensity in function of the frequency. To this end, let us write some relations which will be useful. The speed of light, which we noted c, is known to be equal to $c = \lambda\nu$, where λ is the wavelength and ν the frequency. As we have seen in Eq. 3.16, upon resonance, the distance between the two interfaces has to be a number of times (notes p here) the refractive index-corrected half wavelength, $d = p \times \frac{\lambda}{2n}$ (see Fig. 3.2). In the same way, the resonance frequency can also be written as $\nu = p \times \mathrm{FSR}$. Therefore, the light velocity can be written

$$\begin{aligned} c_n =& \frac{\lambda}{n} p \times \mathrm{FSR} \\ c_n =& 2d \times \mathrm{FSR} \end{aligned} \tag{3.21}$$

Once the relation 3.21 is obtained, expressing the transmitted intensity in Eq. 3.13 in terms of frequency is a matter or replacing kd by its frequency equivalent. This is done by using the dispersion relation for $k = \frac{\omega}{c_n}$ and replacing c_n by its expression from Eq. 3.21 that has just been obtained. This amounts to:

$$I_t(\omega) = \frac{I_1}{1 + m \sin^2(\frac{\omega}{2\mathrm{FSR}})} \tag{3.22}$$

Now, finding the frequencies for which I_t is half its maximum value means to find the frequencies for which the denominator of Eq. 3.13 is equal to 2:

$$\begin{aligned} 1 &= m \sin^2\left(\frac{\omega}{2\mathrm{FSR}}\right) \\ \pm\sqrt{\frac{1}{m}} &= \sin\left(\frac{\omega}{2\mathrm{FSR}}\right) \\ \omega_\pm &\approx \pm 2\mathrm{FSR}\sqrt{\frac{1}{m}} \\ \Rightarrow \mathrm{FWHM} &\approx \frac{\mathrm{FSR}}{\pi} \times \frac{T}{r} \end{aligned} \tag{3.23}$$

where the approximation $\arcsin\left(\sqrt{\frac{1}{m}}\right) \approx \sqrt{\frac{1}{m}}$ has been taken [5].

Here, if we set $R = 98.7\%$ and $T = 1.3\%$ (which corresponds to the reflectivity and transmittivity as the interface quartz-Ag50nm with refractive index taken from [Ciesielski et al., 2017]), with the FSR that we previously calculated in 3.18, then the FWHM is approximately equal to 405 MHz. If we take $R = 99.6\%$ and $T = 0.4\%$, then the FWHM is approximately 124 MHz. Note that the FWHM is inversely proportional to the average lifetime of photons inside the optical cavity.

3.1.2.5/ FINESSE OF THE CAVITY

Finesse in a Fabry-Perot is a useful quantity, which is oftentimes used to characterize a cavity. It is convenient to do so, as it does not depend on the geometrical properties, only

[5] Note that this approximation is almost always valid in realistic Fabry-Perot cavity situations. For $R = 70\%$ and $T = 30\%$, the relative error is of 5×10^{-3}; when $R = 98\%$ and $T = 2\%$ is taken, the relative error drops to 1.7×10^{-5}.

on its reflective and transmissive properties (ignoring the absorption and diverse losses). It is defined as

$$\mathcal{F} = \frac{\mathrm{FSR}}{\mathrm{FWHM}} \tag{3.24}$$

Taking into account Eq. 3.23, we can therefore write that the finesse is [6]:

$$\mathcal{F} \approx \pi \frac{r}{T} \tag{3.25}$$

It is often further simplified, in the case where the reflection is high (i.e. $R \approx r \approx 1$), to be $\mathcal{F} = \frac{\pi}{T}$.

The finesse is also connected to the number of round-trips that a photon undergoes inside the opical cavity before (statistically) leaving it. Indeed, considering that the FWHM is simply the inverse of the lifetime of any individual photon, we can write:

$$\begin{aligned} \mathcal{F} &= \tau_{1/2}\mathrm{FSR} \\ &= \tau_{1/2} \times \frac{C_n}{2d} \\ &= \frac{d_{\mathrm{mean}}}{2d} \\ \Rightarrow \mathcal{F} &= N_{\mathrm{mean}} \end{aligned} \tag{3.26}$$

where we have noted $C_n = C/n$ the light velocity, $\tau_{1/2} = \frac{1}{\mathrm{FWHM}}$ the lifetime, d_{mean} the mean distance which is travelled by an indivual photon and N_{mean} the (mean) number of round trips travalled by an individual photon.

3.1.2.6/ INTRACAVITY INTENSITY, AMPLIFICATION FACTOR

Let us calculate the intracavity intensity. At any point in the cavity, the intensity is defined as the square modulus of the amplitude. In the cavity, the amplitude in each point is constituted from both the propagating and counter-propagating electric field, leading to a total field[7]:

$$E_{in}(z,t) = E_2^+(z,t) + E_2^-(z,t) \tag{3.27a}$$

$$= te^{i\omega t}\left[\frac{e^{-ikz} - re^{ikz}}{1 - Re^{-2ikd}}\right]E_1^+ \tag{3.27b}$$

We therefore define and calculate the ideal amplification factor, $\mathcal{A}_{\mathrm{ideal}}$, as:

$$\mathcal{A}_{\mathrm{ideal}} = \frac{I_{in}}{I_1^+} \tag{3.28a}$$

$$\mathcal{A}_{\mathrm{ideal}} = \frac{|E_{in}|^2}{\left|E_1^+\right|^2} \tag{3.28b}$$

$$\mathcal{A}_{\mathrm{ideal}} = T\frac{(1-r)^2 + 4r\sin^2(kz)}{(1-R)^2 + 4R\sin^2(kd)} \tag{3.28c}$$

$$\Rightarrow \mathcal{A}_{\mathrm{ideal}}^{\mathrm{max}} = \frac{(1+r)^2}{t} \tag{3.28d}$$

[6] This last expression is sometimes found as (and equal to) $\frac{\pi\sqrt{m}}{2}$. See Eq. 7.18-19 from [Steck, 2020].

[7] From Eq. 3.27b, it is possible to note that, in the limit where $r \approx 1$, then $e^{-ikz} - re^{ikz} = (1-r)\cos(kz) + (1+r)i\sin(kz) \approx (1+r)i\sin(kz)$.

were the passage from Eq. 3.28c to Eq. 3.28d was done by setting $kd = p \times \pi$ (which is the on-resonance condition, see Eq. 3.15) and setting $kz = p \times \pi + \frac{\pi}{2}$ to maximize the numerator (i.e. finding a position z for which the intensity is maximum).

The intracavity normalized intensity (the amplification factor $\mathcal{A}$) is represented against the position for an out-of-resonance case and a in-resonance case in Fig. 3.5. In this computation, $R = 98.7\%$ and $T = 1.3\%$ so that $\mathcal{A} \approx 310$. When the reflectivity is $R = 99.6\%$ and the transmission $T = 0.4\%$, then the amplification is of about $\mathcal{A} \approx 1130$. In other words, the intensity inside the cavity is, at best, 310 (1130) times larger than the incoming intensity. Note that in the case where $r \approx 1$, it is possible to relate the amplification factor to the Finesse by rewriting Eq. 3.28d with the help of the expression for the Finesse in Eq. 3.25:

$$\mathcal{A}^{\text{max}}_{\text{ideal}} \approx \frac{4}{\pi}\mathcal{F} \tag{3.29}$$

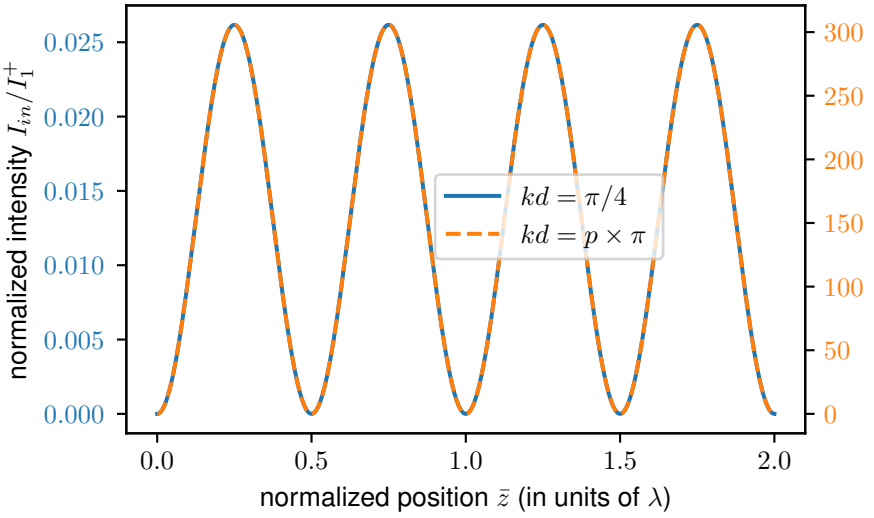

Figure 3.5: *An out-of-resonance (full line, left y axis) and in-resonance (dashed line, right y axis) plot of the normalized intracavity intensity against normalized position inside the cavity (also defined as the amplification factor $\mathcal{A}$ in Eq. 3.28c). The reflectivity is taken to be $R = 98.7\%$, $T = 1.3\%$.*

3.1.3/ Absorbing Thin-Layer Metallic Mirrors

3.1.3.1/ Introduction

Following the ideal lossless Fabry-Perot cavity under study in section 3.1, the present section will focus on the study of a Fabry-Perot cavity with losses, namely, with the metal thin layers electrodes, which also constitute mirrors. The case with absorbing media is treated and developed theoretically in several articles by Monzón and colleagues [Monzón et al., 1996] [Monzón et al., 1992] [Monzón et al., 1991] [Monzón et al., 1995], and is illustrated on Fig. 3.6.

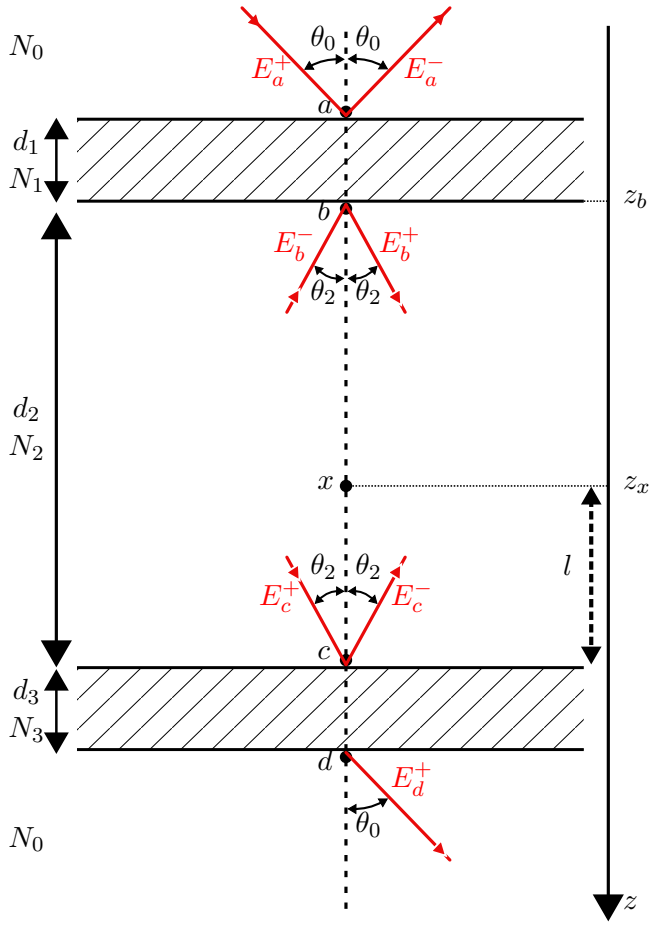

Figure 3.6: *Monzón model ([Monzón et al., 1996]): Thin absorptive layers, constituting the mirrors, are deposited on some medium which is called the spacer. a is the entrance point of the system.*

3.1.3.2/ THEORETICAL DEVELOPMENT

3.1.3.2.1/ Electric field evolution Let us start by defining the forward and backward-propagating electric field at any point in this system by writing

$$\begin{pmatrix} E^+(z) \\ E^-(z) \end{pmatrix}$$

Considering that the entry point is named a and the exit point named d, it is possible to write the relation between the electric fields at these two point with the help of the scattering matrix, S:

$$\begin{pmatrix} E_a^{(+)}(z_a) \\ E_a^{(-)}(z_a) \end{pmatrix} = \begin{pmatrix} S_{11} & S_{12} \\ S_{21} & S_{22} \end{pmatrix} \begin{pmatrix} E_d^{(+)}(z_d) \\ 0 \end{pmatrix} \tag{3.30}$$

In the case at hand, represented on Fig. 3.6, this scattering matrix S is written

$$S = I_{01} L_1 I_{12} L_2 I_{23} L_3 I_{30} \tag{3.31}$$

where we introduced

$$I_{ij} = \frac{1}{t_{ij}}\begin{pmatrix} 1 & r_{ij} \\ r_{ij} & 1 \end{pmatrix} \tag{3.32a}$$

$$L_i = \begin{pmatrix} e^{i\beta_i} & 0 \\ 0 & e^{-i\beta_i} \end{pmatrix} \tag{3.32b}$$

Eq. 3.32a expresses the modification at an interface, and 3.32b introduces a (possibly complex) phase along the path in medium i. Their derivation are found in Ellipsometry and Polarized Light, section 4.6 [Azzam et al., 1977]. In these last quantities, we made use of:

$$\beta_i = \frac{2\pi}{\lambda_0}\tilde{n}_i d_i \cos(\theta_i) \tag{3.33a}$$

$$\tilde{n}_i = n_i - in_i' \tag{3.33b}$$

Eq. 3.33a expresses the phase acquired along the propagation in the medium with d_i the i^{th} layer's thickness, and Eq. 3.33b the complex index of refraction of medium i with r_{ij} and t_{ij} the corresponding Fresnel coefficients (defined just as in Eqs. 3.6).

The introduction of the complex refractive coefficient introduces the absorption. Indeed, consider that if $\beta \in \mathbb{C}$, then $\beta = \beta' - i\beta''$. (with $\beta' = \frac{2\pi}{\lambda_0}\cos(\theta_i)n_i d_i$ and $\beta'' = \frac{2\pi}{\lambda_0}\cos(\theta_i)n_i' d_i$). Let us take the example of points b and c, separated by a distance d_2 (see Fig. 3.6). The relationship between the fields at the two points can be written, using Eqs. 3.30 and 3.32b:

$$\begin{aligned} \begin{pmatrix} E_b^{(+)} \\ E_b^{(-)} \end{pmatrix} &= \begin{pmatrix} e^{i(\beta' - i\beta'')} & 0 \\ 0 & e^{-i(\beta' - i\beta'')} \end{pmatrix}\begin{pmatrix} E_c^{(+)} \\ E_c^{(-)} \end{pmatrix} \\ \begin{pmatrix} E_b^{(+)} \\ E_b^{(-)} \end{pmatrix} &= \begin{pmatrix} e^{\beta''}\left[E_c^{+}e^{i\beta'}\right] \\ e^{-\beta''}\left[E_c^{(-)}e^{-i\beta'}\right] \end{pmatrix} \end{aligned} \tag{3.34}$$

This means that when going through an absorptive medium, each electric field component acquires a phase β', as well as it is attenuated by a factor $e^{-\beta''}$ [8].

3.1.3.2.2/ Transmitted intensity The transmission coefficient for the system described above is simply the fraction of transmitted amplitude over incident amplitude, which, using Eq. 3.30, yields:

$$\frac{E_d^+}{E_a^+} = \frac{1}{S_{11}} \tag{3.35}$$

It is possible to calculate that Eq. 3.35 is written (see Eq. 3.1 from [Monzón et al., 1996] or Eq. 2.11a from [Monzón et al., 1991]):

$$T_{FP} = \frac{T_{012}T_{230}e^{-i\beta_2}}{1 - R_{210}R_{230}e^{-2i\beta_2}} \tag{3.36}$$

[8] It may seem at first glance that there is an inconsistency because of the reversed sign between the two components of the electric field on the right side of Eq. 3.34; However, the two components describe counter-propagating fields, which therefore get attenuated or phase-shifted along their own path. In other words, for the propagating field, point b is anterior in its path to point c, whereas it is anterior in point c with respect to point b for the counter-propagating field.

where β_i is defined as in Eq. 3.33a and the following quantities were introduced:

$$T_{ijk} = \frac{t_{ij}t_{jk}e^{-i\beta_j}}{1 + r_{ij}r_{jk}e^{-2i\beta_j}} \tag{3.37a}$$

$$R_{ijk} = \frac{r_{ij} + r_{jk}e^{-i2\beta_j}}{1 + r_{ij}r_{jk}e^{-2i\beta_j}} \tag{3.37b}$$

These two quantities represent the transmitted (reflected) coefficients for material j stuck between two infinite plates of materials i and k. Note the similarity between these two coefficients and the derived amplitudes for reflected and transmitted fields in Eqs. 3.9 from the section about the three-layers non-absorptive Fabry-Perot (see 3.1.2.1).

To obtain the normalized transmitted intensity, it suffices to take the squared modulus of the amplitude in Eq. 3.36. To that end, let us rewrite Eq. 3.37b as:

$$R_{ijk} = |R_{ijk}|e^{i\Delta_{ijk}} : \tag{3.38}$$

The intensity can then be calculated to yield:

$$\mathcal{T}_{FP} = \frac{|T_{012}T_{230}|^2}{1 + |R_{210}R_{230}|^2 - 2|R_{210}R_{230}|\cos(\delta)} \tag{3.39}$$

where

$$\delta = 2\beta_2 - \Delta_{210} - \Delta_{230} \tag{3.40}$$

This phase δ (which is a real quantity because β_2 is real) represents the difference between the phase acquired along a return-trip in the central part of the cavity (see Fig. 3.6) and the phase acquired at both ends' reflections. These phases were trivially equal to 0 or π for the non-absorbing case, but might be more complicated here. Eq. 3.39 can also be written in the more common-looking form:

$$\mathcal{T}_{FP} = \mathcal{T}_{\text{max}}\frac{1}{1 + F\sin^2(\delta/2)} \tag{3.41}$$

where we used

$$\mathcal{T}_{\text{max}} = \frac{|T_{012}T_{230}|^2}{(1 - |R_{210}R_{230}|)^2} \tag{3.42}$$

$$F = \frac{4|R_{210}R_{230}|}{(1 - |R_{210}R_{230}|)^2} \tag{3.43}$$

Note the very close resemblance of coefficient F in Eq. 3.43 to the coefficient m in Eq. 3.14. Indeed, the finesse can be expressed in a very similar way to the non-absorptive three layers case (see footnote 6):

$$\mathcal{F} \approx \frac{\pi\sqrt{F}}{2} \tag{3.44}$$

More importantly, we note that the form of the transmitted intensity for an absorptive system, in Eq. 3.41, is formally equivalent to the form derived for an ideal non-absorptive system from Eq. 3.13, i.e. it is, near resonance, a Lorentzian peak. This means that they have the same shape and that the absorption of the reflective layers does not alter the Airy nature of the transmitted intensity.

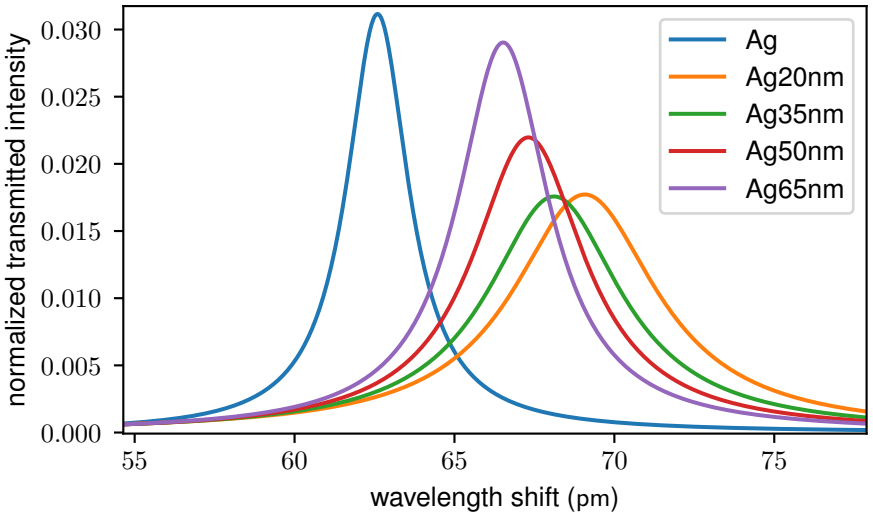

Figure 3.7: *Normalized transmitted intensity against wavelength shift for different material refractive indicess. The system is taken to be as in Fig. 2.2, with a* 1 mm *thick plano-convex quartz and* 50 nm *of silver deposited on each side, with a* 1550 nm *laser input. The refractive index for thin layers are taken from [Ciesielski et al., 2017], whereas the bulk value is taken from [McPeak et al., 2015a].*

Some normalized transmitted intensities are represented on Fig. 3.7. They are all computed for a double 50 nm thin layer film of silver, with the refractive index taken with different values, corresponding to thin films and bulk. We observe, just as in the case of the ideal Fabry-Perot in section 3.1.2, that the FWHM change along with the refractive index: the less reflective, the broader the peak (see Eq. 3.23). Furthermore, the more absorptive the material, the more the peak is shifted towards shorter wavelength. Most importantly, the more reflective (see Eqs. 3.6) the material, the greater the transmitted intensity.

An important fact for the choice of deposition thickness is the study of finesse and total transmission as a function of the both mirrors' thicknesses. Such a study is readily lead by computing both quantities in one graph, as in Fig. 3.8. This figure shows that for a given finesse (transmission), the optimization of the transmission (finesse) is obtained for an equal deposition thickness for both mirrors. This lead the experimental choice of depositing mirrors equally thick on both sides of the quartz.

3.1.3.2.3/ Reflected intensity The reflected amplitude can also be expressed from Eq. 3.30:

$$\frac{E_a^-}{E_a^+} = \frac{S_{21}}{S_{11}} \tag{3.45}$$

Similar to the case from the simple Fabry-Perot cavity and to Eq. 3.9a, the reflected amplitude can be written[9]:

$$R_{\mathsf{FP}} = R_{012}\frac{1 - z_1 z_2 e^{-2i\beta_2}}{1 - R_{210}R_{230}e^{-2i\beta_2}} \tag{3.46}$$

[9]The simplification to get from Eq. 3.9a to Eq. 3.10a in section 3.1.2.1 about the simple non-absorptive three layers Fabry-Perot included using the Stokes relations in Eqs. 3.7. Using the generalized Stokes relations from Eqs. 3.47 gives the result in Eq. 3.46.

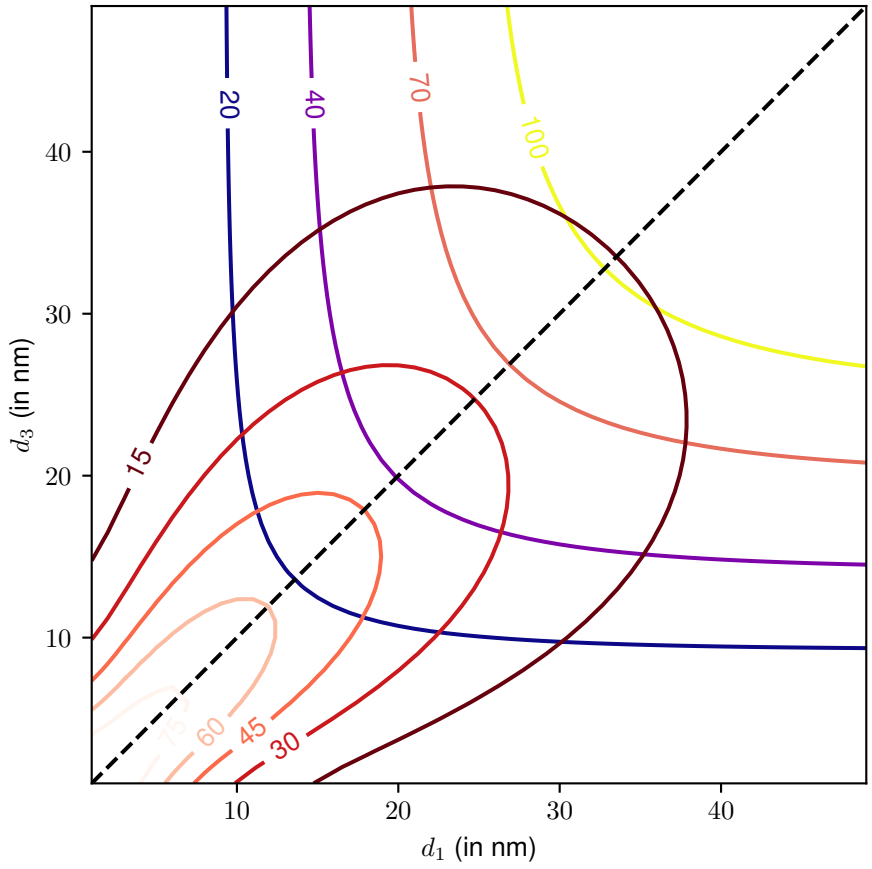

Figure 3.8: *Normalized maximum transmission (expressed in $\%$, starting from the bottom left side) and finesse contours (starting from upper right side) as a function of the first mirror's thickness d_1 and the second mirror's thickness d_3 (assumed to have the same index of refraction). Note that for a given finesse, the maximum possible transmission is for $d_1 = d_3$ and vice versa. Which shows that the best choice to maximize the finesse (transmission) for a given transmission (finesse) is to make both mirrors equally thick.*

where we have used the generalized Stokes relations:

$$T_{012}T_{210} - R_{012}R_{210} = z_1 \tag{3.47a}$$

$$R_{210} = -z_2 R_{012} \tag{3.47b}$$

$$z_1 = \frac{r_{01}r_{12} + e^{-2i\beta_1}}{1 + r_{01}r_{12}e^{-2i\beta_1}} \tag{3.47c}$$

$$z_2 = \frac{r_{12} + r_{01}e^{-2i\beta_1}}{r_{01} + r_{12}e^{-2i\beta_1}} \tag{3.47d}$$

The reflected amplitude from Eq. 3.46 can be rewritten in the more convenient form (See Eq. 4.3 from [Monzón et al., 1996]):

$$R_{\text{FP}} = R_{012}\frac{1 - \zeta_{210}R_{230}e^{-2i\beta_2}}{1 - R_{210}R_{230}e^{-2i\beta_2}} \tag{3.48}$$

where the quantity ζ_{210} was introduced:

$$\begin{aligned}\zeta_{210} =& \frac{R_{012}R_{210} - T_{012}T_{210}}{R_{012}} \\ \zeta_{210} =& \frac{z_1 z_2}{R_{210}} \\ \zeta_{210} =& \frac{1 + r_{21}r_{10}e^{2i\beta_1}}{r_{21} + r_{10}e^{2i\beta_1}}\end{aligned} \tag{3.49}$$

and, just as in Eq. 3.40, we also introduce the norm-argument notation of this quantity:

$$\zeta_{210} = |\zeta_{210}|e^{i\Phi_{210}} \tag{3.50}$$

In order to find the reflected normalized intensity, here too, as in Eq. 3.41, we take the squared modulus of the normalized reflected amplitude Eq. 3.48:

$$\mathfrak{R}_{\mathsf{FP}} = |R_{012}|^2 \frac{1 + |\zeta_{210}R_{230}|^2 - 2|\zeta_{210}R_{230}|\cos(\Delta)}{1 + |R_{210}R_{230}|^2 - 2|R_{210}R_{230}|\cos(\delta)} \tag{3.51}$$

where we made use of the quantity Δ, defined as:

$$\Delta = 2\beta_2 - \Phi_{210} - \Delta_{230} \tag{3.52}$$

Much like δ in Eq. 3.40, Δ is a phase difference. Even though Φ_{210} doesn't have an immediate physical signification, it does account for the non-trivial difference in phase between the wavepacket reflected from the spacer (the part between the two mirrors) of the cavity and the counter-propagating wavepacket, coming out of the spacer (see Fig. 3.9).

Unlike in the ideal Fabry-Perot from section 3.1.2 and the phase equivalence between the transmitted and reflected peaks (see Fig. 3.4), transmitted and reflected peaks happen at different phase here, i.e. different wavelength or frequency. Furthermore, the reflected intensity peak is asymetric [Giust et al., 2000], and is therefore no longer exactly an Airy function. This situation is illustrated on Fig. 3.10

There are three non-trivial situations (considering only the case where the first layer has a non-zero thickness and is not made of the same material as the layer 0 or 2, i.e. $\tilde{n}_1 \neq \tilde{n}_0$ and $\tilde{n}_1 \neq \tilde{n}_2$) for which $\Phi_{210} = \Delta_{210}$, so that $\Delta = \delta$ and the reflected peak returns to being symmetrical and centered at the same wavelength (frequency) as the transmitted one. These three situations are (see [Monzón et al., 1995]):

1. When the first coating is very thick, $T_{012}T_{210} \to 0$ so that $\zeta_{210} \to R_{210}$
2. When the thickness of the first coating is very thin, it is therefore nearly transparant so that the condition $\Delta \approx \delta$ is met
3. When the first coating is actually transparent (non-absorptive)

The first situation (1) will not be of any practical interest for the study of metal thin layers optical cavities because it does not let any light pass through. The second situation (2) is practically unreachable. Indeed, looking at Fig. 3.11, the normalized reflection is plotted against wavelength shift and first mirror's thickness d_1. The transmission, normalized to unity for visual convenience, is also plotted. Even at very small d_1, the two peaks are shifted, thus showing that this situation will not be practically reached. The last situation (3) is of no interest for the study of metal thin layers mirrors, but does point to the possible alternative solutions for optomechanical coupling (see section 5).

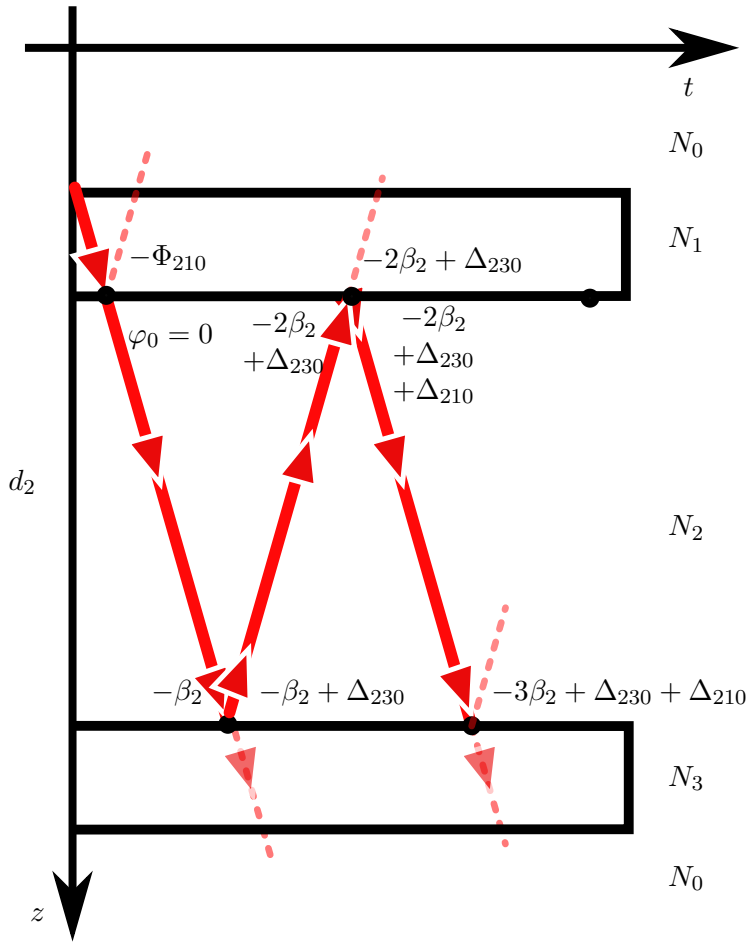

Figure 3.9: *Conceptual phase-matching drawing for a two absorptive mirrors cavity. Considering only the first two iterations of the drawing allows to understand conceptually the difference in phase (wavelength/frequency) between the reflected and transmitted peaks. Contrary to the simple non-absorptive case in Fig. 3.4, the reflection of the wavepacket on interfaces does not impart a trivial 0 or π phase. This non-trivial phase is different at the lower exit of the spacer, where the second mirror starts (transmission), and at the upper exit (reflection), because the firstly reflected wavepacket's phase also depends on the intra-first-mirror dynamics trough the generalized Stokes relations. This amounts to a certain wavelength (or frequency) cancelling the transmitted phase $(3\beta_2 - \Delta_{210} - \Delta_{230}) - \beta_2 = \delta$. The wavelength (frequency) cancelling the reflected phase $-2\beta_2 + \Delta_{230} - (-\Phi_{210}) = \Delta$ is, in general, different from the previous one.*

3.1.3.2.4/ Absorption We briefly introduce the absorption. This model only takes the absorption into account for losses, so that we can write the absorption as the difference between the total intensity and the reflected and transmitted intensity:

$$\bar{A}_{\mathsf{FP}} = 1 - \mathcal{R}_{\mathsf{FP}} - \mathcal{T}_{\mathsf{FP}} \tag{3.53}$$

The essential feature of the absorption, which derives from the particular phase upon reflection when the mirrors are absorbing (see Fig. 3.9) and the conservation of energy, is that the two mirrors do not absorb light equally. As shown by Monzón (see Eqs. 5.1 and 5.2 in [Monzón et al., 1996]), the absorption in each mirror can be calculated by looking at

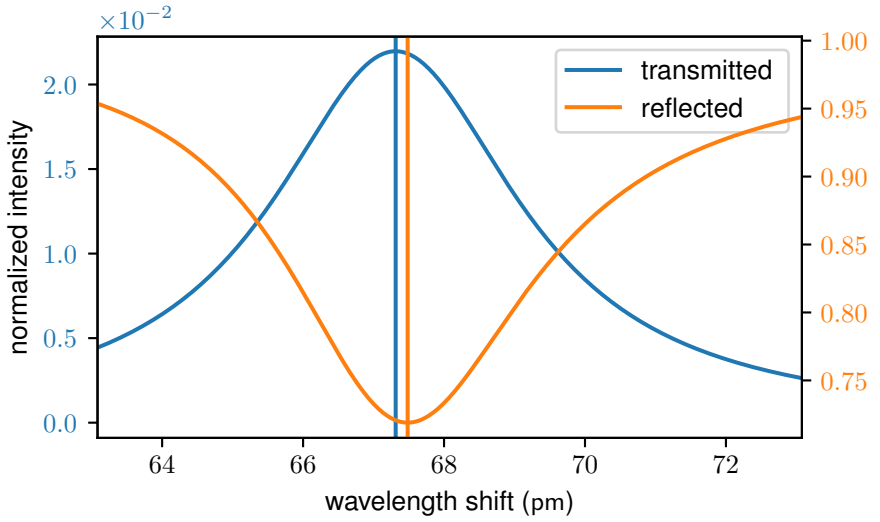

(a) Ag50nm

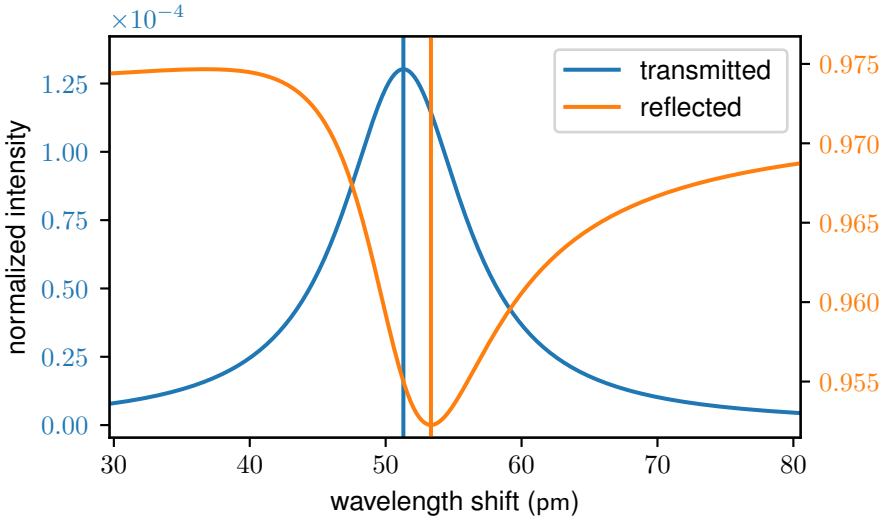

(b) Al

Figure 3.10: *Theoretical normalized transmission and reflection with corresponding vertical line pointing to the center of the peak. The computation is for a* 50 nm *deposit of Ag50nm material in Fig. 3.10a and material Al in Fig. 3.10b, with refractive index values taken from [Ciesielski et al., 2017] for silver and [McPeak et al., 2015a] for aluminium. Note that the two peaks are slightly detuned in wavelength, with the reflection peak being centered at a longer wavelength. Note also that the reflected peak is slightly asymetrical. The two peaks in Fig. 3.10a are shifted by about* 0.17 pm*, which, for a* 1550 nm *laser, amounts to about* 21.2 MHz*. In Fig. 3.10b, they are shifted by about* 2.03 pm*, or approximately* 253 MHz*.*

the difference between amplitudes before and after the mirror (in points a and b or points

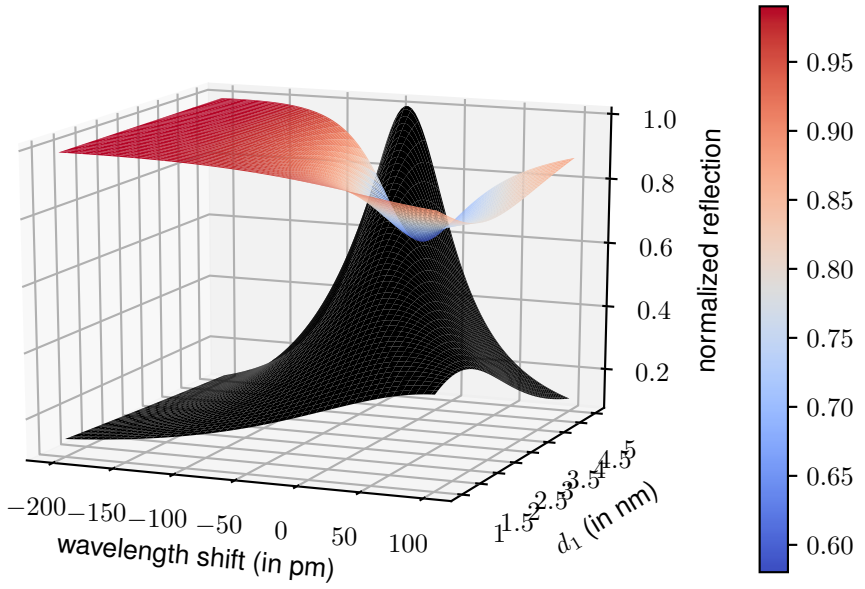

Figure 3.11: *3D plot of the normalized reflection (color) and the transmission (normalized to unity) in black. This plot shows that even for very small thicknesses of d_1, the two peaks are still frequency shifted.*

c and d in Fig. 3.6). Doing so yields:

$$\bar{A}_1 = \tilde{n}_0 \cos(\theta_0)\left(\left|E_a^+\right|^2 - \left|E_a^-\right|^2\right) + \tilde{n}_2 \cos(\theta_2)\left(\left|E_b^-\right|^2 - \left|E_b^+\right|^2\right) \tag{3.54a}$$

$$\bar{A}_2 = \tilde{n}_2 \cos(\theta_2)\left(\left|E_c^+\right|^2 - \left|E_c^-\right|^2\right) - \tilde{n}_0 \cos(\theta_0)\left|E_d^+\right|^2 \tag{3.54b}$$

These equations can also be written:

$$\bar{A}_1 = 1 - \mathcal{R}_{\mathrm{FP}} - \mathcal{T}_{\mathrm{FP}}\left(\frac{\tilde{n}_2 \cos(\theta_2)}{\tilde{n}_0 \cos(\theta_0)} \times \frac{1 - |R_{230}|^2}{|T_{230}|^2}\right) \tag{3.54c}$$

$$\bar{A}_2 = \mathcal{T}_{\mathrm{FP}}\left(\frac{\tilde{n}_2 \cos(\theta_2)}{\tilde{n}_0 \cos(\theta_0)} \times \frac{1 - |R_{230}|^2}{|T_{230}|^2}\right) - \mathcal{T}_{\mathrm{FP}} \tag{3.54d}$$

Fig. 3.12 displays the difference in wavelength betweent the actual resonance at transmission and the peaks of absorption for the total absorption, the first mirror's absorption and the second mirror's absorption. The first mirror's absorption is centered on a different wavelength (frequency) than the transmission. In other words, just as the reflection, its maximum does not happen at the actual resonance.

3.1.3.3/ AMPLIFICATION FACTOR

In the same way as for the non-absorptive ideal Fabry-Perot cavity in section 3.1.2.6, it is possible to define the amplification factor for the cavity with absorbing mirrors described by Monzón. From the theoretical premises we detailed in the previous section, we now derive the amplification factor which will be of use for optomechanical coupling. Indeed,

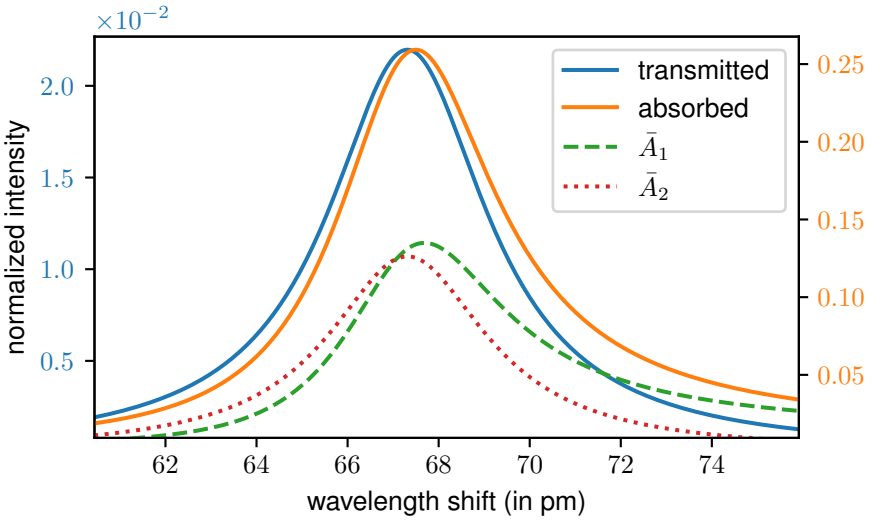

Figure 3.12: *Normalized transmission (left y-axis), total absorption and absorption of the first ($\bar{A}_1$) and second ($\bar{A}_2$) mirror (right y-axis). Note that the first mirror has its maximum absorptance at a greater wavelength than the second one. This is another aspect of the phasematching presented in Fig. 3.9. The computation was made for a refractive index associated with* 50 nm *of silver.*

because the optomechanical coupling depends on the photonic intensity, it is critical to have a knowledge of how much more light lives inside the cavity than what the incoming light provides. To this end, we write, just as in Eq. 3.28c, that the amplification factor is simply the intensity inside the cavity divided by the incoming intensity :

$$\mathcal{A} = \frac{I_{in}}{I_1^+} \tag{3.55}$$

The intensity inside the cavity is the squared amplitude inside the cavity. In the same way as in Eq. 3.27a, we note that this amplitude is the sum of the propagating and counter-propagating amplitude. In order to find these, let us start by calculating the amplitudes at point c in the cavity, located at the spacer-2$^{\text{nd}}$ mirror's interface (see Fig. 3.6). This field is written, according to the method adopted in Eq. 3.30:

$$\begin{pmatrix} E_c^+(z_c) \\ E_c^-(z_c) \end{pmatrix} = I_{23} L_3 I_{30} \begin{pmatrix} E_d^+(z_d) \\ 0 \end{pmatrix} \tag{3.56a}$$

$$\begin{pmatrix} E_c^+(z_c) \\ E_c^-(z_c) \end{pmatrix} = \begin{pmatrix} \frac{T_{\text{FP}}}{T_{230}} E_a^+ \\ \\ \frac{T_{\text{FP}} R_{230}}{T_{230}} E_a^+ \end{pmatrix} \tag{3.56b}$$

with T_{FP} defined in Eq. 3.36.

Once this expression is obtained, the amplification factor is readily found by expressing the field in the point x with maximum amplitude. This amounts to propagating the field in point c to a point x with max amplitude and position z_x so that $z_c - z_x = x$:

$$\begin{pmatrix} E_x^+(z_x) \\ E_x^-(z_x) \end{pmatrix} = L_2(x) \begin{pmatrix} E_c^+(z_c) \\ E_c^-(z_c) \end{pmatrix} \tag{3.57}$$

where we noted

$$L_2(x) = \begin{pmatrix} e^{i\beta_2(x)} & 0 \\ 0 & e^{-i\beta_2(x)} \end{pmatrix} \tag{3.58a}$$

$$\beta_2(x) = \frac{2\pi}{\lambda}\tilde{n}_2 \cos(\theta_2)x \tag{3.58b}$$

These two last equations, Eqs. 3.58, simply express the way the field evolves for a trip of length x instead of the whole layer's thickness d_i as defined in Eqs. 3.32b and 3.33a. Let us express the field at point x, which will then be maximized in order to find $\mathcal{A}$.

$$E_x = E_x^+ + E_x^- = \frac{T_{\mathsf{FP}}}{T_{230}} E_a^+ e^{i\beta_2(x)} \left(1 + R_{230} e^{-2i\beta_2(x)}\right) \tag{3.59}$$

In order to find the amplification factor we combine Eqs. 3.55 and 3.59:

$$\mathcal{A} = \frac{|T_{\mathrm{FP}}|^2}{|T_{230}|^2} \left|1 + |R_{230}| e^{(2i\beta_2(x) + i\Delta_{230})}\right|^2 \tag{3.60}$$

which, with x as the variable, is maximum for $2\beta_2(x) = -\Delta_{230}[2\pi]$. Then, $\mathcal{A}$ yields:

$$\mathcal{A}(\lambda) = \mathcal{T}_{\mathsf{FP}}(\lambda) \frac{(1 + |R_{230}|)^2}{|T_{230}|^2} \tag{3.61}$$

The maximum amplification factor we can get from a specific cavity is when the resonance condition is filled, i.e. when the transmitted intensity is maximized. Using Eq. 3.42, we finally write that the maximum amplification factor is:

$$\mathcal{A} = \mathcal{T}_{\mathsf{max}} \frac{(1 + |R_{230}|)^2}{|T_{230}|^2} \tag{3.62}$$

See Fig. 3.13 for some numerical examples with different refractive indices.

Note the resemblance between this last expression for the amplification factor and the expression given in section 3.1.2.6, which we remind here for convenience:

$$\mathcal{A}_{\mathrm{ideal}}^{\mathrm{max}} = \frac{(1 + r)^2}{t} \tag{3.28d}$$

Identifying R_{230} with r and T_{230} with t, if $\mathcal{T}_{\mathsf{max}} = 1$, then the two equations are equivalent. This last condition is almost verified when the reflectivity of the mirrors are high (see the visual aid of Fig. 3.3). For visual clarity, a figure summing up all interesting quantities (intracavity amplification factor $\mathcal{A}$, absorption, transmission and reflection) against deposition thickness is presented in Fig. 3.14.

Although both situation are described by a similar framework, the introduction of the absorption decreases the intracavity amplification factor, primarily through the coefficient $\mathcal{T}_{\mathsf{max}} < 1$. Indeed, in the ideal case, the normalized maximum transmission is always unity (see Eq. 3.13 and Fig. 3.3).

Furthermore, as Eq. 3.28d shows, the amplification factor in the ideal case is in principle growing infinitely as the reflectivity approaches unity, i.e. $\mathcal{A}_{\mathsf{ideal}}^{\mathsf{max}} \to \infty$ with $r \to 1$. This behavior is very different from what is expected in the absorptive case, as Fig. 3.14 shows. It is apparent from the figure that as the reflectivity grows (with deposition thickness), the transmission decreases and the overall absorption reaches a peak before decreasing

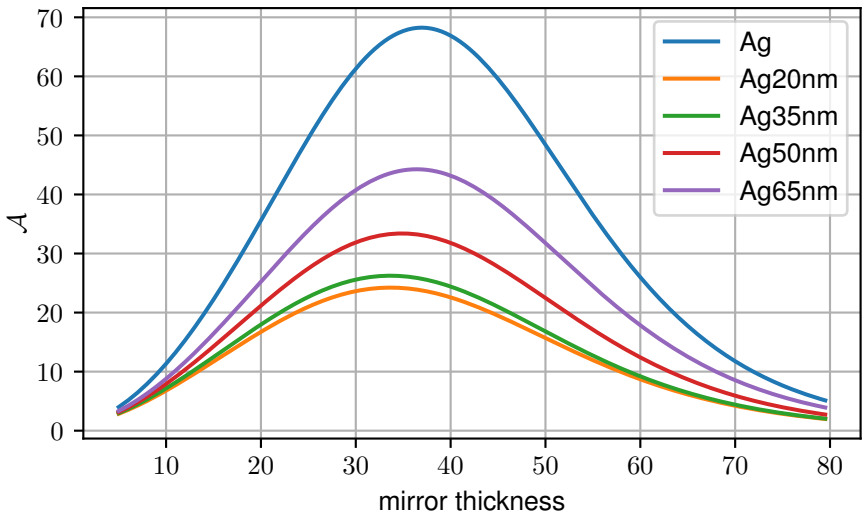

Figure 3.13: *Computed amplification factor $\mathcal{A}$ against mirror thickness (both are taken to be equal), for different refractive indices. The refractive indices are taken constant over the range of thickness. Ag stands for the bulk index taken from [McPeak et al., 2015a] while the others are taken from [Ciesielski et al., 2017]. Note that every maximum happens for a slightly different mirror thickness, although they all lie in the* 30 nm-40 nm *region.*

again to 0. Likewise, the intracavity amplification factor reaches a peak before decreasing again, unlike the ideal case.

As a numerical example, the amplification factor expected with a mirror reflectivity of $R = 98.7\%$ (i.e. the expected reflectevity for a $50\,\text{nm}$ silver deposition), the ideal amplification factor is expected to be $\mathcal{A}^{\text{max}}_{\text{ideal}} = 310$ while the same coefficient with the absorptive silver thin films is calculated to be $\mathcal{A} = 24$ (at $50\,\text{nm}$ deposition thickness). This is a significant decrease, which calls for a deeper understanding of the optomechanical requirements (see section 4 for further details) in order to be able to comment on the possible impact this may have on optomechanical actuation feasability.

In this first part of the 3rd chapter, we have reminded the theoretical developments for the ideal three-layers Fabry-Perot cavity, followed by a comparison with the theoretical developments for the absorptive mirrors version of the optical cavity, basing ourselves on an existing workframe [Monzón et al., 1996] while adding some analysis, such as a visual phase-shift scheme for clarity of how the frequency shift happens, as well a brief analysis of the intracavity amplification factor $\mathcal{A}$. The latter is necessary in order to estimate the optical power inside the optical cavity, which is of importance for optomechanical coupling.

We have highlighted the peculiar effects arising from the absorption of the mirrors with a modified FWHM and a frequency difference between the transmission and reflection peaks, which is of the order of several tens of megahertz for tens of nanometers of deposited metal. We have also noted that within the frame of quartz resonator-based optical cavity with a typical geometry as presented in Fig. 2.2 and a few tens of nanometers of deposited metal, it is impossible to rid oneself of the aforementioned peculiar effects.

The modified (broader) FWHM due to the absorption is of negative influence to optome-

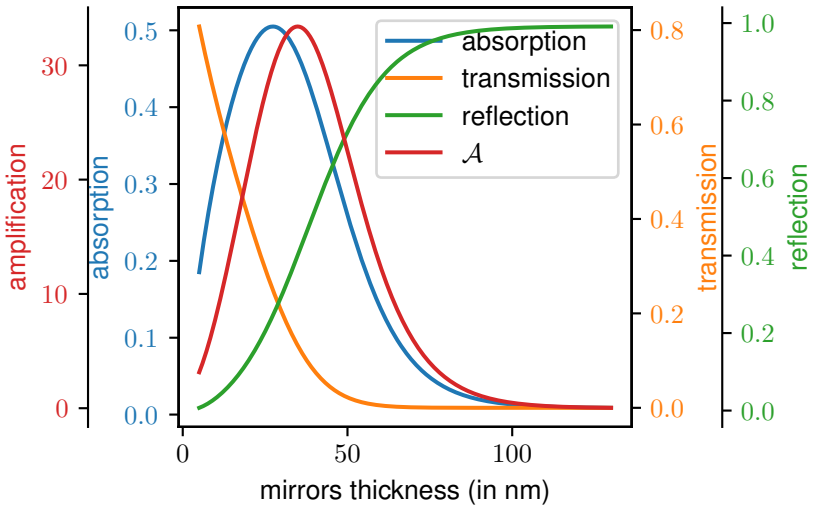

Figure 3.14: *Intracavity amplification factor $\mathcal{A}$, total absorption, transmission and reflection against thickness. Computations are made with a constant refractive index corresponding to a* 50 nm *layer of silver. Note that the points where the curves cross are not significant because each curve has its own scale.*

chanical coupling, as an increased FWHM is synonymous to a decreased lifetime of the photons in the cavity, i.e. to a decreased finesse and ultimately of the amount of light trapped inside the cavity. The asymmetry of the reflection peak and the frequency shift Δf, however, are not as clearly problematic as the increased FWHM could be. In the perspective of a Pound Drever-Hall stabilization scheme, however, the shift between the two peaks may pose an experimental difficulty, as the technique would need to be adapted. Indeed, this technique relies on the stabilization of the frequency around the reflection peak minimum which, in our case, is different from the frequency of the transmission maximum. The latter frequency is the proper resonance frequency, whereas the former is the fruit of an artifact due to the phase acquired by the light upon reflecting on the first film interface (see Fig. 3.9). Furthermore, stabilizing the frequency around the reflection minimum slightly worsens the light coupling in the Fabry-Perot cavity due to the shift with the actual resonance frequency, decreasing the amplification factor for a 50 nm silver cavity by about a factor 1×10^{-3}. We conclude that although the frequency shift is not an immediate obstacle to light coupling in the optical cavity, it should be taken into consideration in the future developments towards an ultrastable clock, should be taken into consideration.

The absorptive feature of the coatings, on the other hand, significantly decreases the intracavity amplification factor. Indeed, the 50 nm silver thin film is calculated to display a reflectivity of approximately $R = 98.7\%$, and as Fig. 3.5 and 3.13 show, the introduction of the absorption decreases this factor from $\mathcal{A} = 310 \to 24$.

Because the quartz resonator has displayed its best quality factors at 4 K, and because earlier literature has noted an improvement of the optical qualities of metals at low temperatures [Bass et al., 1983], in the following, we proceed with the study of the behavior of the amplification factor at cryogenic temperature, in order to assess whether or not the

expected change of optical properties can be beneficial for optomechanical coupling.

3.2/ Experimental Study of Thin Metal Layers

3.2.1/ Experimental Setup

Because of our interest in the typical quartz resonator as a possible optomechanical coupling candidate, it is necessary to look at the optical properties of the electrodes to better grasp its subsequent coupling to mechanical features of the quartz itself. In particular, because the two electrodes face each other, they readily constitute a Fabry-Perot cavity, of whose properties we have given an overview in section 3.1.3.

As seen in the theoretical description from section 3.1.3, some interesting and specific effects arise from the absorption of the metallic thin layers constituting mirrors for our quartz-crystal Fabry-Perot cavities. In particular, the shift in phase-conditions for resonance and anti-resonance (hence wavelength/frequency shift, see Fig. 3.9) are one example, as well as a broadening of the optical peak's FWHM and increased losses by absorption, bringing along a worsening of the peaks' visibility in both reflection and transmission.

In this section, a general look at the experimental setup that is used for the measurement campaign (see [Rosenziveig et al., 2019]) of these optical properties of the Fabry-Perot cavity is presented, as well as the results with different types of deposition layers, under room temperature and cryogenic temperature. A discussion is also lead about the quality of these deposition layers.

3.2.1.1/ Quartz Design

Although the typical quartz-crystal resonator used for time-reference purposes is deposited with a very thin layer of chromium ($\approx 5\,\text{nm}$-$10\,\text{nm}$) on top of which a rather large layer of gold is deposited ($150\,\text{nm}$-$200\,\text{nm}$), this does not permit to detect a significant optical signal for a device used as a Fabry-Perot cavity under these conditions. Therefore, an early interest was put in thinner and more reflective metallic layers, with gold and silver in particular, as we shall see in the section 3.2.2.2.2. These are indeed the most common reflective metallic layer deposited for commercially available optical mirrors (see for example [Smith et al., 1999] or [Ciesielski et al., 2017]).

We have used several types of quartz crystal resonators, with rather close geometrical characteristics. See Fig. 2.2 for a visual description of these typical characteristics.

3.2.1.2/ Optical Table

The optical experimental setup is presented on Fig. 3.15. It consists of a (commercially available from NKT Photonics) Koheras AdjustiK^{TM} piezo-tunable wavelength laser, with center wavelength at $1550\,\text{nm}$, i.e. typical telecom wavelength. It is a continuous wave

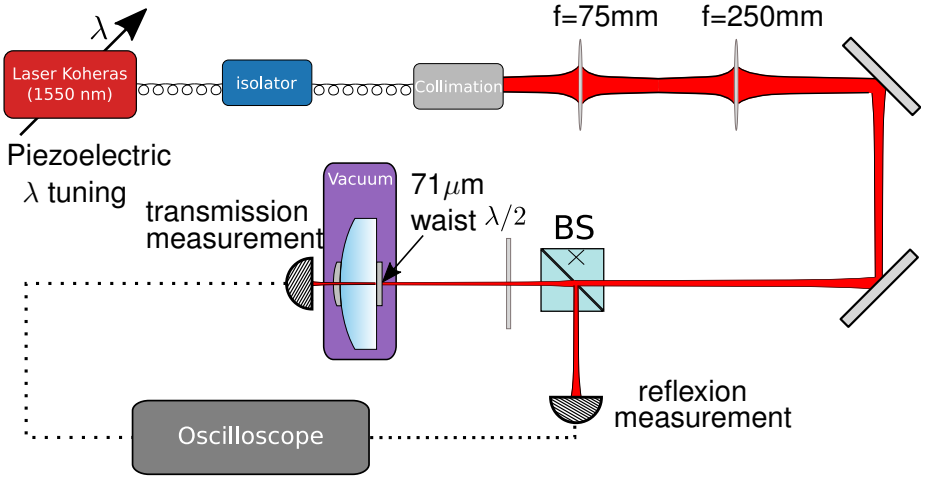

Figure 3.15: *Experimental setup for measuring thin metallic (absorptive) layers properties. It mainly consists in adapting the waist to fit the mirrors' curvatures and measuring the transmitted and reflected signal. The incident polarization is adapted through a* $\lambda/2$ *waveplate, unlike the typical* $\lambda/4$ *scheme. See main text for more information and Fig. 3.16.*

laser with a tunable power output, with range $0.1\,\mathrm{mW}$-$120\,\mathrm{mW}$. We typically use it in order to get an experimental power incident onto the cavity in the range $2\,\mathrm{mW}$-$10\,\mathrm{mW}$.

Its fiber output is plugged into a (fibered) optical isolator to prevent backwards travelling re-entry of light which might damage the laser. The output of which is then collimated through a lens and injected in free-space on the optical table, passing through a set of lenses in order to achieve the mode-matching for the Fabry-Perot cavity. This means that the Gaussian beam laser has a minimum radius (waist) at the entrance of the Fabry-Perot cavity, where the mirror is plane (i.e. infinite radius of curvature), and that it has an appropriate radius of curvature upon reaching the second mirror. It is possible to establish a condition for the waist, relating it to the radius of curvature and the distance from the the waist in the propagation axis:

$$w_0 = \left[\{R(z) - (z - z_0)\}\frac{\lambda^2}{n^2\pi^2}(z - z_0)\right]^{1/4} \tag{3.63}$$

where $R(z)$ is the radius of curvature at distance z along the propagation axis, z_0 is the waist position on the propagation axis, n is the refractive index and λ is the (vacuum) wavelength of the laser. In this case, by taking the refractive index of the quartz to be $n = 1.53$ and by having a $250\,\mathrm{mm}$ radius of curvature at $1\,\mathrm{mm}$ distance from the plane (infinite radius of curvature hence waist position) mirror and a $1550\,\mathrm{nm}$ laser imposes the condition that the waist be equal to

$$w_0 = 71.1\,\mu\mathrm{m} \tag{3.64}$$

After ensuring the modematching of the Gaussiam beam laser, it passes through a $50/50$ non-polarized Beam Splitter (BS). Only 50% of the laser power therefore passes through the BS, while the other 50% is blocked (represented by a cross on the scheme in Fig. 3.15). This is not a very common scheme for retrieving the reflected beam, see the text below and Fig. 3.16.The scheme presented here shows the critical advantage to be polarization-independent, at the cost of some optical power losses.

Indeed, there is an a priori uncertainty on the quartz crystal's fast and slow axes directions. In the typical scheme for retrieving the reflected beam (see footnote **??**), the beam arrives on the mirror with a circular polarization. This does not permit a coupling with only one (slow or fast) axis of the quartz, which is birefringent (see Fig. 3.16a).

The quartz' fast and slow axes directions uncertainty as well as the need for the polarization to be linear upon arriving on the mirror leads to the scheme presented in Fig. 3.16b. The polarization is also sent linear onto the non-polarized beam splitter, so half of it goes through and is then rotated with a $\lambda/2$ waveplate in order to fit one of the two (fast or slow) axes of the quartz. On its way back, the beam, though of a different polarization, partially exits through the opposite port of the beam splitter and it also gets partially reflected through the last port, so we can retrieve the signal there, with the help of a photodiode. Finally, the reflection and transmission signals from the photodiodes are captured by an

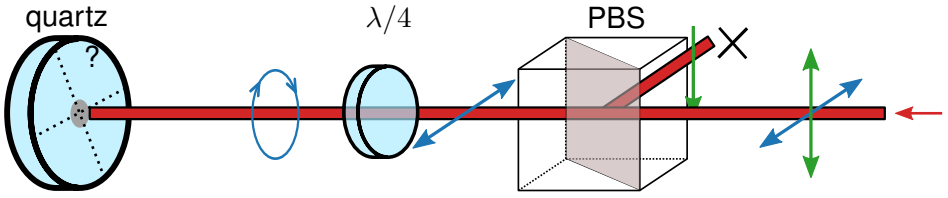

(a) Typical scheme

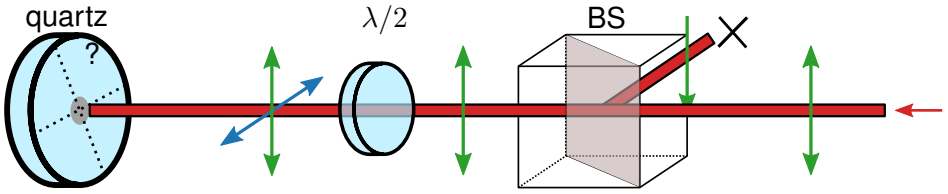

(b) Our scheme

Figure 3.16: *Fig. 3.16a: Illustration of why the typical reflection retrieval scheme described in footnote* **??** *does not work in our case. Indeed, the beam arrives with a circular polarization on the mirror, which is problematic if the goal is to be able to couple light inside the Fabry-Perot only along the fast or the slow axis of the quartz. Also, the orientation of the fast and slow axis is, in general, unknown and would therefore require for the quartz holder to permit rotation in order to hit the quartz with the right rotation, which is not entirely trivial to realize experimentally. Fig. 3.16b shows our scheme, which, at the cost of losing some optical power at the non-polarized beam splitter, permits to eliminate the polarization problem: a particular linear polarization is sent through the beam splitter, and is then rotated with a $\lambda/2$ waveplate. This permits to control the polarization of the beam incident on the quartz, and to adapt it to the fast or slow axis of the quartz, hence permitting coupling inside the Fabry-Perot to a particular axis. Furthermore, upon reflection, another half is then reflected through the other port of the beam splitter and retrieved for reflection analysis (not drawn on the figure). Note that a s-polarization is drawn, but it could be a p-polarization or even any linear polarization just the same.*

oscilloscope and, through a python program of our design, are retrieved on the computer where a further python algorithm permits to to determine their shift in frequency and their width (FWHM) (see Fig. 3.19).

The quartz crystal is kept under vacuum inside the cryo chamber, although not necessarily put at cryogenic temperature. A Polaris mirror holder from Thorlabs has been adapted to welcome a BVA-like device (see chapter 1 for a description of the BVA), see Fig. 3.17

and Fig. 3.17b in particular. This is critical in several respects, but the main concern to be able to simply hold the quartz. Indeed, with the differential thermal dilations of the materials involved, it is not possible to simply hold the quartz crystal in the Thorlabs mount. As a matter of fact, doing so has led to the destruction of the quartz crystal, most probably because of radial contraction of the holder different than the quartz itself. It is therefore critical to be able to hold the quartz without radially constraining it (with anything else than quartz). Hence the solution of using a BVA structure, which presses on the quartz not radially but on its thickness with the same material.

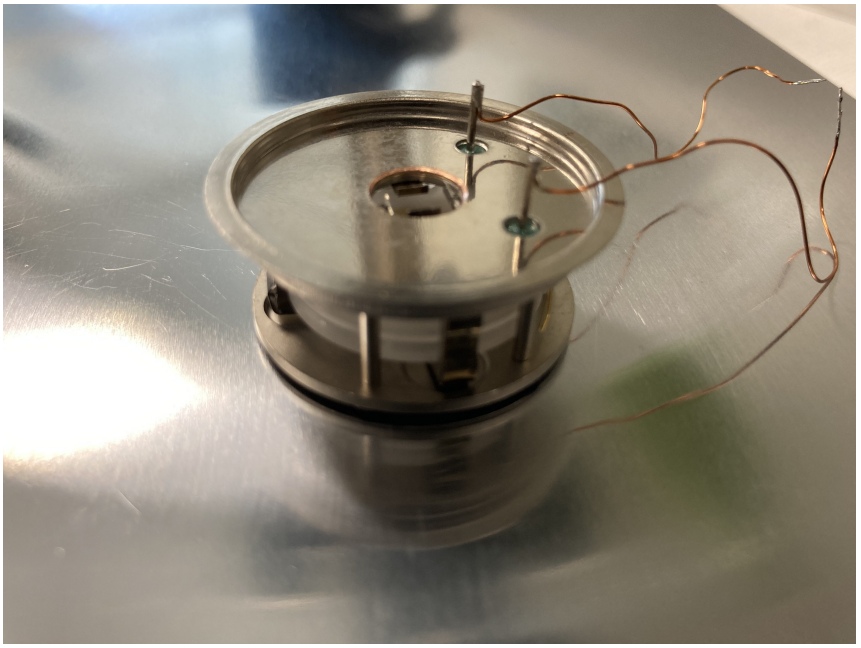

(a) BVA-like structure

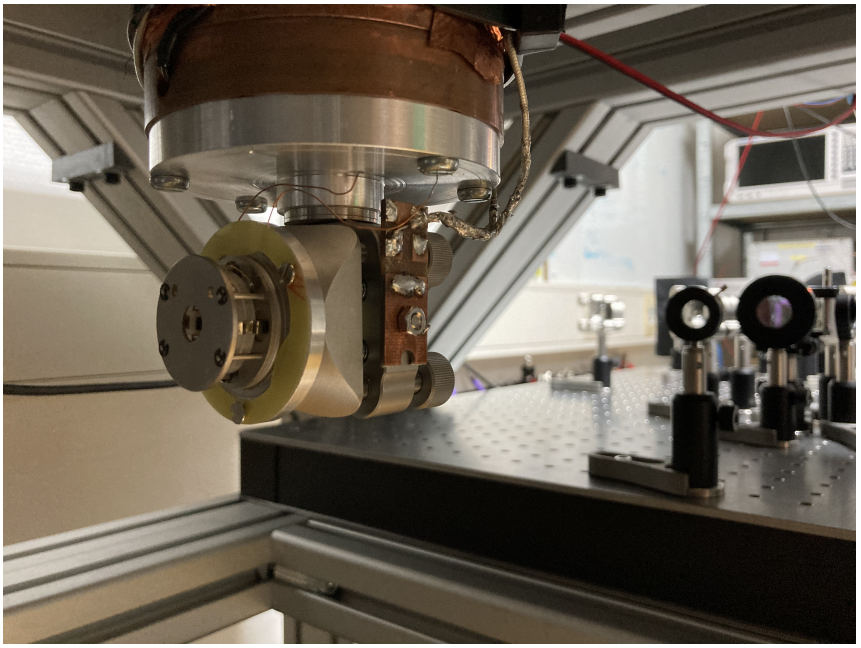

(b) Homemade Quartz Holder

Figure 3.17:

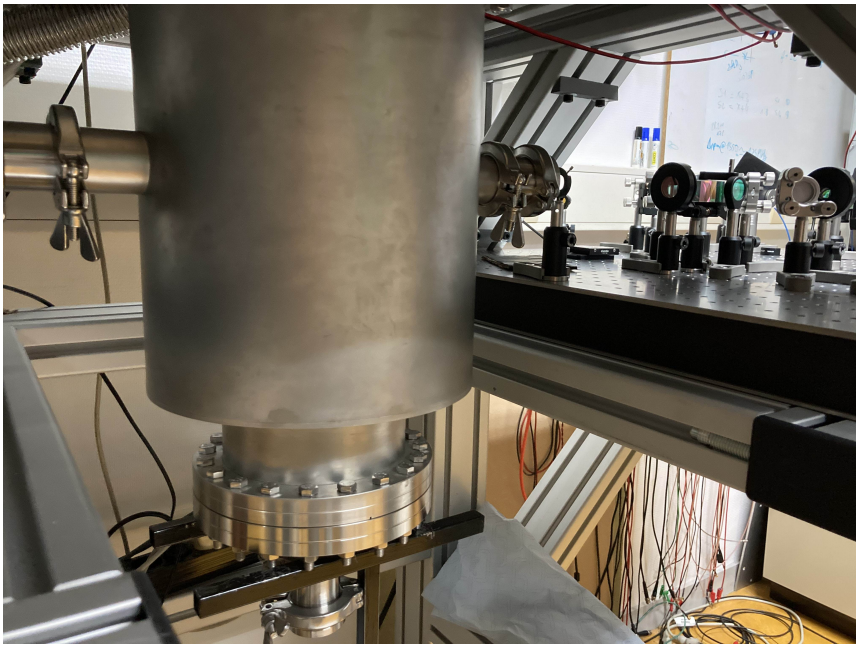

(c) Under Vacuum

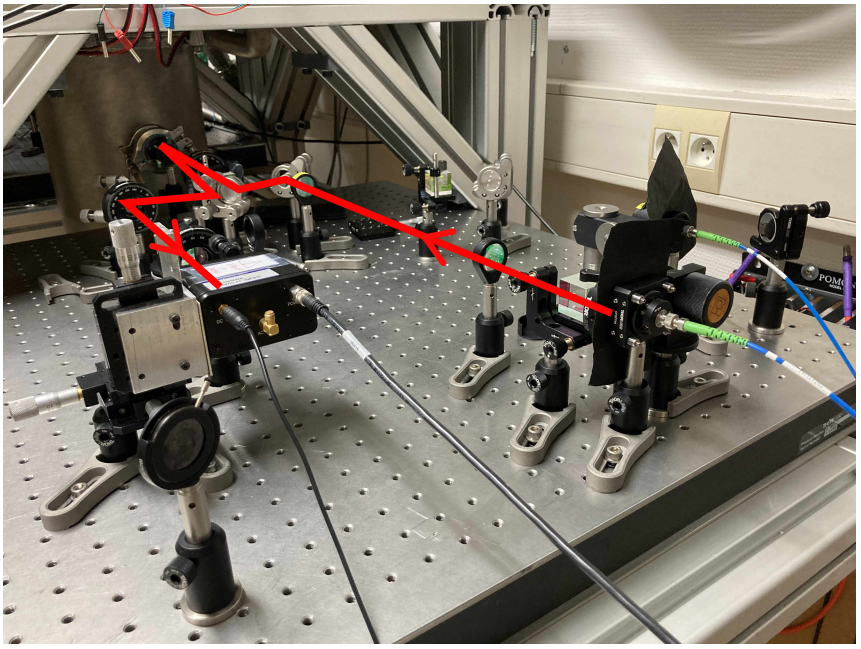

(d) Experiment

Figure 3.17: *Fig. 3.17a: a BVA-like structure with a hole on the bottom and the top metallic holder to permit the optical beam to cross through. Fig. 3.17b: the mirror holder adapted to hold the BVA-like structure. Fig. 3.17c: the same part of the experiment, once the cryogenic cooler has been closed again and vacuum and has been made inside. The two long tubes going out of the main metallic structure permit to have the light pass through, as they have small portholes at the top of these tubes. Fig. 3.17d: the experimental setup as in Fig. 3.15, with the beam traced on the picture in order to follow the propagation.*

3.2.2/ MEASUREMENTS

3.2.2.1/ RESULTS

The measurements are made in transmission with a photodiode PDA20CS(-EC) from Thorlabs, which permits to observe both the DC offset and AC coupling up to 10 MHz (in the 0 dB gain setting). In reflection, on the other hand, a 1611 photodiode from Newport is used, where the DC offset and AC coupling are in different outputs; however, the DC output does not start to (low-pass) filter the output until several hundreds of Hz. This means that with a slow enough scan of the wavelength, the DC output gives an accurate signal.

The Koheras AdjustiK^{TM} can be tuned in wavelength through a temperature shift (built-in) that permits to shift the wavelength for a total range of about 1 nm, from approximately 1549.5 nm-1550.5 nm (which corresponds to approximately one Free Spectral Range of the Fabry-Perot cavity). It also accepts a high-voltage entry to "fine-tune" the wavelength piezoelectrically: a 0 V-200 V input permits to shift by about 27 pm over the whole range, i.e. about 0.135 pm V^{-1}. At 1550 nm central wavelength, this translates into a total frequency shift of about 3.369 GHz, i.e. about 16.85 MHz V^{-1}.

A function generator is connected to a Thorlabs HVA200 high-voltage amplifier to provide the entrance signal for the piezoelectric unit. A ramp-like signal is produced from the signal generator, in order to obtain a smooth sweep of the laser's wavelength over the optical resonance. By comparing the transmission and reflection temporal signals and using the ramp signal to provide a time-to-frequency reference, it is possible to determine the peaks' width and frequency shift, as seen in chapter 3.1.3. The signal are compared and taken on a Rohde & Schwarz RTE1104 from which the datapoints are retrieved.

In order to align the quartz properly and reach a fundamental TEM00 Gaussian mode, we first look at a visual signal with an image sensor G12242-0707W from Hamamatsu. We first scan the temperature (hence wavelength) of the laser while tweaking the alignment of the injection mirror until obtaining an alignment on any optical mode, and then proceed to go as high-up in wavelength as possible while tilting the input mirror in order to keep a signal with the objective of isolating a TEM00 mode. We then put the photodiode in front of the image sensor and maximize the power in this mode by fine-tuning both the injection angle and the quartz rotation angle, as well as by rotating the $\lambda/2$ waveplate at the entrance to hit at best along the fast or slow axis of the quartz, while checking that there are no superpositions of optical modes (see section 3.2.2.2.3)

The typical optical resonance signal is seeable on Fig. 3.18. In order to treat and retrieve the data we are interested in from these graphs, a Python program is designed to approximate with either a Lorentzian function or a parabolic function. The Lorentzian function is especially relevant for the transmission signal, which is predicted to be Lorentzian near resonance, just like a regular profile for a transmitted mode in a Fabry-Perot cavity (see Eq. 3.13 and Eq. 3.41). This permits to obtain both the position of the center of the peak, as well as the peak's width (FWHM). Indeed, as we have shown in Eq. 3.12, the Airy peak is locally equal to a Lorentzian near resonance. A Lorentzian profite has its FWHM directly reachable in its definition [10] , so that if we can fit a particular profile to a Lorentzian,

[10] Indeed, a Lorentzian profile is written

$$f(x; x_0, \gamma) = \frac{1}{\pi\gamma}\left[\frac{\gamma^2}{(x-x_0)^2+\gamma^2}\right] \tag{3.65}$$

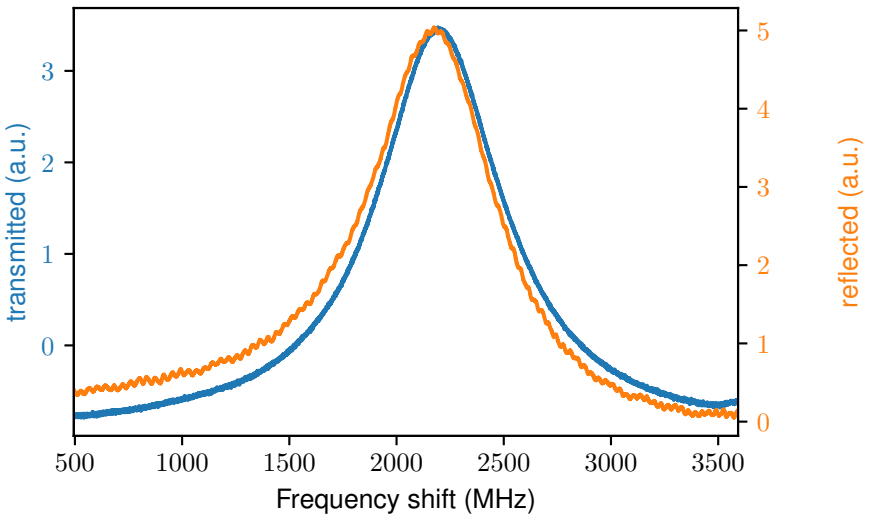

Figure 3.18: *An indicative typical resonance signal, in this case a* 50 nm *silver film. Data was taken with the oscilloscope. The dissymetry of the reflection signal as well as the slight shift in frequency between the reflected and transmitted signal, as predicted in chapter 3.1.3, is apparent here. Note that the reflection signal is obtained with the Newport 1611 photodiode, which has a negative gain, hence the inverted reflection signal.*

its FWHM is immediately extractable.

The reflection, on the other hand, is predicted to be dissymetrical and to have a non-Lorentzian shape, which makes it so that the Lorentzian profile fit is not well adapted. A parabolic fit (i.e. second-order polynomial type fit), however, gives a rather good approximation on the local extremum of the reflection curve. This fit is therefore accurately indicating the extremum position so it can further be converted into a frequency difference from the transmission extremum. A typical example of such fit and data extraction is visible in Fig. 3.19.

The experimental results from several deposition type and thickness are listed in Table 3.1. We mainly measured the FWHM, the frequency shift between the two peaks Δf and the transmission and reflection coefficient. Note that we defined the reflection coefficient in a somewhat peculiar fashion, for we chose to define the reflection as:

$$\begin{aligned} R_{\text{contrast}} &= \frac{P^R_{\text{min}}}{P^{\text{max}}_R} \\ &\neq \frac{P^R_{\text{res}}}{P^{\text{in}}} \\ &\neq \frac{P^R_{\text{res}}}{P^{\text{max}}_R} \end{aligned}$$

where P^R_{res} is the reflected optical power at resonance (i.e. when the transmission is maximum), P^{in} is the incident optical power and P^R_{min} is the minimum reflected power, which, in virtue of the shift Δf that was described earlier (see for example Fig. 3.18), is slightly different from the reflected power at resonance (i.e. when the transmission is maximum).

where x_0 is the center of the peak and γ is the FWHM.

		FWHM (MHz)	Δf	T_{max} (‰)	R_{contrast}
Al 30 nm	theo	1771	251	4	12.6
	expe	1635 ± 60	357 ± 20	1.2 ± 0.1	1.63 ± 0.1
	expe2	1856 ± 80	480 ± 25	0.84 ± 0.1	5.59 ± 0.5
Au 40 nm	theo	1224	92	22.6	27.5
	expe	1274 ± 70	136 ± 10	1.8 ± 0.2	8.4 ± 0.8
Au 50 nm	theo	886	64	6.6	15.5
	expe	577 ± 30	43 ± 4	4.3 ± 0.4	7.2 ± 0.7
Ag 35 nm	theo	1011	45	108	54.6
	expe	100 ± 10	100 ± 10	13 ± 1	10.7 ± 1
Ag 50 nm	theo	531	21	22	27.3
	expe	600 ± 15	56 ± 5	8.2 ± 0.8	15.3 ± 1.5
	expe2	644 ± 15	39 ± 4	15.4 ± 1.5	6.5 ± 0.6
Ag 70 nm	theo	339	13.2	1.3	7.1
	expe	502 ± 10	58 ± 10	0.08 ± 0.01	0.8 ± 0.1
	expe2	573 ± 10	51 ± 5	0.6 ± 0.05	1.9 ± 0.2
Ag 50 nm	theo	493	24.1	10.2	19.1
+ Au 5 nm	expe	724 ± 15	49 ± 5	4.1 ± 0.4	5.5 ± 0.5
TiO_2 10 nm	theo	896	65.9	7.1	16.1
+Au 50 nm	expe	1150 ± 20	179 ± 20	0.9 ± 0.09	5.2 ± 0.5

Table 3.1: *Table of results and measured parameters from different types of deposited thin films. Refractive indices are taken from [Yakubovsky et al., 2017][Ciesielski et al., 2017][McPeak et al., 2015b][Kischkat et al., 2012]. $R_{contrast}$ is defined as earlier in the main text. Only one polarization axis is studied here, as the results do not seem to be dependent on the polarization axis.*

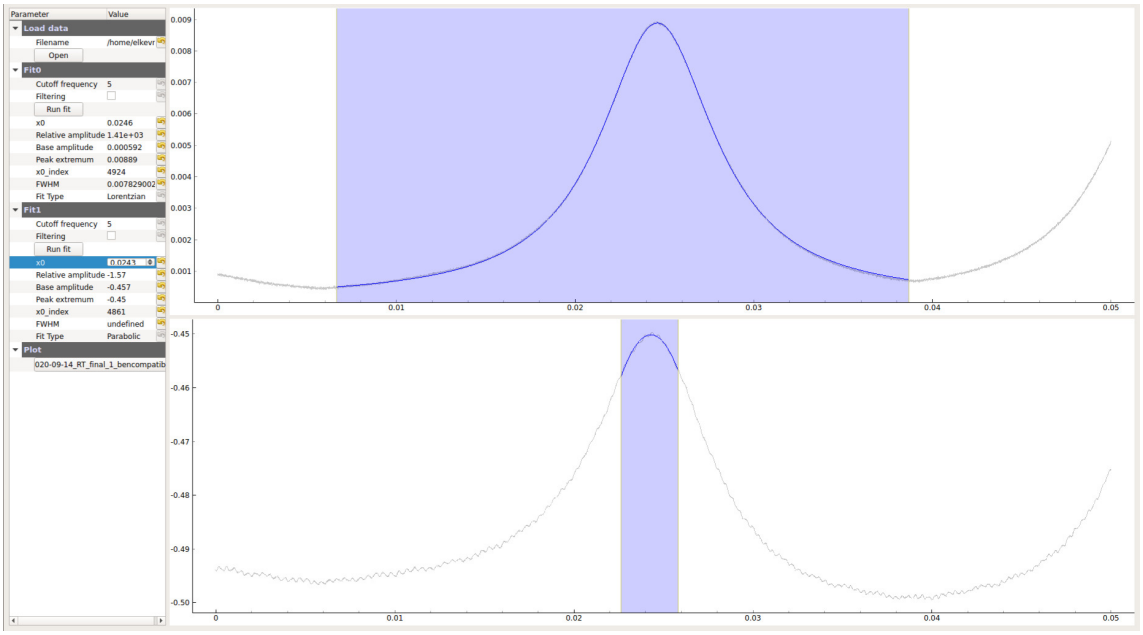

Figure 3.19: *Fitting and data extraction process with a python program of our design. The top figure is the transmission, with the grey curve being the experimental data and the blue curve being the fit displayed on top of the data. The blue area is the zone of interest of the figure that we manually select in order to be able to apply a Lorentzian or parabolic fit on the relevant part of the graph, where some informations about the fit thereafter appear on the left-hand side of the image. We then use these informations to further treat and convert them properly into frequency shifts between the top (transmission) and the bottom (reflection) plots, as well as retrieving the level of each signal and the FWHM for the transmission plot. Note that here too, much like in Fig.f,3.18, the reflected signal comes from the 1611 Newport photodiode and therefore has a negative gain, explaining the reversed shape of the peak.*

In other words, the way we defined the reflection is the minimum of the reflection over the maximum of the reflection. Because of absorption (and some transmission), this maximum of reflection is different from the total incident power. Moreover, the reflection minimum is slightly different from the reflection that we measure at optical resonance because of Δf. We chose this definition because it does not depend directly on the losses and gives therefore a better comparison tool between the different deposited thicknesses.

T_{max} is calibrated through a measurement of the incident optical power onto the quartz resonator with a powermeter, thus blocking the beam. The powermeter is then removed from the laser beam's path, allowing the laser beam to reach the quartz resonator and thus the optical resonance to take place, which output is then measured with a photodiode in order to assess the ratio of the output to the input, permitting the calculation of T_{max}.

3.2.2.2/ DISCUSSION, UNCERTAINTIES

Several sources of errors and uncertainties have to be taken into account regarding the results presented in the last section. Some sources are linked with our method for aligning the Fabry-Perot cavity and its intrinsic properties of birefringence and it is discussed in

the following section 3.2.2.2.3, while some other uncertainty originates in the way we treat the data, see following section 3.2.2.2.4. The deposition quality of the thin metallic films is also a broad source of disparity and uncertainty, as discussed in section 3.2.2.2.2. The particular discrepancy between theoretical and experimental values for the transmission and reflection are discussed in section 3.2.2.2.1.

3.2.2.2.1/ Discrepancy for R and T As is apparent from the results Table 3.1, there are some discrepancies between the theoretically expected and measured reflection and transmission [11]. As to investigate on this matter, two main leads are retained: the surface quality (see section 3.2.2.2.2) and the possible oxydation of the metallic layers.

The oxydation does not seem to immediately affect the results. Indeed, gold is known for being oxidation-resistant; yet, the samples with gold deposition do not seem to display significantly more conform results for T and R. From the oxidation-resistant property of gold, an attempt is made to coat a deposited silver layer (subject to oxidation) with a thin layer of gold; this does not improve significantly the conformity with theory either. Furthermore, because gold does not adhere on quartz just as well as e.g. silver, a doubt could subsist as to whether the poor results obtained with gold could be due to some surface tension buckling of some kind. This is in fact why a thin layer of chromium is usually deposited before gold is deposited. However, because chromium is a poor optical reflector (and was the reason for early and repeated failures at observing a Fabry-Perot resonance with typical quartz crystal resonators simply put and aligned with a laser beam), we attempt to coat the quartz with another material which could be more transparent to telecom wavelength and serve as an adherence layer: TiO_2 (see [Kischkat et al., 2012]). The results, in the last row of Table 3.1, are not particulary more encouraging than the rest. We therefore discard the oxidation as the sole source for discrepancy[12].

3.2.2.2.2/ Discussion about Deposition An early interest was given to gold and silver, as they tend to be the best types of metallic deposition for achieving high reflections. However, following the rather high error in the transmitted and reflected levels signal with respect to the theoretically predicted levels, some attention is given to the quality of the depositions themselves as it may influence the quality of the mirrors (see [Bartek et al., 1999]).

This particular subject has been studiedby [Elie-Caille et al., 2009], specifically on the influence of annealing and thermal treatment on the quality of the surface and on the formation of terraces. The study shows that some particular annealing time permits to reduce the typical roughness of the surface of the thin film of gold (which are on the few nanometer scale) and to create larger terraces to some Angström of roughness only. These island-like terraces are visible on Fig. 3.20, which are taken with a Scanning Electron Microscope (SEM).

Another effect that we observed mostly on silver is buckling. The formation of micrometer-

[11] Note that there are serious discrepancies between most of the expected and measured quantities; however, as Table 3.2 shows, it can be partially explained by the uncertainty of the deposited thickness, and the surface quality does influence the results too, see for example [Reddy et al., 2017] or [Jayanti et al., 2015]

[12] It is clear, however, that although the oxidation does not seem to explain the main discrepancy between experimental and theoretical values for R and T, we have noticed (though not systematically investigated) that it does influence the results on the scale of several days/weeks of time if the sample is kept without a proper vacuum environment

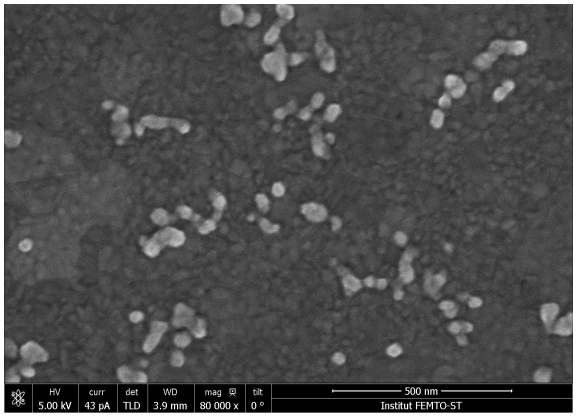

(a) PVD

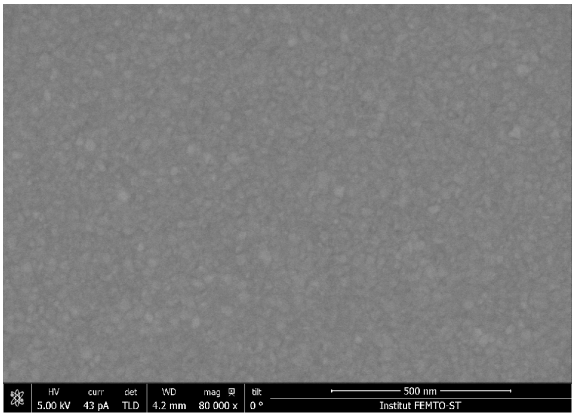

(b) Magnetron Sputtering at room temperature

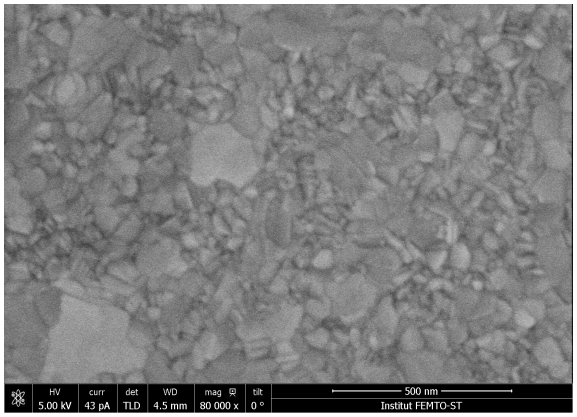

(c) Magnetron Sputtering at 300 °C

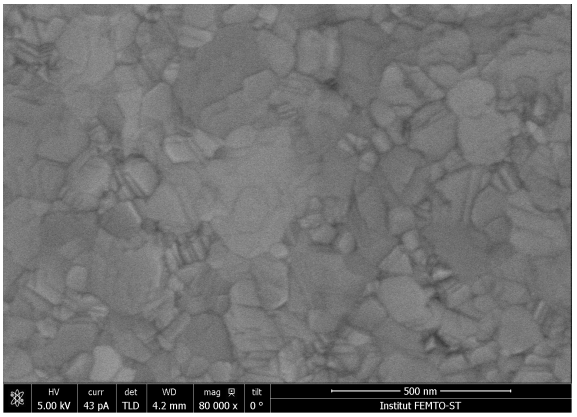

(d) Magnetron Sputtering at 300 °C with 8 h annealing at 300 °C

Figure 3.20: *SEM images of the gold layer deposited with different techniques. 3.20a is deposited with Physical Vapor Deposition, 3.20b with Magnetron Sputtering at room temperature, 3.20c with Magnetron Sputtering at* 300 °C *and 3.20d with Magnetron Sputtering at* 300 °C *followed by* 8 h *annealing at* 300 °C*. We can see island-like structures appearing in the coatings made with MS technique, which does not appear just as much with PVD technique. The bottom-right bar on the figures gives the* 500 nm *reference scale.*

scaled bubbles has been observed and studied in litterature (see [Dahmane et al., 2015], [Coupeau et al., 2004] or [Hutchinson, 2001]).

However, both these effects which are related to the deposited layer's quality, and although they certainly influence the observed refractive index and the exact local thickness which the light goes through, they have not shown any clear-cut effect on the theory-experiment discrepancy observed on transmission and reflexion levels in section 3.2.2.1.

Furthermore, the surface quality of the quartz itself has been, for some of the quartz resonators, polished by an external company to achieve a quartz surface quality of $\lambda/4$ (for our telecom wavelength $\lambda = 1550\,\text{nm}$). This did not seem to induce any specific difference in the results. We therefore do not consider either the quartz' or the deposition surface quality further as the possible source for discrepancy.

The deposition of most materials is done with magnetron sputtering technology

	FWHM (MHz)	Δf (MHz)	Finesse	$T_{\text{max}}\%$	R_{contrast}
Ag 47 nm	569	22.6	167	3.3	33.9
Ag 50 nm	531	21.5	184	2.2	27.3
Ag 53 nm	502	20.8	193	1.4	22.4
Ag 47/53 nm	534	21.2	180	2.1	34.7
Ag 53/47	534	22.4	180	2.1	21.1

Table 3.2: *Table of the influence of the thickness uncertainty on the different quantities involved. Computed with the refractive index for* 50 nm*, extrapolated from [Ciesielski et al., 2017].*

[Billard et al., 2005]. The sputtering happens for one side at a time, and it is therefore a source of discrepancy in deposited thickness between the two faces of the quartz. Although ellipsometric measurements realized after thin silver layer deposition have made it clear that the deposited layer is indeed in the desired range of e.g. 50 nm, direct mechanical measurement is technologically difficult. Indeed, the deposited layer is typically sputtered through a mechanical mask, making the deposited layer slightly thicker at the center than on the edges, so that there is no clear-cut thickness edge. In order to characterize the thickness, a large ($\approx$ 300 nm) layer of material is deposited on a glass wafer to be able to measure it more precisely, so that a simple deduction is made as to how long the deposition should last.

From the analysis of some deposition images with SEM, the total uncertainty on deposited thickness is estimated to be, on average, of ± 3 nm. This is done by depositing a thin metal layer onto a circular wafer which is then cut along a line passing through the center of this circular wafer. The SEM is then performed along the central thickness, which permits to measure the deposted layer.

Table ⚠shows the way the results for FWHM, Δf, T_{max} and R_{contrast} can change when an error of 3 nm is made on the deposition thickness, giving an rough estimation of the tolerance and uncertainty of the computational predictions.

3.2.2.2.3/ Alignment, superposition of modes As we discuss in section 3.1.1, quartz is a birefringent material. It therefore has two different preferred axes for light coupling, the fast and slow axis. Each has a different effective refractive index $\tilde{n}$, which means that the polarization of the incoming light influences the optical path that the beam travels. The wavelength where the phase-matching condition is filled is slightly different for each axis. This is what we observe on Fig. 3.21. The temperature (hence wavelength) of the laser is scanned in time. We see a succession of TEM modes (00, 01, etc) along each one of the two fast and slow axes of the quartz (two distinct measurements along each axis have been superimposed on the graph). These modes are, however, sometimes overlapping.

This creates a situation where two different modes, which have a priori different characteristics and may have different FWHM for example, may coexist at the same time if the polarization of the incoming beam is not exactly set along one axis only. This can affect the exactitude of our measurement. It is for this reason that we mention, in section

3.2.2.1, that we rotate the $\lambda/2$ waveplate to get a polarization which is as purely along one axis as possible, in order to eliminate coupling with the other axis. Since the TEM00 is the right-most (left-most) mode on each succession of modes when increasing (decreasing) the wavelength once set on a particular axis, it is convenient to select the most isolated TEM00, which, on Fig. 3.21, is the right-most mode along the $21°$ axis.

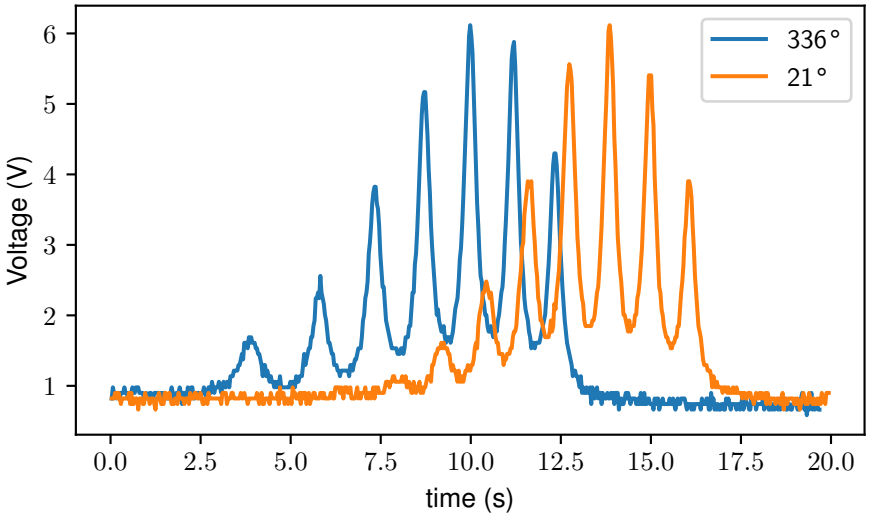

Figure 3.21: *Transmission signal of the Fabry-Perot cavity versus time, which corresponds to wavelength because a temperature (hence large wavelength) sweep is conducted on the laser, with wavelength increasing with time. Two signals are superimposed, with two different orientation of the injection $\lambda/2$ waveplate (see Fig. 3.15), which are along the fast and slow axes of the quartz. These signals correspond to a succession of TEM$_{XY}$ modes, with $XY = 0, 1, 2, \cdots$, which are known to be resonant at different frequencies. Note that in some cases, different modes along a different axis can coexist at the same wavelength (time), showing how polarization of the incoming beam, if not set exactly onto a polarization (fast or slow) axis, can affect the measurements' exactitude. An SC cut quartz was used for this measurement, with a* $50\,\mathrm{nm}$ *silver deposition.*

3.2.2.2.4/ Data treatment As shown in Fig. 3.19, the way we retrieve the data is through a python program of our design where a visual window helps to select the zone of interest (ZOI) in which we perform a fit, either Lorentzian or parabolic. For the transmitted peak, we superimpose a Lorentzian distribution. From this fit, we directly retrieve the FWHM expressed in the same unit as the x axis, namely, time; we also retrieve other relevant informations like maximum and minimum of the peak, as well as its center's position. By deducing the center of the reflected peak with a very local parabolic fit (see Fig. 3.19), again in unit of time, we can multiply this Δt by the scanning velocity, in $\mathrm{MHz\,s^{-1}}$. This scanning velocity is related to the slope of the voltage applied to the piezo unit of our laser, so that we can deduce the total wavelength/frequency shift in this time Δt (see Fig. 3.18). From this, we finally recover both the FWHM and the Δf.

This process, however, is prone to several mistakes and uncertainties, mostly user-dependent and numerical. Indeed, slightly changing the exact width of the ZOI and its central position gives slightly different numerical results for both the FWHM and the cen-

tral frequency timemark. Repeated measurements and attemps at extracting the exact timestamp for a particular file has lead to the conclusion that the distribution of error is approximately Gaussian, and has an approximate standard deviation of $\pm 2\%$ for the Δf and of about 3×10^{-3} for the FWHM. See for example the distribution of error for the timestamp of the transmitted peak's maximum in a particular datafile in Fig. 3.22.

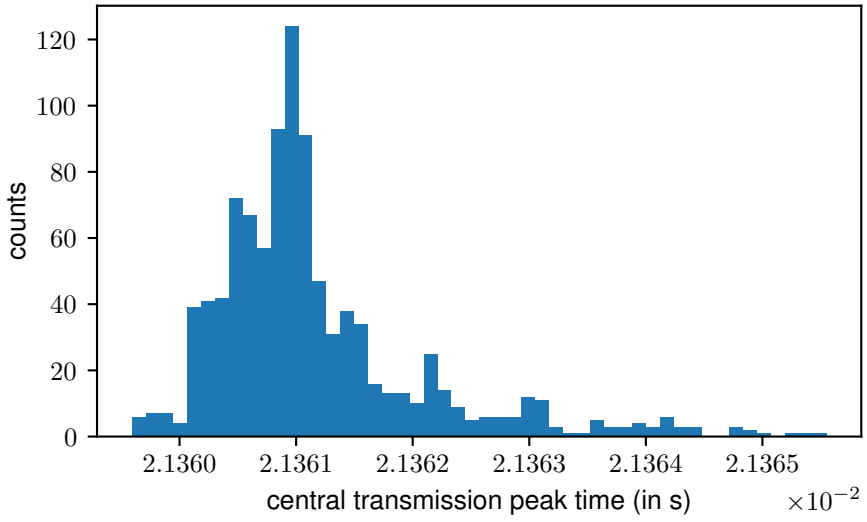

Figure 3.22: *Distribution of the central timestamp of the transmission peak in a particular result file, of the same kind displayed in Fig. 3.18 and with the python program method shown in Fig. 3.19. The treatment was lead with 990 points. The distribution is approximated with a Gaussian, and has a relative standard deviation of* 4×10^{-5} s.

3.2.2.3/ CRYOGENIC TEMPERATURE MEASUREMENTS

As well as with simple vacuum in the chamber left at room temperature, the cryogenerator can be also turned on to the set temperature of approximately 4.2 K. We conducted several measurements of the same type as before at this cryogenic temperature, with expected changes in the optical properties of the silver layers (see [Bass et al., 1983]) hence the Fabry-Perot cavity.

These measurements were lead for several samples of deposited silver thin layers, of thickness 35 nm, 50 nm and 70 nm. The experimental process is fundamentally the same as before, with a necessary realignment of the optical beam to match the contracted and slightly misaligned cavity, as well as a new resonant wavelength setting. Of course, only an outside alignment procedure is possible, so that the only available parameter to tweak is the angle of the incident beam, not the quartz' angle[13].

A notable improvement on both the FWHM and the Δf was observed, as they both decreased, indicating the reflectivity to be higher and the absorption to be lower. Some of the measurements are seeable in the following section 3.2.3.2.

[13] Note that a future improvement includes being able to tweak this angle with a piezo-controlled rotative holder from company Attocube

3.2.3/ $\tilde{n}$ EXTRACTOR

In order to achieve optomechanical coupling, we are primarily interested in the quantity of light present inside the quartz crystal; it is therefore of foremost importance to be able to derive information about this quantity with every possible mean. The theoretical description presented in section 3.1.3 and in particular the amplification factor $\mathcal{A}$ in Eq. 3.62 provided a way of calculating theoretically the light present inside the cavity; the whole description, however, relies on the knownledge of the particular absorptive refractive index $\tilde{n} = n - in'$ of the mirrors. We therefore now look into the possibility to retrieve this refractive index from experimental measurements.

As we have seen and presented in section 3.1.3, the absorptivity of the mirrors made from thin metallic layers bring some unfamiliar effects, among which a modified FWHM and a shift in frequency between the reflected and transmitted peaks, Δf. It is intuitive and obvious from the derivation of equations 3.41 and 3.51 that the optical refractive index n influences the result of these equations, i.e. that the refractive index of the mirrors has an influence on the peaks themselves (see for example Fig. 3.7), be it on the FWHM or the exact location of the peak (hence their frequency shift).

A direct subsequent question is whether there is a bijective relationship between these quantities, and whether we could retrieve the refractive index $\tilde{n}$ with experimental measurements of a particular cavity. As a matter of fact, this section shows that, to within certain limits and uncertainties, it is possible to draw such a relationship and hence retrieve the refractive index from the measurement of the FWHM and Δf, the peaks' frequency shift [Rosenziveig et al., 2021].

3.2.3.1/ METHODS

We start from the observation that we have expressed the refractive index in Eq. 3.33b as a two part index, $\tilde{n} = n - in'$. These real and imaginary part of the refractive index can be considered as two independant quantities that we need to retrieve, hence implying we need two variables to retrieve them from. As we have seen from section 3.2.2.1, the total reflection and transmission are unreliable quantities to work with, as a large dispersion with predicted values are observed, and they are therefore not reliable quantities to try and work with.

Let us stress that a fundamental limitation to this method and its subsequent development is that the refractive index we extract is averaged over both the total active surface and over the two mirrors. Where therefore can obtain the refractive index of the equivalent layer equally deposited on both sides of the quartz. Let us note that all subsequent formulas have therefore been simplified from their versions in section 3.1.3 and include two layers which are deemed the same, so that there is no difference for any of the properties for the two mirrors.

We remind the expression of Eq. 3.39 for the transmitted intensity across a thin metallic layers absorptive mirrors:

$$\mathcal{T}_{FP} = \mathcal{T}_{\text{max}} \frac{1}{1 + F \sin^2(\delta/2)} \tag{3.39}$$

To be able to go further, a capital observation is required: as written in Eq. 3.40:

$$\delta = 2\beta_2 - 2\Delta_{210} \tag{3.40}$$

Although $\beta_2 = \frac{2\pi}{\lambda_0}\tilde{n}_2 d$ has a simple expression (where $\tilde{n}_2 \in \mathbb{R}$ here, because the quartz resonator is taken as non-absorptive), the other two quantities are in fact much more complicated and integrate the refractive indices of the metallic layer in their expressions (see section 3.1.3.2.1 for their definition). However, it is possible to show that they barely vary when λ varies, so that they almost constitute a constant in the equation over a wide range of wavelength, see Fig. 3.23a.

It is in fact rather natural that the evolution is very slow and only trivially dependent on the wavelength (for a constant refractive index): indeed, the quantity R_{230}, as discussed in section 3.1.3.2.1, represents an ideal three-layers Fabry-Perot cavity (such as described in section 3.1.2) with a few-nanometers-thick metallic layer stuck between two infinite stacks of material 2 and 0 (namely quartz and air in this case). The layer being so thin, it is only marginally important how the wavelength changes, as it is so much longer than the layer itself. This is, of course, only true as long as the wavelength remains much longer. In this case, the quantity δ can be considered in the much simpler form, which depends in a very simple linear way on the laser's frequency:

$$\delta = \frac{4\pi f \tilde{n}_2 d}{c} + \text{cst}(\tilde{n}_{\text{Ag}}) \tag{3.66}$$

where the constant is, in fact, constant with respect to the wavelength but does depend on the mirrors' refractive index. Further analysis will be greatly simplified by this fact.

3.2.3.1.1/ FWHM The first variable we get interested in is the FWHM. In virtue of the transmitted intensity equation at the beginning of this section (Eq. 3.39) and the derivations leading to the FWHM for the ideal cavity case in Eq. 3.23, as well as the previous observation about the quantity δ, the FWHM for the absorptive case is derived by noting that the shift in frequency from resonance to half the peak's maximum is written:

$$F \sin^2\left(\frac{\Delta\delta}{2}\right) = 1$$
$$\frac{\Delta\delta}{2} \approx \sqrt{\frac{1}{F}}$$

where we have written $\Delta\delta$ instead of δ because this corresponds to a laser frequency shift from the $\delta = 0$ condition of in-resonance frequency, and in the last equation the first $\Delta\delta$ also designates a small shift. We can therefore write the final form of the FWHM, which is twice as much as the previous condition (twice the shift from $\delta = 0$) by using Eq. 3.66:

$$\text{FWHM} \approx \frac{c}{\pi \tilde{n}_2 d}\sqrt{\frac{1}{F(\tilde{n}_{\text{Ag}})}} \tag{3.67}$$

where the approximation sign holds for high enough reflectivity and in any interesting case for us (see footnote 5 from chapter 3.1) and where all the quantities are defined in the same way as in section 3.1.3.2.1. We have stressed the dependancy of F on the refractive index of the metallic layer by adding explicitly the dependance. There is no specific need to account for the transmission peak's exact central wavelength[14] in this case, as the equation for the intensity shows, it suffices to consider the shift from the $\delta = 0$ on-resonance condition. Furthermore, althouh F has a complicated expression involving

[14] As Fig. 3.7 shows, changing the mirrors' thickness or refractive index changes the peak's central wavelength.

indeed the wavelength, it is possible to compute it against the wavelength and to show, in the same way as for Δ_{210}, that it is only marginally dependent on the wavelength, for much the same reason as before. See Fig. 3.23b

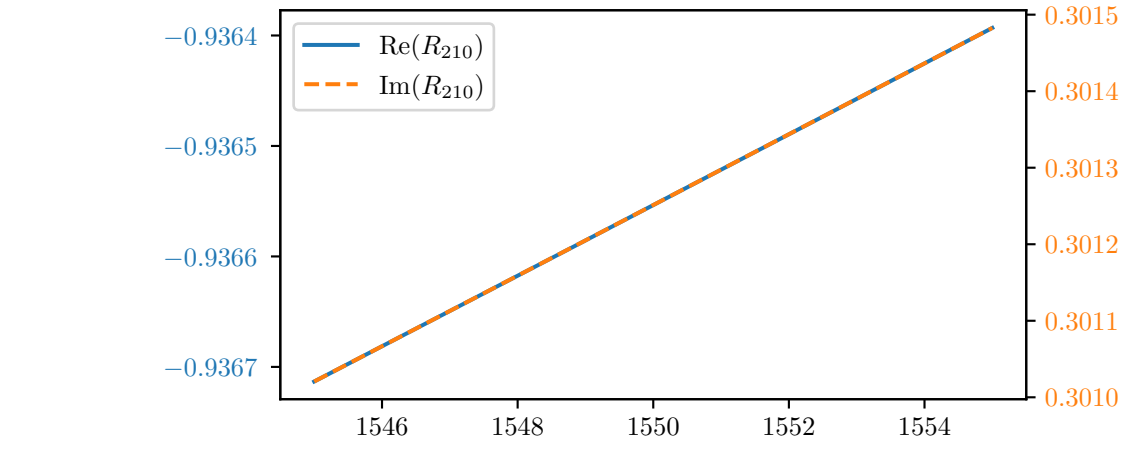

(a) R_{210}

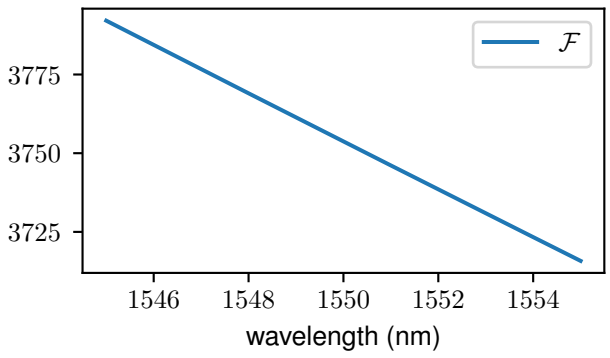

(b) F

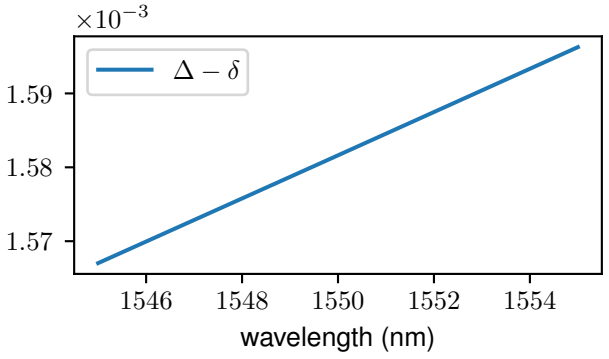

(c) $\Delta - \delta$

Figure 3.23: *Fig. 3.23a: R_{210} against wavelength shift. Computation made for a* 35 nm *silver layer with constant index of refraction. Because we consider both metallic layers identical (i.e. 1st and 3rd layers), this could just as well describe R_{230}. Fig. 3.23b: F against wavelength. As before, the quantity F is only marginally dependent on the wavelength and it is therefore not necessary, once a particular wavelength is chosen, to account for the variations of F with varying wavelength for small variations. Fig. 3.23c: $\Delta - \delta$ is plotted against wavelength for a constant index of refraction. Once again, it is apparent that this quantity barely changes with changing wavelength over a rather large shift. Simulation is lead for a* 35 nm *of silver.*

3.2.3.1.2/ Δf The second quantity we get interested in is the peaks' frequency shift, Δf. We remind the expression for the reflected intensity, written in Eq. 3.51:

$$\Re_{\text{FP}} = |R_{012}|^2 \frac{1 + |\zeta_{210} R_{210}|^2 - 2|\zeta_{210} R_{210}| \cos(\Delta)}{1 + |R_{210}|^4 - 2|R_{210}|^2 \cos(\delta)}$$

where everything is defined just as in section 3.1.3.2.3, and, in particular, Δ is similar to δ and is defined in Eq. 3.52 as

$$\Delta = 2\beta_2 - \Phi_{210} - \Delta_{210}$$

Here, it is critical to be able to define the minimum of the reflected peak. In order to do this, we note that the difference between Δ and δ yields:

$$\Delta - \delta = \Delta_{210} - \Phi_{210} \tag{3.68}$$

Once again, it greatly simplifies further calculations and considerations to note that this quantity too is almost wavelength-independent, as Fig. 3.23c shows. Indeed, with $\Delta - \delta$ being established as almost a constant with respect to wavelength, it is much easier to look for an optimum of Eq. 3.51, which we rewrite in a slightly different way:

$$\Re_{\mathsf{FP}} = |R_{012}|^2 \frac{1 + |\zeta_{210}R_{210}|^2 - 2|\zeta_{210}R_{210}|\cos(\delta + \epsilon)}{1 + |R_{210}|^4 - 2|R_{210}|^2\cos(\delta)} \tag{3.69}$$

where we have written $\epsilon = \Delta - \delta$, a constant with respect to the wavelength which is added to the quantity δ.

If δ is considered as the variable and all the rest of the quantities are considered constant, so far in a pure mathematical reasoning, an optimum for the function exists, and has a rather complicated expression. It can be shown to yield:

$$\begin{aligned}\delta_R = -\arccos\Big(\Big[\Big\{ & B^4(-2D-2)^2E^2sin^4(\epsilon) - 4(A^2E^2 - 2ABDE\cos(\epsilon) \\ & - 2ABE\cos(\epsilon) + 2AE^2 + B^2D^2 + 2B^2D + B^2 - 2BDE\cos(\epsilon) \\ & - 2BE\cos(\epsilon) + E^2)(-A^2E^2 + 2ABDE\cos(\epsilon) + 2ABE\cos(\epsilon) \\ & - 2AE^2 - B^2D^2\cos^2(\epsilon) - 2B^2D\cos^2(\epsilon) + B^2E^2sin^2(\epsilon) \\ & - B^2\cos^2(\epsilon) + 2BDE\cos(\epsilon) + 2BE\cos(\epsilon) - E^2)\Big\}^{\frac{1}{2}} \\ & - B^2(-2D-2)Esin^2(\epsilon)\Big] \Big/ \\ & \Big[2(A^2E^2 - 2ABDE\cos(\epsilon) - 2ABE\cos(\epsilon) + 2AE^2 + B^2D^2 \\ & + 2B^2D + B^2 - 2BDE\cos(\epsilon) - 2BE\cos(\epsilon) + E^2)\Big]\Big)\end{aligned} \tag{3.70}$$

where $A = |\zeta_{210}R_{210}|^2$, $B = 2|\zeta_{210}R_{210}|$, $D = |R_{210}|^4$ and $E = 2|R_{210}|^2$.

This gives us the δ for which the reflected amplitude is minimum. It is sufficient to describe the shift in frequency between the peaks, because $\delta = 0$ corresponds to the transmitted intensity maximum, i.e. the intracavity resonance. Therefore, the only remaining step is to find the frequency shift between the $\delta = 0$ condition and this last condition for δ in Eq. 3.70, which can easily be computed.

As we have seen earlier, δ is dependent on the frequency in a trivial linear way (to within a n dependent constant which has to be calculated, see Eq. 3.66). Because all of the other quantities involved in Eq. 3.69 are also almost wavelength-independent (for the same reason that was introduced in section 3.2.3.1.1), it is possible to consider the optimum with respect to the frequency in a very simple way: from the $\delta = 0$ condition of transmission

maximum to the $\delta = \delta_R$ condition, the only possible shift must come from β_2, as we established from Eq. 3.66. This shift in δ is written:

$$\Delta\delta = 4\pi\tilde{n}_2 d\frac{\Delta f}{c} \tag{3.71}$$

so that the formula we are looking for that describes the shift in frequency between the two peaks is when this shift equals δ_R. This yields the form:

$$\Delta f = \frac{c\,\delta_R(\tilde{n}_{\mathsf{Ag}})}{4\pi\tilde{n}_2 d} \tag{3.72}$$

where we have, here too, added the dependance of δ_R on the refractive index of the mirror n_{Ag} to stress the fact that this is the relevant quantity in the equation.

3.2.3.1.3/ Computational method Once the expressions for Δf (Eq. 3.72) and the FWHM (Eq. 3.67) are obtained, we have two conditions to retrieve the actual refractive index. In fact, for each value of FWHM and Δf, there exists a priori an infinite set of solutions values n and n', the real and imaginary part of the refractive index respectively, that verifies the condition.

We design a python program that rather simply computes the FWHM and the Δf over a certain n and n' span for a particular mirror thickness (considered to be equal on both sides). Because the computational 2D fold of FWHM and Δf is not necessarily a plane over a large-enough n and n' span, it is not possible to resolve it analytically by fitting it a to a plane and this method gives erroneous results. It is therefore more accurate and simpler to consider a calculatory solution of the type local numerical approximation. That is, a certain couple of n_0 and n'_0 are considered a solution for the FWHM if they verify

$$\left|\mathsf{FWHM}(n, n') - \mathsf{FWHM}(n_0, n'_0)\right| < \eta \tag{3.73}$$

where η is small and is chosen arbitrarily. A visual representation of such a situation is presented in Fig. 3.24.

Each of these two a priori semi-infinite sets of n and n' that are solutions (one for FWHM and the other for Δf) locally (i.e. over a small enough span) form a straight line. We fit them to a first order polynom (a line) and calculate their intersection point. This point is the solution of the problem and gives $\tilde{n}_{\mathsf{Ag}}$.

3.2.3.2/ Results

We present here some results, basing ourselves on experimental values for Δf and FWHM that were obtained in the same way as in section 3.2.2, for room and cryogenic temperature at 4.2 K (see section 3.2.2.3).

Some parameters are fixed for the calculations of the refractive indices, such as the quartz thickness $d_2 = 1\,\mathrm{mm}$, the quartz refractive index is taken to be$\tilde{n_2} = 1.54$. These are assumed to be exact and no uncertainty is taken into account regarding their value.

Some experimentally taken data for FWHM and Δf for a particular deposition thickness and particular temperature have been processed both at room and cryo temperature to obtain their corresponding n and n', and tabulated with their uncertainty (see following

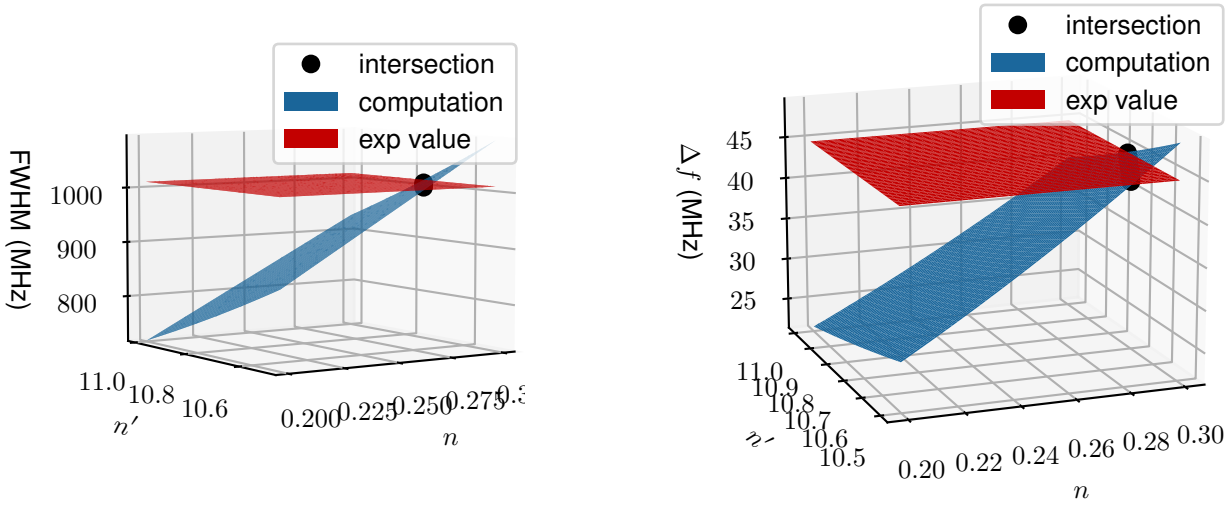

(a) FWHM

(b) Δf

Figure 3.24: *A typical extraction of sets of n and n' that verifies the experimental value conditions, for FWHM and Δf. This produces a locally linear set of solutions, which are a priori different except for their intersection, which therefore gives the actual value of n_{Ag} we are looking for. In this example, the theoretical values for a* 35 nm *of silver are taken from [Ciesielski et al., 2017], $\tilde{n} = 0.2997 - 10.7355j$, which gives FWHM=*1011 MHz *and $\Delta f =$* 45 MHz*. $\eta = 1 \times 10^{-2}$ here (see Eq. 3.73). The program returns a fit value of $\tilde{n} = 0.2999 - 10.7384$, which gives an error of approximately 7×10^{-4} for n and 3×10^{-4} for n'. See section 3.2.3.3 for more details. Note that the calculation is lead with 128bits numpy floats in python, or else with 64bits float, erratic results are returned.*

sections for details). The results are displayed in Table 3.3, and they are also represented graphically in Fig. 3.25.

It is not possible to measure the values at midway temperatures because the cryocooler can only be set to this temperature and the temperature quickly changes to rise when the cryocooler is turned off, so that there is no time to fine-tune the alignment and take the transmission and reflection measurement.

The measured values are processed, knowing the deposition thickness to obtain their corresponding n and k, and are tabulated with their respective uncertainty (see section 3.2.3.3 for details). Let us stress that each extracted value of n, n', FWHM and Δf correspond to a single particular deposition. The values are detailed in Table 3.3. They are also graphically represented in Fig. 3.25, where it is possible to see that the measurements and method meet the ground requirement that it is possible to clearly separate between the room temperature and the cryo temperature results, as the wide spread (including uncertainty bars) between the two results shows.

We observe graphically from Fig. 3.25 that for each thickness, there is a tendency to decrease both the real and imaginary part of the refractive index at 4 K with respect to 300 K. The fact that the index varies with thickness is not surprising and is widely observed in the litterature [Ciesielski et al., 2017] [Mayy et al., 2012] [Reddy et al., 2017]. Furthermore, we observe that the decrease is much more significant for the real part n

($\approx 40-60\%$) than for the imaginary part n' ($\approx 5-8\%$). This is coherent with the tendency found in the litterature (with the data from e.g. [Jayanti et al., 2015]).

Although the obtained values for n and n' are different from the data found in the (scarce) litterature for thin films (e.g. [Ciesielski et al., 2017]), they highly depend on the deposition process and can very by as much as 60% for n and 8% for n' (data from [Jayanti et al., 2015], at 500 nm wavelength). Comparing values for some $d \approx 35$ nm thin film at 594 nm from [Mayy et al., 2012] and [Ciesielski et al., 2017] permits to see that even though the technique of deposition is evaporation in both cases, the variation is still large: $\approx 45\%$ for n and $\approx 6\%$ for n'. Our values for 35 nm of silver, for example, vary by about 16% for n and 8% for n' with respect to the values obtained in [Ciesielski et al., 2017], which we deem satisfactory in view of the aforementioned orders of magnitude.

The extraction method we use inherits an intrinsical imprecision from the fact that we consider the two mirrors as perfectly equal. Incidentally, we also consider the mean refractive index over the whole surface that the light acts upon. We are therefore only able to extract the mean refractive index, averaged over the whole surface and over the two mirrors. Note that this is inherent to any optical detection method for the refractive index, e.g. ellipsometry. The size of the laser beam is 71 µm at the waist, which is small with respect to the typically millimetric beam size in ellipsometry.

This means that the only accessed value for the equivalent refractive index of the thin films is for this particular wavelength. However, the method we use can easily be extended to longer or shorter monochromatic wavelength, as long as two conditions are met: Firstly, a fundamental requirement is to be able to sweep the frequency of the source over the resonance gain to observe any resonance curve. This means that the source's spectral width should be sharper than the Fabry-Perot resonance's spectral width. Second, no intra-silver-layer resonance shoud be observed. The theoretical limit for this to happen is when $d = p \times \lambda/2$, with p any natural number, i.e. deep UV light in this case.

The evolution of the optical properties at 4 K go in the desired direction, i.e. become less absorptive and more reflective. This is coherent with the litterature [Bass et al., 1995] [Smith et al., 1995]. For example, the Fabry-Perot cavity with 35 nm of silver on quartz has a (theoretical) optical finesse of 80 at room temperature, which grows up to 100 at 4 K. The maximum transmission is almost doubled, from 1% at room temperature to 1.8% at 4 K. The contrast of the reflection (i.e. $1 - R_{\text{min}}/R_{\text{max}}$) goes from 18% at room temperature to 65% at 4 K. The maximum absorption goes from 50% at room temperature to 40% at 4 K.

3.2.3.3/ UNCERTAINTIES

First and foremost, we stress that this method is used and is useful for our particular experimental conditions and limitations (such as a systematic interest and deposition of two-layers, experimental difficulty to vary the angle of incidence which is characteristic of the ellipsometric method, see section 3.2.3.4). In the following sections, we discuss different types of sources for error and uncertainty. We then perform a Monte-Carlo statistical analysis in section 3.2.3.3.5 to be able to account for the error bars displayed in the previous result section 3.2.3.2.

		300K	4K	FWHM (MHz) **at 300K**/*at 4K*	Δf (MHz) **at 300K**/*at 4K*
Ag35nm	n	0.2518 **±0.0178** *±0.0146*	0.0951 **±0.00675** *±0.00551*	**1226** *1005*	**50** *20*
	n'	9.8772 **±0.3358** *±0.1185*	9.3608 **±0.3182** *±0.1123*		
Ag50nm	n	0.2609 **±0.01591** *±0.01382*	0.1100 **±0.00671** *±0.00583*	**790** *612*	**35** *13*
	n'	9.6359 **±0.2601** *±0.1445*	8.8149 **±0.2380** *±0.1322*		
Ag65nm	n	0.2330 **±0.01281** *±0.01141*	0.1244 **±0.00684** *±0.00609*	**690** *500*	**31** *12*
	n'	8.7164 **±0.2179** *±0.1656*	8.1323 **±0.2033** *±0.1545*		

Table 3.3: *Table of computations of n and n' with their uncertainty: in **bold green** (first in order of appearance), the uncertainty taking into account the deposition thickness uncertainty (see table 3.6); in italic orange (second in order of appearance), the uncertainty without taking into account the uncertainty on the deposition thickness (see table 3.7 and the discussion in section 3.2.3.3.5). Each of these values is extracted from a single particular deposition and its experimental values of FWHM and Δf (last columns), with the first value appearing in red being the 300 K value, whereas the value in blue is the 4 K value. Note that the values of FWHM and Δf here are different from those of Table 3.1, as they concern different metal deposition runs.*

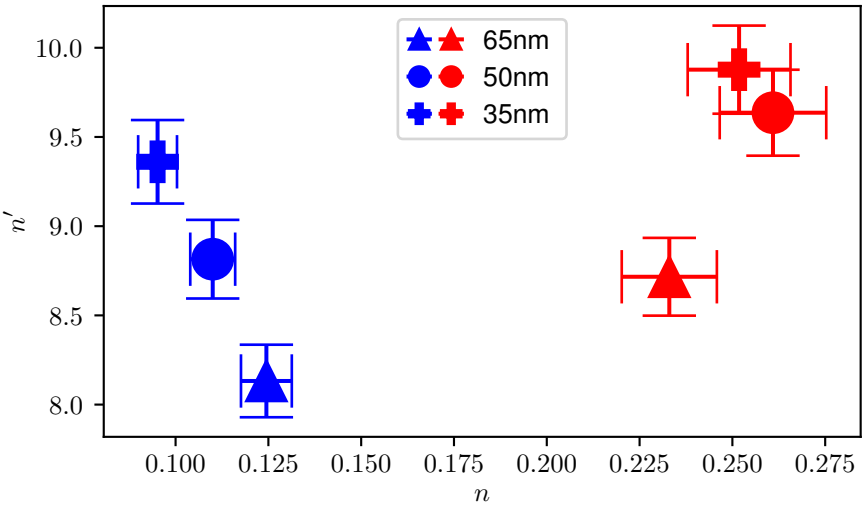

Figure 3.25: *Graphical representation of the results displayed in Table 3.3. The red color (right-most points of the graph) is used for the* 300 K *points, whereas the blue color (left-most points of the graph) is used for the* 4 K *points. The error bars including the thickness uncertainty (see Table 3.6 and the red error bars displayed in the results Table 3.3) are taken here.*

3.2.3.3.1/ Intrinsical and Numerical We start by stressing that this extraction method inherits an intrinsical imprecision from the fact that we consider the two mirrors as perfectly equal, as well as incidentally considering the mean refractive index over the whole surface that the light acts upon. We therefore only are able to extract the mean refractive index, averaged over the whole surface and over the two mirrors.

We verify the numerical error which is intrinsic to the method, and whereas it is good enough, by inputing a FWHM and Δf which are known for a particular thickness. This is what is shown in Table 3.4, where we use data taken for silver thin films from [Ciesielski et al., 2017]. From these values of n and n', displayed in column 1 and 2, we calculate by two different methods the corresponding FWHM and Δf, displayed in columns 3 and 4: one is the method described above in section 3.2.3.1 (see Eqs. 3.67 and 3.72). The other is an iterative numerical method, looking for optima of transmission and reflection peaks, which is therefore less precise. They agree, however, to within 2×10^{-3} with a million iteration points for the iterative method; this varies depending on the wavelength which is spanned. We conclude that although this method is not as good as the previous one, it is useful indeed in confirming the displayed FWHM and Δf results for a particular set of n and n'.

These FWHM and Δf are used to feed the program, out of which columns 5 and 6 are filled. Finally, columns 7 and 8 correspond to the relative error made between the program output and the original value we started from. Note that these errors and all extracted set of n_0 and n'_0 (solutions of the problem) depend slightly on the span of n and n' we allow when running the program. This is easily explained by the quality of the local linear fit, once intersection points are found between the computed surface of FWHM and Δf and the actual experimental value (see Fig. 3.24). For example, for a 50 nm silver layer, with refractive index $\tilde{n} = 0.2522 - 10.8507j$, allowing n to be spanned

	n	n'	FWHM	Δf	n_{fit}	n'_{fit}	$\delta n/n$	$\delta n'/n'$
Ag20nm	0.3130	10.6052	2841	128	0.3132	10.6747	4×10^{-4}	6×10^{-5}
Ag35nm	0.2997	10.7355	1011	45	0.2999	10.7384	7×10^{-4}	3×10^{-4}
Ag50nm	0.2522	10.8507	531	21	0.2512	10.8416	1×10^{-3}	7×10^{-4}
Ag65nm	0.2047	10.9659	339	13	0.2043	10.9639	9.3×10^{-4}	2×10^{-4}

Table 3.4: *Table of extracted values for refractive indices from the python program described in section 3.2.3.1 (columns n_{fit} and n'_{fit}), starting from known values of refractive indices (columns n and n') taken from [Ciesielski et al., 2017], and subsequent FWHM and Δf characteristics. The relative errors are displayed in the last two columns. We note that the error grows as the thickness grows, due to rounding errors in the calculations. Note that calculations were lead with numpy 128 bit floats in python. Note also that the table is indicative, as changing the span over which n and n' are swept changes (slightly) the quality of the local linear fit (see section 3.2.3.1 about the linear fit).*

between $0.24 < n < 0.26$ and $10.84 < n' < 10.86$ gives the correspond estimated error in table 3.4, namely 1.4×10^{-3} for n and 7×10^{-4} for n'. Allowing for $0.07 < n < 0.32$ and $10 < n' < 12$, however, increases this error to 3.9×10^{-3} for n and 8×10^{-4} for n'.

Note also that the calculations are lead with numpy 128bit floats. This is of importance, as if regular 64bit floats were used instead, rounding errors would make Δf unusable for high enough thickness (starting at around 50 nm). See for example Fig. 3.26.

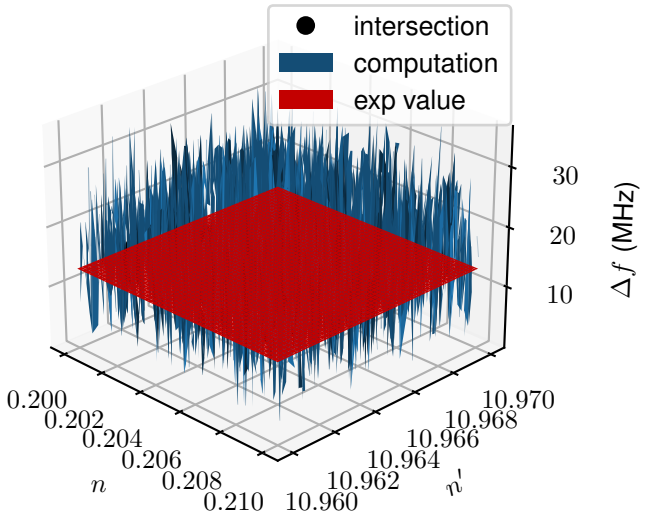

Figure 3.26: *Rounding errors have a dramatic effect when increasing the thickness, in particular because of the presence of an arccos in Eq. 3.70 which is very sensitive to rounding errors. This is the reason why numpy 128 bits floats are required for calculating properly the intersection points. The calculation was made for a* 65 nm *silver layer.*

Another source of error we classify as numerical comes from the errors described in earlier experimental section 3.2.2.2.4, namely, the numerical extraction of experimental FWHM and Δf from the transmission and reflexion curves, inducing errors on these values hence subsequently influencing the extracted set of n and n'. We estimated the error on Δf to be of the order $\pm 2\%$ and the error on FWHM to be on the order of 3×10^{-3}.

		20 nm	35 nm	50 nm	65 nm
Upper Bound	n	9.2%	5.6%	4.3%	3.6%
	n'	7.5%	4.6%	3.1%	2.2%
Lower Bound	n	7.9%	6.7%	4.4%	3.7%
	n'	9.2%	5.4%	3.4%	2.4%

Table 3.5: *Table of errors on thickness, with an uncertainty of* ± 3 pm*. The upper bound means we calculated the set of solutions* n_0 *and* n_0' *for a certain set of FWHM and* Δf *with a thickness of* $x + 3$ *nm, whereas the lower bound is the opposite.*

In the case of a 50 nm layer with characteristic values as in table 3.4, this leads to an estimated higher bound (i.e. error when the Δf and FWHM are both taken higher than their actual value) for this error of 4.3% for n and 1.1% for n'. The lower bound, on the other hand, is estimated to be of 5.1% for n and 1.3% for n'.

3.2.3.3.2/ Optical alignment The error made from each different optical alignment, i.e. each different realization of the alignment protocol, is estimated to be on the order of $\pm 5\%$ for Δf and $\pm 1\%$ for FWHM. We attribute this shift to the fact that the waist is of 71 µm, so that any small change of alignment will probe a different region of the silver layer, hence giving a slighly different averaged index of refraction. Changing the optical alignment procedure from one polarization axis (fast or slow) to the other on the QR does not modify the results significatively more than any renewal of the optical alignment procedure.

Let us stress that one of the requirements that leads to the use of this particular technique is the experimental difficulty to vary the angle of incidence on the quartz by more than 2°, so that any optical angular misalignment is contained within a fraction of this quantity. Once again, taking an example with the 50 nm thick silver layer, this leads to an upper bound error (defined as in the previous paragraph) of 4.5% for n and 1% for n'. The lower bound, on the other hand, is calculated to be 5.3% for n and 1.1% for n'. When calculated for 35 nm and 65 nm, the numbers do not change dramatically and stay in the same order of magnitude.

3.2.3.3.3/ Deposition thickness The deposition thickness uncertainty is estimated to be ± 3 nm.

This fixed uncertainty incidentally implies that it weighs more on the smaller thicknesses. For example, 3 nm represents 15% of a 20 nm layer, whereas it represented only 4% of a 65 nm layer. It is therefore rather natural that this changes much more dramatically the results for thinner deposited layers. The results are displayed in table 3.5.

Note that the thickness uncertainty, however, has a particular status within the accounted errors. Indeed, although the general uncertainty on the measurement remains, it is irrelevant when comparing the cryogenic values to the room temperature values. When a particular extraction is made with and particular thickness decided upon, the error made on this measurement with respect to its true value (for which we would need the true exact value for thickness) has no consequence on the error bar when comparing the cryogenic value against the room temperature one, as we make the same mistake over its thickness too (when neglecting the difference in thermal expansion and taking an average

uncertainty, as described in section 3.2.3.3.4).

3.2.3.3.4/ Thickness at cryogenic temperature Thermal expansion and contraction is a phenomenon which is mostly known and measured for bulk materials [McLean, 1969], and it does not change much with the heat treatment (annealing) or deposition conditions [Marquardt et al., 2000]. However, the thin-film Coefficients of Thermal Expansion (CTE) are shown to vary from their bulk counterpart (see [Chen et al., 2004], [Fang et al., 2000] or [Mag-isa et al., 2014]), so that the thickness is not only altered by the temperature, but it is altered in a different pattern than we are able to calculate due to lack of available data on thermal expansion for silver thin films.

For the needs of calculating an approximative total contraction between room temperature and cryogenic temperature, we have used the integrated CTEs over the whole range of temperature. As the thermal expansion changes with temperature, it is not possible to chose only one CTE over the whole range; it is, however, possible to write the total contraction coefficient as the integral over the range of the relevant temperatures:

$$\alpha^{\text{tot}}_{\text{300K-4K}} = -\int_{\text{4K}}^{\text{300K}} \alpha(\text{T})\,\mathrm{d}T \tag{3.74}$$

Unfortunately, to the best of our knowledge, there is no publication where the coefficients for silver have been measured over the wide range of temperature we are interested in (4 K-300 K), so that we have aggregated coefficients from different publications: from 2.4 K to 29.6 K, we used the values from [White et al., 1972]; from 32.5 K to 95 K, we used the values from [Fraser et al., 1965]; and finally from 100 K to 270 K, we used the values from [Waterhouse et al., 1968].

In order to better integrate these values to calculate the total contraction between 300 K and 4 K, the values has been divided into two series, which each has been fitted to a 5$^{\text{th}}$ power polynomial fit. The litterature values and the fit values are visible on Fig. 3.27 (note that the values from 270 K to 300 K are extrapolated from the previous ones). This leads to a raw total contraction coefficient (i.e. without taking the thin-layer nature of our sample) of:

$$\alpha^{\text{tot}}_{\text{300K-4K}} = 4.26 \times 10^{-3} \tag{3.75}$$

Fang [Fang et al., 2000], however, shows that the thin film bevahior is rather different and the order of magnitude of change in CTE is of about a factor 2. The total thickness of the cryocooled thin silver layer can be estimated to be roughly comprised between 99.43% and 99.78% of the original thickness:

$$d^{\text{4K}}_{\text{Ag}} \approx 0.9943 - 0.9978 \times d^{\text{300K}}_{\text{Ag}} \tag{3.76}$$

Including the original uncertainty on the deposited thickness as well as the contraction uncertainty, the total uncertainty on the thickness at cryogenic temperature yields:

$$\Delta d^{\text{4K}} = \Delta d^{\text{300K}} + \Delta\alpha^{\text{tot}} d^{\text{300K}} + \alpha^{\text{tot}} \Delta d^{\text{300K}} \tag{3.77}$$

that is to say, for a 50 nm thick layer

$$\Delta d^{\text{4K}} \approx 3\,\text{nm} + 7 \times 10^{-2}\,\text{nm} \approx 3\,\text{nm}$$

which can be essentially identified with the uncertainty of the deposited layer itself, so that we discard it in the following.

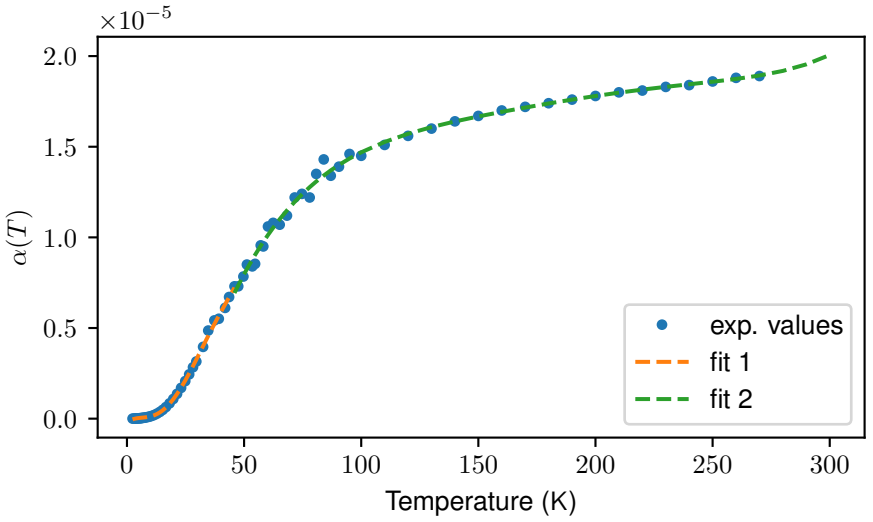

Figure 3.27: *Coefficients of Thermal Expansion (CTE) in the range* 4 K-300 K. *Values are taken from [White et al., 1972], [Fraser et al., 1965] and [Waterhouse et al., 1968]. Values from* 270 K *onwards are extrapolated from the previous fit.*

3.2.3.3.5/ Statistical analysis In order to analyze the propagation of errors on the different parameters we have discussed throughout this session, we perform a Monte-Carlo type analysis. Because there is no evident analytical dependence of the extracted n and n' on the different variables we feed the program, the easiest to obtain an estimation of the total error made on the extracted set of values for n and n' is to run the extraction program many times with slightly different values of FWHM, Δf and thickness d.

We evaluate the error on the FWHM and Δf to be distributed in a Gaussian fashion, namely following a so-called normal distribution, by repeating many times the central value numerical extraction as described in section 3.2.3.3.1. The amplitude of the error was already reported in the previous sections.

The error on the thickness deposition, on the other hand, is not directly measurable. Mostly because measuring a statistical error distribution on such deposition would require a large amount of runs and proper means of measuring the exact deposited thickness, none of which we possess. By using the central limit theorem, however, it is possible to estimate that all the possible human errors and the machine imprecisions and errors would lead to another normal (Gaussian) distribution. The amplitude of which we discussed earlier as well, as is taken to be always ± 3 nm.

Once those different sources of uncertainty are taken into account, we run the extraction program numerous times, by varying the input FWHM, Δf and thickness d following a normal distribution, each centered on their theoretical values and with a deviation given by the previously discussed values: we took a deviation of 2 nm for the thickness deposition, of 4% for Δf and of 7×10^{-3} for FWHM. These values are selected so that the returned value from their respective normal distribution barely ever exceeds the nominal error value that we set in the previous sections[15]. An example of a distribution obtained by this mean is presented in Fig. 3.28 The calculations is lead for 35 nm, 50 nm and 65 nm. The results

[15]Note in particular that this is a rather pessimistic guess for all thicknesses except the 20 nm deposition thickness, which, in practice, we do not use nor study experimentally.

		35nm	50nm	65nm
error on central value	n	9.9×10^{-3}	8×10^{-5}	5.4×10^{-4}
	n'	7.6×10^{-3}	7×10^{-4}	6.9×10^{-4}
deviation	n	7.1%	6.1%	5.5%
	n'	3.4%	2.7%	2.5%

Table 3.6: *Error on central value (w.r.t. the known litterature value) and deviation of the distribution of n and n' for different deposition thickness, following a Monte-Carlo type simulation where all previously described uncertainties* ***including*** *thickness uncertainty are taken into account. This permits to quantify the overall expected uncertainty on values extracted from our program. The results for n and n' displayed in the section for our experimental results 3.2.3.2 make use of these error bars.*

are presented and listed in Table 3.6.

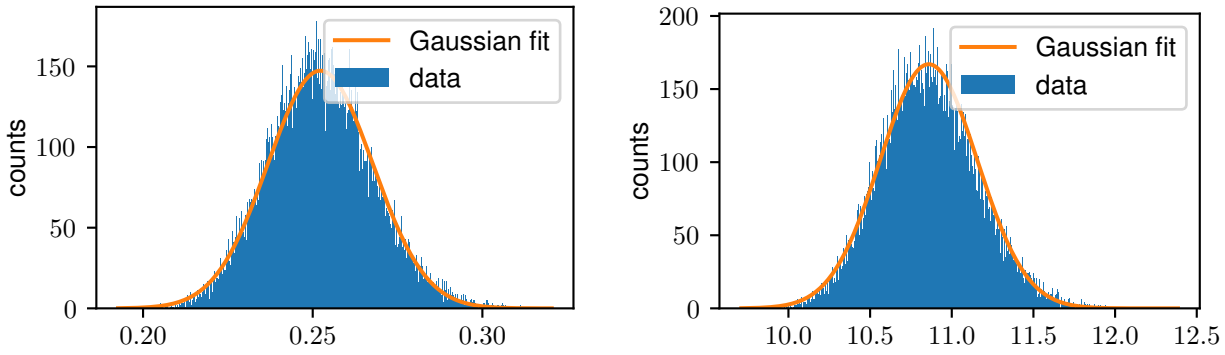

(a) n (b) n'

Figure 3.28: *Monte-Carlo-type method to evaluate the error on n and n' for a 50 nm silver layer, taking into account the uncertainties, all of them following a normal distribution around their expected value: on thickness d (deviation ± 2 pm), FWHM (deviation $\pm 7 \times 10^{-3}$) and Δf (deviation $\pm 4\%$). The gaussian fit is rather good and gives a typical deviation of about 6.1% on n and 2.7% on n', with central values for n and n' equal to their nominal values to within 1×10^{-5} for n and 7×10^{-4} for n' (see Table 3.6). Graphs is made with 500 bins on 22650 points.*

These error bars, however, account for the uncertainty of the thickness, which is useful when treating the total uncertainty of the claimed values (within the intriscal bounds discussed in section 3.2.3.3.1) but lose their interest when treating the relative uncertainty between the room temperature and cryogenic values. The same systematic error on the thickness is made between room temperature and cryogenic temperature. The uncertainty is therefore evaluated without the thickness uncertainty and is presented in Table 3.7.

3.2.3.4/ CONTEXT: COMPARISON WITH OTHER METHODS

There are other methods to obtain the refractive index for a single layer. In particular, the most used and most widespread is the ellipsometric method [Ciesielski et al., 2017]

		35nm	50nm	65nm
error on central value	n	2.4×10^{-3}	3.7×10^{-3}	2×10^{-3}
	n'	6.9×10^{-4}	7.6×10^{-4}	5.5×10^{-5}
deviation	n	5.8%	5.3%	4.9%
	n'	1.2%	1.5%	1.9%

Table 3.7: *Same as Table 3.6, except that the uncertainty on thickness has **not** been taken into account here for the reasons explained in the main text of section 3.2.3.3.5.*

[Weber et al., 2010] [Yang et al., 2015] [Jayanti et al., 2015]. It relies on incident light at an angle, however, which is problematic in our case as the setup gives a vey small angular freedom (about $2°$). Some other method rely only on the reflectance spectrum [Lévêque et al., 1990].

As mentioned, this measurement method can only extract an average refractive index. It is averaged over both the illuminated surface, and over the both mirrors, so that we obtain the equivalent refractive index, i.e. the would-be refractive index of two identical layers deposited on both sides. Note that the index is always averaged over the illuminated surface, which, in our case, is rather small ($71\,\mu m$), as compared to the millimetric spot size of a typical ellipsometry measurement. Furthermore, like all other methods, our method inherits the refractive index - thickness inseparability, because light ultimately is subject to optical path (i.e. refractive index balanced distance), not absolute path.

At any rate, it is possible to establish that some errors are of the same nature as when using ellipsometry (e.g. angle of incidence, wavelength errors, see [Tompkins et al., 2005]).

In this second part of the Chapter 3, we have confirmed the ability of the model presented in section 3.1 to describe the experimental behavior of metallic coated optical resonators. We lead here a novel systematic measurement campaign of several metal depositions onto the quartz resonator, both at room temperature and cryogenic temperature. We seek to establish the possible improvements that the cryogenic temperature can bring to reflectivity and absorption of the deposited thin films mirrors towards achieving optomechanics. The experimental results are in good agreement with Literature to pick, reflectivity-wide, silver as the best candidate.

Discrepancies were obtained between the theoretically predicted values and the experimentally measured values for several observables (e.g. the total transmitted power, the FWHM, reflected power ratio), which we attribute to the different sources of errors both on the measurement and data treatment as well as the deposition uncertainty. This is not necessarily problematic for the light coupling itself, as a measurement of the FWHM and the peaks' frequency shift Δf suffice to characterize the mirrors.

Indeed, we have developped a novel way of extracting the refractive index $\tilde{n}$ from the measurement of the specific FWHM and Δf inherent to the absorptive mirrors Fabry-Perot cavities [Rosenziveig et al., 2021]. This allows us to gain a better understanding of the optical properties of the deposited thin films, about which litterature is scarce. The results agree with the litterature, and establish that going from room temperature to cryogenic temperature ($4\,K$), the real part of the refractive index decreases by about $40 - 60\%$ whereas the imaginary part decreases by about $5 - 9\%$. This translates into a typical $50\,nm$ thin silver deposition optical cavity to increase its finesse by about 30%,

i.e. $\mathcal{F} = 120 \rightarrow 160$. This is a positive outcome for our optomechanical coupling horizon, although the major decrease of the imaginary part would have been preferred over the actual major decrease of the real part, because the imaginary part of the refractive index corresponds to the absorptivity which has been identified as possibly problematic in section 3.1.3.

We therefore proceed with the study of the light actuation of the quartz resonator with three main sources: the photothermal force, the radiation pressure force and the electrostrictive force, to evaluate, based on derived cryogenic optical parameters, the capacity of metallic coatings to actuate the quartz crystal.

4

LIGHT-INDUCED MECHANICAL RESONANCE

This chapter focuses on the the possibility of driving mechanical resonances by incoming light from the laser. A 1D model for the photothermal actuation scheme is given along with an experimental study. A theoretical study follows, for the equations governing resonance with radiation pressure force and electrostrictive force. An application to the silver thin films Fabry-Perot is explored in both cases.

4.1/ PHOTO-THERMAL EXCITATION

4.1.1/ INTRODUCTION

It has been demonstrated that a (power with time) oscillating thermal source permits to actuate a mechanical mode in an object, here more specifically in a quartz crystal resonator (see for example [Dieulesaint et al., 1982]). The idea is to modulate a laser's intensity at the mechanical resonance frequency and send it onto the quartz. This in turn causes the metal layer deposited as an electrode on the quartz to partially absorb the optical energy, hence creating a local temperature fluctuation which in turns implies a local deformation on the quartz crystal. If the frequency of the laser's intensity fluctuations is tuned to the acoustic resonance frequency, an oscillation is observable.

Although this excitation is known and has been studied to a large extent (see for example [Dieulesaint et al., 1989], [Bontempi et al., 2014]), it has mostly been restrained to kHz frequencies [Bontempi et al., 2014] and exceptionally up to 1 MHz [Dieulesaint et al., 1982], and, to the best of our knowledge, has not been used on cryogenic temperature materials or coupled with a Fabry-Perot architecture of the resonator.

We perform an exploratory study, both theoretical and experimental, of the photothermal excitation of a quartz crystal resonator metallized with electrodes on both side (thus with absorbing mirrors providing the incoming heat flux).

One of the advantages of photo-thermal actuation over piezoelectric actuation has been pointed by [Bontempi et al., 2014]: the antiresonance is cancelled, as the equivalent circuit is different with this type of actuation (see section 4.1.3.2) with respect to the typical piezoelectric actuation. Another important advantage is that this actuation method does not require a piezoelectric material, as the effect spanning the mechanical response is

thermal and not piezoelectric, thus answering the thesis problematic of avoiding piezoelectric actuation. As we shall see in this section, although the photothermal effect does not classify as an optomechanical effect, it is possible to use it in our typical configuration originally planned for optomechanics, and it is readily functional.

4.1.2/ THEORETICAL DESCRIPTION

Applying heat on a material and looking for the temperature tendency or the subsequent deformation can take rather complicated forms in the most general case, e.g. if the heating is ultrafast. In this case, the heat and mechanical quantities appear as coupled in a generalized heat equation (see e.g. [Li et al., 2020]). In the following study of the thermoacoustical problem, the generalized heat equation is not necessary because the heating rate is not ultrafast[1], and the spatial variation of the temperature is also sufficiently slow to consider both problems (mechanical and heat) as decoupled from one another (see [Sellitto et al., 2019]). In this section, we will derive the dynamics equations in order to investigate the mechanical mode. Although our quartz crystal has a primary function for the shear thickness C3 mode, we chose to study the shear thickness B3 mode. Indeed, as it appears throughout this section, a simplified thermal and mechanical model can be obtained through some simplifications. However, this model is limited in its validity and the coupling coefficient for thermal and mechanical dynamics is zero for the relevant axes for the C3 mode (β_6 coefficient, see Annex A), whereas it is non-zero for the B3 mode (β_4), see Eq. 4.18.

We therefore start by solving the heat equation in order to obtain the temperature increment resulting from the incoming heat which is absorbed by the electrode (section 4.1.2.1). We then use this temperature increment in the mechanical equations where it is the source for the movement, so as to estimate the subsequent mechanical displacement (section 4.1.2.2).

4.1.2.1/ THERMAL PROBLEM

4.1.2.1.1/ Assumptions We start by noting that we will consider a simplified version of the heat diffusion problem for the quartz slab. The situation is rather complicated, because a silver electrode is deposited on the plano-convex quartz disk (see Fig. 4.7) so that we should therefore consider the 3D problem of heat diffusion in all spatial direction with some interface between both materials.

However, in order to simplify the modelling, only the temperature increment is considered. This means that the total temperature, $\theta^{\text{tot}} = \theta_0 + \Delta\theta$, is comprised of a mean temperature θ_0 (or a so-called “DC” component) and the fluctuating part $\Delta\theta$ (or the so-called “AC” component). The fluctuating part is treated in more detail in this section. The mean temperature, on the other hand, will be considered as originating from the mean incoming heat flux. The flow of this flux throughout the quartz towards the extremities will therefore give a spatially dependent mean-temperature, thus building up the local static (temperature-related) stress which could simply be taken into account by modifying lo-

[1] Typically, the heating rate is considered ultrafast for femtosecond pulsed laser, with atomic collisions on the timescale of femto to pico seconds [Tzou et al., 2010], which is not the case here.

cally the elastic constants (or stiffness)[2]. In the following, for notation simplicity, we adopt $\theta \equiv \Delta\theta$.

We only consider the problem after the optical power has been turned into local heat applied on the boundary, which we will note ϕ (for more details about this conversion, see [Lax, 1977]). Some possible phase difference happens between the two quantities, which we will discard for now and take the actually converted heat as the reference. Thermal exchanges through radiation are neglected. Moreover, we do not consider the interface between the electrode and the quartz (in fact, we discard the electrode altogether, see next section 4.1.2.2).

We also consider only the dynamics along the direction for which the quartz is thinner, i.e. the x_2 direction. This is possible because it is much smaller than the other two directions (by about a factor 10) and because the source of heat, i.e. the laser beam, is much smaller than the heated area (see [Lammerink et al., 1991]). A simplified electronic equivalent scheme permits to establish this. The scheme is presented in Fig. 4.1.

Fig. 4.1a shows the full equivalent scheme for the current $I = \bar{I} + i$, with $\bar{I}$ the mean current and i the fluctuating current. The point M_1 is located at the center of the quartz, M_2 is near the border of the inner ring that resonates, whereas M_3 is located near the outer (holding) ring which is decoupled from the vibrating part except for four bridges (see Fig. 2.2). The latter part is assumed to be maintained at ambient temperature θ_{amb}. Fig. 4.1b, on the other hand, presents the scheme for the fluctuating part of the current. The capacitance and resistance along direction x_i are noted on the scheme. For the calculations, the mean resistance $R_{13} = (R_1 + R_3)/2$ are taken because the thermal conductivity slightly changes, due to quartz anisotropy.

The equivalent voltage, current, resistance and capacitance for the electronic equivalent circuit of the thermal problem are written:

$$V_{th} \quad \text{is the temperature, in K} \tag{4.1a}$$
$$I_{th} \quad \text{is the energy flux, expressed in W} \tag{4.1b}$$
$$R_{th} = \frac{d}{KS} \quad \text{expressed in K W}^{-1} \tag{4.1c}$$
$$C_{th} = C_p \rho d S \quad \text{expressed in J K}^{-1} \tag{4.1d}$$

where d is the length along the direction considered and S is the area perpendicular to the considered direction. K and C_p are respectively the thermal conductivity and the heat capacity.

This permits to calculate several quantities in order to compare the impedance along the direction x_2 and along the direction x_1 to determine whether the heat will preferentially go along either direction. At $300\,\text{K}$, the thermal conductivities can be calculated to be $K_1 = 6.4895\,\text{W m}^{-1}\,\text{K}^{-1}$, $K_2 = 8.805\,\text{W m}^{-1}\,\text{K}^{-1}$ and $K_3 = 11.626\,\text{W m}^{-1}\,\text{K}^{-1}$ (see Annex A and [Kanamori et al., 1968]) for the SC cut, whereas at the calorific capacity is $C_p = 733\,\text{J kg}^{-1}\,\text{K}^{-1}$ (see [Kanamori et al., 1968]). We therefore calculate the different interesting quantities from Fig. 4.1 with the mean coefficient $K_{13} = (K_1 + K_3)/2$:

[2] Note that although the thermal losses are neglected throughout, taking them into account is necessary to treat the mean temperature as finite, for the incoming flux not to raise temperature to an infinite value.

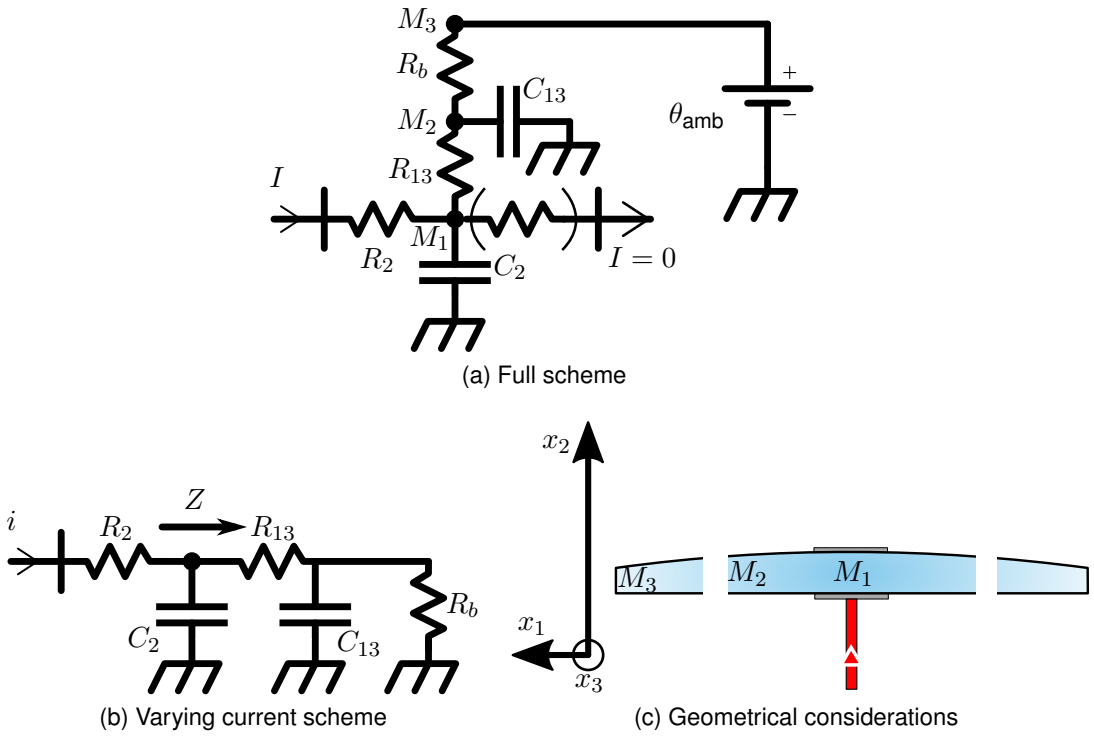

Figure 4.1: *Simplified electrical equivalent scheme to the heat diffusion situation explained in main text. Fig. 4.1a: scheme for $I = \bar{I} + i$ where $\bar{I}$ is the mean current and i is the fluctuating current. The points M_1, M_2 and M_3 represent different areas of the quartz, see Fig. 4.1c. The point M_3, located on the outer ring of the resonator, is assumed to be maintained at ambient temperature θ_{amb}. Note that the resistor between parenthesis represents the losses by radiation, which are assumed to be negligeable so that this resistor is actually infinite in this scheme. Fig. 4.1b: equivalent scheme for the fluctuating part of the current. R_i designates the resistance in the direction x_i, and C_i the capacitance in the direction x_i and R_b is the resistance of the bridges. Note that the mean resistance R_{13} and capacitance C_{13} along directions x_1 and x_3 is taken. Fig. 4.1c: Scheme of the quartz resonator with the discreet M_1, M_2 and M_3 points considered in the electronic scheme. The white spaces represent the bridges. Let us remind that x_2 is the direction of the thickness of the quartz, as well as the direction favored by the thermal dynamic, as the simplified analysis in the main text shows.*

$$R_{13} = \frac{1}{4} \times \frac{1}{9.0575} \times \frac{7.8.10^{-3}}{1.5.10^{-3} \times 1.10^{-3}} = 143.3\,\mathrm{K\,W^{-1}} \tag{4.2a}$$

$$R_2 = \frac{1}{8.805} \times \frac{1.10^{-3}}{\pi \times \left(\frac{71.10^{-6}}{2}\right)^2} = 2.86 \times 10^4\,\mathrm{K\,W^{-1}} \tag{4.2b}$$

$$R_b = \frac{1}{4} \times \frac{1}{9.0575} \times \frac{3.5.10^{-3}}{1.10^{-3} \times 1.5.10^{-3}} = 64.3\,\mathrm{K\,W^{-1}} \tag{4.2c}$$

$$C_{13} = 2648 \times 733 \times 1.10^{-3} \times \pi \times \left(7.8.10^{-3}\right)^2 = 0.371\,\mathrm{J\,K^{-1}} \tag{4.2d}$$

$$C_2 = 2648 \times 733 \times 1.10^{-3} \times \pi \times \left(\frac{71.10^{-6}}{2}\right)^2 = 7.68 \times 10^{-6}\,\mathrm{J\,K^{-1}} \tag{4.2e}$$

$$Z_{C_{13}} = \frac{1}{C_{13} \times 2\pi f_0} = 7.8 \times 10^{-8}\,\mathrm{K\,W^{-1}} \text{ at } 5.47\,\mathrm{MHz} \tag{4.2f}$$

$$Z_{C_2} = \frac{1}{C_2 \times 2\pi f_0} = 3.78 \times 10^{-3}\,\mathrm{K\,W^{-1}} \text{ at } 5.47\,\mathrm{MHz} \tag{4.2g}$$

$$Z_{C_{13}} /\!\!/ R_b \approx Z_{C_{13}} \tag{4.2h}$$

$$Z = R_1 + Z_{C_{13}} /\!\!/ R_b \approx R_{13} \gg Z_{C_2} \tag{4.2i}$$

where d is the thickness of the quartz and the area of the laser beam is used for R_2, with the laser beam's radius being half the waist, $w_0/2$ (see Fig. 4.5). On the other hand, for R_1, d is the quartz' radius and the area used is that of the bridge. Similarly, the length of the bridge and its area is used for R_b.

For C_2, the situation is similar to R_2. For C_1 on the other hand, the whole volume of the inner inner vibrating part should be taken into account, which results in d being the thickness of the quartz and the area being the whole surface of the quartz. We note that the factor $1/4$ appears for R_1 and R_b because there are four bridges.

With the obtained orders of magniture, it is possible to calculate the mean temperature in the presence of the incoming flux, which can be written as:

$$\theta_0 = \theta_{amb} + (R_{13} + R_b)\bar{I} \tag{4.3}$$

At 300 K, and with an incoming laser power of 5 mW and a non-reflected part of the beam at 1.3% of the incoming beam, the mean temperature elevation is calculated to be:

$$(R_{13} + R_b)\bar{I} = 13\,\mathrm{mK} \tag{4.4}$$

From Eq. 4.2, it is seeable that because $Z \gg Z_{C_2}$, the hypothesis that the dynamics can be considered exclusively along x_2 hold well and should be accurate. Leading the same calculation at 4 K yields different results, because $K_1 = 150\,\mathrm{W\,m^{-1}\,K^{-1}}$, $K_2 = 196\,\mathrm{W\,m^{-1}\,K^{-1}}$ and $K_3 = 253\,\mathrm{W\,m^{-1}\,K^{-1}}$ (see [Hofacker et al., 1981] and Annex A), so that $K_{13} = 224$, and with $C_p = 8 \times 10^{-2}\,\mathrm{J\,kg^{-1}\,K^{-1}}$ (see [Hofacker et al., 1981]):

$$R_{13} = 6.45\,\mathrm{K\,W^{-1}} \tag{4.5a}$$
$$R_2 = 1288\,\mathrm{K\,W^{-1}} \tag{4.5b}$$
$$R_b = 2.21\,\mathrm{K\,W^{-1}} \tag{4.5c}$$
$$C_{13} = 4.05 \times 10^{-5}\,\mathrm{J\,K^{-1}} \tag{4.5d}$$
$$C_2 = 8.38 \times 10^{-10}\,\mathrm{J\,K^{-1}} \tag{4.5e}$$
$$Z_{C_{13}} = 7.18 \times 10^{-3}\,\mathrm{K\,W^{-1}} \text{ at } 5.47\,\mathrm{MHz} \tag{4.5f}$$
$$Z_{C_2} = 34.7\,\mathrm{K\,W^{-1}} \text{ at } 5.47\,\mathrm{MHz} \tag{4.5g}$$
$$Z \approx R_1 = 6.45\,\mathrm{K\,W^{-1}} < Z_{C_2} \tag{4.5h}$$

Here again, the mean temperature elevation can be calculated the same way as in Eq. 4.3, and it yields:

$$(R_{13} + R_b)\bar{I} = 0.56\,\mathrm{mK} \tag{4.6}$$

From Eq. 4.5, we conclude that the hypothesis that the dynamics is only along x_2 is to be taken with caution at 4 K, as the impedance Z_{C_2} is of the same order of magnitude than Z. It appears that the theory and the experimental results do not match very well at cryogenic temperature, see sections 4.1.3.3.2 and 4.1.2.2.

4.1.2.1.2/ Heat equation With these assumptions, the 1D heat equation for the temperature increment θ with the situation depicted in Fig. 4.3 can be written as the well-known Fourier law for heat:

$$K_4 \frac{\partial^2 \theta}{\partial x_2^2} - \rho C_p \frac{\partial \theta}{\partial t} = 0 \tag{4.7}$$

with K_4 the anisotropic thermal conductivity coefficient (in an SC cut) and C_p is the calorific capacity and ρ the volumic mass.

We know that the temperature follows the tendency of the laser power, which is oscillating sinusoidally in time at frequency Ω, so that we can write and separate the variables for the temperature in the following form:

$$\theta(x_2, t) = e^{i\Omega t}\left[Ae^{i\bar{\beta}x_2} + Be^{-i\bar{\beta}x_2}\right] \tag{4.8}$$

and injecting Eq. 4.8 in Eq. 4.7, it is possible to find that:

$$\bar{\beta} = (1+i)\beta = (1+i)\sqrt{\frac{\Omega}{2\kappa}} \quad \text{with } \kappa = \frac{K_4}{\rho C_p} \tag{4.9}$$

where κ is the thermal diffusivity.

One can obtain the expression for the temperature by considering boundary conditions, either with a temperature condition or a flux condition. On the incoming optical power side of the quartz, the very thin metallic (50 nm) layer deposited allows to consider a flux per unit surface rather than a temperature condition. On the opposite face, the metallic layer imposes a very low thermal emissivity and the convection is also negligeable under

vacuum, which permits to impose the null flux condition on this face. These conditions are formally written [3] :

$$\begin{cases} \phi(0) = \phi & \text{(4.10a)} \\ \phi(d) = 0 & \text{(4.10b)} \end{cases}$$

We remind that the thermal flux per unit area is proportional to the temperature gradient:

$$\phi = -K_4 \frac{\partial \theta}{\partial x_2} \tag{4.11}$$

and in this particular case, it is equal (in first approximation) to the non-reflected part of the incident light power per unit surface:

$$\phi \approx (1 - \mathfrak{R}_{\text{FP}}) \frac{P_{\text{in}}}{\pi w_0^2} \tag{4.12}$$

where $\mathfrak{R}_{\text{FP}}$ is as defined in Eq. 3.51, P_{in} is the incident optical power and w_0 is the waist of the incident laser beam.

With the aformentioned context, we obtain the following condition on A by inserting the general temperature form Eq. 4.8 into the boundary conditions of Eq. 4.10:

$$A = Be^{-2\bar{\beta}d} \tag{4.13}$$

so that the expression for the temperature increment reads:

$$\theta(x_2, t) = e^{i\Omega t}\theta_0 \left[e^{-\bar{\beta}x_2} + e^{-2\bar{\beta}d} e^{\bar{\beta}x_2} \right] \tag{4.14}$$

$$\theta_0 = \frac{\phi}{K_4 \bar{\beta} \left(1 - e^{-2\bar{\beta}d} \right)} \tag{4.15}$$

The diffusion length is very small at 300 K and remains negligeable with respect to the quartz thickness at 4 K:

$$\beta^{-1} = \sqrt{\frac{2K_4}{\Omega \rho C_p}} \overset{5.47\,\text{MHz}}{\approx} \begin{array}{ll} 0.336\,\mu\text{m} & \text{at } 300\,\text{K} \\ 144\,\mu\text{m} & \text{at } 4\,\text{K} \end{array} \tag{4.16}$$

so that the temperature problem could be approximated by a semi-infinite plane model (see [Dieulesaint et al., 1982]). We will keep, however, the generalized expression throughout which is easily usable analytically.

4.1.2.2/ MECHANICAL PROBLEM

The system is simplified, considering it to be a slab of quartz and neglecting the presence of the electrodes.

We have presented the constitutive equations for the motion in the continuum mechanics frame, in section 2.3, which we will now make use of. The equations of motion for the shear thickness displacement u_3 reads, with the same conventions as in section 2.3:

$$T_{31,1} + T_{32,2} + T_{33,3} = \rho \ddot{u_3} \tag{4.17}$$

[3] Note that this is a first approximation and is true only for the non-optically-resonant case. Indeed, upon optical resonance, the light is also present on the other surface and this conditions is no longer valid.

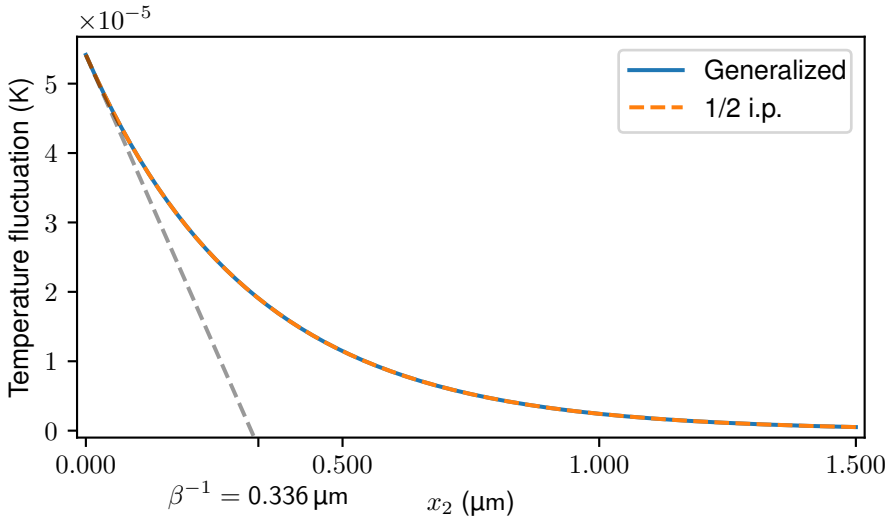

(a) 300K

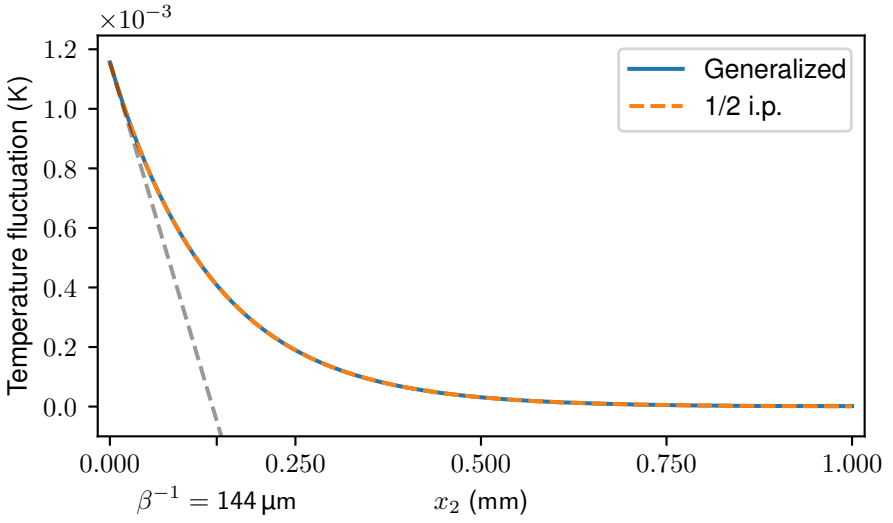

(b) 4K

Figure 4.2: *Generalized curve for temperature fluctuation (Eq. 4.14) and with simplified 1/2 i.p. (semi-inifite-plane) model (see [Dieulesaint et al., 1982]). An input power of* 1 mW *is used for the calculation at frequency* $\Omega = 2\pi \times 5.46$ MHz *(resonance frequency of the B3 mode, see section 4.1.3). It works rather well for both the room and cryogenic temperatures because of low diffusion length with respect to the thickness (see Eq. 4.16). The diffusion length is noted on both plot, and it is much shorter in the* 300 K *case.*

Because the quartz is in an SC cut (related quantities which are relevant for the problem are given in appendix A), all the tensorial components for the stiffness, the piezoelectric and the thermal diffusivity tensors have a priori no strictly null component so that all possible components are taken into account for the development of the expressions. We therefore give the expanded expression for the interesting stresses, accounting for the fact that the total strain is the sum of the internal strain S_{ij}^{int}, the electrically-induced strain $S_{ij}^{\text{el}} = e_{kij}E_k$ and the thermally induced strain $S_{ij}^{\text{th}} = \alpha_{ij}\theta$ with α_{ij} the thermal expansion

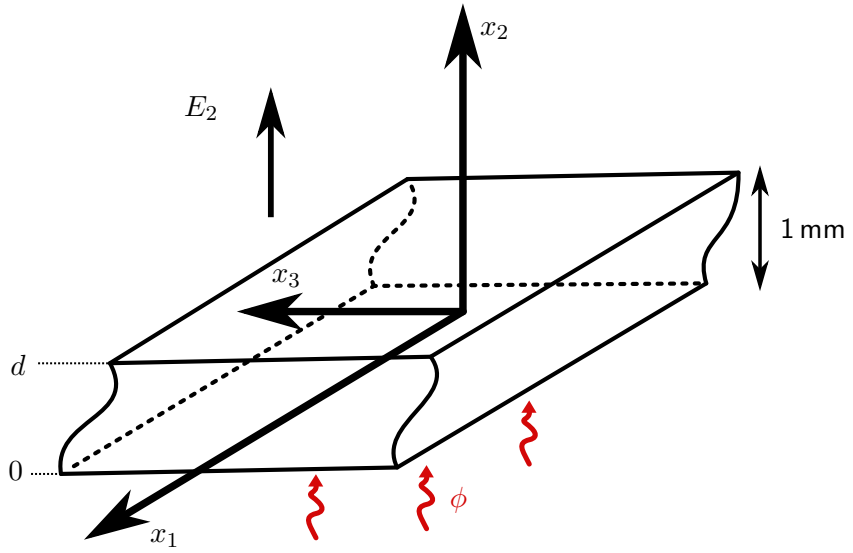

Figure 4.3: *Scheme of the mechanical problem. The slab is infinite in the x_1 and x_3 directions and goes from 0 to e in the x_2 direction. An incoming thermal flux (which is the unreflected part of an optical flux) is displayed on the lower part of the slab, giving rise to the boundary thermal conditions in Eq. 4.10.*

coefficients (see section 2.3):

$$T_{31} = T_5 = C_{51}S_1 + C_{52}S_2 + C_{53}S_3 + 2C_{54}S_4 + 2C_{55}S_5 + 2C_{56}S_6 - \beta_5\theta - e_{15}E_1 - e_{25}E_2 - e_{35}E_3 \tag{4.18a}$$

$$T_{32} = T_4 = C_{41}S_1 + C_{42}S_2 + C_{43}S_3 + 2C_{44}S_4 + 2C_{45}S_5 + 2C_{46}S_6 - \beta_4\theta - e_{14}E_1 - e_{24}E_2 - e_{34}E_3 \tag{4.18b}$$

$$T_{33} = T_3 = C_{31}S_1 + C_{32}S_2 + C_{33}S_3 + 2C_{34}S_4 + 2C_{33}S_3 + 2C_{36}S_6 - \beta_3\theta - e_{13}E_1 - e_{23}E_2 - e_{33}E_3 \tag{4.18c}$$

where we have noted the stress-temperature coefficients $\beta_i = C_{ij}\alpha_j$.

Here, however, we will make the same type of simplification as is usually the case (see [Nassour, 1982] [Gagnepain, 1972] [Gufflet, 2000]): we will limit the study to a pure shear thickness motion in the x_3 direction, which means that the only displacement that we keep is along the x_3 axis, i.e. u_3. This corresponds to an almost pure B mode (see details in [Nassour, 1982] p121). By taking this into account, replacing the strains as the derivatives of the displacement and injecting Eqs. 4.18 in Eq. 4.17, we get:

$$\begin{aligned}\rho\ddot{u_3} = {} & C_{55}u_{3,11} + C_{44}u_{3,22} + C_{33}u_{3,33} + (C_{54} + C_{45})u_{3,21} + (C_{34} + C_{43})u_{3,32} + \\ & + (C_{53} + C_{35})u_{3,31} - \beta_5\theta_{,1} - \beta_4\theta_{,2} - \beta_3\theta_{,3} - e_{15}E_{1,1} - e_{25}E_{2,1} - \\ & - e_{35}E_{3,1} - e_{16}E_{1,2} - e_{24}E_{2,2} - e_{34}E_{3,2} - e_{13}E_{1,3} - e_{23}E_{2,3} - e_{33}E_{3,3}\end{aligned} \tag{4.19}$$

So far in these mechanical equations, we have considered the slab as finite. It is, however, reasonable to consider an infinite plane in the x_1 and x_3 directions because the dimensions of the quartz are so much bigger in these directions. This is also reasonable

temperature-wise, as it decreases rapidly in space (see Eq. 4.16). Mathematically, this translates into the fact that the derivatives of the quantities in Eq. 4.19 are non-zero only when derivated with respect to x_2. We also make the assumption that the electric field, deriving from an electric potential, is only along x_2.

Rewriting Eq. 4.19 with these assumptions yields:

$$C_{44}\frac{\partial^2 u_3}{\partial x_2^2} - \beta_4\frac{\partial \theta}{\partial x_2} - e_{24}E_{2,2} = \rho\ddot{u_3} \tag{4.20}$$

In the following, we will simply call u the displacement along x_3, as it is the only displacement that we will consider. Because it is known that the equation of motion relates the second temporal derivative of the displacement to the spatial derivative of the stress (see Eq. 2.6), we can retrieve the total interesting stress from this last equation of motion Eq. 4.20. We also ignored the mechanical losses, which can be taken into account. Doing this permits to establish equations of motions which are similar to some equations found in the litterature (e.g. [Gagnepain, 1972]), although we also include the thermal excitation in the expression for the stress:

$$\begin{cases} T_4 = C_{44}\dfrac{\partial u}{\partial x_2} + \eta_{44}\dfrac{\partial^2 u}{\partial t \partial x_2} - e_{24}E_2 - \beta_4\theta & \text{(4.21a)} \\ D_2 = e_{24}\dfrac{\partial u}{\partial x_2} + \epsilon_{22}E_2 & \text{(4.21b)} \\ \rho\dfrac{\partial^2 u}{\partial t^2} = \dfrac{\partial T_4}{\partial x_2} & \text{(4.21c)} \\ \displaystyle\int_0^d E_2 \,\mathrm{d}x_2 = V_0\cos(\Omega t) \quad \text{and} \quad E_2 = -\frac{\partial V}{\partial x_2} & \text{(4.21d)} \\ I = \dfrac{\partial}{\partial t}\displaystyle\int \vec{\mathbf{D}}\,\mathrm{d}\vec{\mathbf{S}} & \text{(4.21e)} \\ \dfrac{\partial D_2}{\partial x_2} = 0 & \text{(4.21f)} \\ T_4\binom{e}{0} = 0 & \text{(4.21g)} \end{cases}$$

where $\beta_4 = C_{4i}\alpha_i$ where α_i is the thermal expansion coefficient, $\mathcal{V}(x_2)$ is the electric potential and $\mathcal{V}(0) - \mathcal{V}(e) = V_0$ is the experimentally measured voltage at the quartz' ends (see section 4.1.3 and Fig. 4.11 in particular).

At any rate, by injecting Eq. 4.21b in Eq. 4.21a, and deriving this expression with respect to x_2 (using Eq. 4.21f to simplify), it is therefore possible to write the equation for the dynamics Eq. 4.21c in the form:

$$\frac{\partial^2 u}{\partial t^2} - c^2\frac{\partial^2 u}{\partial x_2^2} - \alpha\frac{\partial^3 u}{\partial t \partial x_2^2} = -\frac{\beta_4}{\rho}\frac{\partial \theta}{\partial x_2} \tag{4.22}$$

that is, in a sinusoidal steady state:

$$\frac{\partial^2 \bar{u}}{\partial t^2} - \bar{z}^2\frac{\partial^2 \bar{u}}{\partial x_2^2} = -\frac{\beta_4}{\rho}\frac{\partial \theta}{\partial x_2} \tag{4.23}$$

with $\bar{u}$ is the complex displacement (i.e. with a possible phase), $\alpha = \eta_{44}/\rho$, with $c^2 = (C_{44} + \frac{e_{24}^2}{\epsilon_{22}})/\rho$ and $\bar{z}^2 = c^2 + i\alpha\frac{\partial}{\partial t} = c^2 + i\Omega$ if in a sinusoidal state (the bar stands to stress

the complex value of $\bar{z}$), and where Eq. 4.23 is obtained from Eq. 4.22 by considering that the displacement can be decomposed into a time-dependent and space-dependent function, i.e. $\bar{u}(x,t) = \bar{U}(x_2)e^{i\Omega t}$.

Let us rewrite further this dynamics equation, leaving only the spatial dependency $\bar{U}(x_2)$ and, in order to simplify the notation, we will write this quantity $U(x_2)$ instead:

$$\bar{z}^2 U_{,22} + \Omega^2 U = \frac{\beta_4}{\rho}\theta_{,2} \tag{4.24}$$

We also write the electric potential, injecting Eq. 4.21b into Eq. 4.21f and integrating two times:

$$\mathcal{V}(x) = \frac{e_{24}}{\epsilon_{22}}U + L_1 x_2 + L_2 \tag{4.25}$$

where L_1 and L_2 are integration constants, to be determined. Because the potential is always defined to within a constant L_2, we arbitarily impose $L_2 = 0$. It is now possible to rewrite the stress equation Eq. 4.21a for $T_4(x_2)$ by replacing the electric field by the derivative of the electric potential, $E_2 = -\mathcal{V}_{,2}$:

$$T_4(x_2) = \bar{C}^+_{44}U_{,2} + e_{24}L_1 - \beta_4\theta(x_2) \tag{4.26}$$

We therefore get to the following mathematical problem:

$$\begin{cases} u_{tt} - \bar{z}^2 u_{,22} = -\dfrac{\beta_4}{\rho}\theta_{,2} & \text{(4.23)} \\ u_{,2}(e) = h(t) = Ae^{i\Omega t} & \text{(4.27a)} \\ u_{,2}(0) = j(t) = Be^{i\Omega t} & \text{(4.27b)} \end{cases}$$

where $A = U_{,2}(e)$ and $B = U_{,2}(0)$ are adimensional coefficients defined with the help of the boundary condition Eq. 4.21g and using the expression for the stress Eq. 4.26. They are written explicitly:

$$\begin{cases} A = \dfrac{1}{\bar{C}^+_{44}}\left\{-e_{24}L_1 + \beta_4\theta_0 2e^{-\bar{\beta}e}\right\} & \text{(4.28a)} \\ B = \dfrac{1}{\bar{C}^+_{44}}\left\{-e_{24}L_1 + \beta_4\theta_0\left(1 + e^{-2\bar{\beta}e}\right)\right\} & \text{(4.28b)} \end{cases}$$

The problem exposed in Eq. 4.27 is a typical non-homogeneous wave equation problem (simplified in its temporal dependency) with non-homogeneous Neumann boundary conditions. The way to proceed is to make the boundary conditions homogeneous by defining a function w which will shift the original data U. After which we solve the homogeneous wave equation with the newly defined w, which makes it possible to solve also the non-homogeneous wave-equation for w by decomposing the source term in the basis of the eigenfunctions of the homogeneous wave equation. Finally, it is possible to retrieve the interesting solution U by shifting once again the data (see this lesson by Viktor Grigoryan from South Carolina Beaufort University).

The details of the calculations are given in Annex C. One can express the complete near-resonance displacement as:

$$u_{n_0}(x_2,t) = \left[\lambda_{n_0}\cos(\beta_{n_0}x_2) + \left(x_2 - \frac{x_2^2}{2e}\right)B + \frac{x_2^2}{2e}A\right]e^{i\Omega_{n_0}t} \tag{4.29}$$

where n_0 is the index of the resonant mode (e.g. $n_0 = 3$ in our experimental study), λ_{n_0} is the eigenvalue to the non-homogeneous boundary problem, β_{n_0} is the wavevector for the homogeneous boundary problem and A and B are defined as above (see Annex C for a full expression of these quantities).

With these expressions, one can do a numerical application for $U_3(0) = \lambda_3^{res}$, at 300 K with $C_p = 733\,\mathrm{J\,kg^{-1}\,K^{-1}}$, $e = 1\,\mathrm{mm}$, $\rho = 2648\,\mathrm{kg\,m^{-3}}$, $\Omega = (5.476 \times 2\pi)$ MHz with $P_{\mathrm{in}} = 1\,\mathrm{mW}$ and the (experimentally measured[4], see Fig. 4.11) voltage $V_0 = 48\,\mathrm{nV}$ and thermal flux per unit area $\phi = 820\,\mathrm{W\,m^{-2}}$, and the properly rotated coefficients in the SC cut i.e. using $K_4 = 3.452\,\mathrm{W\,m^{-1}\,K^{-1}}$, $\eta_{44} = 0.247 \times 10^{-3}\,\mathrm{Pa\,s}$, $C_{44} = 42.04 \times 10^9\,\mathrm{N\,m^{-2}}$, $e_{24} = -0.086\,\mathrm{C\,m^{-2}}$ and $\beta_4 = -0.117 \times 10^6\,\mathrm{N\,m^{-2}\,K^{-1}}$. This leads to a coefficient for the displacement $|\lambda_3^{res}| = 3.4 \times 10^{-8}\,\mathrm{m}$. This order of magnitude seems rather high at first glance, although comparing it with the displacement values of some 10^{-8} m obtained in [Iijima et al., 1976] with a current of 1 mA (the calculated current is of 0.9 mA in our case, see Eq. 4.21e) shows that this result is within reasonable bounds set by previous litterature.

Because the phase is imposed on the temporal part of the displacement, a possible phase shift is accessible through the imaginary part of the displacement. The latter (i.e. $\pi/2$ out of phase with the excitating incident flux) is plotted in Fig. 4.4, while the real part is an order of magnitude smaller.

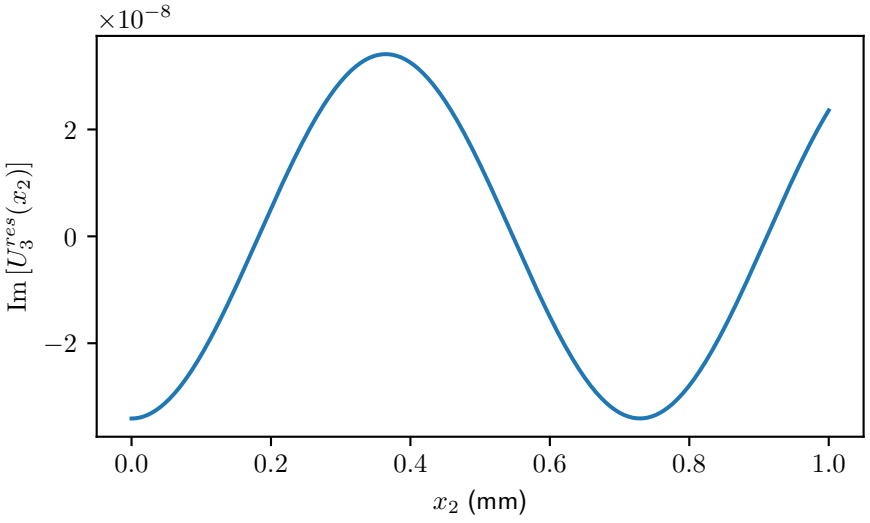

Figure 4.4: *Imaginary (i.e. $\pi/2$ out of phase) part of the displacement $U_3(x_2)$ at 300 K, with input power 1 mW and the rest of the values of the calculation detailed in main text. The real part has a similar shape, but is an order of magnitude smaller.*

For the 4 K case, the calculation using $C_p = 8 \times 10^{-2}\,\mathrm{J\,kg^{-1}\,K^{-1}}$ (see [Hofacker et al., 1981]), and tensorial properties $K_4 = 69.4\,\mathrm{W\,m^{-1}\,K^{-1}}$ (see [Hofacker et al., 1981], with python routine to rotate for the SC cut, see Annex A), $C_{44} = 59.6 \times 10^9\,\mathrm{N\,m^{-2}}$ so as to get $\beta_4 = -129.7\,\mathrm{N\,m^{-2}\,K^{-1}}$, leading to a predicted displacement of some $|\lambda_3^{res}| = 8 \times 10^{-10}\,\mathrm{m}$, which is substantially lower than at room temperature. However, this last prediction is not verified experimentally, as the measured

[4]Note that this value is necessary because in this model, the voltage is assumed to be known.

voltage is higher for 4 K than for 300 K (see section 4.1.3.3). This might be explained by the fact that the thermal model has a limited validity at cryogenic temperature, as section 4.1.2.1.1 shows.

4.1.3/ EXPERIMENTAL STUDY

4.1.3.1/ EXPERIMENTAL SETUP

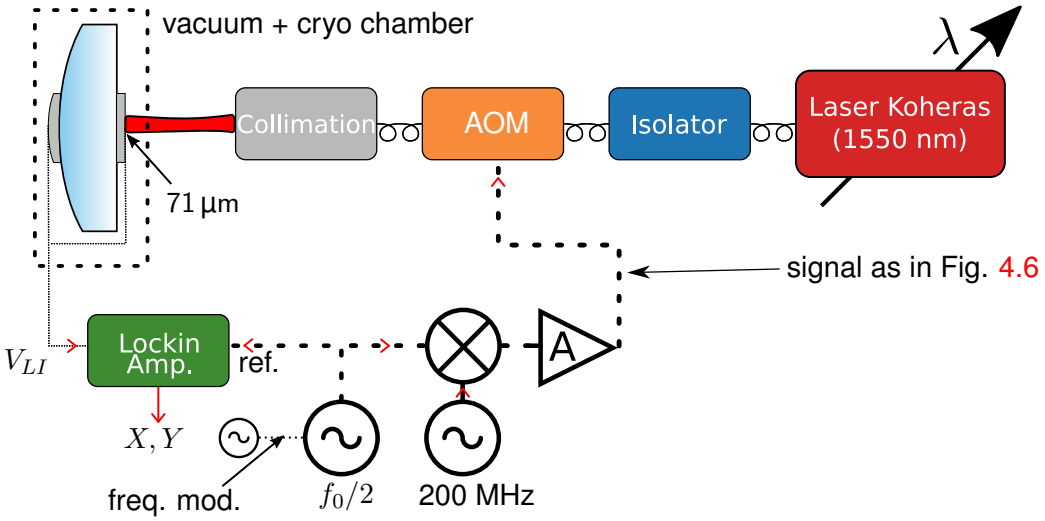

Figure 4.5: *Simplified experimental setup for photothermal excitation and measurement. The laser goes through a* 200 MHz *AOM. The latter is actuated with an electrical signal whose voltage oscillates in intensity at frequency* f_0*, the acoustical frequency of the quartz. The reference signal of frequency* $f_0/2$ *is sent both into the frequency mixer which permits to feed the AOM (see Fig. 4.6), and into the Lockin Amplifier to provide the reference signal to compare the test signal to. See main text of section 4.1.3.1.*

The experimental setup is simple, and is presented in Fig. 4.5. The laser is going through a fibered AOM, to which we feed an electronic signal consisting of a 200 MHz sine wave (the AOM driving frequency) whose intensity oscillates at the acoustic frequency f_0 (see Fig. 4.6), with a possible remainder of mean optical power:

$$P_{\text{in}} = P^{\text{mean}} + \Delta P \cos(2\pi f_0 t) \tag{4.30}$$

with $\Delta P = P^{\text{mean}}$ in the ideal case, so that the power oscillates to reach 0 periodically. The resulting laser power is therefore modulated at the acoustic frequency f_0, in phase with the RF signal (see Fig. D.2 and annex section D), providing the alternating source of heat to excite the mechanical mode of the quartz.

The $f_0/2$ signal, sent into the mixer, is also sent into the Lockin Amplifier (Stanford Research System, model SR844) as the reference signal with which the Lockin will compare the test signal from the quartz. A phase calibration of the Lockin amplifier is performed and it consists of securing a 0 phase between the reference and the signal when these are in phase, which can be done by injecting the reference signal in both the reference and measurement channel and forcing the phase to be 0 with the appropriate setting on the Lockin amplifier. The Lockin is able to take the second harmonic of the $f_0/2$ signal, in

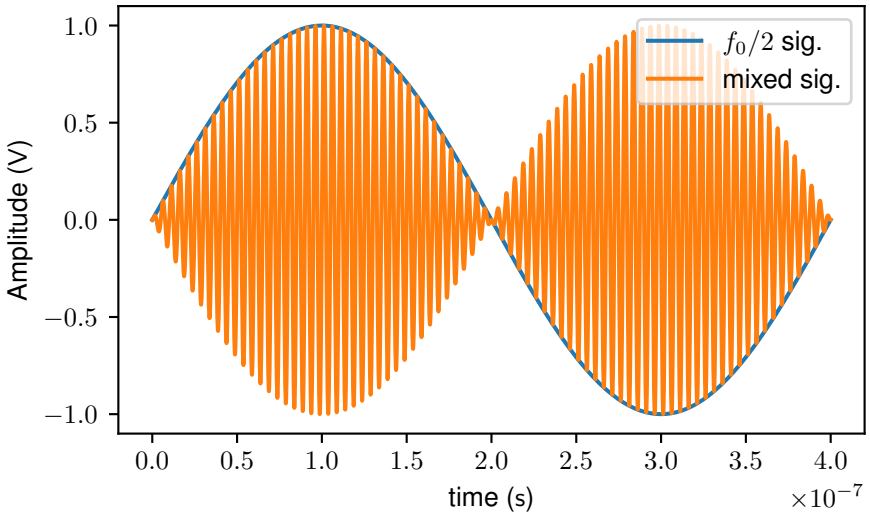

Figure 4.6: *Output of an electronic mixer, with input signal at* $f_0 = 5$ MHz *(*$f_0/2 = 2.5$ MHz*, represented on the figure) and* 200 MHz *which is the center frequency of the AOM. It is seeable that to within a phase factor shifting from* 1 *to* -1*, this signal, which is fed to the AOM, oscillates in intensity at frequency* 5 MHz *(i.e.* $2 \times f_0/2$ *).*

order to compare the test signal with f_0 rather than $f_0/2$. By sweeping the frequency of the $f_0/2$ signal generator, it is possible to observe a mechanical resonance, as presented in the experimental results.

In order to retrieve an electric signal from the quartz, the quartz holder from Fig. 1.6d is slightly adapted by piercing the so-called condensators, as seen on Fig. 4.7. Indeed, the condensators (the quartz plates made from the same crystalline cut as the working quartz resonator that hold it in place, see Fig. 4.7) are metallized with a typical chromium-gold layer in order to retrieve the electric signal. This signal is sent through cables which are coiled around the cold finger of the cryogenerator all the way towards the user SMA plug outside the cryogenerator. This coil-like rolling is done in order to keep them at best in a thermalized state and avoid extra thermal extension noise.

The laser's wavelength can be set to a range of values (see section 3.2.1 for more informations about the laser used). Incidentally, the wavelength can therefore be set to either an optically resonant or non-resonant value for the Fabry-Perot cavity formed by the set of metallic mirrors deposited on the quartz(see section 3.1.3 for more details about the optical resonance). An experimental study concerning the possibility to set an optically resonant wavelength is discussed in section 4.1.3.3.

4.1.3.2/ EQUIVALENT CIRCUIT

In order to modelize the behavior of the photo-elastically induced resonance, it is possible to give an equivalent electrical circuit. From Eq. 4.21e, one can calculate that in the steady state, and by naming S the surface of the electrodes:

$$I_0 = i\Omega DS \tag{4.31}$$

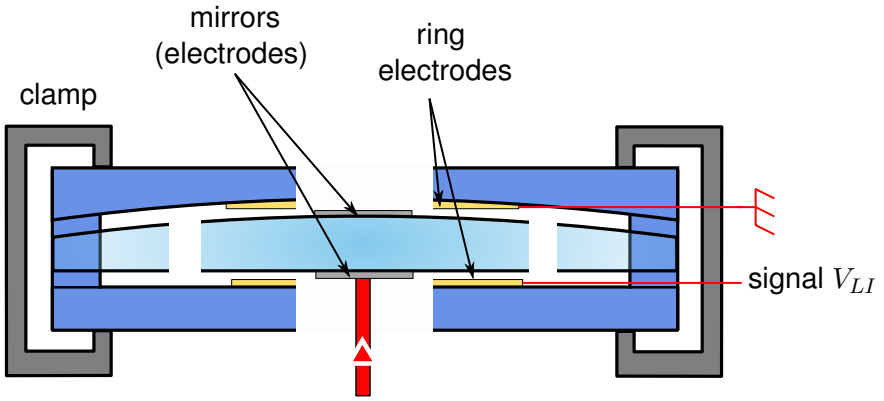

Figure 4.7: *BVA-like structure to hold the quartz which is metallized with thin silver layers, and the holders are metallized with typical chromium and gold layers to retrieve the piezoelectric signal from the quartz' mechanical resonance because of the photo-thermal effect. The output of the gold electrodes are plugged into the Lockin amplifier (see Fig. 4.5).*

By inserting the expression for $U(e) - U(0)$ (Eq. C.18 or Eq. C.19) in the expression for the electrical potential (Eq. 4.25) and in the electric displacement Eq. 4.21b, one can obtain a cumbersome analytical expression for the electric current. In this expression, one can formally identify several parts, suggesting different parallel currents going through different branches of equivalent (R,L,C...) components. It is possible to rearrange the circuit in order to arrive to an equivalent model, which is displayed in Fig. 4.8a (see e.g. [Bontempi et al., 2014]).

Contrary to the typical Butterworth-Van Dyke model, the generator is included in the motion branch. This is similar to models in the field of energy harvesting (see [Liang et al., 2012] [Liao et al., 2019]).

It consists of an excitation reference signal ($f_0/2$ signal in Fig. 4.5) which is split to be sent both to the Lockin amplifier as a reference, and to the AOM (after mixing) as a way to modulate the laser's power. Because the laser power and the reference $f_0/2$ signal are in-phase and vary from one another only by a scaling factor (see annex D), we will consider the exciting signal as the optical power P_{in} instead [5] . This optical power is transformed, through an a priori unknown transfert function T_{th} to a voltage V_x exciting the quartz crystal. This quartz crystal, which is modelized by a typical RLC circuit, has a parasitic C_0 coming from the presence of electrodes (see Fig. 4.7) and the cables driving the signal. Note also the presence of a load resistor R_L, plugged onto the quarz, equivalent to the input impedance of the Lockin amplifier.

There are two extreme cases for the scheme presented on Fig. 4.8a: $R_L \gg 1/(C_0\omega)$ and $R_L \ll 1/(C_0\omega)$. An impedancemeter measurement permits to establish that the order of magnitude of C_0 (including both the cables and the parasitic electrodes capacitance) is

[5] Because the $f_0/2$ signal feeds both the reference input of the Lockin and also the AOM (see Fig. 4.5) changing its output power is problematic; although it does not influence the results of the Lockin amplifier, it would indeed influence the optical power which is modulated through the AOM. However, because the $f_0/2$ signal passes first through a frequency mixer, as described in Fig. 4.6, the RF power needed is fixed and should not be tweaked. Because the optical power and the $f_0/2$ RF power only vary by a factor and are in phase, it is therefore simpler for all experimental considerations to take P_{in} as the reference excitation signal, see Annex D.

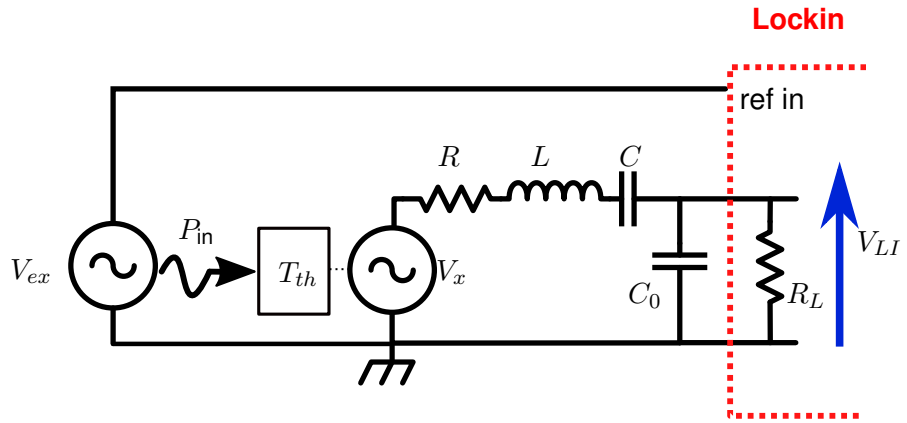

(a) Equivalent circuit

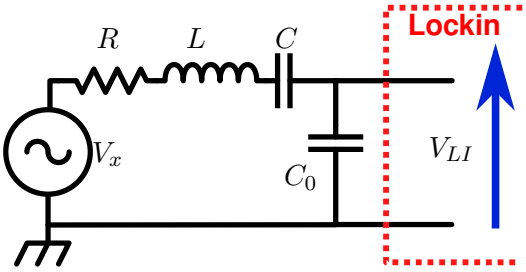

(b) Crystal part with $R_L = 1\,\text{M}\Omega$

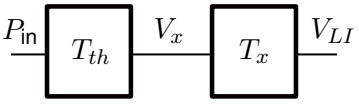

(c) Transfer functions

Figure 4.8: *Fig. 4.8a: equivalent circuit of the total system. For details about the relation between P_{in} and V_{ex}, see Annex D. See the main text for a complete description of the different quantities. Fig. 4.8b: focus on the crystal part of the system when the input impedance of the Lockin amplifier is set to $1\,\text{M}\Omega$. This simplifies the theoretical description, as seen in the main text. Fig. 4.8c: a small reminder scheme for the two transfer functions acting on the input excitation and reference optical signal P_{in}, transformed (through a to-be-determined transfer function T_{th}) into voltage V_x which excites the crystal, which, in turn, is transformed (through transfer function T_x) into the measured voltage V_{LI} which is measured at the parasitic capacitor's ends.*

of about 300 pF-500 pF. With a typical resonance frequency ranging in 5 MHz-10 MHz, this gives an impedance for C_0 of Z_0 =30 Ω-100 Ω. It is therefore simpler to set the Lockin input to $1\,\text{M}\Omega$ (as the capacitance will act as a short-circuit for the latter), so that the details of the subsequent simplified expression follows.

With the transfer function defined in Fig. 4.8c, V_{LI} can be expressed as a function of P_{in} :

$$V_{LI} = T_{tot} P_{\text{in}} = (T_{th} T_x) P_{\text{in}} \tag{4.32}$$

Let us write T_{th} as:

$$T_{th} = \frac{V_x}{P_{\text{in}}} = A e^{i\varphi} \tag{4.33}$$

where A is the attenuation factor and φ is the imparted phase, which is possibly different from 0.

It is therefore possible to write the full expression for V_{LI}, by determining the analytical expression for T_x and inserting it as well as Eq. 4.33 in Eq. 4.32:

$$V_{LI} = \frac{P_{\text{in}} A Z^{-1}}{C_0 \omega} e^{i(\varphi - \frac{\pi}{2})} \tag{4.34}$$

where Z^{-1} is the admittance of the motional RLC part of the circuit, along with C_0:

$$Z^{-1} = \frac{1}{R + iL\omega + \frac{1}{iC\omega} + \frac{1}{iC_0\omega}} \tag{4.35}$$

where the R, L and C are a priori unknown but can be determined through a prior impedancemeter measurement.

This expression permits to relate the measured voltage V_{LI} to other experimentally accessible quantities. The measurement of the transfer function T_{th} is therefore allowed by this theoretical model, and is shown in the following section 4.1.3.3 (see Fig. 4.12).

4.1.3.3/ RESULTS AND DISCUSSION

In this section, some experimentally obtained data is shown, with the setup presented in section 4.1.3.1. We start by giving some example of the measured X, Y data or the $|V_{LI}|$ and accompanying phase φ. We proceed with a brief analysis of the changes of the maximum voltage at mechanical resonance in the four following cases:

1. Simple mechanical resonance at room temperature
2. Mechanical resonance at room temperature, with the laser set to be at the optical resonance wavelength
3. Simple mechanical resonance at cryogenic temperature
4. Mechanical resonance at cryogenic temperature, with the laser set to be at optical resonance wavelength

Indeed, as discussed in section 4.1.3.1, the laser's wavelength can be set to be optically resonant for the Fabry-Perot cavity. We conclude this section by an experimental identification of the coefficients A and φ from Eq. 4.33.

4.1.3.3.1/ Typical resonance The quartz crystal under use is an SC cut crystal, with a plano-convex feature and 50 nm of deposited silver electrodes, which can also be used as mirrors for Fabry-Perot cavity regime (see section 2.2 and section 3.1 for more details). A variable optical power of around 5 mW arrives at the quartz inside the vacuum chamber, with a linear polarization along one of the quartz' polarization axis (see section 3.1.1).

The Lockin amplifier gives, by default, an output in X and Y, the usual output of a Lockin amplifier, which corresponds to the in-phase and out-of-phase (with respect to the reference) components of the test signal, respectively, i.e. it compares the difference in phase $\Delta\theta$ between the tested signal and the reference. The tested signal $V_{LI} = |V_{LI}|e^{i\Delta\theta}$ is then expressed:

$$|V_{LI}| = \sqrt{X^2 + Y^2} \tag{4.36a}$$

$$\Delta\theta = \arctan\left(\frac{Y}{X}\right) \tag{4.36b}$$

The raw signal, which is phase-calibrated (see section 4.1.3.1), is seeable on Fig. 4.9a. The amplitude-phase signal, on the other hand, is seeable on Fig. 4.10.

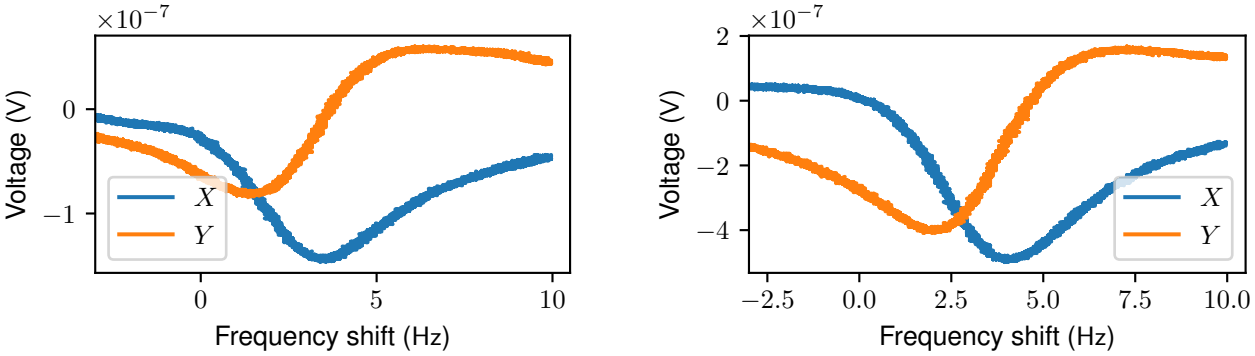

(a) Raw data

(b) Raw data at optical resonance

Figure 4.9: *Raw data X and Y (in and out-of-phase signals respectively) from the Lockin amplifier for a C3 mode (which has the largest signal), simply sending the laser on the metallized quartz and shifting its power modulation frequency (see Fig. 4.6) with* 5 mW *mean power in Fig. 4.9a. On Fig. 4.9b, on the other hand, the input power is the same, but the wavelength of the laser is set to be on-resonance with the Fabry-Perot cavity, which amplifies the light inside the cavity and hence results in a higher level signal. Note also a slight displacement in the peaks' central frequency, which we attribute to a change in the mean temperature of the quartz due to the increased presence of light dissipating in the thin metal layers.*

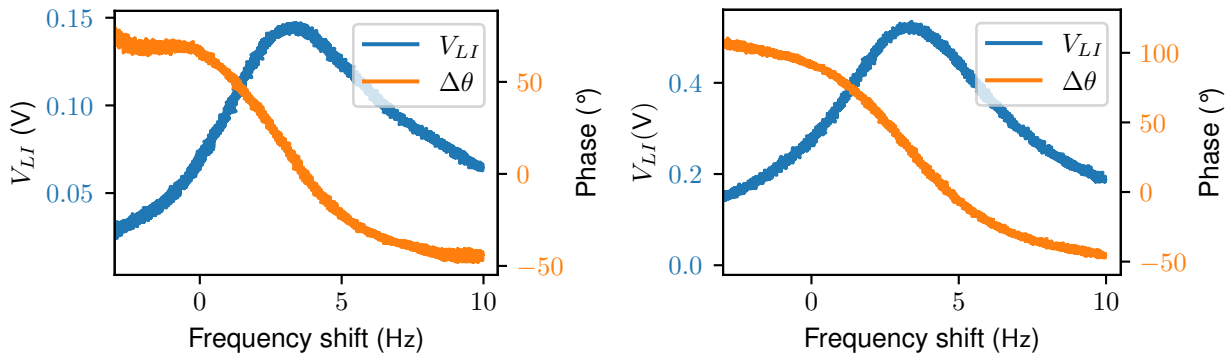

(a) Amplitude-Phase

(b) Amplitude-Phase at optical resonance

Figure 4.10: *Same as Fig. 4.9, but with the test signal voltage $V_{LI} = |V_{LI}|e^{i\Delta\theta}$ instead of the raw X-Y signal (see Eq. 4.36), without (Fig. 4.10a) or with (Fig. 4.10b) optical resonance. Note that the phase transition is closer to the maximum predicted* 180° *in the optical resonance case.*

A similar signal can be obtained for several modes. In particular, we performed the measurement mainly on three modes: at room temperature, the C3 mode is at 4 999 014 Hz (shown in Figs. 4.9 and 4.10), B3 mode at 5 475 748 Hz (5 475 774 Hz) for the optically-resonant (non-resonant) signal, and for the A3 mode at 9 102 355 Hz (9 102 381 Hz) for the optically-resonant (non-resonant) signal. This difference in frequency for the B3 and A3 mode are attributed to a shift in the mean temperature of the quartz because of the increased light absorbtion on the electrodes which is simply due to the increased presence

	A	A^{res}	A_{4K}	A_{4K}^{res}
A	1	1.805	X	0.376
A^{res}		1	X	0.208
A_{4K}			1	X
A_{4K}^{res}				1

Table 4.1: *Table of the amplification (attenuation) for the A3 mode, i.e. ratio of the top quantity by the side quantity: e.g. A^{res}/A = 1.805. A is the basis (optically) non-resonant* 300 K *situation, A^{res} is the optically resonant case at* 300 K*, A_{4K} is the non-resonant* 4 K *situation, A_{4K}^{res} is the resonant* 4 K *situation. In the specific case of the A3 mode, a very poor signal for the non-resonant* 4 K *situation prevented measurement in this particular scenario. One can note the generally poor results for the resonant case and the cryogenic resonant case, in particular with respect to the B3 and C3 modes. Base voltage is* 6.30×10^{-8} V*.*

of light inside the optical cavity [6] .

Indeed, the frequency thermal sensitivity of the B3 mode for an SC cut is of about $-29 \times 10^{-6}\,\mathrm{K}^{-1}$. Considering the amplification factor to be $\mathcal{A} = 22$, that would lead to a temperature elevation 22 times that predicted in Eq. 4.4 in the case of optical resonance, meaning a total elevation of approximately $\theta = 286\,\mathrm{mK}$. With the considered frequency thermal sensitivity, this would lead to a change of frequency of $\Delta f_0 \approx -45\,\mathrm{Hz}$, which is in reasonable agreeement with the experimentally reported difference of $\Delta f_0 = -26\,\mathrm{Hz}$.

Although this effect is also observable for the C3 mode, the latter is specifically designed to be relatively insensitive to temperature fluctuations in the SC cut with a frequency temperature sensitivity of only $1.5 \times 10^{-6}\,\mathrm{K}^{-1}$, which results in a small shift of resonance frequency with increased mean temperature. Theoretical predictions of the same kind as for the B3 mode lead to a calculated $\Delta f_0 \approx 1.5\,\mathrm{Hz}$, which is reasonably agreeing with the slight shift observable on Fig. 4.10

At 4 K, on the other hand, these frequencies get to 4 992 242 Hz (4 992 233 Hz) for the resonant (non-resonant) C3 mode, 5 504 280 Hz for both resonant and non-resonant B3 modes and 9 608 980 Hz for the resonant A3 mode (for the absence of non-resonant A3 mode, see main text below.

In the non-resonant use, an increased incoming optical power results in an approximately linearly increasing output voltage, see Fig. 4.11. A first order polynom fit gives the slope to be of approximately $8.35 \times 10^{-6}\,\mathrm{V\,mW^{-1}}$, whereas the offset at the origin is of about $3.9 \times 10^{-5}\,\mathrm{V\,mW^{-1}}$, which indicates that the voltage does not behave linearly anymore at lower optical power.

4.1.3.3.2/ Signal level As one can observe on Fig. 4.10, the signal at optical resonance is somewhat increased in amplitude with respect to the non-resonant case. A numerical treatment permits to establish the amplification to be dependent on the particular mechanical mode investigated, see the sum-up tables 4.1 - 4.3.

From these tables, we note that the signal is generally improved with optical resonance

[6] In the light of section 4.2.2, one might wonder if the frequency shift can be attributed so some potential optomechanical coupling. It is very unlikely to be the case, for the orders of magnitude involved for the shift involved by this type of interaction is far smaller than the shifts observed here.

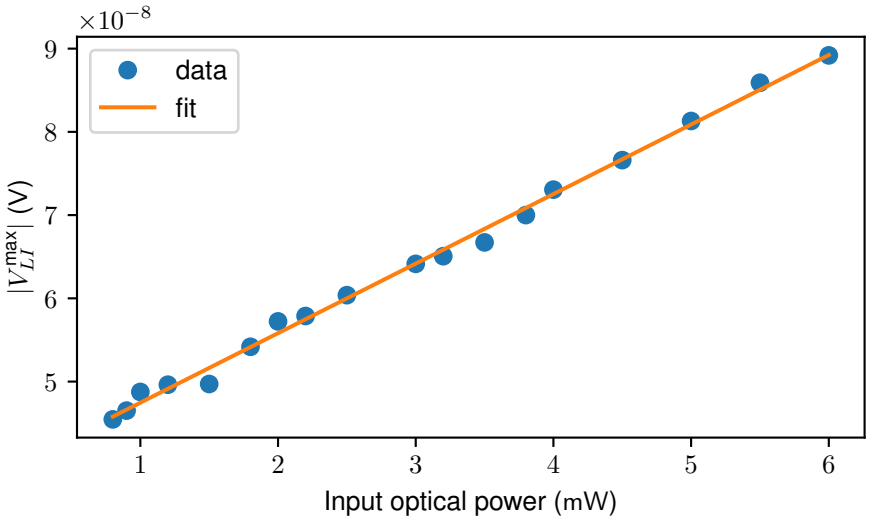

Figure 4.11: *Maximum test signal voltage $|V_{LI}|$ (e.g. max of V_{LI} curve in Fig. 4.10a) against input optical power P_{in} for a C3 mode at* 4 999 008 Hz*. It is almost affine with input optical power, with a slope of approximately* $8.35 \times 10^{-9}\,\mathrm{V\,W^{-1}}$*. The offset at the origin is of about* $3.9 \times 10^{-8}\,\mathrm{V\,W^{-1}}$*, which indicates that the voltage does not behave linearly at lower optical power. Indeed, an absence of optical power physically results in an absence of measured voltage, so that the offset does not translate a physical phenomenon at null incident optical power.*

	B	B^{res}	B_{4K}	B_{4K}^{res}
B	1	4.072	2.395	14.402
B^{res}		1	0.588	3.536
B_{4K}			1	6.013
B_{4K}^{res}				1

Table 4.2: *Same as table 4.1, with the B3 mode. Here, the amplification for the optically-resonant case with respect to the non-optically-resonant case is much higher than for the A3 mode, as well as the amplification at* 4 K *with respect to the* 300 K *case, which is not explained by the theory (see main text).*

with respect to the non-resonant case. It is, however, not proportional to the theoretical amplification of light inside the optical cavity which is of about $\mathcal{A} \approx 22$ for a 50 nm silver deposition (see Fig. 3.13). Furthermore, Fig. 4.11 predicted a linearly dependent output voltage with input optical power. The fact that the amplification factor listed in table 4.1 between the non-resonant case and the resonant case changes depending on the mechanical mode indicates that some non-linear effect is at hand, or that the coupling no longer produces a linear response of the voltage in function on the input optical power for modes other than the C mode (see Fig. 4.11). Another possible explanation is that the boundary conditions change altogether upon imposing an optical resonance inside the optical cavity. Indeed, the situation then turns out to be symmetrical and the theoretical framework developed thus far has to be be modified consequently. This last hypothesis is strenghtened by the previously reported frequency shift (see previous section 4.1.3.3.1) which is compatible with a linear response to increasing optical power. At any rate, further investigation is required to fully understand the coupling between the mechanical modes

	C	C^{res}	C_{4K}	C^{res}_{4K}
C	1	3.630	1.245	7.367
C^{res}		1	0.342	2.029
C_{4K}			1	5.917
C^{res}_{4K}				1

Table 4.3: *Same as table 4.2, although the amplification is slightly lower than for the B3 mode. See main text.*

and the laser, and in particular through testing an excitation with a laser split and sent on both sides of the quartz to compare with the one-sided incidence results.

From these same tables, we observe a trend to increase the maximum amplitude when going from room temperature to cryogenic temperature, except for the A3 mode. Some other results for other modes, which are not displayed in this thesis, tend to validate the tendency to improve the signal at cryogenic temperature. This is not in agreement with the attenuation factor of a hundred for the displacement predicted by our simple model from section 4.1.2.2 for the cryogenic displacement with respect to the room temperature displacement. The discrepancy is probably due to the neglected directions of coupling in the model and to its limited applicability (see section 4.1.2.1.1).

Lastly, the tables also show that at 4 K, the optical resonant case with respect to the non-resonant case display a signal approximately 6 times stronger for both the B3 and C3 mode, with a lack of data for the A3 mode due to an absence of non-resonant cryogenic signal. Here, both the B3 and C3 mode display an approximately equal amplification factor for the resonant case whereas it was rather different at room temperature. Another cryogenic measurement for the C5 mode, at 8 295 762 Hz, shows that the amplification factor in this case is of approximately 4.15. The A5 mode at 15 728 268 Hz shows an amplification factor of about 1.77. Unfortunately, no other mode was available for measurement in both the resonant and non-resonant cases at 4 K, so that this issue can be investigated no further. This limitation comes mainly from the frequency involved: indeed, the scheme described in Fig. 4.6 consists in sending two signals at $200\text{MHz} \pm f_0/2$ to the AOM. The latter, however, has a limited bandwith around 200 MHz in which it produces an efficiently diffracted first order. We measured this bandwidth to be of about 10 MHz. Therefore, resonances with increasing frequency are increasingly hard to observe because the diffracted first order of the AOM is decreasingly efficient, i.e. the total oscillating optical power decreases so that $\Delta P < P^{\text{mean}}$ and P_{in} decreases too (see Eq. 4.30).

4.1.3.3.3/ Equivalent circuit The equivalent circuit for the excitation scheme, detailed in Fig. 4.8 and section 4.1.3.2, is further studied experimentally with the C3 mode in particular. Indeed, measuring the signal against frequency sweep for different input optical powers permit to obtain the unknown transfer function T_{th} from Eq. 4.33 at mechanical resonance:

$$Ae^{i\varphi} = \frac{V_{LI} C_0 \omega e^{i\frac{\pi}{2}}}{P_{\text{in}} Z^{-1}} \tag{4.37}$$

where V_{LI} is obtained from experimental measurements such as the ones presented in Fig. 4.11 and the other quantities can be determined experimentally or by computation. In particular, a prior impedancemeter measurement is taken as the reference in order to determine Z^{-1}, the admittance of the motional part of the quartz.

From these experimentally measured V_{LI}, the attenuation factor is obtained by computing with a python program the max amplitude of the signal for each incoming power. The resonance phase, on the other hand, is obtained with a python routine that fits the experimental signal to an admittance circle; indeed, to within some constants and a phase at resonance, $V_{LI} \propto Z^{-1}$ i.e. to an admittance. This leads to the results represented on Fig. 4.12.

The transfer function at mechanical resonance seems to vary with incoming optical power. This comes from the fact that the measured resonance signal is not exactly affine with incoming optical, contrary to what transpires in Fig. 4.11 This might be due to some non-linear coupling effects that requires further investigation. At any rate, the phase offset of V_{LI} at mechanical resonance goes closer and closer to 0 with increasing optical power, which indicates that at hight enough optical power, the phase of the transfer function, φ, gets closer and closer to $\pi/2$ (because of the $e^{-i\frac{\pi}{2}}$ factor in Eq. 4.34). This is adding to the previously discussed fact that achieving higher optical power is also associated with a phase transition closer to π.

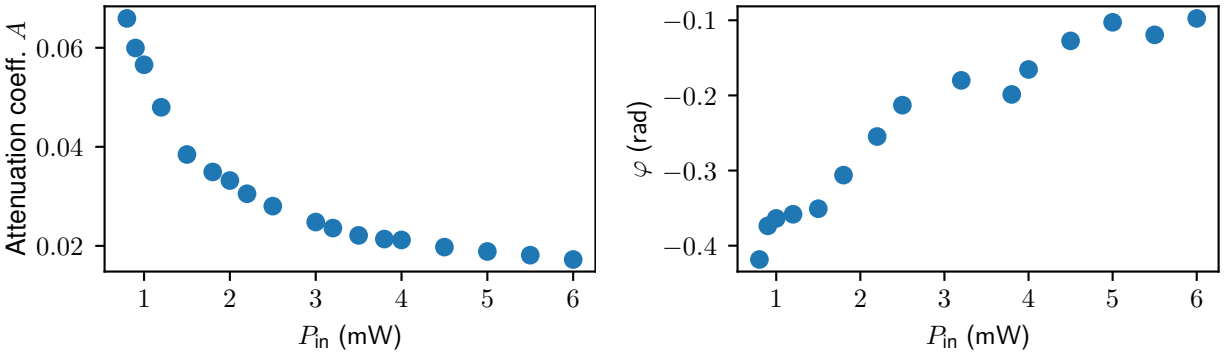

(a) Attenuation factor

(b) Phase offset

Figure 4.12: *Transfer function $T_{th} = Ae^{i\varphi}$ against optical power at mechanical resonance and without optical resonance, see Eq. 4.37.*

We have lead here an experimental study which is limited to a restricted number of mechanical modes due to technological constraints such as the achievable frequency of the oscillating optical power, input optical power after AOM (and light coupling thereof) etc. However, to the best of our knowledge, this is the first time that this photo-thermal excitation is achieved at cryogenic temperature and at high frequencies, i.e. several MHz. To describe the mechanical dynamics with a more refined model would require a lengthy theoretical description or another approach algotether with e.g. a numerical finite element method. A lack of time prevented such a work, although one can only conclude from the achieved experimental work that the coupling between the thermal source and the mechanical movement does happen although quite weakly, at high frequency (A3 mode at 15 MHz for example), and even for apparently prohibited modes.A better theoretical understanding is therefore required to make more refined predictions, although the present exploratory work permits to establish the photo-thermal actuation as a possible and rather easy way of actuating the quartz optically.

Piezoelectric readout was preferred for the accessibility ease and the necessary time to implement experimentally, although an optical readout would offer the advantages that

are required by the metrological use we are seeking (see chapter 1). Such a readout is presented in the future perspectives, in Appendix E.

This 1st part of chapter 4 reports on our investigations concerning the photothermal excitation scheme, both theoretical and experimental.

The novel 1D theoretical framework that we developed has shown to be more accurate at room temperature than at cryogenic temperatures. Since it is an approximation of the more complex 3D dynamics, it now requires to be completed with Finite Element Methods (FEM, see e.g.)<++> in order to confirm the predictions of remarkable displacements at room temperature. Indeed, several tens of nm displacements for the C3 mode at 5 MHz have been observed by piezoelectric measurements. This indicates that optical readout, with e.g. heterodyne detection, should be possible (see Annex E).

The experimental study has permitted to establish several points:

- This actuation method allows displacement measurement readout up until several MHz, with the detection of a weak signal up to 15 MHz at 4 K. The limitation is most certainly due to the setup with the limited bandwidth of the AOM, and higher frequencies should be achievable with the appropriate equipment.
- The excitation is generally more efficient at cryogenic temperatures, with a signal which is improved in a variable proportion depending on the mode (at the exception of the A3 mode).
- The photothermal excitation is reinforced while the laser is tuned to be on-resonance with the Fabry-Perot cavity, allowing for a slightly better signal.

The latter point might be explained by the increased amount of light inside the quartz. Indeed, the observed central resonance frequency shift obtained at optical resonance corresponds to an intracavity amplification factor of the order of $\mathcal{A} = 20$, i.e. the theoretically predicted value from section 3.1.3 for a 50 nm silver thin films optical cavity. The observed mechanical resonance signal, however, does not seem to follow the same simple trend of a multiplicative factor due to increased light. This discrepancy could originate from the new and different boundary conditions in the presence of a stationary optical field within the quartz.

Finally, under certain hypotheses, we have identified the transfer function that relates the input optical power P_{in} to the intracrystal excitation voltage V_x. It is found to have a variable attenuation factor with incident optical power, as well as a variable phase with incident optical power. This point requires further study.

We conclude from this study that photothermal excitation is a good candidate for mechanical actuation with light, and that it is readily usable with our thin silver films coated quartz resonators. Furthermore, one could consider coating the resonators with non-metallic films, with e.g. dielectric coatings which are highly absorbtive at some functioning wavelength in order to maximize the optical power transfer into heat or even using some absorbing wavelength of the resonator material (e.g. in the UV region for quartz), at the expense of the possibility to tune the laser to optical resonance.

4.2/ OPTOMECHANICS

4.2.1/ STATE OF THE ART IN OPTOMECHANICS

4.2.1.1/ BRIEF HISTORICS

Optomechanics is the coupling between light (optics) and mechanics. Generally, it can refer to both the action of light on mechanics or the opposite, although it is most commonly used in the former sense. The most widespread optomechanical effects that are of use are the radiation pressure and the electrostriction.

The first mechanical effects of light on matter[7] were demonstrated in the early 20th century, with radiation pressure (see [Lebedew, 1901] and [Nichols et al., 1901]) being carefully differentiated from thermal effects. In fact, this effect had a wide enough popularity to be the research subject of a fictional character in a novel by Natsume Soseki in 1908 (Sanshiro, see Soseki [Natsume, 2020]), which studies the "pressure exerted by light on objects". It consists in imparting momentum from the photon to the object, either through absorption, reflection or through light which is otherwise emitted from the object (e.g. black body radiation). A significant advance in the field was demonstrated in the 70's by Hänsch [Hänsch et al., 1975] and Wineland [Wineland et al., 1975] independently, making use of radiation pressure in order to cool atoms with a laser. Wide experimental demonstrations of this technique, and even furthermore trapping the cooled atoms, have since been made [Ashkin, 1978] [Phillips et al., 1982] [Metcalf et al., 1999]. This effect of radiation pressure for cooling atomic gases is widely used nowadays in experiments for atomic and ionic clocks [Vallet, 2018] [Lauprêtre et al., 2020] [Huang et al., 2019] [McGrew et al., 2018], where the effect is often combined with a magnetic field to create a so called Magneto-Optical Trap (MOT): see [Raab et al., 1987]. An extensive theoretical (and experimental review) discussion about the radiation pressure effect is presented in the rather recent article by Aspelmeyer [Aspelmeyer et al., 2014b]. Radiation pressure is discussed at more length in part 4.2.2.

Another widely used effect arising from optomechanical coupling is the electrostriction. Electrostriction is similar in its nature to piezoelectricity, although the former depends on the square of the electric field and is therefore independent on the field's direction (sign) whereas the latter does depend on the field's direction and is a linear effect at first order (and more generally dependent on the electric field at an odd number power). Piezoelectricity was discovered in the late 19th century by the Curie brothers [Curie et al., 1880], and it would appear that electrostriction had been studied by Röntgen at around the same time (see [Katzir, 2006], p.46). Although the effect of a material's density fluctuations on light and subsequent scatterings was known and shown by Brillouin [Brillouin, 1922] early on, different origins for these density fluctuations are possible. Brillouin described effects induced by thermal fluctuations. It is only with the work of Osterberg [Osterberg et al., 1937] that a proper theoretical description emerges for the electrostriction effect, understood as the complementary effect of the piezodielectric effect (the effect of mechanical perturbations on dielectric constants of a material, as defined by this last author). The electrostrictive effect is discussed in part 4.2.3.

[7] Although the discovery of electrostriction is anterior to that of radiation pressure, visible light's effects were indeed discovered and envisioned with radiation pressure, even though it was already known when electrostriction was studied by Rötgen in 1880 that light was an electromagnetic radiation (it had been inferred by Faraday and consolidated by Maxwell, see [Longair, 2003], p87)

4.2.1.2/ DEVICES AND APPLICATIONS

As mentioned in section 4.2.1.1, the two mainly used effects of optomechanics are radiation pressure and electrostriction. In some pionneering work by Chiao [Chiao et al., 1964], electrostriction was applied to achieve coherent phonons production with laser light (with a Mandel'shtam-Brillouin type interaction). Some years later, Braginsky [Braginskii et al., 1970] showed the opposite effect with radiation pressure, namely that some suspended mirror could be cooled down with electromagnetic radiation (in the microwave domain), which is a major concern in the highly sensitive field of interferometric gravitational-wave detection [Cohadon et al., 1999].

Some related works with the production of stimulated phonons by means of electrostriction followed, e.g. Kroll [Kroll, 1965], Starunov [Starunov et al., 1970] and later, by Nelson [Nelson, 1982] by varying the angle of incidence of the laser (hence the frequency of the phonons, see section 4.2.3). Using both electrostriction and radiation pressure for the excitation of mechanical modes and coherent phonons or cooling and their suppression also was achieved again in a quartz crystal with laser light, rather recently by Renninger [Renninger et al., 2018] and in an optical (Fabry-Perot) cavity by Kharel [Kharel et al., 2019].

A major part of the electrostriction community is actually interested in its application (and the issue that it might constitutes) within optical fibers (see e.g. [Aoki et al., 1988] [Beugnot et al., 2012] [Kobyakov et al., 2010] [Laude et al., 2013] [Rakich et al., 2010] [Shelby et al., 1985]) and, more generally, within nanoscaled devices (see e.g. [Wolff et al., 2015] [Wiederhecker et al., 2019] [Carvalho et al., 2019] [Bahl et al., 2011]). In fact, as we discuss in part 4.2.3, electrostriction is (one of the possible) origin to the presence of Brillouin-scattering. These forces are prominent in optical fibers, both because of the very way that light is transported and the intensity of circulating light as well as the size of the transporting area. The intensity of the phenomenon can even dramatically increase by several orders of magnitudes when subwavelength scale are achieved, see [Rakich et al., 2012]).

It is, however, sometimes used and observed in bulk material too (see [Bon et al., 2018] [Kharel et al., 2019] [Renninger et al., 2018] [Grimsditch et al., 1975]). Electrostriction gives rise to Brillouin scattering, which can be used to either excite the mechanical modes with the optical field ([Nelson, 1982] [Chiao et al., 1964] [Kroll, 1965]) or to do the opposite- that is, to cool the device ([Chan et al., 2011] [Agarwal et al., 2013]).

4.2.2/ RADIATION PRESSURE

Radiation pressure corresponds to the cumulative collective effect of the momentum that each individual photon imparts to the matter that it scatters with. There exists several descriptive frameworks for this effect: in particular, continuum mechanics can account for radiation pressure through boundary conditions (see e.g. [Rakich et al., 2010] [Wang et al., 2016] [Laude et al., 2015]). We will mainly focus on the Hamiltonian description which is much more usual for cavity radiation pressure optomechanics ([Aspelmeyer et al., 2014b] [Agarwal et al., 2013]). The Hamiltonian descriptive framework for the radiation pressure has been developed by [Law, 1995], and has beeen widely used ever since ([Rakich et al., 2010] [Siciliani de Cumis et al., 2009]). We then specialize the calculation to the thin film quartz optical cavity which has been studied optically in

section 3. We draw the conclusions as to the apparent lack of feasability of optomechanical actuation through radiation pressure in this particular case.

4.2.2.1/ HAMILTONIAN DESCRIPTION

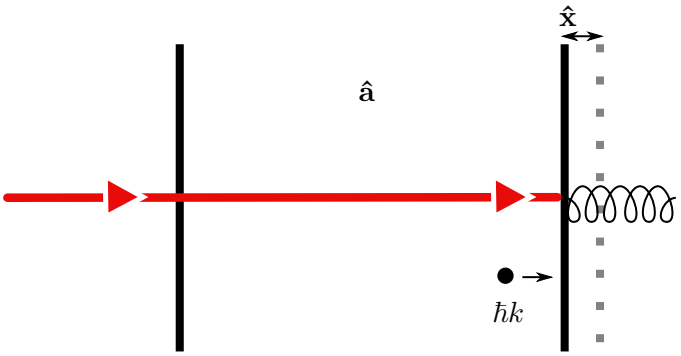

Figure 4.13: *Depiction of the radiation pressure within Hamiltonian framework. The input mirror is considered as fixed and only partly reflective, whereas the output mirror is considered as moving and entirely reflective. The displacement operator $\hat{\mathbf{x}}$ measures the displacement with respect to the mean position.*

Throughout this section, we take the notation and development from [Aspelmeyer et al., 2014a]. The situation is considered to be as depicted on Fig. 4.13.

The first input mirror is only partly reflective and is stationary, whereas the second mirror is considered perfectly reflective and moving. This means that in this framework, the optical cavity length and thus its optical characteristics (FWHM of the peaks and FSR) will depend on the second mirror's position. Its position is described by the operator $\hat{\mathbf{x}}$. Let us write that the cavity resonance frequency ω is in fact dependent on the position:

$$\omega(x) = \omega + x\frac{\partial\omega}{\partial x} + \cdots \tag{4.38}$$

On the other hand, the Hamiltonian of the mechanical and optical system is as follows:

$$\hat{H} = \hbar\omega\hat{\mathbf{a}}^\dagger\hat{\mathbf{a}} + \hbar\Omega_m\hat{\mathbf{b}}^\dagger\hat{\mathbf{b}} \tag{4.39}$$

where $\hbar$ is Planck's constant (divided by 2π) and $\hat{\mathbf{a}}^\dagger$ ($\hat{\mathbf{b}}^\dagger$) and $\hat{\mathbf{a}}$ ($\hat{\mathbf{b}}$) are respectively the creation and destruction operator for the optical (mechanical) field.

This leads to write the interaction part of the Hamiltonian, after injecting Eq. 4.38 in Eq. 4.39 and reminding that the position operator is proportional to the mechanical field operators, $\hat{\mathbf{x}} \propto \left(\hat{\mathbf{b}}^\dagger + \hat{\mathbf{b}}\right)$:

$$\hat{H}_{int} = -\hbar g_0\hat{\mathbf{a}}^\dagger\hat{\mathbf{a}}\left(\hat{\mathbf{b}}^\dagger + \hat{\mathbf{b}}\right) \tag{4.40}$$

where g_0 is the 1photon-1phonon coupling strength expressed as a frequency, which is expressed as:

$$g_0 = \frac{\omega}{d}\sqrt{\frac{\hbar}{2m_{eff}\Omega_m}} \tag{4.41}$$

with d the cavity length and m_{eff} the effective mass of the vibrating part of the system.

Unfortunately, the expression 4.40 is not linear in the optical field operators. As shown in [Law, 1995], it is possible to linearize the expression by decomposing the optical field into its average coherent amplitude and the fluctuating part $\hat{\mathbf{a}} = \langle\hat{\mathbf{a}}\rangle + \delta\hat{\mathbf{a}}$:

$$\hat{H}_{int}^{lin} = -\hbar g_0 \sqrt{\bar{N}_{cav}}\left(\delta\hat{\mathbf{a}}^\dagger + \delta\hat{\mathbf{a}}\right)\left(\hat{\mathbf{b}}^\dagger + \hat{\mathbf{b}}\right) \tag{4.42}$$

where we have introduced $\bar{N}_{cav}$, the mean photon number inside the cavity.

It is possible to derive the coupled linear equation of motions for the field operators and solve it. Solving these coupled equations in Fourier space is easier and leads to the extra contributions to the typical mechanical susceptibility of a mechanical oscillator[8], with a modified expression (see Eq. 4.43) which depends on the Fourier frequency ω and the detuning from cavity's resonance frequency Δ:

$$\chi^{opt}[\Delta,\omega] = \frac{1}{m_{eff}[(\Omega_m^2 - \omega^2 + 2\omega\delta\Omega_m(\Delta,\omega)) + i\omega(\Gamma_m + \Gamma_{opt})]} \tag{4.44}$$

In the last expression, the optomechanically induced damping Γ_{opt} (which can be positive or negative) and the frequency shift $\delta\Omega$ have been added to the typical expression (see Eq. 4.43), with the following expressions:

$$\delta\Omega_m(\Delta,\omega) = \frac{\Omega_m}{\omega} g_0^2 \bar{N}_{cav}\left(\frac{(\Delta+\omega)}{(\Delta+\omega)^2 + \text{FWHM}^2/4} + \frac{(\Delta-\omega)}{(\Delta-\omega)^2 + \text{FWHM}^2/4}\right) \tag{4.45a}$$

$$\Gamma_{opt}(\Delta,\omega) = \frac{\Omega_m}{\omega} g_0^2 \bar{N}_{cav}\left(\frac{\text{FWHM}}{(\Delta+\omega)^2 + \text{FWHM}^2/4} - \frac{\text{FWHM}}{(\Delta-\omega)^2 + \text{FWHM}^2/4}\right) \tag{4.45b}$$

From Eq. 4.44, we gather that the total mechanical losses, $\Gamma^{tot} = \Gamma_m + \Gamma_{opt}$, can be either negative or positive. The intrinsic mechanical losses of the system, are related to the quality factor Q (see Eq. 1.13) through $\Gamma_m = \Omega_m/Q$. Therefore, in order to gain knowledge about the behavior of the system, one needs to compare Γ_m to Γ_{opt}, i.e. to compare the mechanical damping of the system to the optomechanically induced damping which can be positive or negative.

When $\Gamma^{tot} > 0$, the damping impedes a lasting mechanical resonance. This is accompanied by a loss of phonons number, associated with cooling the device (see e.g. [Cohadon et al., 1999] [Siciliani de Cumis et al., 2009] [Vahala, 2008] [Neuhaus, 2016]).

When $\Gamma^{tot} < 0$, on the other hand, the system can reach the so-called "mechanical lasing" point (see e.g. [Braginsky et al., 2001] [Siciliani de Cumis et al., 2009] [Carvalho et al., 2019]). It is the latter state we are interested in, in order to actuate the mechanical modes of the quartz resonator.

[8] A typical mechanical oscillator has an equation of motion:

$$\frac{\mathrm{d}^2x(t)}{\mathrm{d}t^2} + \Gamma_m\frac{\mathrm{d}x(t)}{\mathrm{d}t} + \Omega_m^2 x(t) = \frac{F}{m_{eff}}$$

with x the position, Γ_m the mechanical losses and F the external force and m_{eff} the effective mass. In Fourier space, this same equation is written $X[\omega] = \chi[\omega]F$ with $X[\omega]$, the fourier transform of $x(t)$ and $\chi[\omega]$ the mechanical susceptibility with expression:

$$\chi[\omega] = \frac{1}{m_{eff}(\Omega_m^2 - \omega^2 + i\Gamma_m\omega)} \tag{4.43}$$

4.2.2.2/ APPLICATION TO THIN FILMS

From what is established in chapter 3 of this thesis, it is known that the power incident on the optical cavity gives rise to a higher intracavity optical power and that the FWHM is different from a regular Fabry-Perot cavity. Therefore, in order to predict the possibility to have an optomechanically induced mechanical lasing, one needs to know about the exact parameters of the optical system in order to evaluate Γ^{tot}. In particular, we establish that:

$$\bar{N}_{cav}(\Delta) = \frac{\mathcal{A}(\Delta) P_{\text{in}}}{\text{FWHM} \times \hbar\omega_{\text{l}}} \tag{4.46}$$

$$\mathcal{A}(\Delta) = \frac{\mathcal{A}}{1 + \left(\frac{\Delta}{\text{FWHM}/2}\right)^2} \tag{4.47}$$

with P_{in} the incoming laser power. Eq. 4.46 is simply the fraction of the total intracavity power to the typical photon power. Note that Eq. 4.47 is a first order expansion of an Airy peak around a local maximum (see Eq. 3.62 for the expression of $\mathcal{A}$ in the case of an absorptive thin film mirrors).

A previous work has shown that the best mechanical frequency to work at for optimizing the displacement with a plano-convex $d = 1\,\text{mm}$ quartz is of about $\Omega_m = 50\,\text{MHz}$, at which frequency the effective mass is of about $m_{eff} = 1\,\text{mg}$ (see [Bon et al., 2018]). This mass is calculated by integrating the resonant volume and setting aside any optomechanically induced change, because the relevent responses will be studied around the mechanical resonance frequency, unlike some other treatments (see [Pinard et al., 1999]).

It is possible to determine that the solutions for the max (min) of Γ_{opt} in Eq. 4.45b, which we note Δ_+ (Δ_-), are:

$$\Delta_\pm \approx \mp 0.288675 \sqrt{-\text{FWHM}^2 + 4\Omega_m^2 + 2\sqrt{\text{FWHM}^4 + 4\Omega_m^2\,\text{FWHM}^2 + 16\Omega_m^4}} \tag{4.48}$$

In our case, $\Omega_m \ll$ FWHM (see Table 3.1), the opposite case to the known sideband-resolved. Indeed, Ω_m has be within an interesting range of frequencies for the quartz crystal resonator, i.e. $1\,\text{MHz} < \Omega_m/2\pi < 50\,\text{MHz}$. On the other hand, the FWHM has been shown to be within the range of $500\,\text{MHz} <$ FWHM $< 1200\,\text{MHz}$ for reasonably thick silver thin films.

Eq. 4.45b can thereafter be approximated at the first order in $\frac{\Omega_m}{\text{FWHM}}$ to get:

$$\Gamma_{opt}^{\approx}(\Delta) = -4g_0^2 N_{cav} \Omega_m \frac{\Delta\text{FWHM}}{(\text{FWHM}^2/4 + \Delta^2)^2} \tag{4.49}$$

We also approximate at the first order in Ω_m Eq. 4.48 to get the approximate detuning for the max (min) of Γ_{opt}:

$$\Delta_\pm^{\approx} \approx \mp 0.288675\text{FWHM} \tag{4.50}$$

so that using Eq. 4.50 and 4.49 along with the relation $\mathcal{F} = \frac{\text{FSR}}{\text{FWHM}}$, we get to the result that the minimum is reached for Δ_- and reads:

$$\Gamma_{opt}^{\approx} = -10.3923 g_0^2 \frac{P_{\text{in}}}{\hbar\omega_l} \mathcal{A} \frac{\mathcal{F}^3}{\text{FSR}^3} \tag{4.51}$$

Eq. 4.51 and Fig. 4.14 show that it does not suffice to maxime the amplification factor $\mathcal{A}$ as it may intuitively seem in order to maximize the optomechanical coupling. Instead, the important quantity to maximize is the product $\mathcal{A} \times \mathcal{F}^3$, while keeping the FSR constant for geometry-imposed reasons. This is done for a thickness $d \approx 52\,\text{nm}$.

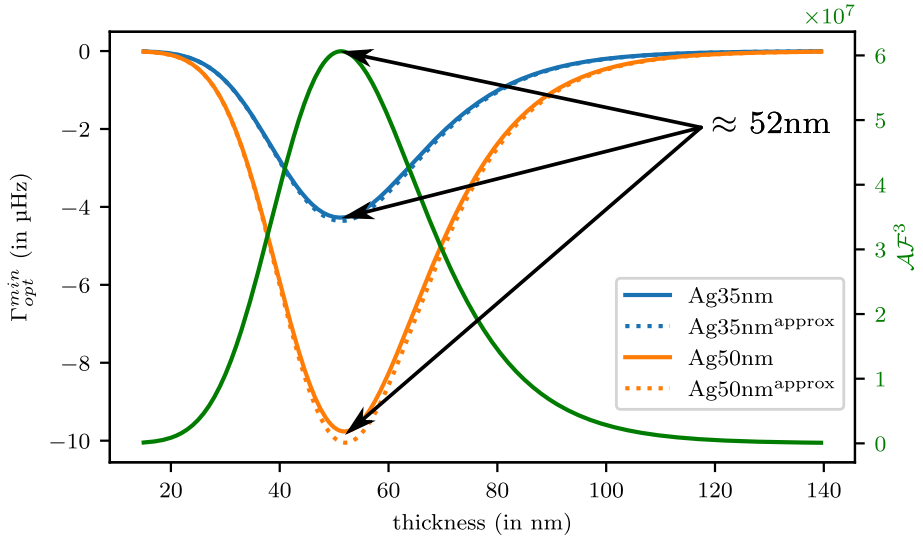

Figure 4.14: *Minimum of the optomechanically induced damping Γ_{opt}^{min}, computed for the refractive index for* 35 nm *silver and* 50 nm *silver taken from [Ciesielski et al., 2017]. Ag35nm designates the computation with Eq. 4.45b, whereas Ag35^{approx} designates the calculation with the approximated form in Eq. 4.51. In both the Ag35nm and Ag50nm computations, the optimal seems to be at around* 52 nm *of coating thickness. One can note that the minimum of the curve for Γ_{opt}^{min} against deposition thickness, be it with the approximated formula or the exact formula, coincides with the maximum of the product $\mathcal{A}\mathcal{F}^3$, which indicates that this is the important quantity in order to determine the optimal value of Γ_{opt}^{min}.*

We perform a numerical application for $d = 52\,\text{nm}$ of silver with refractive index $\tilde{n} = 0.2609 - 9.6359j$ (see Table 3.3), which is the point where Γ_{opt} is minimum on Fig. 4.14. For $\Omega_m/2\pi = 50\,\text{MHz}$ and $m_{eff} = 1\,\text{mg}$ this yields FWHM $= 790\,\text{MHz}$, $\Delta_- = 0.288675\text{FWHM} = 228.0\,\text{MHz}$ amounting to an amplification factor at this detuning of $\mathcal{A}(\Delta_-) = 20.5$ and allowing to calculate $g_0 = 1.6\,\text{mHz}$, . For an input optical power of 1 mW, this gives a total optomechanically induced mechanical losses of $\Gamma_{opt}(\Delta_-, \Omega_m) \approx -1.65 \times 10^{-6}\,\text{Hz}$, far from the mechanical losses of approximately $\Gamma_m \approx 0.1\,\text{Hz-1 Hz}$.

Doing the same calculation with a $\Omega_m/2\pi = 5\,\text{MHz}$ mode yields that $m_{eff} = 5\,\text{mg}$, $g_0 = 5.2\,\text{mHz}$ and $\Gamma_{opt}(\Delta_-, \Omega_m) \approx -2.79 \times 10^{-6}\,\text{Hz}$ which is also far from the mechanical losses, of approximately $\Gamma_m \approx 0.1\,\text{Hz} - 0.5\,\text{Hz}$ (with $Q \approx 1 \times 10^7 - 5 \times 10^7$).

These numbers show that the optics need to be improved in order to achieve sufficient optomechanically induced mechanical losses and compensate for the intrinsic mechanical losses Γ_m. As is discussed in section 3.2.2.3 and as Table 3.3 shows, there is a tendency to improve the reflectivity at cryogenic temperature, so that one may wonder whether using the same scheme with a cryogenic temperature environment might improve the optics enough so as to allow for radiation pressure actuation.

To verify this, we inject the numbers once again, with this time refractive index $\tilde{n} = 0.1100 - 8.8149j$ (see Table 3.3). Again, we start with $\Omega_m/2\pi = 50\,\text{MHz}$ and $m_{eff} = 1\,\text{mg}$. The optical index yields FWHM = 612 MHz with a optimal detuning $\Delta_- = 176\,\text{MHz}$ and an intracavity amplification factor at this detuning of $\mathcal{A} = 58$, which gives $g_0 = 1.6\,\text{mHz}$ like before. The optomechanically induced losses in this case are of $\Gamma_{opt}(\Delta_-, \Omega_m) \approx -6.15 \times 10^{-6}\,\text{Hz}$, which are still far away from the required $\Gamma_m \approx 0.1\,\text{Hz} - 1\,\text{Hz}$.

At the mechanical frequency $\Omega_m/2\pi = 5\,\text{MHz}$ and $m_{eff} = 5\,\text{mg}$, with once again $g_0 = 5.2\,\text{mHz}$, one finds that the optomechanically induced losses are $\Gamma_{opt}(\Delta_-, \Omega_m) = -1.47 \times 10^{-5}\,\text{Hz}$, far away from the required $\Gamma_m \approx 0.1\,\text{Hz} - 5\,\text{Hz}$.

As these orders of magnitude show, even the use of cryogenic temperature on the thin silver films does not provide sufficient reflectivity in order to achieve mechanical lasing through radiation pressure [Rosenziveig et al., 2020]. Only the use of highly reflective mirrors could provide the required light quantity in order to achieve actuation. Such higly reflective mirrors are mentioned and briefly studied in the future perspectives, section 5.2.

4.2.3/ ELECTROSTRICTION

4.2.3.1/ INTRODUCING THE EFFECT, ESTABLISHING FIELDS EQUATIONS

Electrostriction is a material deformation effect arising from non-linear coupling with the applied electric field. It also gives rise to the Stimulated Brillouin Scattering (see for example [He, 2009] chapter 4, [Boyd, 2008] chapter 9 or [Fabelinskii, 1968] section 34), which is the main source of optomechanical coupling in matter. To get a first though incomplete grasp about electrostriction, we can follow the development given by [Boyd, 2008].

Let us assume a solid in an electric field. The potential energy stored in a solid because of the electromagnetic field is given by[9]:

$$\mathcal{U} = \frac{1}{2}\epsilon_0 \epsilon \mathbf{E}^2 \tag{4.52}$$

where ϵ_0 is the eletric permittivity of the vacuum and ϵ is the relative permittivity. In all of the following, the notation ϵ_r will be simplified to ϵ. The permittivity of the vacuum ϵ_0 will be put every time that it is needed. Any small volume will develop a dipole moment $\delta\mathbf{P} = \epsilon_0 \chi_e \mathbf{E}$ with χ_e the electric susceptibility[10]. In the presence of the electric field, this will cause a force to act on each small volume, proportional to ∇E^2, pushing them towards stronger field regions. This, in turn, causes a deformation of the material on the macroscopic scale, which will change the permittivity by a quantity $\Delta\epsilon$ so that it is now $\epsilon + \Delta\epsilon$. The total potential energy stored in the solid therefore has changed by a quantity

$$\Delta\mathcal{U} = \frac{1}{2}\epsilon_0 \Delta\epsilon \mathbf{E}^2 \tag{4.53}$$

This means work was done on the system, by a force which is called the electrostrictive force.

[9] Eq. 4.52 is true only when the energy of E^2 the electric field and H^2 the magnetic field are equal, which is not true in general for forced solutions of the wave equation.

[10] Note that ϵ and χ_e are related through the definition of the electric displacement $\mathbf{D} = \epsilon_0\mathbf{E} + \mathbf{P} = \epsilon_0\epsilon\mathbf{E} = \epsilon_0(1 + \chi_e)\mathbf{E}$ so that $\chi_e = \epsilon - 1$

4.2.3.2/ COUPLED EQUATIONS

The presence of an electrostrictive force gives rise to an influence on both the mechanical and the electromagnetic fields, which influence one another through the Brillouin scattering. In the next sections, we will see the coupled equations for the mechanical part in section 4.2.3.2.1, followed by the perturbed wave equation in section 4.2.3.2.2.

4.2.3.2.1/ Mechanical equations In the presence of an electric field, if the material is piezoeletric, the piezoelectric (noted pz) stress arises (see section 2):

$$T_{ij}^{pz} = -e_{kij}E_k \tag{4.54}$$

where e_{kij} is the piezoelectric tensor and E_k is the component of the electric field along the k axis.

Because of the presence of the optical field, electrostriction may come to play an important role, as some previous works have thoroughly shown [Rakich et al., 2010] [Laude et al., 2013] [Kharel et al., 2019] [Agarwal et al., 2013]. We therefore now have to account for this force.

Energy conservation arguments (see Royer, Eq. 3.32 [Royer et al., 2000a] or the appendix of Rakich [Rakich et al., 2010]) permit to derive the following relation between the strain and the stress:

$$\frac{\mathrm{d}\mathfrak{E}}{\mathrm{d}S_{ij}} = T_{ij} \tag{4.55}$$

where $\mathfrak{E}$ is the elastic potential energy stored in the solid.

We can therefore write that because of the presence of the electric field and its non-linear coupling with the solid under study, the variation in elastic energy in the solid $\mathrm{d}\mathfrak{E}$ and the variation in electromagnetic field potential energy stored $\mathrm{d}\mathcal{U}$ are taken to be equal, $\mathrm{d}\mathfrak{E} = \mathrm{d}\mathcal{U}$. Eq. 4.53 already established $\mathrm{d}\mathcal{U}$. Therefore, the elastic energy variation is, for an anisotropic solid,

$$\mathrm{d}\mathfrak{E} = \frac{1}{2}\epsilon_0 \Delta\epsilon_{ij} E_i E_j \tag{4.56}$$

with the same definitions as in section 4.2.3.1.

Next, let us find the expression for the variation $\Delta\epsilon$ caused by the deformation of the solid. The canonical relation between the strain and the inverse permittivity is (see for example Nye [Nye, 1984]chapter XIII Eq. 16 or Rouvaen [Rouvaen et al., 1979] Eq. 17)

$$\Delta\epsilon_{ij}^{-1} = z_{ijk}E_k + p_{ijkl}S_{kl} \tag{4.57}$$

where we introduced z_{ijk}, the electro-optic tensor applied to the electric field E_k and p_{ijkl}, the elasto-optic tensor applied to the strain S_{kl} [11], which is dimensionless. We see that the change in the inverse electrical permittivity, or impermittivity, depends on the strain and on the electric field.

The dynamic response of the solid, however, is several orders of magniture slower than the fast-oscillating optical field. The temporal mean value will have to be taken for the electric field. It is reasonable to assume the harmonic behavior of the time dependance

[11] Note that this tensor and its application to the strain is taken in the particular case where no local rotations are considered, therefore ignoring the Nelson and Lax tensor

for the electric field, which leads to consider the mean-value of a sinusoidal function, which is 0. $\langle E \rangle = \int_t E(t)\,\mathrm{d}t = 0$. Furthermore, although the inverse piezoelectric effect will lead to an electric field following the dynamic of S_{kl}, which does not average to 0 in the same way as presented above, it is a second order term [12] because the strain is field-induced (see Eq. 4.62) and is therefore nelected. It is therefore possible to rewrite Eq. 4.57 and simplify it by eliminating the dependence on the electric field:

$$\Delta\epsilon_{ij}^{-1} = p_{ijkl}S_{kl} \tag{4.58}$$

On the other hand, $\epsilon_{ij}\epsilon_{jk}^{-1} = \delta_{ik}$ with δ_{ik} the Kronecker delta, equal to 1 if $i = k$, 0 if not. The derivative of a Kronecker delta (in the distribution sense) is 0, and it is therefore written (see Eq. 8.12 from Royer vol.2 [Royer et al., 2000b])

$$\begin{aligned} \mathrm{d}\left(\epsilon_{ij}\epsilon_{jk}^{-1}\right) &= 0 \\ \Rightarrow \qquad 0 &= \Delta\epsilon_{ij}\epsilon_{jk}^{-1} + \epsilon_{ij}\Delta\epsilon_{jk}^{-1} \qquad (4.59a) \\ \Delta\epsilon_{ij}\epsilon_{jk}^{-1}\epsilon_{kl} &= -\epsilon_{ij}\Delta\epsilon_{jk}^{-1}\epsilon_{kl} \\ \Delta\epsilon_{il} &= -\epsilon_{ij}\Delta\epsilon_{jk}^{-1}\epsilon_{kl} \qquad (4.59b) \end{aligned}$$

Using Eq. 4.58 in Eq. 4.59b we obtain the expression of $\Delta\epsilon_{ij}$:

$$\Delta\epsilon_{ij} = -\epsilon_{il}p_{lkmn}\epsilon_{kj}S_{mn} \tag{4.60}$$

Now it suffices to insert Eq. 4.60 in Eq. 4.56 for the case of a small strain due to electrostriction, noted δS_{ij}^{es}. This reads:

$$\mathrm{d}\mathfrak{E} = -\frac{1}{2}\epsilon_0\epsilon_{il}p_{lkmn}\epsilon_{kj}\delta S_{mn}^{es}E_iE_j \tag{4.61}$$

From this last equation 4.61, we finally derive the stress induced by the electrostriction in the same way as in Eq. 4.55:

$$T_{ij}^{es} = -\frac{1}{2}\epsilon_0\epsilon_{ml}\epsilon_{kn}p_{lkij}E_mE_n \tag{4.62}$$

The radiation pressure can also influence the shape of the solid and generate an interesting actuation method, see [Aspelmeyer et al., 2014a] [Braginskii et al., 1970] [Cohadon et al., 1999] [Bon et al., 2018] (see section 4.2.2). It has been shown that the electromagnetic field exerts a stress on the solid through the radiation pressure (see Eq. 6.120 of [Jackson, 1998] or Eq. 1 of Rakich [Rakich et al., 2010]). This stress reads:

$$T_{ij}^{rp} = D_iE_j - \frac{1}{2}D_iE_j\delta_{ij} + H_iB_j - \frac{1}{2}H_iB_j\delta_{ij} \tag{4.63}$$

where we introduced the magnetic fields B and $H = \mu_0\mu B$ with μ_0 the permeability of the vacuum and μ the relative permeability. Because quartz is non-magnetic, $\mu \approx 1$.

[12] Note that the expression for $\vec{\mathbf{D}}$ should include a term due to the inverse piezoelectric effect, therefore proportional to the strain, $w_{ijk}S_{jk}$ (see for example Royer [Royer et al., 2000a] Eq. 3.86). But because this strain is caused by the field itself here, this last term acting on the electric displacement is of higher order, and we therefore neglect it, see paragraph 2.4, chapter XIII of Nye [Nye, 1984].

Because the system is linear, the total stress acting on the solid is given by the addition of all previous contributions[13]:

$$T_{ij}^{tot} = T_{ij}^{in} + T_{ij}^{pz} + T_{ij}^{es} + T_{ij}^{rp} \tag{4.64}$$

where $T_{ij}^{in} = C_{ijkl}S_{kl}$ (the stress described by the linear elastic response), so that the total volumic force is simply

$$f_i^{tot} = \frac{\partial T_{ij}^{tot}}{\partial x_j} \tag{4.65}$$

4.2.3.2.2/ Electric Field Equations To be able to establish the wave equation for the electric field, we remind Maxwell's equations in a non-magnetic dielectric (See Eqs. 6.6 from Jackson [Jackson, 1998]):

$$\boldsymbol{\nabla}\vec{\mathbf{D}} = 0 \tag{4.66a}$$

$$\boldsymbol{\nabla}\vec{\mathbf{B}} = 0 \tag{4.66b}$$

$$\boldsymbol{\nabla} \times \vec{\mathbf{E}} = -\frac{\partial \vec{\mathbf{B}}}{\partial t} \tag{4.66c}$$

$$\boldsymbol{\nabla} \times \vec{\mathbf{H}} = \frac{\partial \vec{\mathbf{D}}}{\partial t} \tag{4.66d}$$

where, as defined in section 4.2.3.2.1, $\vec{\mathbf{E}}$ is the electric field, $\vec{\mathbf{D}} = \epsilon_0\epsilon\vec{\mathbf{E}}$ is the electric displacement field, $\vec{\mathbf{B}}$ is the magnetic field and $\vec{\mathbf{H}} = \mu_0\mu\vec{\mathbf{H}} \approx \mu_0\vec{\mathbf{H}}$ is the H magnetic field [14]. We omitted from Eqs. 4.66 the terms which are zero in the case of a dielectric, such as the term proportional to the free charges current $\vec{\mathbf{J}}$ or the free charges volumic density ρ_e. Note that ϵ is a tensor which, because of the anisotropy of our medium, lets the electric displacement field be in a slightly different direction than the electric field.

The usual development to find the propagation equation for the electric field is to take the curl of Eq. 4.66a. Doing so yields

$$\begin{aligned}
\boldsymbol{\nabla} \times (\boldsymbol{\nabla} \times \vec{\mathbf{E}}) &= \frac{\partial}{\partial t} \\
&= -\mu_0 \left(\frac{\partial^2 \vec{\mathbf{D}}}{\partial t^2} \right) \\
&= -\frac{1}{\epsilon_0 c^2} \frac{\partial^2 \vec{\mathbf{D}}}{\partial t^2} \\
\boldsymbol{\nabla} \times (\boldsymbol{\nabla} \times \vec{\mathbf{E}}) &= -\frac{1}{c^2} \frac{\partial^2 \epsilon \vec{\mathbf{E}}}{\partial t^2}
\end{aligned} \tag{4.67}$$

where the relation $\epsilon_0\mu_0 = \frac{1}{c^2}$ was used, c being the light velocity in vacuum.

The electric displacement field $\vec{\mathbf{D}}$ accounts for the appeance of dipole moments in matter, notably through the displacement of electric charges. This is described through the

[13] Note that the same result can be obtained through accounting for the different fields through e.g. a Lagrangian method, see [Laude et al., 2015]

[14] Quartz is a non-magnetic material, hence the simplification that the relative magnetic susceptibility is approximately equal to the unit tensor.

relation

$$\vec{\mathbf{D}} = \epsilon_0 \vec{\mathbf{E}} + \vec{\mathbf{P}} \tag{4.68a}$$

$$\vec{\mathbf{D}} = \epsilon_0 \epsilon \vec{\mathbf{E}} \tag{4.68b}$$

$$\Delta\vec{\mathbf{D}} = \Delta\vec{\mathbf{P}} \tag{4.68c}$$

$$\Delta\vec{\mathbf{D}} = \epsilon_0 \Delta\epsilon \vec{\mathbf{E}} \tag{4.68d}$$

where $\vec{\mathbf{P}}$ is the density of permanent and induced dipole moments in the solid.

We have seen from section 4.2.3.2.1 that the dielectric permittivity ϵ was subject to a change under the influence of the electric field and the strain. We can consider a slight change in the dielectric permittivity $\Delta\epsilon$, such that ϵ now becomes $\epsilon + \Delta\epsilon$. This is obviously due to a change in the dipole moment field which we will write $\Delta\vec{\mathbf{P}}$. Indeed, the presence of matter impacts on the total displacement field because of the presence of a polarizability, which gives the difference between the vacuum case and the case inside matter. $\vec{\mathbf{E}}$ is therefore constant so that $\vec{\mathbf{P}}$ is source of variation in Eq. 4.68a. As in section 4.2.3.2.1, any effect on the dielectric permittivity change $\Delta\epsilon$ due to the inverse piezoelectric will be discarded because it was shown that the high (optical) frequency electric field do no contribute to the mechanical actuation (see Eq. 4.57). With this, we therefore write $\Delta\epsilon$ just as we did in Eq. 4.60:

$$\Delta\epsilon_{ij} = \chi_{ijkl}\delta S_{kl} \tag{4.69}$$

where we introduced the tensor $\chi_{ijkl} = \epsilon_{jn} p_{mnkl} \epsilon_{im}$, closely related to the usual definition of the electric susceptibility[15] [16].

Knowing that $\vec{\mathbf{D}}$ will be changed into $\vec{\mathbf{D}} + \Delta\vec{\mathbf{D}}$, and with the expression of $\Delta\vec{\mathbf{D}}$ in Eq. 4.68c, we can insert this into Eq. 4.67 to obtain:

$$\boldsymbol{\nabla} \times (\boldsymbol{\nabla} \times \vec{\mathbf{E}}) = \frac{1}{c^2} \frac{\partial^2 (\epsilon\vec{\mathbf{E}} + \Delta\vec{\mathbf{P}})}{\partial t^2} \tag{4.70}$$

so that we can, in the end, write the anisotropic perturbed wave equation for the electric field:

$$\boldsymbol{\nabla} \times (\boldsymbol{\nabla} \times \vec{\mathbf{E}}) - \frac{1}{c^2} \frac{\partial^2 \epsilon\vec{\mathbf{E}}}{\partial t^2} = \frac{1}{\epsilon_0 c^2} \frac{\partial^2 \Delta\epsilon\vec{\mathbf{E}}}{\partial t^2} \tag{4.71}$$

In the following, however, we will only consider that the incident and diffracted optical fields are sufficiently strong to be unaffected by the acoustic answer, so that the evolution of the electric fields will be ignored.

4.2.3.3/ PHASE-MATCHING CONSIDERATIONS

The electrostrictive force gives rise to the Brillouin scattering, thus permitting further interaction between optics and acoustics (see [Boyd, 2008]). Brillouin scattering, which is a 3 waves interaction, imposes a phase condition on the diffracted light beam and the phonon created in order to be efficient (i.e. stimulated Brillouin scattering), called the

[15] The usual definition of χ in isotropic media relates the polarisation with the electric field, through writing that $\mathbf{P} = \chi\mathbf{E} + \chi^{(2)}\mathbf{E}^2 + \chi^{(3)}\mathbf{E}^3 + \mathcal{O}(E^4)$.

[16] Note that the same χ_{ijkl} tensor is also present in the definition of the stress induced by electrostriction in Eq. 4.62, although is is not explicitly written.

Bragg condition. For the Stokes band, i.e. the diffracted light beam at lower frequency, the phase and energy conservation conditions are written:

$$\vec{\mathbf{k}}_i = \vec{\mathbf{k}}_d + \vec{\mathbf{q}} \tag{4.72a}$$
$$\omega_i = \omega_d + \Omega \tag{4.72b}$$

where k_i and k_d are the incident and diffracted optical beams' wavevector respectively, and q is the acoustic wavevector. ω_i and ω_d are the incident and diffracted beams' frequencies, respectively, and Ω the acoustic frequency.

It can be shown that the most favorable interaction for Brillouin Scattering is the all-colinear backwards interaction, i.e. with the incident and diffracted optical fields with opposite directions, although this type of interaction happens at a high acoustical frequency in general. For quartz, it happens around 12 GHz (see [Kharel et al., 2019] [Renninger et al., 2018]). The forwards interaction, on the other hand, is less favorable (see [Corvo et al., 1988]) but the acoustical frequency is much lower.

A forward interaction is represented with a small angle on Fig. 4.15.

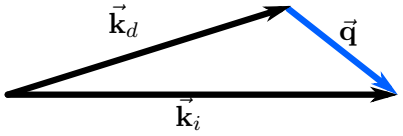

Figure 4.15: *Phase-matching diagram for wavevectors of a Stokes Brillouin interaction. All waves are forward-propagating.*

Chosing a simple plane-wave dispersion relation for the electromagnetic and acoustic waves permits to write the relationships:

$$k_\alpha = \frac{\tilde{n}_\alpha \omega_\alpha}{c} = 2\pi \tilde{n}_\alpha \frac{1}{\lambda_\alpha} \tag{4.73a}$$
$$q = \frac{\Omega}{v} = 2\pi \frac{1}{\Lambda} \tag{4.73b}$$

where v is the acoustic wave's velocity, c is light's velocity in the vacuum, $\tilde{n}_\alpha$ is the refractive index for each wave and λ_α (Λ) are the wavelength of the electromagnetics (acoustic) waves. For a colinear interaction (i.e. $\vec{\mathbf{k}}_i$, $\vec{\mathbf{k}}_\mathbf{d}$ and $\vec{\mathbf{q}}$ all in the same axis) the acoustic wavevector can be obtained from Eqs. 4.72 and 4.73:

$$\begin{aligned} q &= k_i - k_d \\ q &= \frac{\tilde{n}_i \omega_i - \tilde{n}_d \omega_d}{c} \\ \frac{\Omega}{v} &= \frac{\tilde{n}_i(\omega_i - \omega_d) + \Delta\tilde{n}\omega_d}{c} \\ \frac{\Omega}{v} &= \frac{\tilde{n}_i \Omega}{c} + \frac{\Delta\tilde{n}\omega_d}{c} \end{aligned} \tag{4.74}$$

where $\Delta\tilde{n} = \tilde{n}_d - \tilde{n}_i$.

In the case of quartz with an SC cut, with a beam propagating along the x_2 direction (see

Fig. 4.17), the major axis has an index[17]:

$$\tilde{n}_d = \tilde{n}_e - \Delta\tilde{n}\sin^2(\theta) \tag{3.3}$$

which leads to an interaction frequency of:

$$\frac{\Omega}{2\pi} = \frac{v(\tilde{n}_d - \tilde{n}_i)}{\lambda_0} \tag{4.75}$$

which, for a longitudinal A-mode with $V \approx 6000\,\mathrm{m\,s^{-1}}$, $\theta = 33.88°$, $\tilde{n}_0 = 1.5276$, $\tilde{n}_e = 1.5361$ and $\lambda_0 = 1550\,\mathrm{nm}$ gives an acoustical frequency of $\Omega/2\pi \approx 15\,\mathrm{MHz}$.

It is easy to see that if $\Delta\tilde{n} = 0$ in Eq. 4.74, the phase relation cannot be satisfied, as the velocity of the acoustic wave would need to be equal to the incident electromagnetic wave's velocity. This permits to conclude that a change in refractive index between the incident and refracted EM wave has to happen in the colinear forward Stokes interaction in order to take place efficiently.

It can be shown that, given a certain electromagnetic wave's frequency and direction of propagation, at most two (perpendicular) polarizations can exist, which are lying in the plane perpendicular to the propagation axis. These directions are the directions of the minor and the major axis of the plane perpendicular to D intersecting the index ellipsoid (see Fig. 3.1).

It is thereafter obvious that the only possible way for the refractive index to change and satisfy the phase-matching condition of Eq. 4.74 is for the polarization to change, that is, to rotate $90°$ [18]. This is illustrated in Fig. 4.16.

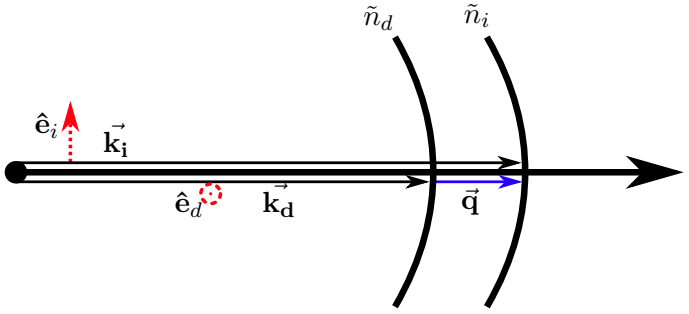

Figure 4.16: *Phase-matching diagram for forward Brillouin Stokes band scattering. The polarizations are represented here with their unit polarization vector $\hat{\mathbf{e}}_i$ and $\hat{\mathbf{e}}_d$ of the incident and diffracted beams. Note that the incident wave should be along the higher index direction in order to achieve a Stokes-band interaction.*

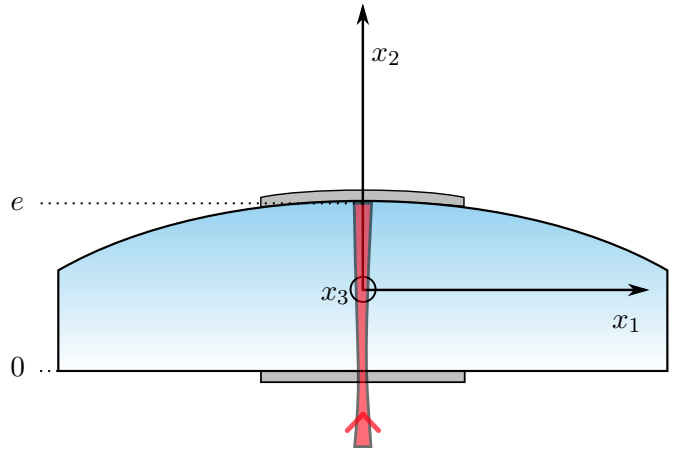

Figure 4.17: *Scheme of the quartz system under study.*

4.2.3.4/ ESTABLISHING THE EQUATIONS

In order to obtain and solve a simplified version of Eq. 4.65, the equation of motion for the mechanical mode, we start by writing the volumic electric field (in the same way as in [Agarwal et al., 2013] or in [Wolff et al., 2015]), taking into account our current situation sketched in Fig. 4.17, with all the implied waves propagating in the $\hat{\mathbf{x}}_2$ direction:

$$D = \sum_{\alpha=i,d} D^\alpha = \hat{\epsilon}^\alpha \tilde{D}^\alpha(x_1, x_3)\phi^\alpha(t)\sin(k_\alpha x_2)\cos(\omega_\alpha t) \tag{4.76}$$

where $\alpha = i, d$ designates the incident and diffracted beam respectively, $\hat{\epsilon}^\alpha$ the polarization unit vector, $\tilde{D}^\alpha$ the transverse spatial profiles for the electric field, ϕ the slowly varying[19] envelopes for the electric and acoustic fields, ω_α the electric frequency, k_α the electromagnetic wavevector.

The electric field's spatial profile verifies the equations:

$$\nabla^2 \tilde{D}^\alpha + \frac{\omega^\alpha}{c^2}\tilde{D}^\alpha = 0 \tag{4.77a}$$

$$\boldsymbol{\nabla} \cdot \tilde{D}^\alpha = 0 \tag{4.77b}$$

Eq. 4.77a represents the fact that the transverse profile verifies as of itself the wave equation and is a stable mode of the wave equation. Eq. 4.77b is one of the Maxwell equations.

As established in Eq. 4.62, the electrostriction induced stress T_{ij}^{es} (see [Nelson, 1982]) is

[17] Indeed, in a non-rotated Y-cut, the major and minor axes correspond to the extraordinary and ordinary indices; for the SC cut, on the other hand, the first rotation is around Z so that no change is made for the refractive index because $n_x = n_y$. But the second rotation is around X, so that with a fixed direction of propagation along x_2, the index decreases from n_e to n_0, see section 3.1.1.

[18] Note that, in general, because any electromagnetic wave in the medium is always decomposed into its two polarizations components, even though a particular component of the diffracted beam may be mathematically allowed to be created by optical and acoustical interactions, it will not in fact be created if the phase-matching condition is not fufiled.

[19] With respect to the optical frequency. The expected order of magnitude for the time variations are of the order of the acoustic frequency Ω

written[20]:

$$T_{ij}^{\text{es}} = -\frac{1}{2\epsilon_0} p_{ijmn} D_m D_n \tag{4.78}$$

so that the total stress applied is written:

$$T_{ij}^{\text{tot}} = c_{ijkl}\frac{\partial u_k}{\partial x_l} + \eta_{ijkl}\frac{\partial^2 u_k}{\partial x_l \partial t} - \frac{1}{2\epsilon_0} p_{ijkl} D_k D_l \tag{4.79}$$

with the losses tensor η_{ijkl}.

so that the perturbed wave equation (Equation Of Motion, EOM) for the acoustic field is written (ignoring the radiation pressure):

$$\rho\ddot{u}_i - c_{ijkl}u_{k,jl} - \eta_{ijkl}\dot{u}_{k,jl} = -\frac{1}{2\epsilon_0} p_{ijmn}(D_m D_n)_{,j} \tag{4.80}$$

This calls for a closer look at the product $D_l D_k$, because only phase-matched elements will be kept (i.e., elements where $\omega_0 - \omega_d = \Omega$). The interesting terms are the crossed terms between the frequencies ω_i and ω_d, so that the frequency difference (hence a priori phase-matched) terms are the only relevant ones:

$$\begin{aligned} D_m D_n &= \tilde{D}^i \tilde{D}^d \varphi^i \varphi^d \sin(k_i x_2)\sin(k_d x_2)\cos(\omega_i t)\cos(\omega_d t) \\ D_m D_n &\approx \tilde{D}^i \tilde{D}^d \varphi^i \varphi^d \frac{1}{4}\cancel{\cos(qx_2)} - \cos\left([k_i + k_d]x_2\right)][\cos(\Omega t) + \cancel{\cos((\omega_i + \omega_d)t)}] \\ &\quad \times \left[\hat{\epsilon}_m^i \hat{\epsilon}_n^d + \hat{\epsilon}_m^d \hat{\epsilon}_n^i\right] \end{aligned} \tag{4.81}$$

where we have striked through and neglected the part that oscillates at the frequency $\omega_i + \omega_d$, as it oscillates too fast for any acoustical response to take place. Furthermore, the part that slowly depends on the position, $\cos(qx_2)$ we also neglected, as it oscillates so much more slowly than the $\cos\left([k_i + k_d]x_2\right) \approx \cos(2kx_2)$ part, so it is practically negligible when considering the derivative of the previous expression (for the equation of motion, see Eq. 4.80).

In order to simplify greatly the problem, which is a priori a 3D problem with all possible components for all possible values, we will start by supposing that the optical beams and their electric fields are not affected by the acoustical dynamics, so that we set the electric enveloppes as constants, normalized to 1 for convenience: $\phi^\alpha = 1$. We will also set the spatial dependence $\tilde{D}$, that will be limited in space but constant within the radius w of the optical beam. That is, $\tilde{D}_i(x_1, x_3) = \tilde{D}$, a constant, for x_1 and $x_3 \in [-\frac{w}{2}, \frac{w}{2}]$ and 0 outside these bounds. It is normalized so that the optical power is

$$P = \frac{\tilde{n}c}{4\epsilon_0}\pi w^2 |D|^2 \tag{4.82}$$

which implies that

$$|D| = \frac{1}{w}\sqrt{\frac{4\epsilon_0 P}{\tilde{n}c\pi}} \tag{4.83}$$

[20] Note that the original equation is given with the electric fields and the permittivities, but because $\epsilon_{ij}E_j = D_i$ at first order, it is possible to express it in the form 4.62

With these assumptions, we are left with the easier expressions for the product $D_m D_n$ and its derivative:

$$D_m D_n \approx \left[\hat{\epsilon}_m^i \hat{\epsilon}_n^d + \hat{\epsilon}_m^d \hat{\epsilon}_n^i\right] \tilde{D}^i \tilde{D}^d \varphi^i \varphi^d \sin(k_i x_2) \sin(k_d x_2) \cos(\Omega t) \tag{4.84}$$

$$(D_m D_n)_{,2} \approx \left[\hat{\epsilon}_m^i \hat{\epsilon}_n^d + \hat{\epsilon}_m^d \hat{\epsilon}_n^i\right] \tilde{D}^i \tilde{D}^d \varphi^i \varphi^d \frac{k}{2} \sin(2kx_2) \cos(\Omega t) \tag{4.85}$$

In order to solve Eq. 4.80, one notes that the only dependency left of the quantities involved is in x_2 (because we have set the spatial dependency of the wavefunction to be a constant in the other directions), so that in the right-hand side of the equation, j is set to be $j = 2$. For the same reason, the left-hand side also needs to have $l = j = 2$.

Because we set the quartz to be in an SC cut, the stiffness, elasto-optic and viscosity tensors have a priori no null element (see Annex A). Therefore, we can deduce that the non-zero elements for the equation of motion in Eq. 4.80 are:

1. on the right hand side of the equation, $j = 2$ so that the non zero elements are:
   - $i = 1$: $p_{61}, p_{62}, p_{63}, p_{64}, p_{65}, p_{66}$
   - $i = 2$: $p_{21}, p_{22}, p_{23}, p_{24}, p_{25}, p_{26}$
   - $i = 3$: $p_{41}, p_{42}, p_{43}, p_{44}, p_{45}, p_{46}$
2. on the left hand side of the equation, $j = k = 2$ so that the non-zero elements are:
   - $i = 1$: C_{66}, C_{62}, C_{64}
   - $i = 2$: C_{26}, C_{22}, C_{24}
   - $i = 3$: C_{46}, C_{42}, C_{44}

We can now write the equations for the three axes. To this end, let us examine the equation for e.g. the first axis x_1:

$$\rho \ddot{u}_1 - \left(\bar{C}_{66} u_{1,22}\right) - \left(\bar{C}_{62} u_{2,22}\right) - \left(\bar{C}_{64} u_{3,22}\right) = \frac{kD^2}{2\epsilon_0} \sin(2kx_2) \cos(\Omega t) \times$$
$$\times \left[\cancel{(\hat{\epsilon}_1^i \hat{\epsilon}_1^d) p_{61}} + \cancel{(\hat{\epsilon}_2^i \hat{\epsilon}_2^d) p_{62}} + \cancel{(\hat{\epsilon}_3^i \hat{\epsilon}_3^d) p_{63}} + \cancel{(\hat{\epsilon}_2^i \hat{\epsilon}_3^d + \hat{\epsilon}_3^i \hat{\epsilon}_2^d) p_{24}} + (\hat{\epsilon}_3^i \hat{\epsilon}_1^d + \hat{\epsilon}_1^i \hat{\epsilon}_3^d) p_{65} + \cancel{(\hat{\epsilon}_2^i \hat{\epsilon}_1^d + \hat{\epsilon}_1^i \hat{\epsilon}_2^d) p_{66}}\right] \tag{4.86}$$

where $\bar{C}_{ij} = (C_{ij} + \eta_{ij} \frac{\partial}{\partial t})$ the modified stiffness that takes into account the losses. Many polarization products have been equated to zero and striked through, as it is impossible for the polarization to be along the same axis as the propagation axis (i.e. along x_2), and it is also impossible to have the same polarization on both the incident and reflected optical wave, see Eq. 4.74.

From these observation, we write the equations for the three axes:

$$\rho \ddot{u}_1 - \bar{C}_{66} u_{1,22} - \bar{C}_{62} u_{2,22} - \bar{C}_{64} u_{3,22} = \frac{kD^2 p_{65}}{2\epsilon_0} \sin(2kx_2) \cos(\Omega t) \times \left[(\hat{\epsilon}_3^i \hat{\epsilon}_1^d + \hat{\epsilon}_1^i \hat{\epsilon}_3^d)\right] \tag{4.87}$$

$$\rho \ddot{u}_2 - \bar{C}_{26} u_{1,22} - \bar{C}_{22} u_{2,22} - \bar{C}_{24} u_{3,22} = \frac{kD^2 p_{25}}{2\epsilon_0} \sin(2kx_2) \cos(\Omega t) \times \left[(\hat{\epsilon}_3^i \hat{\epsilon}_1^d + \hat{\epsilon}_1^i \hat{\epsilon}_3^d)\right] \tag{4.88}$$

$$\rho\ddot{u}_3 - \bar{C}_{46}u_{1,22} - \bar{C}_{42}u_{2,22} - \bar{C}_{44}u_{3,22} = \frac{kD^2p_{45}}{2\epsilon_0}\sin(2kx_2)\cos(\Omega t) \times \left[(\hat{\epsilon}_3^i\hat{\epsilon}_1^d + \hat{\epsilon}_1^i\hat{\epsilon}_3^d)\right] \quad (4.89)$$

From this, it is immediately seeable that all modes along all directions are mixed. The only relevant polarization coupling term here is for the incident optical field to be polarized along the $\hat{\mathbf{x}}_3$ direction, because it is along this direction that the optical refractive index is higher (see Fig. 4.16).

4.2.3.5/ SOLVING THE DISPLACEMENT EQUATION

We will now proceed to solve Eq. 4.88, simplifying the resolution by taking into account only the C_{22} coefficient, as the other coefficients are much smaller (see Annex A). Let us rewrite the equation in the form:

$$u_{,tt} - \bar{z}^2u_{,22} = \frac{kD^2p_{25}}{2\rho\epsilon_0}\sin(2kx_2)\cos(\Omega t) \quad (4.90)$$

where we simplify notations with $u \equiv u_2$, as it is the only relevant displacement, $\bar{z}^2 = z^2 + i\Omega\alpha$ with $z = \sqrt{\frac{C_{22}}{\rho}}$ and $\alpha = \frac{\eta_{22}}{\rho}$.

The situation is very similar to section 4.1.2.2, although this time, the wave-equation is inhomogeneous but the boundary condition is homogeneous. Indeed, without the radiation pressure taken into account, Eq. 4.79 yields 0 in $x_2 = 0$ and $x_2 = e$, at the boundaries. This is because the electric field at the boundaries is zero when at optical resonance, see Eq. 3.15. Here both the incident and diffracted fields are assumed to be at optical resonance, so they are both approximately 0 at the boundaries.

$$\begin{aligned} T_2\begin{pmatrix} e \\ 0 \end{pmatrix} &= 0 \\ \Rightarrow u_{,2}\begin{pmatrix} e \\ 0 \end{pmatrix} &= 0 \end{aligned} \quad (4.91)$$

This situation is simpler than that of section 4.1.2.2, because there is no need to shift the data, as the boundary conditions are homogeneous. In the same manner as Eq. C.4, it is possible to write a condensed version of the system (leaving aside the losses for now):

$$\begin{cases} u_{tt} - z^2u_{,22} = \tilde{\theta}(x_2, t) & (4.92a) \\ u_{,2}(e, t) = 0 & (4.92b) \\ u_{,2}(0, t) = 0 & (4.92c) \end{cases}$$

where

$$\tilde{\theta} = \frac{kD^2p_{25}}{2\rho\epsilon_0}\sin(2kx_2)\cos(\Omega t)$$

The solutions of the freely oscillating wave equation have the same form as in section 4.1.2.2:

$$u_n' = \cos(\beta_n x_2)\cos(\Omega_n t) \quad (C.7a)$$

$$\beta_n = \frac{n\pi}{e} \quad (C.7b)$$

$$\Omega_n = \frac{n\pi z}{e} \quad (C.7c)$$

The solutions to the forced wave equation Eq. 4.92a are found by decomposing its solutions and the forcing term $\tilde{\theta}$ on the (eigen)basis of the freely oscillating wave basis, which has the same form as earlier Eq. C.7:

$$U(x_2) = \sum \lambda_n \cos\left(\frac{n\pi}{e}x_2\right) \tag{4.94a}$$

$$\tilde{\theta} = \sum \tilde{\theta}_n \cos\left(\frac{n\pi}{e}x_2\right) \tag{4.94b}$$

and one obtains the equation for coefficient λ_n by injecting these last two decompositions into Eq. 4.92a:

$$-\Omega^2\lambda_n + \left(\frac{n\pi z}{e}\right)^2 \lambda_n = \tilde{\theta}_n \tag{4.95}$$

where $\tilde{\theta}_n$ can be calculated to be:

$$\tilde{\theta}_n = \frac{kD^2 p_{25}}{2\rho\epsilon_0}\int_0^e \sin(2kx_2)\cos\left(\frac{n\pi}{e}x_2\right)\mathrm{d}x_2 \tag{4.96}$$

$$\tilde{\theta}_n = \frac{k^2e^2D^2p_{25}}{\rho\epsilon_0} \times \frac{\left(\overset{\approx 1}{\cancel{\cos(2ke)}}\cos(n\pi) - 1\right)}{n^2\pi^2 - 4k^2e^2} \tag{4.97}$$

where in the last equation, because we work near resonance, $\cos(2ke) \approx 1$.

Like in section 4.1.2.2, at resonance, only one coefficient of index n_0 is to be taken into account, and it can be calculated to be:

$$\lambda_{n_0}^{\text{res}} = \frac{c^2}{i\alpha\omega_{n_0}^3}\tilde{\theta}_{n_0} \tag{C.10}$$

A numerical application is taken for a 50 nm silver deposition on each side of the quartz at 300 K, with an input power of $P_{\text{out}} = 5\,\text{mW}$ which leads to an optical power inside the quartz of about $P_{\text{in}} = \mathcal{A}P_{\text{out}} \approx 110\,\text{mW}$ with $\mathcal{A} = 22$ defined as in Eq. 3.62 and a beam waist of 73 µm as well as a refractive index of $\tilde{n}_0 = 1.5276$, this leads to an electric displacement field of $D = 8.861 \times 10^{-7}\,\text{C m}^{-2}$. $\rho = 2649\,\text{kg m}^{-3}$, $C_{22} = 11.53 \times 10^{10}\,\text{N m}^{-2}$, $\eta_{22} = 5.978 \times 10^{-4}\,\text{Pa s}$, $p_{25} = -1.84 \times 10^{-3}$, $\Omega/(2\pi) = 15.07\,\text{MHz}$ as established in Eq. 4.75. The coefficient for the displacement of the mode of order $n = 5$ (wich is closest to the calculated value of Ω, see Eq. C.7b) is thus calculated to be on the order of $\lambda_5^{\text{res}} \approx 4.52 \times 10^{-18}\,\text{m}$.

This quantity is obviously extremely small and does not seem, at first glance, to allow for any displacement to be measured. In particular, taking into account that the ideal shot-noise limited detection noise floor in a perfect homodyne detection is calculated to be (see [Briant, 2004], Eq. 1.24) of about $\delta x_{min} \approx 2.9 \times 10^{-18}\,\text{m}/\sqrt{Hz}$, with the true floor of sensitivity even higher, one concludes that the expected several Hz-wide mechanical resonance will not be able to be differentiated from the noise.

There is, however, another descriptive framework with which one may make predictions (see e.g. [Kharel et al., 2019] [Agarwal et al., 2013] [Laude et al., 2015]). In the Hamiltonian description frame, and similarly to the radiation pressure description, a self-oscillating power threshold should be accessible. This is when the effective mechanical

losses (the intrinsic mechanical losses with the electrostrictive-induced) become negative, i.e. an amplification regime is reached, much like with the radiation pressure in section 4.2.2. This effect is not predicted by the current theory and requires to analyze the situation with the Hamiltonian framework.

The second part of this chapter 4 focuses briefly of the optomechanical possibilities with the radiation pressure force and the electrostrictive force.

The main properties have been reminded for the radiation pressure force in cavity optomechanics, in particular with the optomechanically induced damping Γ_{opt} which can be either positive or negative, thus possibly compensating the intrinsic mechanical losses Γ_m to achieve the so-called "mechanical lasing" point. The calculation is then specialized to the case where the mechanical frequency is included within the optical cavity's gain, i.e. $\Omega_m <$ FHWM which is always true for reasonably thin silver films mirrors coatings ($500\,\text{MHz} <$ FWHM $< 1200\,\text{MHz}$) along with interesting frequency range $1\,\text{MHz} < \Omega_m/2\pi < 50\,\text{MHz}$. This allows to establish that the best optomechanically induced damping Γ_{opt} is achieved for a thickness of about $50\,\text{nm}$ due to the dependency of $\Gamma_{opt} \propto \mathcal{A}\mathcal{F}^3$. This means that the optimum is not achieved for the optimum intracavity intensity, but rather for the optimum of the product $\mathcal{A}\mathcal{F}^3$, which is the reason why we took the $50\,\text{nm}$ silver thin film as the reference film throughout this thesis.

We have also given a brief introduction and reminder to the electrostrictive force, which can be of interest for actuation through the Brillouin scattering. We have also derived the equations governing the mechanical actuation with co-propagating beams in order to achieve the lowest frequencies for a SC quartz cut, i.e. around $15\,\text{MHz}$, under a 1D simplification and the assumption that the light fields are sufficiently strong to ignore their amplitude dynamics.

The numerical application of the optical characteristics of the silver thin films to either forces with derived equations shows that the reflectivity of the thin films is not sufficient to actuate the resonator in this configuration. As discussed in section 3.1.3, the absorptivity of the mirrors also impacts negatively the overall expected finesse and intracavity amplification factors, so that this adds negatively to an insufficient maximum reachable reflectivity. This permits to conclude that even by performing a precise-enough measurement, e.g. with a perfect heterodyne detection, we should not be able to detect a mechanical resonance based on optomechanical forces alone.

The possible use of more reflective and less absorptive mirrors arises in this context. This is discussed in the perspective section 5.2 as a possible way to achieve a sufficient optomechanical coupling in order to actuate the quartz resonator, at the expense of worsening the mechanical quality factor of the resonator.

5

CONCLUSION AND PERSPECTIVES

5.1/ CONCLUSION

This thesis work enters into the frame of one of the developped research themes in the Time and Frequency department at FEMTO-ST, namely the study of quartz crystal Bulk Acoustic Wave resonators at cryogenic temperatures and its promising features. Indeed, an extremely high mechanical quality factors as high as a few billion at cryogenic temperature was found for the very best quartz crystal resonators some years ago in our team [Galliou et al., 2013]. We have summed up the reasons why this could lead to an improved frequency stability, and in particular how this would permit to achieve a stability (Allan deviation floor) down to 10^{-16}, provided the environmental sources of unstability are well controlled, with e.g. temperature fluctuations, vibrations, acceleration. Another previous work in our team has shown that there exists a compensated cut for frequency-temperature fluctuations at 4 K [Bon, 2018], which paves the way towards the realization of an ultrastable clock.

In order to do that, we worked with the hypothesis that optomechanical actuation of these quartz crystals could constitute a promising alternative to the usual piezoelectric actuation. Optomechanics is a quite unique and slightly peculiar thematics to our department and we have done an exploratory work.

In particular, we have systematically studied experimentally and theoretically the absorptive Fabry-Perot cavities that a typical quartz resonator coated with metallic thin-films readily constitutes. The absorptivity of these coatings brings several effects specific features, especially the frequency shift between the reflection and absorption peaks and the broadened FWHM. We have developed an original method that takes advantage of these particular effects of the apsorbtive Fabry-Perot cavity in order to extract the thin films refractive index. We have successfully confronted it to existing litterature, giving reasonable confidence in its accuracy.

We have also studied both experimentally and theoretically the photothermal actuation of the quartz crystal. From the knowledge of the refractive index and optical properties of the thin-films Fabry-Perot cavities, we have been able to study theoretically the possibility to actuate optomechanically the quartz, either through radiation pressure or electrostriction. With the limited reflectivity offered by the thin-film mirrors, we have established that it does not seem possible, in this configuration, to obtain optomechanical actuation of the quartz crystal resonator.

We have mentioned, however, as a possible future perspective, how other geometries

could offer this possibility, and in particular with the use of super mirrors at the cost of reducing the mechanical quality factor of the quartz.

There are several points that require further study and some question left unanswered, mainly due to a lack of time. In particular, two main axes are left with unanswered questions: photothermal excitation and optomechanical excitation.

Unfortunately, the study of photothermal excitation had to be simplified in order to make theoretical predictions within the available time. This means that we have chosen to simplify the problem to a 1D problem, both thermal-wise and mechanics-wise. Although we have shown that this is fairly accurate at room temperature, it is not anymore at cryogenic temperature. This might explain the discrepancies between the displacement levels which are predicted to be smaller at cryogenic temperature. This is both counterintuitive with the known mechanical constants values and inaccurate experimentally. Furthermore, the question of signal levels at optical resonance would need to be clarified through some further experimental and theoretical work. Indeed, as pointed out in section 4.1.3.3.2, the frequency shift indicates a temperature elevation which is compatible with the announced intracavity amplification factor. The measured signal level, however, is not compatible with this elevation. Further study is required over this part, possibly involving more sophisticated 3D resolution of the problem, or even Finite Element Methods softwares.

The other main point is that the optomechanical actuation has not been measured, though it has been predicted to be too small. In order to measure the smallest possible displacements, we consider an optical readout, such as heterodyne detection (see Annex E) which was unfortunately not implemented due to a lack of time. The Hamiltonian framework for the electrostrictive force is known to provide a threshold power, over which a self-oscillating “mechanical lasing” phenomenon is known to arise. This is not predicted by the continuum physics framework, which, so far, does not include the radiation pressure force in the treatment of the boundary conditions due to a lack of time. Further study is therefore required to analyze the difference in physical predictions that the Hamiltonian framework might bring.

Regardless, this thesis work has several upsides to it. In particular, to the best of our knowledge, there never has been before a systematic measurement campaign to confirm the exactitude of Monzón theoretical framework [Monzón et al., 1996]. We performed this systematic measurement campaign with several metallic films at different thicknesses, both at room and cryogenic temperature to observe the difference. From this, we have been able to extract a refractive index from an original numerical method that we developed and gave rise to an article ([Rosenziveig et al., 2021], to be published) which, when compared to the (scarce) litterature, stands as reasonably agreeing (see section 3.2.3). We have been able to confirm the validity of this descriptive frame through our measurement campaign.

Another main point to this thesis work has been to demonstrate the feasability of photothermal excitation for the quartz crystal resonators, taken out of the box. To the best of our knowledge, although it had been previously demonstrated that this excitation was possible, it had only been shown for rather low frequencies (up to $1\,\mathrm{MHz}$ [Dieulesaint et al., 1982]). We have demonstrated that the excitation works even to rather high frequencies, up to $15\,\mathrm{MHz}$ at $4\,\mathrm{K}$ although with weak signal at higher frequencies (possibly due to the AOM bandwidth, see section 4.1.3). What’s more, we also demonstrated experimentally that the excitation works better at cryogenic temperature, which had also not been done before, inspite of the fact that we lack a proper theoretical frame-

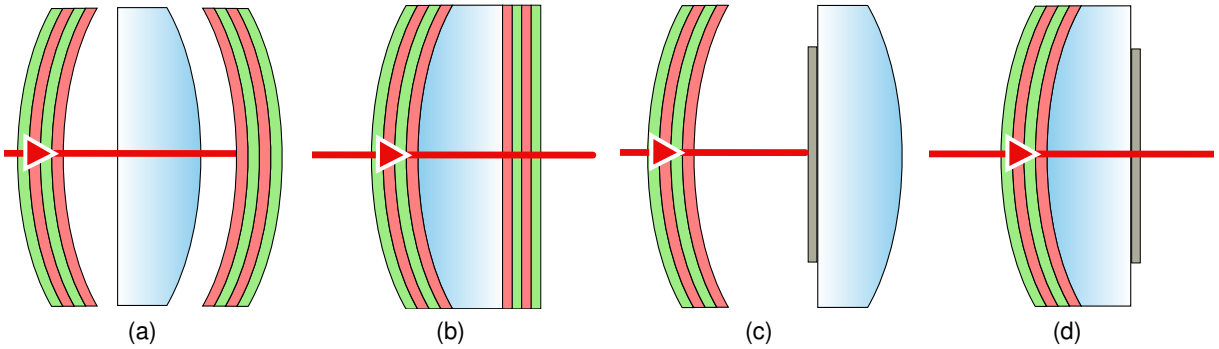

Figure 5.1: *Fig. 5.1a: 2 super mirrors are decoupled from the resonator, like in [Kharel et al., 2019]. This has the advantage of allowing the maximum mechanical Q factor, though only electrostriction is accessible this way. Fig. 5.1b: 2 super mirrors are deposited right on the resonator. This has the advantage of allowing both electrostriction and radiation pressure, but dramatically decreases the Q factor. Fig. 5.1c: 1 super mirror is decoupled from the resonator, which is deposited with one metal electrode. This allows for a rather high Q, and both the photo-thermal effect as well as radiation pressure. Fig. 5.1d: 1 super mirror is deposited on the quartz, as well as a metal electrode. All three forces are achievable this way, though the Q is diminished.*

work to properly describe the results.

Lastly, although we did not demonstrate experimentally the lack of resonance, we have demonstrated that the optomechanical actuation is unlikely for the quartz resonators coated with metallic thin films, due to the poor reflectivity properties as well as the absorption of the thin metallic layers coating, even at cryogenic temperature which has been shown to improve the optical qualities of metals. This permits to discard optomechanical actuation as an easy and likely candidate to replace piezoelectric actuation in a typical quartz crystal resonator with typical geometry.

5.2/ PERSPECTIVE: OTHER POSSIBLE GEOMETRIES

A possible perspective for the future of the experiment is to change the geometry of the quartz and accompanying mirrors, both in their nature and exact placing. Throughout this section, we consider other such geometries in order to assess the feasability of optomechanical coupling. By changing the nature of the mirror (silver, super-mirror with dielectric layers) and its position (input side, output side) the forces, coupling rate and expected displacements are affected. Four main possibilities are considered in this section, which are visually summed up in Fig. 5.1. Table 5.1 also sums up their main characteristics with the acting forces, the expected mechanical quality factor losss, the expected optical finesse, and whereas an actuation is possible.

Note that in all of these options, the input mirror is always a super-mirror, indicating that its absorption is of the order of some ppm.

5.2.1/ OPTION 5.1A

In this geometry, which is the solution used in [Kharel et al., 2019], both mirrors are decoupled from the quartz resonator and are held at a distance. The thermal absorption of the quartz at telecom wavelength is extremely small thus leading to almost no thermal excitation (see section 4.1). Likewise, because of the quartz faces display very small reflectivity, the radiation pressure is too small to be considered. The only acting force is therefore the electrostrictive force.

The remote mirrors present the obvious advantage to provide a contactless Fabry-Perot cavity, which is not solidary to the resonator, thus avoiding the deposition mechanical losses. Throughout this section Q_0 is the maximum (bare quartz) mechanical quality factor and Q the quality factor in the present geometry. Avoiding to deposit extra layers directly onto the quartz translates into $Q/Q_0 = 1$.

Envisioning the use of super mirrors 10CV00SR.70F from Newport, with a reflectivity $R > 99.97\%$, this would lead to a minimum finesse of $\mathcal{F} \approx 10400$ (see Eq. 3.25). The provider even claims finesse exceeding 30000, which we will therefore take as the reference finesse. Using Eq. 3.29, the intracavity amplification factor $\mathcal{A} \approx 38200$. Applying this new amplification coefficient to the previously calculated order of magnitude for the displacement in section 4.2.3.5 (see Eq. C.10), one predicts a displacement coefficient $\lambda_5^{res} \approx 7.86 \times 10^{-15}$ m. This is very small, although the ideal theoretical shot-noise limit in a perfect homodyne detection (see [Briant, 2004]) predicts a displacement detection limit at $2.9 \times 10^{-20}\,\mathrm{m}/\sqrt{Hz}$.

5.2.2/ OPTION 5.1B

In this geometry, two super-mirrors are deposited right on the quartz resonator, much like the typical quartz resonator geometry: the common electrodes are replaced with a succession of dielectric layers permitting to obtain a super-mirror. It has the obvious advantage of achieving very high finesse (thus amplification factor $\mathcal{A}$), much higher than in the thin metallic deposition geometry studied throughout this thesis. Furthermore, with respect to option 5.1a, here both electrostriction and radiation pressure are a priori achievable, although it is possible they might work against one another (see [Rakich et al., 2010]). On the other hand, main inconvients include the difficulty of the deposition process leading to high costs and an incapacity to process the deposition in the local clean room without a substantial work, far exceeding the reach of this PhD. More importantly, a major topic in the high-reflectivity coatings is to be able to reduce the thermal noise and thus the mechanical losses, in particular towards the improvement of gravitational wave detectors (see [Cole, 2012] [Vajente et al., 2021] [Harry et al., 2002]). This solution is counterproductive in terms of mechanical resonance effect. Indeed the dielectric layers constituting the mirrors also have an impact on the mechanical losses of the resonator as discussed in section 1.3.2, even more so than metallic depositions (see [Galliou et al., 2016c]).

Several different types of depositions can be considered, leading to different results for both the mechanical and optical characteristics. We will study in more details some options in this section.

5.2.2.1/ Ta_2O_5/SiO_2

In some previous works [Galliou et al., 2016c] [Galliou et al., 2016a], it has been established that the deposited layers of Ta_2O_5/SiO_2 hinders the mechanical resonance and adds mechanical losses to the intrinsical resonator losses. The order of magnitude of the losses that the coating induces is estimated, at cryogenic liquid helium temperatures, to be of $\frac{1}{Q_{\text{coating}}} \approx 1.6 \times 10^{-5}$, generally much larger than the intrinsic losses for good resonators (some 10^{-8}). This leads to a mechanical quality factor reduction of about 10^3.

They also displayed a reflectance of about $R = 99.99\%$, leading to a finesse of about $\mathcal{F} \approx 31000$. Using once again Eq. 3.29, this gives an intracavity amplification factor of about $\mathcal{A} \approx 40000$.

Leading again the same calculation as before for the electrostrictive force leads to the similar result $\lambda_5^{\text{res}} \approx 8.23 \times 10^{-15}$ m and to the similar conclusion that this small but can theoretically be detected, as the finesse of the cavity is very high in this case and allows for a shot-noise theoretical detection limit of around $\delta x_{min} \approx 2.9 \times 10^{-20}\,\text{m}/\sqrt{Hz}$. Inserting the numbers in Eq. 4.45b permits to establish that with an input laser power of 5 mW, then $\Gamma_{opt} \approx 535$ Hz for a $\Omega_m = \Delta\omega = 2\pi \times 5$ MHz mechanical resonance frequency and detuning from optical resonance. This value of optomechanically induced losses is much larger than the typical mechanical peak's width at 5 MHz: considering a good resonator with $Q = 1 \times 10^7$, this leads to a FWHM of about FWHM ≈ 0.5 Hz $\ll \Gamma_{opt}$, i.e. the optomechanical actuation with the radiation pressure is predicted to be accessible in this configuration for this frequency. The same calculation at 50 MHz leads to a $\Gamma_{opt}^{max} \approx 529$ Hz, which is still much larger than the typical mechanical peak's width of around 0.5 Hz for a quality factor $Q = 1 \times 10^8$.

We conclude that the optomechanical actuation is possible through the radiation pressure with this configuration, and, again, through the developed theoretical description, does seem reachable through electrostriction. It is, however, highly damageable to the mechanical resonance, leading to a mechanical quality factor reduction of around $100 - 1000$.

5.2.2.2/ GaAs/AlGaAs

A promising solution would consist in alterning layers of GaAs/AlGaAs, with a separate epitaxial growing of the layers, followed by a removal of the layers from the substrate and a final bonding to the host substrate as described in [Cole et al., 2013]. The mechanical losses for such layers has been measured to provide an improvement with previously available types of coating of about a factor 10 (see [Cole et al., 2013]), which reaches a value of $\frac{1}{Q_{\text{coating}}} \approx 10^{-5}$ (see [Penn et al., 2019]) [1] . This lead, once again, to a mechanical quality factor reduction of about 10^{-3} (assuming the reference 10^{-8} intrinsic mechanical losses for the bare resonator).

The optical properties of these substrates are shown to yield, in the infrared region, extremely low absorption and very high reflectivities, leading to a finesse of up to

[1] Note that this value has in fact been found for rather low frequencies, in the Hz to kHz range because of its gravitational wave detection use. Although we lack data in the interestin MHz frequency range, we extrapolate the result on the basis that the total coating losses do not seem to vary significantly over a large frequency range, e.g. over 5 decades in [Crooks et al., 2004].

$\mathcal{F} = 3 \times 10^5$ (see [Cole et al., 2016]) amounting to a reflectivity of around 99.998%[2] and thus an amplification factor of $\mathcal{A} \approx 3.8 \times 10^5$.

We can once again use Eq. C.10 to calculate $\lambda_5^{\text{res}} \approx 7.8 \times 10^{-14}\,\text{m}$ for the electrostrictive force, once again a small a result that can theoretically be detected, with an ideal shot-noise limited detection floor of about $\delta x_{min} \approx 2.9 \times 10^{-21}\,\text{m}/\sqrt{Hz}$. On the other hand, calculating from Eq. 4.45b establishes a $\Gamma_{opt} \approx 9.8 \times 10^5\,\text{Hz}$ for $P_{\text{in}} = 5\,\text{mW}$ and $\Omega_m = 2\pi \times 5\,\text{MHz}$. This is more than sufficient to actuate the quartz throuh radiation pressure with its typical FWHM $\approx 0.5\,\text{Hz} \ll \Gamma_{opt}$.

Similarly to the Ta_2O_5/SiO_2 deposition, we conclude that the optomechanical actuation is once again possible through radiation pressure, and that the electrostriction is calculated to provide weak though sufficient actuation to be observed through appropriate measurement means.

5.2.2.3/ aSi/SiN

A previous work has also shown that layers of aSi/SiN (amorphous silicium) is also a good candidate in order to reduce the existing thermal noise on gravitational wave detectors (see [Steinlechner et al., 2018]). Furthermore, the deposition relies on the intervention of a commercial entity, Tafelmaier Dünnschicht Technik GmbH which could easily provide its service and is therefore easily accessible for consideration without further technical developments.

Although the aim functioning is for a $2\,\mu\text{m}$, the $1550\,\text{nm}$ regime is still attractive for the mechanical losses, given a 22 alterning stacks. The total mechanical losses in this case is close to $\frac{1}{Q_{\text{coating}}} \approx 10^{-5}$ in the cryogenic temperature range (at $20\,\text{K}$). This is once again bringing a factor $\approx 10^{-3}$ onto the bare resonator mechanical quality factor (assuming 10^{-8} intrinsic mechanical losses).

These mechanical properties accompany a reflectivity of $R = 99.997\%$ with very low optical absorption (< 27ppm), which gives an optical finesse of $\mathcal{F} = 105000$ (see Eq. 3.25) and an amplification factor of about $\mathcal{A} = 1.3 \times 10^5$.

Following the same type of calculation as earlier, one calculates that for electrostriction, $\lambda_5^{\text{res}} \approx 2.6 \times 10^{-14}\,\text{m}$, which too small but is possible to be observed through the same calculation as in section 5.2.2.1. The optomechanically induced damping, however, is of about $\Gamma_{opt} \approx 2.1 \times 10^4\,\text{Hz}$, which is sufficient to obtain mechanical lasing, as calculated earlier with FWHM $\approx 0.5\,\text{Hz} \ll \Gamma_{opt}$.

We conclude that this deposition too permits to obtain actuation through the radiation pressure force, with a reduced efficacy with respect to the previously discussed deposition of section 5.2.2.2. It is, however, bringing about a similar losses to the mechanical quality factor of the quartz resonator, by a factor ≈ 1000.

5.2.3/ Option 5.1c

In this geometry, one super-mirror is detached from the quartz resonator, and facing a thin metallic mirror deposited on the quartz. This has the advantage to limit the me-

[2] Inverting Eq. 3.25 with no losses, one can find the reflectivity from the finesse to be approximately $R \approx (1 - \frac{\pi}{2\mathcal{F}})^2$

chanical quality factor losses with respect to the all super-mirror solution, as shown in [Galliou et al., 2016a], and is better than doing the opposite geometry around. It has been estimated that coating with chromium and gold (at cryogenic temperatures) worsens the (uncoated) mechanical quality factor by about a factor 10 (see [Galliou et al., 2016a]). The coating with silver, with far thinner electrodes than the the typical chromium + gold electrodes ($\approx 200\,\mathrm{nm}$ thickness) is assumed to give a similar result.

Furthermore, both the radiation pressure and photothermal effects are achievable, although the optical finesse in this case is rather low. Indeed, the maximal achievable reflectivity with the silver deposition is of about $R_m = 98.7\%$ (for a $50\,\mathrm{nm}$ silver layer, with index from [Ciesielski et al., 2017]), along with a super-mirror (e.g. the 10CV00SR.70F from Newport) with reflectivity of about $R_{sm} = 99.97\%$, which yields a finesse of around $\mathcal{F} \approx 450$. This is much lower than for two super-mirrors as in option 5.1b. An amplification factor of about $\mathcal{A} \approx 560$ is predicted from this.

One can therefore lead the same calculations as for the other options, for the radiation pressure force and calculate that, for an incoming $P_{\mathrm{in}} = 5\,\mathrm{mW}$, the optomechanically induced damping $\Gamma_{opt} \approx 3.1 \times 10^{-3}\,\mathrm{Hz}$ at $\Omega_m = 2\pi \times 5\,\mathrm{MHz}$. This is insufficient to actuate the resonator, assuming a mechanical quality factor of about $Q = 10^8$.

On the other hand, one can expect quite a dramatic effect from the photothermal excitation. Indeed, as section 4.1.3 has shown, even without optical resonance, the effects of photothermal excitation are visible with an input laser of some mW income power. The operation in the optical resonance regime was shown to improve the signal (see section 4.1.3.3.2), with a (theoretical) amplification factor of about $\mathcal{A} = 20$. An operation with $\mathcal{A} = 560$ should provide an even more easily observable signal, although it is hard to predict how much more visible (see the theory/experiment discrepencies in section 4.1.3.3.2).

We conclude that the performances are clearly limited by the worst mirror, i.e. the metallic mirror in this case. Although optomechanical actuation is not expected, it should be possible to obtain an improved photothermal excitation (with respect to the situation described in section 4.1.3.1).

5.2.4/ OPTION 5.1D

In this geometry, which is very similar to option 5.1c, a metallic mirror and a super-mirror are both deposited onto the quartz. The main advantage of this option is to provide a possibility for all the different forces studied thus far to act upon it, although it is clear from the previous results that this possibility will not be filled by theoretical predictions.

One can expect a similar reflectivity of both mirrors with respect to the previously discussed solution 5.1c, namely $R_m \approx 98.7\%$ for the silver ($50\,\mathrm{nm}$ layer) mirror and $R_{sm} \approx 99.998\%$ (see section 5.2.2.2). This leads to a similar result of $\mathcal{F} \approx 480$ and an intracavity amplification factor of $\mathcal{A} \approx 610$, which is slightly better than the previous configuration.

We chose to evaluate the best possible dielectric coating, namely the GaAs/AlGaAs so that the mechanical losses are comparable to those that are expected within the framework discussed in section 5.2.2.2 (see [Penn et al., 2019]), with a factor 10^{-3} with respect to the reference quality factor $Q \approx 10^8$.

We therefore get to the orders of magnitude for the electrostriction which are similarly small, i.e. with an input power of 5 mW, one finds that $\lambda_5^{res} \approx 1.2 \times 10^{-16}$ m, which is small but could theoretically be observed, with a similar calculation as before leading to a detection floor of about $\delta x_{min} \approx 1.44 \times 10^{-18}\,\mathrm{m}/\sqrt{Hz}$. Once again, leading the calculation for the radiation pressure force yields a $\Gamma_{opt} \approx 4.1 \times 10^{-3}$ Hz at $\Omega_m = 2\pi \times 5$ MHz, which is smaller than the reference $\Gamma_m \approx 0.5$ Hz. One therefore concludes that the radiation pressure force is too weak in enough in order to actuate the quartz, but the electrostrictive force gives a very weak actuation which could be accessible in ideal homodyne detection conditions.

The photothermal force, however, is again expected to actuate the quartz in a measurable way, as the intracavity power is once again much higher than the experimental (optically non-resonant) case discussed in section 4.1.3.

5.2.5/ DISCUSSION

	$\mathcal{F}$	Q/Q_0	forces	actuation? (which force?)
5.1a	30000	1	ES	yes, ES
5.1b	$3 \times 10^4 - 3 \times 10^5$	10^{-3}	ES, RP	yes, RP, ES
5.1c	450	10^{-1}	RP, PT	yes, PT
5.1d	480	10^{-3}	RP, ES, PT	yes, PT, ES

Table 5.1: *Other possible geometries, and their different optical and mechanical characteristics. Q/Q_0 is the mechanical quality factor divided by the maximum (bare quartz) quality factor Q_0 ($\approx 10^8$). ES stands for electrostriction, RP for radiation pressure and PT for photothermal.*

We have have studied four main alternative geometries, each one presenting its advantages and inconvenients for actuating the quartz resonator. Some of their main characteristics are summed up in table 5.1.

Unfortunately, there is no clear-cut criteria to improve all the forces coupling at once. Indeed, absorption of the mirrors is damageable to radiation pressure and electrostriction though it is desirable for photothermal actuation, and so forth. Because the horizon goal of this thesis is to conceive the actuation means towards an ultrastable oscillator, preserving the mechanical Q factor is of primary importance (see section 1.3 for details). For this reason, the main classification tool that we use will therefore be that the lesser the mechanical attenuation, the better the actuation scheme.

In this regard, the solution 5.1a is undoubtedly the best among the four studied options. Indeed, it allows for an all-contactless actuation and readout, as described in [Kharel et al., 2019]. Some technicalities should be taken into careful consideration, such as properly aligning the quartz in order to insert it inside an external Fabry-Perot cavity while keeping coupling, as well as minding its exact position within the latter in order not to nullify the coupling (see details in [Kharel et al., 2019]). The contactless (i.e. no layer is deposited directly onto the quartz resonator) actuation allows for a preservation of the mechanical Q factor. One might therefore simply tune at will the reflectivity and absorptivity of the external supermirrors without worrying oneself with direct consequence on the mechanical qualities of the resonator.

The next solution which least dampens the mechanical Q factor is the option 5.1c, with a single deposition of a thin silver film onto the quartz. As a previous study shows [Galliou et al., 2016a], the metallic thin layers tend to dampen the Q factor less than the dielectric layers. Here, only the photothermal force is available, which should be enough to actuate the quartz resonator, much in the same way as section 4.1. Indeed, the situation is similar if no optical resonance is cast [3]. If the laser is tuned to be optically resonant, on the other hand, the amplification factor is even slighly better than in section 4.1 so that photothermal excitation should be readily accessible. It might even be advantageous to use another metal than silver, such as chromium which is less reflective than silver, thus ultimately allowing more light to be absorbed along the path within the thin film.

The other two solutions have relatively similar mechanical dampening, so that they are not clearly classifiable. However, solution 5.1d might be preferable in that photothermal actuation has been demonstrated to be easily and readily accessible, as well as to provide a displacement which is about 7 orders of magnitude larger than the electrostrictive scheme. This makes it easier to detect and easier to implement. It is also possible to leave out the dielectric supermirror altogether in solution 5.1d in order to decrease the damping, making it effectively similar to option 5.1c Q factor-wise (at the cost of being able to use optical cavity amplification of light). This is not possible with option 5.1b, as both mirrors are required to achieve cavity amplification of the optomechanical forces.

It is worth noting that the mechanical damping of the dielectric layers in all the solutions including dielectric layers have been estimated for a very high reflectivity of about 99.99%, which corresponds to a large number of alterning layers of materials ($15 - 30$ depending on the chosen material solution). Specifically, the number of layers is larger than necessary. As briefly discussed in some previous work [Rosenziveig et al., 2020], achieving a finesse of about $\mathcal{F} = 3000$ (with non-absorptive dielectric supermirrors) would allow to overcome the intrinsic mechanical losses of $\Gamma_m 0.1\,\text{Hz} - 1\,\text{Hz}$. This finesse is a factor $10 - 100$ lower than the finesse achieved with the dielectric supermirrors discussed in this section. This means that the number of necessary dielectric layers could be divided by a factor, thus allowing to decrease the mechanical damping. The latter decrease, however, is expected to be only relatively small and would therefore constitute a tradeof discussion.

[3] Provided that the laser is incident from the opposite side than that drawn on the scheme. Indeed, if the laser is tuned out of optical resonance, the light will hardly enter the cavity if incident on the supermirror.

A

TENSORS FOR QUARTZ CRYSTAL

Here are listed some quantities for quartz crystal which are of use:

$$C = \begin{pmatrix} 8.68 & 0.704 & 1.19 & -1.804 & 0 & 0 \\ 0.704 & 8.68 & 1.19 & 1.804 & 0 & 0 \\ 1.19 & 1.19 & 10.58 & 0 & 0 & 0 \\ -1.804 & 1.804 & 0 & 5.82 & 0 & 0 \\ 0 & 0 & 0 & 0 & 5.82 & -1.804 \\ 0 & 0 & 0 & 0 & -1.804 & 3.988 \end{pmatrix} \quad (\times 10^{10}\ \mathrm{N\,m^{-2}}) \qquad \text{(A.1)}$$

The values from [Tichý et al., 2010] are used here for the stiffness of quartz.

$$C_{4K} = \begin{pmatrix} 8.765 & 0.942 & 1.280 & -1.783 & 0 & 0 \\ 0.942 & 8.765 & 1.280 & 1.783 & 0 & 0 \\ 1.280 & 1.280 & 10.765 & 0 & 0 & 0 \\ -1.783 & 1.783 & 0 & 5.960 & 0 & 0 \\ 0 & 0 & 0 & 0 & 5.960 & -1.783 \\ 0 & 0 & 0 & 0 & -1.783 & 3.988 \end{pmatrix} \quad (\times 10^{10}\ \mathrm{N\,m^{-2}}) \qquad \text{(A.2)}$$

The values from [Tarumi et al., 2007] are used here for the cryogenic stiffness of quartz.

$$C^{\mathrm{SC}} = \begin{pmatrix} 8.680 & 0.207 & 1.686 & -0.039 & -1.380 & -0.927 \\ 0.207 & 11.53 & -0.426 & 0.883 & 0.093 & 1.917 \\ 1.686 & -0.426 & 10.95 & 0.261 & 1.287 & -0.989 \\ -0.039 & 0.883 & 0.261 & 4.204 & -0.989 & 0.093 \\ -1.381 & 0.093 & 1.287 & -0.989 & 5.897 & 0.581 \\ -0.927 & 1.917 & -0.989 & 0.093 & 0.583 & 3.910 \end{pmatrix} \quad (\times 10^{10}\ \mathrm{N\,m^{-2}}) \qquad \text{(A.3)}$$

Calculated with a python routine from the values taken from [Tichý et al., 2010].

$$C^{\mathrm{SC}}_{4K} = \begin{pmatrix} 8.765 & 0.407 & 1.814 & -0.105 & -1.364 & -0.916 \\ 0.407 & 11.74 & -0.433 & 0.948 & 0.092 & 1.894 \\ 1.814 & -0.433 & 11.21 & 0.238 & 1.272 & -0.978 \\ -0.105 & 0.948 & 0.238 & 4.246 & -0.978 & 0.092 \\ -1.364 & 0.092 & 1.272 & -0.978 & 5.962 & 0.686 \\ -0.916 & 1.894 & -0.978 & 0.092 & 0.686 & 3.908 \end{pmatrix} \quad (\times 10^{10}\ \mathrm{N\,m^{-2}}) \qquad \text{(A.4)}$$

Calculated with a python routine from the values taken from [Tarumi et al., 2007].

$$\alpha = \begin{pmatrix} 13.672 & 0 & 0 \\ 0 & 13.672 & 0 \\ 0 & 0 & 7.508 \end{pmatrix} \quad (\times 10^{-6}\ \mathrm{K}^{-1}) \tag{A.5}$$

The values from [Kosinski et al., 1991] are used here for the thermal expansion.

$$\alpha_{5K} = \begin{pmatrix} 1.8 & 0 & 0 \\ 0 & 1.8 & 0 \\ 0 & 0 & -1.6 \end{pmatrix} \quad (\times 10^{-9}\ \mathrm{K}^{-1}) \tag{A.6}$$

The cryogenic thermal expansion coefficients the values from [Barron et al., 1982] are used here (note that only values for 5 K are available, which we will assimilate to values at 4 K throughout).

$$\beta^{\mathrm{SC}} = \begin{pmatrix} 1.37 & 0 & 0 \\ 0 & 1.29 & -0.117 \\ 0 & -0.117 & 1.19 \end{pmatrix} \quad (\times 10^{-6}\ \mathrm{N\,m^{-2}\,K^{-1}}) \tag{A.7}$$

The thermo-acoustical coefficients are calculated with a python routine from the values taken from [Tichý et al., 2010] for the C_{ijkl} and from [Kosinski et al., 1991] for the α_{ij}.

$$\beta^{\mathrm{SC}}_{4K} = \begin{pmatrix} 154.24 & 7.60 & 0 \\ 0 & 67.10 & -129.77 \\ 0 & -129.77 & -39.02 \end{pmatrix} \quad (\mathrm{N\,m^{-2}\,K^{-1}}) \tag{A.8}$$

The thermo-acoustical coefficients calculated with a python routine from the values taken from [Tarumi et al., 2007] for the C_{ijkl} and from [Barron et al., 1982] for the α_{ij}.

$$K = \begin{pmatrix} 6.4895 & 0 & 0 \\ 0 & 6.4895 & 0 \\ 0 & 0 & 13.942 \end{pmatrix} \quad (\mathrm{W\,m^{-1}\,K^{-1}}) \tag{A.9}$$

The values from [Kanamori et al., 1968] are used here for the thermal conductivity.

$$K_{4K} = \begin{pmatrix} 150 & 0 & 0 \\ 0 & 150 & 0 \\ 0 & 0 & 300 \end{pmatrix} \quad (\mathrm{W\,m^{-1}\,K^{-1}}) \tag{A.10}$$

The values from [Hofacker et al., 1981][1] are used here for the cryogenic thermal conductivity.

$$K^{\mathrm{SC}} = \begin{pmatrix} 6.489 & 0 & 0 \\ 0 & 8.805 & 3.449 \\ 0 & 3.449 & 11.626 \end{pmatrix} \quad (\mathrm{W\,m^{-1}\,K^{-1}}) \tag{A.11}$$

The thermal conductivity coefficients in the SC cut are calculated with a pyton routine from the values taken from [Kanamori et al., 1968].

[1] Only the K_3 value is available in the reference, so that we extrapolated the results from [Kanamori et al., 1968] and took K_1 to be half of the K_3 value.

$$K_{4K}^{\mathrm{SC}} = \begin{pmatrix} 150 & 0 & 0 \\ 0 & 196 & 69 \\ 0 & 69 & 253 \end{pmatrix} \quad (\mathrm{W\,m^{-1}\,K^{-1}}) \tag{A.12}$$

The cryogenic thermal conductivity coefficients in the SC cut are calculated with a python routine from the values taken from [Hofacker et al., 1981][1].

B

PICTURES OF THE DEVICE

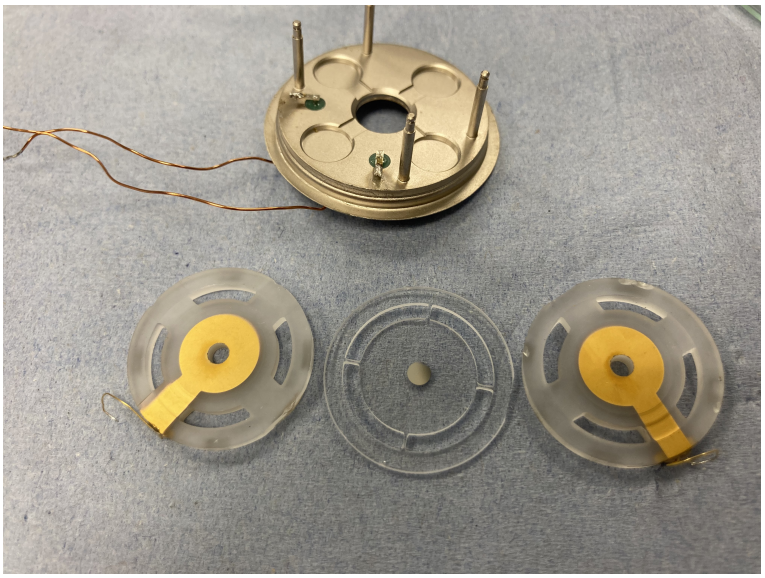

Figure B.1: *The quartz crystal resonator (middle), with its accompanying condensators, designed to hold it and provide electrical contact through their metallic coating. Notice the hole in the condensators, which are designed to let the laser beam pass through for photothermal excitation (see chapter 4.1). The golden holder on the top allows to hold the sandwiched condensators and QR.*

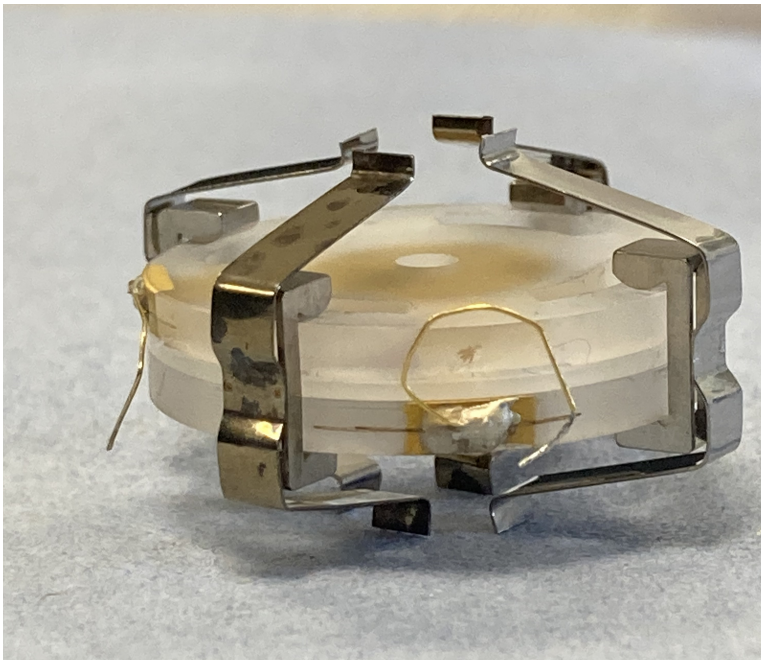

Figure B.2: *The quartz crystal resonator is sandwiched between the condensators, with the electrical contact from the condensator visible on the side.*

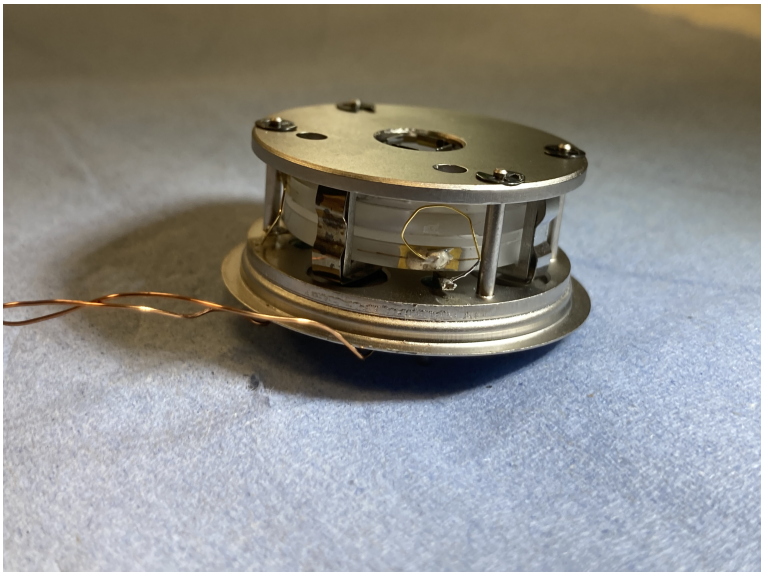

Figure B.3: *Same as B.2, with the BVA holder also in place. Note the hole on top of the structure, allowing the laser to pass by.*

C

PHOTOTHERMAL CALCULATION

Let us remind that the problem to be solved is:

$$\begin{cases} u_{tt} - \bar{z}^2 u_{,22} = -\dfrac{\beta_4}{\rho}\theta_{,2} & \text{(4.23)} \\ u_{,2}(e) = h(t) = Ae^{i\Omega t} & \text{(C.1a)} \\ u_{,2}(0) = j(t) = Be^{i\Omega t} & \text{(C.1b)} \end{cases}$$

In order to shift the data, i.e. to render the boundary conditions equal to zero, let us start by defining the function:

$$v(x_2,t) = V(x_2)e^{i\Omega t} = \left(x_2 - \frac{x_2^2}{2e}\right)Be^{i\Omega t} + \frac{x_2^2}{2e}Ae^{i\Omega t} \tag{C.2}$$

By deriving V with respect to x_2, it is possible to see that if we define a shifted displacement:

$$w(x_2,t) = W(x_2)e^{i\Omega t} = u - v \tag{C.3}$$

then this shifted displacement $w(x_2),t$ obeys homogeneous boundary conditions:

$$\begin{cases} w_{tt} - \bar{z}^2 w_{,22} = \tilde{\theta}(x_2,t) & \text{(C.4a)} \\ w_{,2}(e,t) = 0 & \text{(C.4b)} \\ w_{,2}(0,t) = 0 & \text{(C.4c)} \end{cases}$$

where $\tilde{\theta}$ can be obtained by injecting w in the equation of motion Eq. 4.24:

$$\tilde{\theta}(x_2,t) = \left\{-\frac{\beta_4}{\rho}\theta_{,2} + \Omega^2\left[\left(x_2 - \frac{x_2^2}{2e}\right)B + \frac{x_2^2}{2e}A\right] - \bar{z}^2\left(\frac{B}{e} - \frac{A}{e}\right)\right\}e^{i\Omega t} \tag{C.5}$$

We solve the homogeneous wave equation for w with Neumann boundary conditions, leaving aside the losses for now (so that $\bar{z}^2 \to c^2$):

$$\begin{cases} w'_{tt} - c^2 w' = 0 \\ w'_{,2}(e,t) = 0 \\ w'_{,2}(0,t) = 0 \end{cases} \tag{C.6}$$

The solutions can be shown to be exclusively symmetrical. It has the form:

$$w'_n = \cos(\beta_n x_2) e^{i\Omega_n t} \tag{C.7a}$$
$$\beta_n = \frac{n\pi}{e} \tag{C.7b}$$
$$\Omega_n = \frac{n\pi c}{e} \tag{C.7c}$$

Let us now solve the wave equation with the source term from Eq. C.4a, leaving the losses for now. Furthermore, we solve for the forced oscillation frequency Ω. In order to do this, we use the completeness of the basis of eigenfunctions we just found for the homogeneous problem in order to decompose the shifted displacement w and the source term $\tilde{\theta}$:

$$\tilde{\theta}(x_2) = \sum_{n=0} \tilde{\theta}_n \cos(\beta_n x_2) \quad \text{where } \tilde{\theta}_n = \int_0^e \tilde{\theta}(x_2) \cos(\beta_n x_2)\, \mathrm{d}x_2 \tag{C.8a}$$
$$W(x_2) = \sum_{n=0} \lambda_n \cos(\beta_n x_2) \quad \text{and} \quad W_{,22} = \sum_{n\geq 1} -\lambda_n \left(\frac{n\pi}{e}\right)^2 \cos(\beta_n x_2) \tag{C.8b}$$

where the temporal dependency of $\tilde{\theta}$ is omitted so as to leave only the spatial dependency. The coefficient for the term of order n is then found by injecting these sum decompositions in Eq. C.4a and using the completeness of the basis, i.e. solving for each individual term:

$$\begin{aligned} -\Omega^2 \lambda_n + \left(\frac{n\pi c}{e}\right)^2 \lambda_n &= \tilde{\theta}_n \\ \Rightarrow \lambda_n &= \frac{\tilde{\theta}_n}{\left(\frac{n\pi c}{e}\right)^2 - \Omega^2} \end{aligned} \tag{C.9}$$

Of course, near resonance, Eq. C.9 is not valid anymore, as the denominator vanishes. In this case, the way around to keep the amplitude finite is to reintroduce the losses through the frequency, and give it a complex value (see [Tiersten, 1975] Eq. 60). Specifically, this can be done in two different ways: writing $c^2 \to \bar{z}^2 = c^2 + i\alpha\Omega$ or writing that $\tilde{\Omega}_n = \Omega_n + i\Omega_n/Q_n$ where $Q_n = c^2/(\alpha\Omega_n)$. In either case, this leads to the following expression at resonance:

$$\lambda_n^{\text{res}} = \frac{c^2}{i\alpha\Omega_n^3} \tilde{\theta}_n \tag{C.10}$$

There remains to calculate $\tilde{\theta}_n$ in order to find the total displacement. This is done by injecting Eq. C.5 in Eq. C.8a. This leads to write:

$$\begin{aligned} \tilde{\theta}_n = \int_0^e \Bigg\{ \frac{\beta_4 \bar{\beta} \theta_0}{\rho} \left(-e^{-\bar{\beta} x_2} + e^{-2\bar{\beta} e} e^{\bar{\beta} x_2}\right) + \Omega^2 \left[\left(x_2 - \frac{x_2^2}{2e}\right) B + \frac{x_2^2}{2e} A \right] \\ + \frac{c^2}{e}(-B + A) \Bigg\} \cos(\beta_n x_2)\, \mathrm{d}x_2 \end{aligned} \tag{C.11}$$

Calculating each integration separately yields:

$$\int_0^e e^{\bar{\beta}x_2}\cos\left(\frac{n\pi}{e}x_2\right)\mathrm{d}x_2 = \bar{\beta}e^2\left[\frac{e^{\bar{\beta}e}\cos(n\pi)-1}{\bar{\beta}^2e^2+n^2\pi^2}\right] \tag{C.12a}$$

$$\int_0^e x_2^2\cos\left(\frac{n\pi}{e}x_2\right)\mathrm{d}x_2 = \frac{2e^3\cos(n\pi)}{n^2\pi^2} \tag{C.12b}$$

$$\int_0^e x_2\cos\left(\frac{n\pi}{e}x_2\right)\mathrm{d}x_2 = \frac{e^2(\cos(n\pi)-1)}{n^2\pi^2} \tag{C.12c}$$

$$\int_0^e \cos\left(\frac{n\pi}{e}x_2\right)\mathrm{d}x_2 = 0 \tag{C.12d}$$

so that by using Eq. C.12 in Eq. C.11, the total integral yields:

$$\begin{aligned}\tilde{\theta}_n =& \frac{\beta_4\theta_0}{\rho}\bar{\beta}^2e^2\left[\frac{2e^{-\bar{\beta}e}\cos(n\pi)-1-e^{-2\bar{\beta}e}}{\bar{\beta}^2e^2+n^2\pi^2}\right]+\\ &-\frac{\Omega^2e^2\cos(n\pi)}{n^2\pi^2}\beta_4\theta_0\left(1-e^{-\bar{\beta}e}\right)^2+\frac{\Omega^2e^2B}{n^2\pi^2}(\cos(n\pi)-1)\end{aligned} \tag{C.13}$$

In order to do a numerical application, coefficient $\tilde{\theta}_n$ is injected in Eq. C.10. However, coefficients A and B are left with the quantity $U(e)-U(0)$ which is unknown. With the expression for the coefficients λ_n composing $w(x_2,t)$, it is now possible to find this difference by using Eq. C.3, noting that because experimental work is performed near resonance, one particular term of index n_0 in the sum in Eq. C.8b will be significant while the rest can be discarded:

$$u_{n_0}(x_2,t) = \left[\lambda_{n_0}\cos(\beta_{n_0}x_2)+\left(x_2-\frac{x_2^2}{2e}\right)B+\frac{x_2^2}{2e}A\right]e^{i\Omega_{n_0}t} \tag{4.29}$$

which can be rewritten, omitting the temporal part:

$$U_{n_0}(x_2) = W_{n_0}(x_2)+V(x_2) \tag{C.14a}$$

$$U_{n_0}(0) = W_{n_0}(0) \tag{C.14b}$$

$$U_{n_0}(e) = W_{n_0}(e)+\frac{e}{2}(A+B) \tag{C.14c}$$

$$\text{where}\quad (A+B) = \frac{1}{\bar{C}_{44}^+}\left[-2e_{24}L_1+\beta_4\theta_0\left(1+e^{-\bar{\beta}x_2}\right)^2\right]\quad\text{(from Eq. 4.28)} \tag{C.14d}$$

In Eq. C.14b and Eq. C.14c, the quantity $W_{n_0}(x_2)$ appears. In $x_2=0$, $W_{n_0}(0)=\lambda_{n_0}^{res}$, whereas in $x_2=e$, the value of $\cos(\beta_{n_0}e)=\pm1$ depending on the value of n_0:

$$W_{n_0}(0) = \lambda_{n_0}^{res} \tag{C.15a}$$

$$W_{n_0}(e) = \begin{cases}\lambda_{n_0}^{res}, & \text{if } n_0=2,4,6\cdots\\ -\lambda_{n_0}^{res}, & \text{if } n_0=1,3,5\cdots\end{cases} \tag{C.15b}$$

From this, we gather that $U(e)-U(0)$[1] must depend on the parity of the mode one is considering to be resonant:

$$U(e)-U(0) = \begin{cases}\frac{e}{2}(A+B), & \text{if } n_0=2,4,6\cdots\\ -2\lambda_{n_0}^{res}+\frac{e}{2}(A+B), & \text{if } n_0=1,3,5\cdots\end{cases} \tag{C.16}$$

In order to go any further, we have to set the value of L_1, which, so far, has been left unknown in the expression of A and B. This can be done by imposing that the electric potential $\mathcal{V}(x_2)$ obeys the boundary condition that $\mathcal{V}(e) - \mathcal{V}(0) = V_0$, which, from Eq. 4.25, leads to write that:

$$L_1 = \frac{V_0}{e} - \frac{e_{24}}{e\epsilon_{22}}(U(e) - U(0)) \tag{C.17}$$

From this last condition, the final expression for $U(e) - U(0)$ in the near-resonance approximation[1] is found to be:

$$U(e) - U(0) = \frac{\epsilon_{22}}{\bar{C}_{44}^{+}\epsilon_{22} - e_{24}^2}\left[-e_{24}V_0 + \frac{e\beta_4\theta_0}{2}\left(1 + e^{-\bar{\beta}e}\right)\right], \quad \text{for } n_0 = 2, 4, 6\cdots \tag{C.18}$$

$$\begin{aligned} U(e) - U(0) = \Bigg\{ & \frac{-2c^2}{i\alpha\Omega^2}\left[\frac{-\beta_4\theta_0\bar{\beta}^2e^2}{\rho}\frac{\left(1 + e^{-\bar{\beta}e}\right)^2}{\bar{\beta}^2e^2 + n_0^2\pi^2} + \frac{\Omega^2e^2\beta_4\theta_0}{n_0^2\pi^2}\left(1 - e^{-\bar{\beta}e}\right)^2\right] \\ & + \left[\frac{-e_{24}}{e}V_0 + \beta_4\theta_0(1 + e^{-2\bar{\beta}e})\right]\left(\frac{e}{\bar{C}_{44}^{+}} + \frac{4c^2e^2}{i\alpha\Omega n_0^2\pi^2\bar{C}_{44}^{+}}\right)\Bigg\} \times \\ & \times \left[1 - \frac{e_{24}^2}{\epsilon_{22}\bar{C}_{44}^{+}}\left(1 + \frac{4c^2e}{i\alpha\Omega^2n_0^2\pi^2}\right)\right]^{-1} \quad \text{for } n_0 = 1, 3, 5\cdots \end{aligned} \tag{C.19}$$

Note that throughout this section, V_0 has been considered as the experimentally measured voltage at the quartz' ends and is thus deemed known. Conceptually, the voltage is a consequence of the incoming heat flux which is transformed into motion of the quartz (at resonance), giving rise to the said voltage. Within the present theoretical framework, however, it is not possible to express V_0 as a function of θ, the temperature fluctuation. See section 4.1.3 for measurements of V_0.

[1] This should formally be written as $U_{n_0}(e) - U_{n_0}(0)$, although the n_0 is dropped for simplicity

D

PD AND RF PHASE RELATION

In chapter 4.1 and specifically in section 4.1.3.2, we introduced the idea that the optical input power was to be used as the reference signal instead of the excitation RF signal. We verify that the electronics and optics response do not have a delay and are indeed in phase. Several measurements for the photodiode response to the input (modulated) optical power are taken, with each time a different cable length (see Fig. D.1). This permits to compensate for the unavoidable phase shift linked with the cable from the photodiode to the oscilloscope. A linear first order fit is conducted on the obtained phases, to extrapolate to the 0 m long cable. The 0 m long cable photodiode signal is then compared with the radiofrequency signal that feeds the AOM. The result is as shown in Fig. D.2, and shows that the two signals are indeed in phase, thus validating the optical power reference.

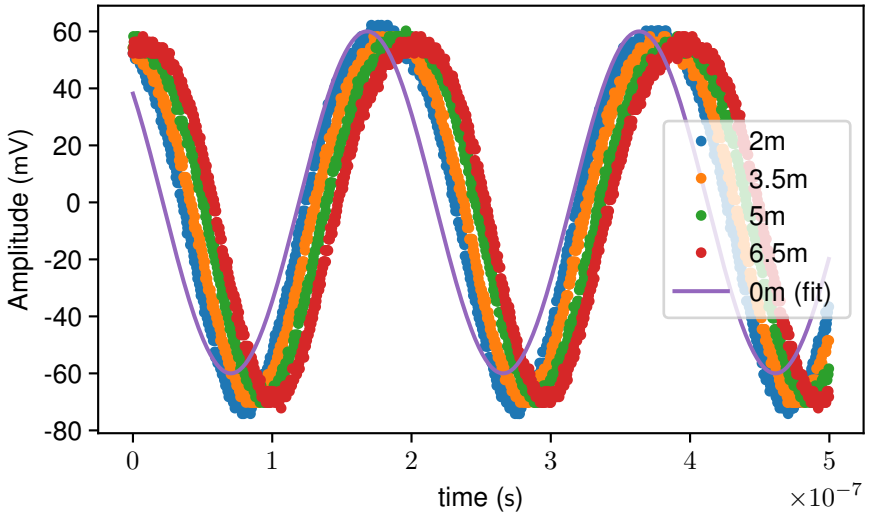

Figure D.1: *Signal from the PhotoDiode (PD) with different cable length. This permits to extract the phase relation to cable length, hence to extrapolate the actual signal with a* 0 m *long cable.*

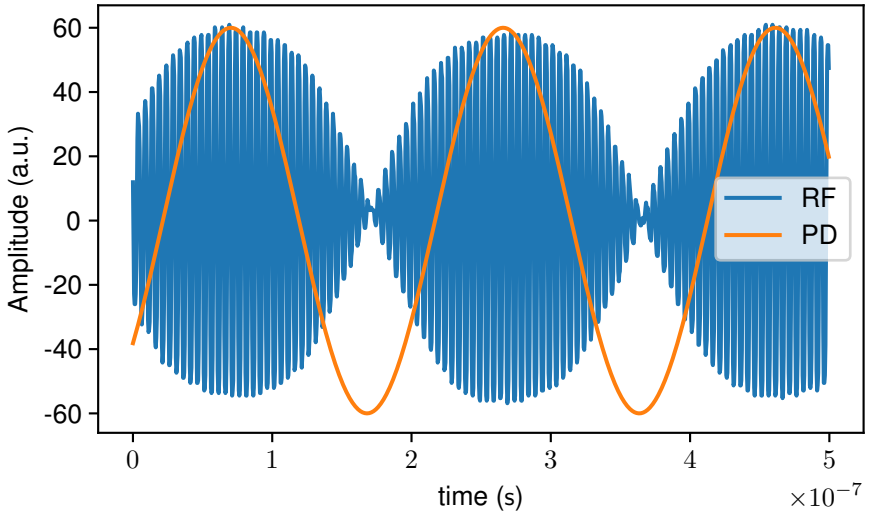

Figure D.2: *The Radio Frequency (RF) signal feeding the AOM, and the PhotoDiode (PD) AC signal measuring the laser's intensity. The AC coupled signal does not reflect the general offset, which means it is impossible to determine whether the optical power indeed drops to 0 from this graph alone. It suffices, however, to note that they do indeed oscillate at the same frequency and are in-phase. A fit for removing cable-related phase delay has been led upon various cable lengths for the photodiode signal (see Fig. D.1). The displayed PD signal is therefore the fit for a* 0 m *cable. Note that the signals have been normalized in amplitude to fit on the same scale, and that the amplitude is therefore purely indicative and is shown in arbitrary units (a.u.). The RF signal in this graph is at frequency* $f_0 = 5\,116\,136$ Hz*, which is the resonant frequency of this particular quartz at cryogenic temperature (*4.2 K*).*

E

HETERODYNE DETECTION

Another important feature to be implemented for the future of the experiment is to be able to measure the displacement optically, in order to investigate whether optomechanical coupling is taking place or not.

Indeed, as we have emphasized in section 1.3.2, the presence of the electrodes serving as both readout and (piezoelectric) excitation is a drawback, which gave the background for this research on optomechanical coupling. This means that in the other geometries considered in section 5.2, a piezoelectric readout (such as that lead in the photothermal experiment of section 4.1) is impossible, because of the absence of proper electrodes to read it from. Hence the need for another type of mechanical displacement measurement solution.

The most obvious solution is an optical readout, with e.g. an heterodyne detection measurement. Conceptually, only a small mirror displacement is expected from an optomechanically induced actuation, so that looking at the reflection curve of a Fabry-Perot cavity the intensity should barely change with the (slightly) moving mirrors. However, the phase change rate is maximum at resonance[1], see Fig. E.1. Considering this fact, the best option is therefore to measure the phase fluctuations and look at the component at the expected mechanical resonance frequency.

Experimentally, this phase measurement translates into the setup presented on Fig. E.2. The laser beam is split into two beams: one is injected on the optical table just as in the optical setup previously discussed in this thesis (see section 3.2.1 and Fig. 3.15), which goes through the mode-matching elements and is incident onto the optical cavity made by the quartz and its mirrors. It is then deflected by the beam splitter to reach the lower part of the scheme, where it first goes through a polarizer and a $\lambda/2$ waveplate to control the incoming polarization. It is set so that part of it passes the polarized beam splitter.

The other part of the incident beam, on the other hand, is set to be deflected by the polarized beam splitter so as to mix with the frequency shifted beam (which has been properly prepared in polarization at the fiber output). They are both undergo a $45°$ rotation in polarization with the help of a $\lambda/2$ waveplate before arriving to another polarized beam splitter, in order to combine the both beams and have them interact by projecting the polarization state onto the same axis [2] . This is where the phase measurement happens.

The process is known and can be broken down as follows. Let us focus on the PBS1

[1] Note that this fact is also the ground consideration to achieve a Pound Drever Hall laser stabilization, see [Black, 2001].

[2] We remind that two wavepackets of light only intereacts when in the same polarization state.

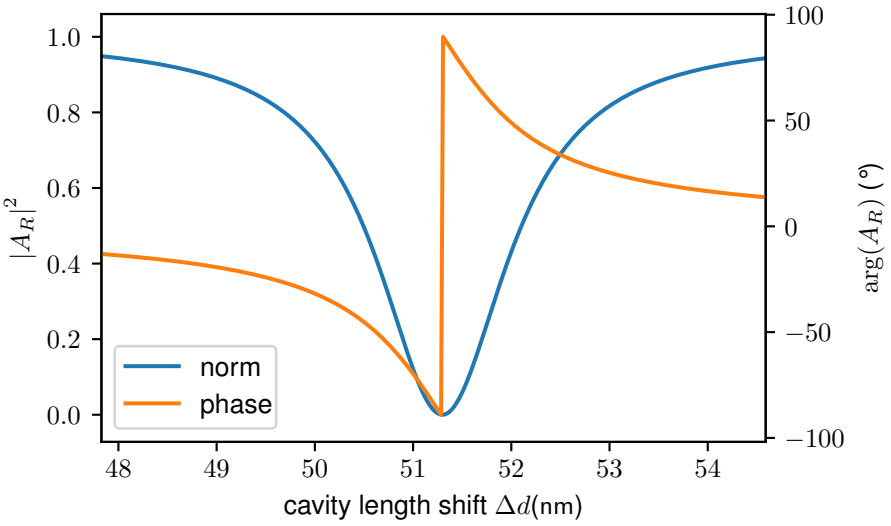

Figure E.1: *Normalized intensity and phase of the reflected amplitude against cavity length shift Δd for an ideal Fabry-Perot cavity, with $A_R = \frac{A_1^-}{A_1^+}$ (see Eq. 3.10a), around basis cavity length $d = 1\,\text{mm}$. Note that although the intensity reaches a minimum and has very small fluctuations near resonance, the phase has its maximum change rate precisely at resonance. This permits to measure small displacements of the input mirror, i.e. of the cavity length.*

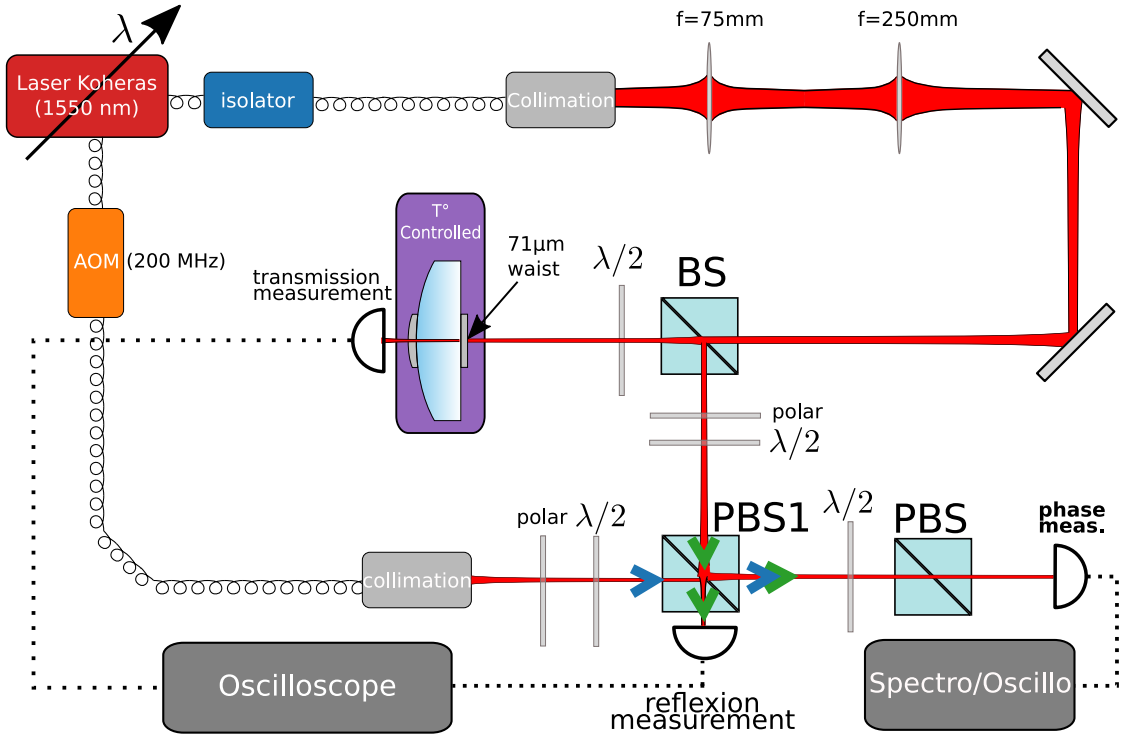

Figure E.2: *Experimental setup for heterodyne optical detection of movement. The PBS1 part of the setup is further analyzed in the main text and Fig. E.3.*

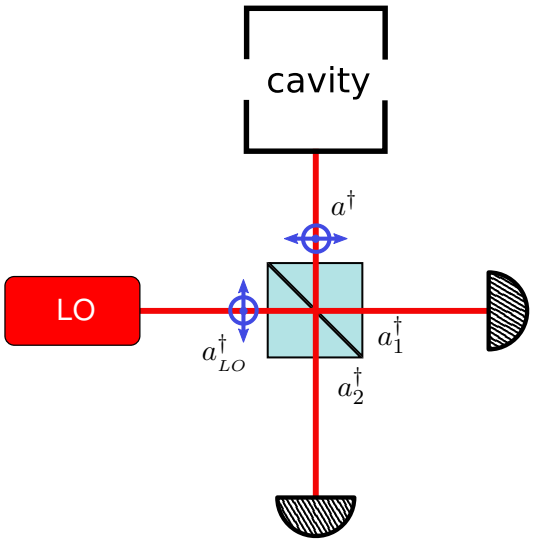

Figure E.3: *Polarized Beam Splitter 1 (PBS1) part of the setup in Fig. E.2. $a^\dagger_{LO}$ and $a^\dagger$ and respectively the quantum field creation operators of the local oscillator (LO) and of the field coming from the cavity, which we are interested in. $a^\dagger_1$ and $a^\dagger_2$, on the other hand, describe the fields exiting the PBS1.*

part of the setup, shown in Fig. E.3. The incoming wave fields are described by the quantum operators $a^\dagger_{LO}$ and $a^\dagger$, respectively the local oscillator (LO) and Fabry-Perot creation fields operators. The polarization is a priori considered linear along any axis. Because the PBS1 is a $50/50$ beams splitter, the output creation field operators $a^\dagger_1$ and $a^\dagger_2$ are described by the following equations:

$$a^\dagger_1 = \frac{1}{\sqrt{2}}\left(a^\dagger + a^\dagger_{LO}\right) \tag{E.1a}$$

$$a^\dagger_2 = \frac{1}{\sqrt{2}}\left(a^\dagger - a^\dagger_{LO}\right) \tag{E.1b}$$

The same results hold for the classical fields going through the beamsplitter (see [Kučera, 2007]). Let us describe now the fields by their classical counterparts, so that we define $E_{LO} = a_{LO}\cos\left([\omega + \Omega_{LO}]t\right)$ and $E = (a + \delta a)\cos(\omega t + \vartheta)$. E_{LO} is the local oscillator field, which is considered to be perfect (i.e. without amplitude or phase fluctuations), whereas the field E coming from the cavity has the amplitude and phase fluctuations, δa and ϑ respectively.

It is possible to write the intensity $I_1 = a_1^2$ in the following way:

$$\begin{aligned} I_1 &= \frac{1}{2}\left(E^2_{LO} + E^2 + 2E_{LO}E\right) \\ &\approx 2E_{LO}E \quad \text{(keeping only the crossed AC term that fluctuate at frequency } \Omega_{LO}) \\ &= a_{LO}(a + \delta a)\cos\left([\omega + \Omega_{LO}]t\right)\cos\left(\omega t + \vartheta\right) \\ &\approx \frac{a_{LO}(a + \delta a)}{2}\cos\left(\Omega_{LO}t + \vartheta\right) \quad \text{(keeping only terms at frequency } \Omega_{LO}) \end{aligned}$$

$$I_1 = \frac{a_{LO}(a + \delta a)}{2}\left[\cos(\Omega_{LO}t) - \sin(\Omega_{LO}t)\vartheta\right] \tag{E.2a}$$

From this last expression, we get to the conclusion that by observing the AC output of the branch a_1 of the PBS1 and demodulating with a signal at frequency Ω_{LO} with the right phase, one can observe the $\sin(\Omega_{LO}t)$ part of expression Eq. E.2a. Observing the component of this signal at the mechanical frequency Ω_m gives the wanted quantity, i.e. the phase fluctuations ϑ (more precisely, its component at the mechanical frequency) which are proportional to the movement of the input mirror. If a peak is visible at this particular frequency, a mechanical resonance of the system can be infered.

BIBLIOGRAPHY

[Agarwal et al., 2013] Agarwal, G. S., et Jha, S. S. (2013). **Multimode phonon cooling via three-wave parametric interactions with optical fields**. *Physical Review A*, 88(1). (5 citations located at pages 107, 107, 113, 119, and 123.)

[Almirall et al., 2019] Almirall, A., Oliveri, S., Daniau, W., Margueron, S., Baron, T., Boulet, P., Ballandras, S., Chamaly, S., et Bartasyte, A. (2019). **High-frequency surface acoustic wave devices based on epitaxial Z-LiNbO $_3$ layers on sapphire**. *Applied Physics Letters*, 114(16):162905. (1 citation located at page 10.)

[Aoki et al., 1988] Aoki, Y., Tajima, K., et Mito, I. (1988). **Input power limits of single-mode optical fibers due to stimulated Brillouin scattering in optical communication systems**. *Journal of Lightwave Technology*, 6(5):710–719. (1 citation located at page 107.)

[Ashkin, 1978] Ashkin, A. (1978). **Trapping of Atoms by Resonance Radiation Pressure**. *Physical Review Letters*, 40(12):729–732. (1 citation located at page 106.)

[Aspelmeyer et al., 2014a] Aspelmeyer, M., Kippenberg, T. J., et Marquardt, F. (2014a). **Cavity Optomechanics**. *Reviews of Modern Physics*, 86(4):1391–1452. (2 citations located at pages 108 and 114.)

[Aspelmeyer et al., 2014b] Aspelmeyer, M., Kippenberg, T. J., et Marquardt, F., editors (2014b). **Cavity Optomechanics: Nano- and Micromechanical Resonators Interacting with Light**. Quantum Science and Technology. Springer, Berlin. (2 citations located at pages 106 and 107.)

[Audoin et al., 2001] Audoin, C., et Guinot, B. (2001). **The Measurement of Time: Time, Frequency and the Atomic Clock**. Cambridge University Press. (1 citation located at page 12.)

[Auld, 1973] Auld, B. A. (1973). **Acoustic Fields and Waves in Solids Vol.1**. Wiley & sons, inc. edition. (1 citation located at page 22.)

[Azzam et al., 1977] Azzam, R. M. A., et Bashara, N. M. (1977). **Ellipsometry and Polarized Light**. North-Holland Publishing Company. (1 citation located at page 40.)

[Bahl et al., 2011] Bahl, G., Zehnpfennig, J., Tomes, M., et Carmon, T. (2011). **Stimulated optomechanical excitation of surface acoustic waves in a microdevice**. *Nature Communications*, 2(1):403. (1 citation located at page 107.)

[Ballandras et al., 2012] Ballandras, S., Baron, T., Lebrasseur, E., Martin, G., Gachon, D., Reinhardt, A., Lassagne, P.-P., Friedt, J.-M., Chommeloux, L., et Rabus, D. (2012). **High overtone Bulk Acoustic Resonators: Application to resonators, filters and sensors**. *Proceedings of the Acoustics 2012 Nantes Conference*, page 8. (1 citation located at page 17.)

[Baron et al., 2013] Baron, T., Lebrasseur, E., Bassignot, F., Martin, G., Ptrini, V., et Ballandras, S. (2013). **High-Overtone Bulk Acoustic Resonator**. In Beghi, M. G., editor, *Modeling and Measurement Methods for Acoustic Waves and for Acoustic Microdevices*. InTech. (1 citation located at page 17.)

[Barron et al., 1982] Barron, T. H. K., Collins, J. F., Smith, T. W., et White, G. K. (1982). **Thermal expansion, Gruneisen functions and static lattice properties of quartz**. *Journal of Physics C: Solid State Physics*, 15(20):4311–4326. (2 citations located at pages 136 and 136.)

[Bartek et al., 1999] Bartek, M., et Novotný, I. (1999). **Quality Factor of Thin-Film Fabry-Perot Resonators: Dependence on Interface Roughness**. In *EUROSENSORS XIII*, page 5, The Hague, Netherlands. (1 citation located at page 61.)

[Bass et al., 1983] Bass, M., et Bennett, J. (1983). **Optical Properties of Metals**. Technical Report, University of Southern California Los Angeles center for LASER studies. (2 citations located at pages 51 and 65.)

[Bass et al., 1995] Bass, M., et Optical Society of America, editors (1995). **Handbook of Optics. Vol. 2: Devices, Measurements, and Properties**. McGraw-Hill, New York, NY, 2. ed edition. (1 citation located at page 72.)

[Beugnot et al., 2012] Beugnot, J.-C., et Laude, V. (2012). **Electrostriction and guidance of acoustic phonons in optical fibers**. *Physical Review B*, 86(22):224304. (1 citation located at page 107.)

[Billard et al., 2005] Billard, A., et Perry, F. (2005). **Pulvérisation cathodique magnétron**. *Techniques de l'ingénieur Traitements de surface des métaux par voie sèche et en milieu fondu*, base documentaire : TIB360DUO.:23. (1 citation located at page 63.)

[Black, 2001] Black, E. D. (2001). **An introduction to Pound–Drever–Hall laser frequency stabilization**. *American Journal of Physics*, 69(1):79–87. (1 citation located at page 147.)

[Bon, 2018] Bon, J. (2018). **Résonateurs à ondes acoustiques de volume piégées à très basses températures: application à l'optomécanique**. PhD thesis, Université Bourgogne Franche-Comté, Besançon. (8 citations located at pages 13, 22, 23, 23, 23, 23, 26, and 125.)

[Bon et al., 2018] Bon, J., Neuhaus, L., Deléglise, S., Briant, T., Abbé, P., Cohadon, P.-F., et Galliou, S. (2018). **Cryogenic optomechanic cavity in low mechanical loss material**. *Journal of Applied Physics*, 124(7):073104. (3 citations located at pages 107, 110, and 114.)

[Bontempi et al., 2014] Bontempi, A., Teyssieux, D., Friedt, J.-M., Thiery, L., Hermelin, D., et Vairac, P. (2014). **Photo-thermal quartz tuning fork excitation for dynamic mode atomic force microscope**. *Applied Physics Letters*, 105(15):154104. (4 citations located at pages 83, 83, 83, and 97.)

[Bourhill et al., 2015] Bourhill, J., Ivanov, E., et Tobar, M. (2015). **Precision Measurement of a low-loss Cylindrical Dumbbell-Shaped Sapphire Mechanical Oscillator using Radiation Pressure**. *Physical Review A*, 92(2):023817. (2 citations located at pages 1 and 19.)

[Boyd, 2008] Boyd, R. W. (2008). **Nonlinear Optics (Third Edition)**. Academic Press, third edition edition. (3 citations located at pages 112, 112, and 116.)

[Braginskii et al., 1970] Braginskii, B., Manukin, A. B., et Tikhonov, M. Y. (1970). **Investigation of Dissipative Ponderomotive Effects of Electromagnetic Radiation**. *Sov. Phys. JETP*, 31(5):829. (2 citations located at pages 107 and 114.)

[Braginsky et al., 2001] Braginsky, V., Strigin, S., et Vyatchanin, S. (2001). **Parametric oscillatory instability in Fabry–Perot interferometer**. *Physics Letters A*, 287(5-6):331–338. (1 citation located at page 109.)

[Briant, 2004] Briant, T. (2004). **Caractérisation du couplage optomécanique entre la lumière et un miroir : bruit thermique et effets quantiques**. PhD thesis, Université Paris VI, Paris. (2 citations located at pages 123 and 128.)

[Brillouin, 1922] Brillouin, L. (1922). **Diffusion de la lumière et des rayons X par un corps transparent homogène - Influence de l'agitation thermique**. *Annales de Physique*, 9(17):88–122. (1 citation located at page 106.)

[Bushev et al., 2019] Bushev, P. A., Bourhill, J., Goryachev, M., Kukharchyk, N., Ivanov, E., Galliou, S., Tobar, M. E., et Danilishin, S. (2019). **Testing of Quantum Gravity With Sub-Kilogram Acoustic Resonators**. *arXiv:1903.03346 [cond-mat, physics:gr-qc, physics:quant-ph]*. (2 citations located at pages 1 and 20.)

[Carvalho et al., 2019] Carvalho, N. C., Bourhill, J., Goryachev, M., Galliou, S., et Tobar, M. E. (2019). **Piezo-optomechanical coupling of a 3D microwave resonator to a bulk acoustic wave crystalline resonator**. *Applied Physics Letters*, 115(21):211102. (2 citations located at pages 107 and 109.)

[Chan et al., 2011] Chan, J., Alegre, T. P. M., Safavi-Naeini, A. H., Hill, J. T., Krause, A., Gröblacher, S., Aspelmeyer, M., et Painter, O. (2011). **Laser cooling of a nanomechanical oscillator into its quantum ground state**. *Nature*, 478(7367):89–92. (1 citation located at page 107.)

[Chen et al., 2004] Chen, T.-C., Lin, W.-J., et Chen, D.-L. (2004). **Effect of temperature gradient on simultaneously experimental determination of thermal expansion coefficients and elastic modulus of thin film materials**. *J. Appl. Phys.*, 96(7):8. (1 citation located at page 77.)

[Chiao et al., 1964] Chiao, R. Y., Townes, C. H., et Stoicheff, B. P. (1964). **Stimulated Brillouin Scattering and Coherent Generation of Intense Hypersonic Waves**. *Physical Review Letters*, 12(21):592–595. (2 citations located at pages 107 and 107.)

[Ciesielski et al., 2017] Ciesielski, A., Skowronski, L., Trzcinski, M., et Szoplik, T. (2017). **Controlling the optical parameters of self-assembled silver films with wetting layers and annealing**. *Applied Surface Science*, 421:349–356. (17 citations located at pages 36, 42, 46, 50, 52, 59, 63, 71, 71, 72, 72, 72, 74, 75, 79, 111, and 131.)

[Cohadon et al., 1999] Cohadon, P. F., Heidmann, A., et Pinard, M. (1999). **Cooling of a mirror by radiation pressure**. *Physical Review Letters*, 83(16):3174–3177. (3 citations located at pages 107, 109, and 114.)

[Cole, 2012] Cole, G. D. (2012). **Cavity optomechanics with low-noise crystalline mirrors**. In Dholakia, K., et Spalding, G. C., editors, *SPIE NanoScience + Engineering*, page 845807, San Diego, California, USA. (1 citation located at page 128.)

[Cole et al., 2016] Cole, G. D., Zhang, W., Bjork, B. J., Follman, D., Heu, P., Deutsch, C., Sonderhouse, L., Robinson, J., Franz, C., Alexandrovski, A., Notcutt, M., Heckl, O. H., Ye, J., et Aspelmeyer, M. (2016). **High-performance near- and mid-infrared crystalline coatings**. *Optica*, 3(6):647. (1 citation located at page 130.)

[Cole et al., 2013] Cole, G. D., Zhang, W., Martin, M. J., Ye, J., et Aspelmeyer, M. (2013). **Tenfold reduction of Brownian noise in high-reflectivity optical coatings**. *Nature Photonics*, 7(8):644–650. (2 citations located at pages 129 and 129.)

[Corvo et al., 1988] Corvo, A., et Gavrielides, A. (1988). **Forward stimulated Brillouin scattering**. *Journal of Applied Physics*, 63(11):5220–5227. (1 citation located at page 117.)

[Coupeau et al., 2004] Coupeau, C., Goudeau, P., Belliard, L., George, M., Tamura, N., Cleymand, F., Colin, J., Perrin, B., et Grilhé, J. (2004). **Evidence of plastic damage in thin films around buckling structures**. *Thin Solid Films*, 469–470:221–226. (1 citation located at page 62.)

[Crooks et al., 2004] Crooks, D. R. M., Cagnoli, G., Fejer, M. M., Gretarsson, A., Harry, G., Hough, J., Nakagawa, N., Penn, S., Route, R., Rowan, S., et Sneddon, P. H. (2004). **Experimental measurements of coating mechanical loss factors**. *Classical and Quantum Gravity*, 21(5):S1059–S1065. (1 citation located at page 129.)

[Curie et al., 1880] Curie, P., et Curie, J. (1880). **Développement par compression de l'électricité polaire dans les cristaux hémièdres à faces inclinées**. *Bulletin de la Société minéralogique de France, volume 3, 4, 1880.* (1 citation located at page 106.)

[Dahmane et al., 2015] Dahmane, N. B., Parry, G., et Estevez, R. (2015). **Cloquage de films minces ductiles sur substrat rigide**. In *CFM 2015*, page 4, Lyon. (1 citation located at page 62.)

[De Marchi, 1989] De Marchi, A., editor (1989). **Frequency Standards and Metrology: Proceedings of the Fourth Symposium, Ancona, Italy, September 5 – 9, 1988**. Springer Berlin Heidelberg, Berlin, Heidelberg. (2 citations located at pages 13 and 16.)

[Dieulesaint et al., 1974] Dieulesaint, E., et Royer, D. (1974). **Ondes Élastiques Dans Les Solides: Application Au Traitement Du Signal**. Masson. (1 citation located at page 17.)

[Dieulesaint et al., 1989] Dieulesaint, E., Royer, D., de HOND, P., et Morbieu, B. (1989). **Résonateur Miniature à Entrée et Sortie Optiques**. In *EFTF*, page 3, Besançon. (2 citations located at pages 17 and 83.)

[Dieulesaint et al., 1982] Dieulesaint, E., Royer, D., et Rakouth, H. (1982). **Optical Excitation of Quartz Resonators**. *Electronics Letters*, 18(9):381–382. (5 citations located at pages 83, 83, 89, 90, and 126.)

[Dieulesaint et al., 1986] Dieulesaint, E., Royer, D., et Servajan, X. (1986). **Sapphire Resonator**. *Electronics Letters*, 22(5):266–268. (1 citation located at page 17.)

[Driscoll et al., 1992] Driscoll, M. M., Jelen, R. A., et Matthews, N. (1992). **Extremely Low Phase Noise UHF Oscillators Utilizing High-Overtone, Bulk-Acoustic Resonators**. *IEEE TRANSACTIONS ON ULTRASONICS, FERROELECTRICS, AND FREQUENCY CONTROL*, 39(6):6. (1 citation located at page 11.)

[Echániz et al., 2014] Echániz, T., Pérez-Sáez, R. B., et Tello, M. J. (2014). **Optical properties of metals: Infrared emissivity in the anomalous skin effect spectral region**. *Journal of Applied Physics*, 116(9):093508. (2 citations located at pages 1 and 18.)

[Elie-Caille et al., 2009] Elie-Caille, C., Rauch, J.-Y., Rouleau, A., et Boireau, W. (2009). **Preparation of flat gold terraces for protein chip developments**. *Micro & Nano Letters*, 4(2):88–94. (1 citation located at page 61.)

[Fabelinskii, 1968] Fabelinskii, I. L. (1968). **Molecular Scattering of Light**. Springer New York, Boston, MA. (1 citation located at page 112.)

[Fachberger et al., 2004] Fachberger, R., Bruckner, G., Knoll, G., Hauser, R., Biniasch, J., et Reindl, L. (2004). **Applicability of LiNbO3, Langasite and GaPO4 in High Temperature SAW Sensors Operating at Radio Frequencies**. *ieee transactions on ultrasonics, ferroelectrics, and frequency control*, 51(11):5. (1 citation located at page 10.)

[Fang et al., 2000] Fang, W., et Lo, C.-Y. (2000). **On the thermal expansion coefficients of thin films**. *Sensors and Actuators A: Physical*, 84(3):310–314. (2 citations located at pages 77 and 77.)

[Fraser et al., 1965] Fraser, D. B., et Hallett, A. C. H. (1965). **The Coefficient of Thermal Expansion of Various Cubic Metals Below 100 °K**. *Canadian Journal of Physics*, 43(2):193–219. (2 citations located at pages 77 and 78.)

[Gagnepain, 1972] Gagnepain, J.-J. (1972). **Mécanismes Non-Linéaires dans les Résonateurs à Quartz**. PhD thesis, Université de Besançon, Besançon. (2 citations located at pages 91 and 92.)

[Galliou et al., 2016a] Galliou, S., Deléglise, S., Goryachev, M., Neuhaus, L., Cagnoli, G., Zerkani, S., Dolique, V., Bon, J., Vacheret, X., Abbé, P., Pinard, L., Michel, C., Karassouloff, T., Briant, T., Cohadon, P.-F., Heidmann, A., Tobar, M. E., et Bourquin, R. (2016a). **A new method of probing mechanical losses of coatings at cryogenic temperatures**. *Review of Scientific Instruments*, 87(12):123906. (6 citations located at pages 1, 1, 129, 131, 131, and 133.)

[Galliou et al., 2016b] Galliou, S., Goryachev, M., Abbe, P., Vacheret, X., Tobar, M. E., et Bourquin, R. (2016b). **Quality Factor Measurements of Various Types of Quartz Crystal Resonators Operating Near 4 K**. *IEEE Transactions on Ultrasonics, Ferroelectrics, and Frequency Control*, 63(7):975–980. (2 citations located at pages 13 and 15.)

[Galliou et al., 2013] Galliou, S., Goryachev, M., Bourquin, R., Abbé, P., Aubry, J. P., et Tobar, M. E. (2013). **Extremely Low Loss Phonon-Trapping Cryogenic Acoustic Cavities for Future Physical Experiments**. *Scientific Reports*, 3(1). (6 citations located at pages 1, 12, 14, 16, 19, and 125.)

[Galliou et al., 2016c] Galliou, S., Vacheret, X., Abbe, P., Bourquin, R., Deleglise, S., Neuhaus, L., Karassouloff, T., Briant, T., Cohadon, P.-F., Heidmann, A., Goryachev, M., Tobar, M. E., Dolique, V., Pinard, L., Michel, C., et Cagnoli, G. (2016c). **Impact of coatings on the quality factor of a quartz crystal resonator at liquid helium temperature**. In *2016 IEEE International Frequency Control Symposium (IFCS)*, pages 1–3, New Orleans, LA, USA. IEEE. (2 citations located at pages 128 and 129.)

[Giordano et al., 2016] Giordano, V., Grop, S., Fluhr, C., Dubois, B., Kersalé, Y., et Rubiola, E. (2016). **The Autonomous Cryocooled Sapphire Oscillator: A Reference for Frequency Stability and Phase Noise Measurements**. *Journal of Physics: Conference Series*, 723:012030. (1 citation located at page 11.)

[Giust et al., 2000] Giust, R., Vigoureux, J.-M., et Sarrazin, M. (2000). **Asymmetrical properties of the optical reflection response of the Fabry–Pérot interferometer**. *Journal of the Optical Society of America A*, 17(1):142. (1 citation located at page 44.)

[Grimsditch et al., 1975] Grimsditch, M. H., et Ramdas, A. K. (1975). **Brillouin scattering in diamond**. *Physical Review B*, 11(8):3139–3148. (1 citation located at page 107.)

[Grop et al., 2010] Grop, S., Bourgeois, P.-Y., Boudot, R., Kersalé, Y., Rubiola, E., et Giordano, V. (2010). **10 GHz cryocooled sapphire oscillator with extremely low phase noise**. *Electronics Letters*, 46(6):420. (2 citations located at pages 11 and 18.)

[Gufflet, 2000] Gufflet, N. (2000). **Défaut d'isochronisme Des Résonateurs à Quartz Vibrant En Cisaillement d'épaisseur : Théorie et Expériences**. PhD thesis. (1 citation located at page 91.)

[Hänsch et al., 1975] Hänsch, T., et Schawlow, A. (1975). **Cooling of gases by laser radiation**. *Optics Communications*, 13(1):68–69. (1 citation located at page 106.)

[Harry et al., 2002] Harry, G. M., Gretarsson, A. M., Saulson, P. R., Kittelberger, S. E., Penn, S. D., Startin, W. J., Rowan, S., Fejer, M. M., Crooks, D. R. M., Cagnoli, G., Hough, J., et Nakagawa, N. (2002). **Thermal noise in interferometric gravitational wave detectors due to dielectric optical coatings**. *Classical and Quantum Gravity*, 19(5):897–917. (1 citation located at page 128.)

[He, 2009] He, G. S. (2009). **Chapter 4 Stimulated Scattering Effects of Intense Coherent Light**. In *Progress in Optics*, volume 53, pages 201–292. Elsevier. (1 citation located at page 112.)

[Hofacker et al., 1981] Hofacker, M., et v. Löhneysen, H. (1981). **Low temperature thermal properties of crystalline quartz after electron irradiation**. *Zeitschrift für Physik B Condensed Matter*, 42(4):291–296. (6 citations located at pages 87, 87, 94, 94, 136, and 137.)

[Huang et al., 2019] Huang, Y., Guan, H., Zeng, M., Tang, L., et Gao, K. (2019). **$^{40}Ca^{+}$ ion optical clock with micromotion-induced shifts below 1×10^{-18}**. *Physical Review A*, 99(1):011401. (1 citation located at page 106.)

[Hudson et al., 2019] Hudson, A. I., Iyanu, G. H., Wang, H., Bloch, M. B., McClelland, T., et Terracciano, L. (2019). **Long-Term Performance of a Space-System OCXO**. In *2019 Joint Conference of the IEEE International Frequency Control Symposium and European Frequency and Time Forum (EFTF/IFC)*, pages 1–5, Orlando, FL, USA. IEEE. (1 citation located at page 11.)

[Hutchinson, 2001] Hutchinson, J. W. (2001). **Delamination of compressed films on curved substrates**. *J. Mech. Phys. Solids*, page 18. (1 citation located at page 62.)

[IEEE, 1987] IEEE (1987). **ANSI/IEEE Std 176-1987 An American National Standard IEEE Standard on Piezoelectricity**. page 74. (3 citations located at pages 21, 23, and 29.)

[Iijima et al., 1976] Iijima, K., Tsuzuki, Y., Hirose, Y., et Akiyama, M. (1976). **Laser interferometric measurement of the vibration displacements of a plano-convex AT-cut quartz crystal resonator**. *Proceedings of the IEEE*, 64(3):386–387. (1 citation located at page 94.)

[Jackson, 1998] Jackson, J. D. (1998). **Classical Electrodynamics**. Wiley, 3rd edition edition. (2 citations located at pages 114 and 115.)

[Jayanti et al., 2015] Jayanti, S. V., Park, J. H., Dejneka, A., Chvostova, D., McPeak, K. M., Chen, X., Oh, S.-H., et Norris, D. J. (2015). **Low-temperature enhancement of plasmonic performance in silver films**. *Optical Materials Express*, 5(5):1147. (4 citations located at pages 61, 72, 72, and 80.)

[Kanamori et al., 1968] Kanamori, H., Fujii, N., et Mizutani, H. (1968). **Thermal diffusivity measurement of rock-forming minerals from 300° to 1100°K**. *Journal of Geophysical Research*, 73(2):595–605. (5 citations located at pages 85, 85, 136, 136, and 136.)

[Katzir, 2006] Katzir, S. (2006). **The Beginnings of Piezoelectricity: A Study in Mundane Physics**. Number 246 in Boston Studies in the Philosophy of Science. Springer, Dordrecht. (1 citation located at page 106.)

[Kharel et al., 2019] Kharel, P., Harris, G. I., Kittlaus, E. A., Renninger, W. H., Otterstrom, N. T., Harris, J. G. E., et Rakich, P. T. (2019). **High-frequency cavity optomechanics using bulk acoustic phonons**. *Science Advances*, 5(4):eaav0582. (10 citations located at pages 1, 107, 107, 113, 117, 123, 127, 128, 132, and 132.)

[Kischkat et al., 2012] Kischkat, J., Peters, S., Gruska, B., Semtsiv, M., Chashnikova, M., Klinkmüller, M., Fedosenko, O., Machulik, S., Aleksandrova, A., Monastyrskyi, G., Flores, Y., et Ted Masselink, W. (2012). **Mid-infrared optical properties of thin films of aluminum oxide, titanium dioxide, silicon dioxide, aluminum nitride, and silicon nitride**. *Applied Optics*, 51(28):6789. (2 citations located at pages 59 and 61.)

[Kobyakov et al., 2010] Kobyakov, A., Sauer, M., et Chowdhury, D. (2010). **Stimulated Brillouin scattering in optical fibers**. *Advances in Optics and Photonics*, 2(1):1. (1 citation located at page 107.)

[Kosinski et al., 1991] Kosinski, J., Gualtieri, J., et Ballato, A. (1991). **Thermal expansion of alpha quartz**. In *Proceedings of the 45th Annual Symposium on Frequency Control 1991*, pages 22–28, Los Angeles, CA, USA. IEEE. (2 citations located at pages 136 and 136.)

[Kotler et al., 2017] Kotler, S., Simmonds, R. W., Leibfried, D., et Wineland, D. J. (2017). **Hybrid quantum systems with trapped charged particles**. *Physical Review A*, 95(2). (1 citation located at page 20.)

[Kroll, 1965] Kroll, N. M. (1965). **Excitation of Hypersonic Vibrations by Means of Photoelastic Coupling of High-Intensity Light Waves to Elastic Waves**. *Journal of Applied Physics*, 36(1):34–43. (2 citations located at pages 107 and 107.)

[Kubena et al., 2018] Kubena, R. L., Stratton, F. P., Nguyen, H. D., Kirby, D. J., Chang, D. T., Joyce, R. J., Yong, Y.-K., Garstecki, J. F., Cross, M. D., et Seman, S. E. (2018). **A Fully Integrated Quartz MEMS VHF TCXO**. *IEEE Transactions on Ultrasonics, Ferroelectrics, and Frequency Control*, 65(6):904–910. (1 citation located at page 11.)

[Kučera, 2007] Kučera, P. (2007). **Quantum Description of Optical Devices Used in Interferometry**. *Radioengineering*, 16(3):6. (1 citation located at page 149.)

[Lammerink et al., 1991] Lammerink, T., Elwenspoek, M., et Fluitman, J. (1991). **Optical excitation of micro-mechanical resonators**. In *[1991] Proceedings. IEEE Micro Electro Mechanical Systems*, pages 160–165, Nara, Japan. IEEE. (1 citation located at page 85.)

[Laude et al., 2013] Laude, V., et Beugnot, J.-C. (2013). **Generation of phonons from electrostriction in small-core optical waveguides**. *AIP Advances*, 3(4):042109. (2 citations located at pages 107 and 113.)

[Laude et al., 2015] Laude, V., et Beugnot, J.-C. (2015). **Lagrangian description of Brillouin scattering and electrostriction in nanoscale optical waveguides**. *New Journal of Physics*, 17(12):125003. (3 citations located at pages 107, 115, and 123.)

[Lauprêtre et al., 2020] Lauprêtre, T., Groult, L., Achi, B., Petersen, M., Kersalé, Y., Delehaye, M., et Lacroûte, C. (2020). **Absolute frequency measurements of the $^1S_0 \rightarrow {}^1P_1$ transition in ytterbium**. *OSA Continuum*, 3(1):50. (1 citation located at page 106.)

[Law, 1995] Law, C. K. (1995). **Interaction between a moving mirror and radiation pressure: A Hamiltonian formulation**. *Physical Review A*, 51(3):2537–2541. (2 citations located at pages 107 and 109.)

[Lax, 1977] Lax, M. (1977). **Temperature rise induced by a laser beam**. *J. Appl. Phys.*, 48:7. (1 citation located at page 85.)

[Lebedew, 1901] Lebedew, P. (1901). **Untersuchungen über die Druckkräfte des Lichtes**. *Annalen der Physik*, 311(11):433–458. (1 citation located at page 106.)

[Lelievre et al., 2017] Lelievre, O., Crozatier, V., Berger, P., Baili, G., Llopis, O., Dolfi, D., Nouchi, P., Goldfarb, F., Bretenaker, F., Morvan, L., et Pillet, G. (2017). **A Model for Designing Ultralow Noise Single- and Dual-Loop 10-GHz Optoelectronic Oscillators**. *Journal of Lightwave Technology*, 35(20):4366–4374. (1 citation located at page 12.)

[Lévêque et al., 1990] Lévêque, G., et Villachon-Renard, Y. (1990). **Determination of optical constants of thin film from reflectance spectra**. *Applied Optics*, 29(22):3207. (1 citation located at page 80.)

[Li et al., 2020] Li, C., Guo, H., Tian, X., et He, T. (2020). **Generalized piezoelectric thermoelasticity problems with strain rate and transient thermo-electromechanical responses analysis**. *ZAMM - Journal of Applied Mathematics and Mechanics / Zeitschrift für Angewandte Mathematik und Mechanik*, 100(5). (2 citations located at pages 24 and 84.)

[Liang et al., 2012] Liang, J., et Liao, W.-H. (2012). **Impedance Modeling and Analysis for Piezoelectric Energy Harvesting Systems**. *IEEE/ASME Transactions on Mechatronics*, 17(6):1145–1157. (1 citation located at page 97.)

[Liao et al., 2019] Liao, Y., et Liang, J. (2019). **Unified modeling, analysis and comparison of piezoelectric vibration energy harvesters**. *Mechanical Systems and Signal Processing*, 123:403–425. (1 citation located at page 97.)

[Lo et al., 2016] Lo, A., Haslinger, P., Mizrachi, E., Anderegg, L., Müller, H., Hohensee, M., Goryachev, M., et Tobar, M. E. (2016). **Acoustic Tests of Lorentz Symmetry Using Quartz Oscillators**. *Physical Review X*, 6(1). (1 citation located at page 20.)

[Löbl et al., 2001] Löbl, H., Klee, M., Milsom, R., Dekker, R., Metzmacher, C., Brand, W., et Lok, P. (2001). **Materials for bulk acoustic wave (BAW) resonators and filters**. *Journal of the European Ceramic Society*, 21(15):2633–2640. (1 citation located at page 11.)

[Longair, 2003] Longair, M. S. (2003). **Theoretical Concepts in Physics: An Alternative View of Theoretical Reasoning in Physics**. Cambridge University Press, Cambridge, second edition. (1 citation located at page 106.)

[Mag-isa et al., 2014] Mag-isa, A. E., Jang, B., Kim, J.-H., Lee, H.-J., et Oh, C.-S. (2014). **Coefficient of thermal expansion measurements for freestanding nanocrystalline ultra-thin gold films**. *International Journal of Precision Engineering and Manufacturing*, 15(1):105–110. (1 citation located at page 77.)

[Marquardt et al., 2000] Marquardt, E. D., Le, J. P., et Radebaugh, R. (2000). **Cryogenic Material Properties Database**. In *Cryocoolers 11*, Keystone, CO, USA. (1 citation located at page 77.)

[Mayy et al., 2012] Mayy, M., Zhu, G., Mayy, E., Webb, A., et Noginov, M. A. (2012). **Low temperature studies of surface plasmon polaritons in silver films**. *Journal of Applied Physics*, 111(9):094103. (2 citations located at pages 71 and 72.)

[McCarthy et al., 2009] McCarthy, D. D., et Seidelmann, P. K. (2009). **Defition and Role of a Second**. In *Time - From Earth Rotation to Atomic Physics*. Wiley-VCH Verlag GmbH & Co. KGaA, Weinheim, Germany. (1 citation located at page 12.)

[McGrew et al., 2018] McGrew, W. F., Zhang, X., Fasano, R. J., Schäffer, S. A., Beloy, K., Nicolodi, D., Brown, R. C., Hinkley, N., Milani, G., Schioppo, M., Yoon, T. H., et Ludlow, A. D. (2018). **Atomic clock performance enabling geodesy below the centimetre level**. *Nature*, 564(7734):87–90. (2 citations located at pages 5 and 106.)

[McLean, 1969] McLean, K. O. (1969). **Low Temperature Thermal Expansion of Copper, Silver, Gold and Aluminum**. PhD thesis, Iowa State University, Ames, Iowa. (1 citation located at page 77.)

[McPeak et al., 2015a] McPeak, K. M., Jayanti, S. V., Kress, S. J. P., Meyer, S., Iotti, S., Rossinelli, A., et Norris, D. J. (2015a). **Plasmonic Films Can Easily Be Better: Rules and Recipes**. *ACS Photonics*, 2(3):326–333. (3 citations located at pages 42, 46, and 50.)

[McPeak et al., 2015b] McPeak, K. M., Jayanti, S. V., Kress, S. J. P., Meyer, S., Iotti, S., Rossinelli, A., et Norris, D. J. (2015b). **Plasmonic Films Can Easily Be Better: Rules and Recipes (Supplementary Material)**. *ACS Photonics*, 2(3):326–333. (1 citation located at page 59.)

[Metcalf et al., 1999] Metcalf, H. J., et van der Straten, P. (1999). **Laser Cooling and Trapping**. Graduate Texts in Contemporary Physics. Springer New York, New York, NY. (1 citation located at page 106.)

[Monzón et al., 1992] Monzón, J. J., et Sánchez-Soto, L. L. (1992). **On the definition of absorption for a Fabry-Perot interferometer**. *Pure and Applied Optics: Journal of the European Optical Society Part A*, 1(4):219–226. (1 citation located at page 38.)

[Monzón et al., 1995] Monzón, J. J., et Sánchez-Soto, L. L. (1995). **Reflected fringes in a Fabry–Perot interferometer with absorbing coatings**. *Journal of the Optical Society of America A*, 12(1):132. (2 citations located at pages 38 and 44.)

[Monzón et al., 1996] Monzón, J. J., et Sánchez-Soto, L. L. (1996). **On the concept of absorption for a Fabry–Perot interferometer**. *American Journal of Physics*, 64(2):156–163. (7 citations located at pages 38, 39, 40, 43, 45, 50, and 126.)

[Monzón et al., 1991] Monzón, J. J., Sánchez-Soto, L. L., et Bernabeu, E. (1991). **Influence of coating thickness on the performance of a Fabry–Perot interferometer**. *Applied Optics*, 30(28):4126. (2 citations located at pages 38 and 40.)

[Nakamura et al., 2020] Nakamura, T., Davila-Rodriguez, J., Leopardi, H., Sherman, J. A., Fortier, T. M., Xie, X., Campbell, J. C., McGrew, W. F., Zhang, X., Hassan, Y. S., Nicolodi, D., Beloy, K., Ludlow, A. D., Diddams, S. A., et Quinlan, F. (2020). **Coherent optical clock down-conversion for microwave frequencies with 10 $^{-18}$ instability**. *Science*, 368(6493):889–892. (1 citation located at page 12.)

[Nassour, 1982] Nassour, D.-A. (1982). **Influence des Paramètres de Construction sur le Défaut d'Isochronisme des Résonateurs Piézoélectrique à Simple ou Double Rotation**. PhD thesis, Université Franche-Comté, Besançon. (2 citations located at pages 91 and 91.)

[Natsume, 2020] Natsume, S. (2020). **Sanshiro**. Picquier. (1 citation located at page 106.)

[Nawrodt et al., 2008] Nawrodt, R., Zimmer, A., Koettig, T., Schwarz, C., Heinert, D., Hudl, M., Neubert, R., Thürk, M., Nietzsche, S., Vodel, W., Seidel, P., et Tünnermann, A. (2008). **High mechanical Q-factor measurements on silicon bulk samples**. *Journal of Physics: Conference Series*, 122:012008. (1 citation located at page 19.)

[Nelson, 1982] Nelson, K. A. (1982). **Stimulated Brillouin scattering and optical excitation of coherent shear waves**. *Journal of Applied Physics*, 53(9):6060–6063. (3 citations located at pages 107, 107, and 119.)

[Neuhaus, 2016] Neuhaus, L. (2016). **Cooling a Macroscopic Mechanical Oscillator Close to Its Quantum Ground State**. PhD thesis, Université Pierre et Marie Curie, Paris. (1 citation located at page 109.)

[Nichols et al., 1901] Nichols, E. F., et Hull, G. F. (1901). **A preliminary communication on the pressure of heat and light radiation**. *Phys. Rev. (Series I)*, 13(5):307–320. (1 citation located at page 106.)

[Nietzsche et al., 2006] Nietzsche, S., Nawrodt, R., Zimmer, A., Schnabel, R., Vodel, W., et Seidel, P. (2006). **Cryogenic Q -factor measurement of optical substrates for optimization of gravitational wave detectors**. *Superconductor Science and Technology*, 19(5):S293–S296. (1 citation located at page 19.)

[Nye, 1984] Nye, J. F. (1984). **Physical Properties of Crystals: Their Representation by Tensors and Matrices**. Clarendon Press ; Oxford University Press, Oxford [Oxfordshire] : New York, 1st published in pbk. with corrections, 1984 edition. (5 citations located at pages 24, 24, 27, 113, and 114.)

[Ohsato et al., 2012] Ohsato, H., Iwataki, T., et Morikoshi, H. (2012). **Mechanism of Piezoelectricity for Langasite Based on the Framework Crystal Structure**. *Transactions on Electrical and Electronic Materials*, 13(2):51–59. (1 citation located at page 10.)

[Osterberg et al., 1937] Osterberg, H., et Cookson, J. W. (1937). **The Piezodielectric Effect and Electrostriction in Anisotropic or Isotropic Media**. *Physical Review*, 51(12):1096–1101. (1 citation located at page 106.)

[Penn et al., 2019] Penn, S. D., Kinley-Hanlon, M. M., MacMillan, I. A. O., Heu, P., Follman, D., Deutsch, C., Cole, G. D., et Harry, G. M. (2019). **Mechanical ringdown studies of large-area substrate-transferred GaAs/AlGaAs crystalline coatings**. *Journal of the Optical Society of America B*, 36(4):C15. (2 citations located at pages 129 and 131.)

[Phillips et al., 1982] Phillips, W. D., et Metcalf, H. (1982). **Laser Deceleration of an Atomic Beam**. *Physical Review Letters*, 48(9):596–599. (1 citation located at page 106.)

[Pinard et al., 1999] Pinard, M., Hadjar, Y., et Heidmann, A. (1999). **Effective mass in quantum effects of radiation pressure**. *The European Physical Journal C*, 7(1):107–111. (1 citation located at page 110.)

[Pound, 1946] Pound, R. V. (1946). **Electronic Frequency Stabilization of Microwave Oscillators**. *Review of Scientific Instruments*, 17(11):490–505. (1 citation located at page 18.)

[Prokopenko et al., 2011] Prokopenko, O., Bankowski, E., Meitzler, T., Tiberkevich, V., et Slavin, A. (2011). **Spin-Torque Nano-Oscillator as a Microwave Signal Source**. *IEEE Magnetics Letters*, 2:3000104–3000104. (1 citation located at page 12.)

[Pulskamp et al., 2011] Pulskamp, J. S., Bedair, S. S., Judy, D., et Bhave, S. A. (2011). **Ferroelectric PZT RF MEMS Resonators**. In *2011 Joint Conference of the IEEE International Frequency Control and the European Frequency and Time Forum (FCS) Proceedings*, page 6, San Francisco, CA, USA, USA. (1 citation located at page 11.)

[Raab et al., 1987] Raab, E. L., Prentiss, M., Cable, A., Chu, S., et Pritchard, D. E. (1987). **Trapping of Neutral Sodium Atoms with Radiation Pressure**. *Physical Review Letters*, 59(23):2631–2634. (1 citation located at page 106.)

[Rakich et al., 2010] Rakich, P. T., Davids, P., et Wang, Z. (2010). **Tailoring optical forces in waveguides through radiation pressure and electrostrictive forces**. *Optics Express*, 18(14):14439. (9 citations located at pages 1, 25, 107, 107, 107, 113, 113, 114, and 128.)

[Rakich et al., 2012] Rakich, P. T., Reinke, C., Camacho, R., Davids, P., et Wang, Z. (2012). **Giant Enhancement of Stimulated Brillouin Scattering in the Subwavelength Limit**. *Physical Review X*, 2(1). (1 citation located at page 107.)

[Reddy et al., 2017] Reddy, H., Guler, U., Chaudhuri, K., Dutta, A., Kildishev, A. V., Shalaev, V. M., et Boltasseva, A. (2017). **Temperature-Dependent Optical Properties of Single Crystalline and Polycrystalline Silver Thin Films**. *ACS Photonics*, 4(5):1083–1091. (2 citations located at pages 61 and 71.)

[Renninger et al., 2018] Renninger, W. H., Kharel, P., Behunin, R. O., et Rakich, P. T. (2018). **Bulk crystalline optomechanics**. *Nature Physics*, 14(6):601–607. (4 citations located at pages 17, 107, 107, and 117.)

[Riehle, 2004] Riehle, F. (2004). **Frequency Standards - Basics and Applications**. Wiley, Weinheim. (3 citations located at pages 6, 8, and 11.)

[Rosenbaum, 1988] Rosenbaum, J. F. (1988). **Bulk Acoustic Wave Theory and Devices**. The Artech House Acoustics Library. Artech House, Boston. (1 citation located at page 29.)

[Rosenziveig et al., 2020] Rosenziveig, K., Bon, J., Abbe, P., Soumann, V., Giust, R., Passilly, N., Cohadon, P.-F., et Galliou, S. (2020). **Quartz Crystal Resonator Used as an Optical Fabry-Perot Cavity for Optomechanical Coupling**. In *2020 Joint Conference of the IEEE International Frequency Control Symposium and International Symposium on Applications of Ferroelectrics (IFCS-ISAF)*, pages 1–5, Keystone, CO, USA. IEEE. (2 citations located at pages 112 and 133.)

[Rosenziveig et al., 2019] Rosenziveig, K., Bon, J., Abbe, P., Soumann, V., Passilly, N., Cohadon, P.-F., et Galliou, S. (2019). **Quartz Crystal Resonator Used as an Optical Fabry-Perot Cavity**. In *2019 Joint Conference of the IEEE International Frequency Control Symposium and European Frequency and Time Forum (EFTF/IFC)*, pages 1–3, Orlando, FL, USA. IEEE. (1 citation located at page 52.)

[Rosenziveig et al., 2021] Rosenziveig, K., Soumann, V., Abbé, P., Dubois, B., Cohadon, P.-F., Passilly, N., et Galliou, S. (2021). **Measurement of Refractive Index at Cryogenic Temperature of Absorptive Silver Thin Films Used as Reflectors in a Fabry-Perot Cavity**. *Applied Optics*, 60(35). (3 citations located at pages 66, 80, and 126.)

[Rouvaen et al., 1979] Rouvaen, J. M., Ghazaleh, M. G., Bridoux, E., et Torguet, R. (1979). **On a general treatment of acousto-optic interactions in linear anisotropic crystals**. *Journal of Applied Physics*, 50(8):5472. (1 citation located at page 113.)

[Rowan et al., 2000] Rowan, S., Cagnoli, G., Sneddon, P., Hough, J., Route, R., Gustafson, E., Fejer, M., et Mitrofanov, V. (2000). **Investigation of mechanical loss factors of some candidate materials for the test masses of gravitational wave detectors**. *Physics Letters A*, 265(1-2):5–11. (1 citation located at page 19.)

[Royer et al., 2000a] Royer, D., Dieulesaint, E., et Lyle, S. (2000a). **Elastic Waves in Solids Vol. 1**, volume 1 of *Advanced Texts in Physics*. Springer. (5 citations located at pages 24, 24, 29, 113, and 114.)

[Royer et al., 2000b] Royer, D., Dieulesaint, E., et Lyle, S. (2000b). **Elastic Waves in Solids Vol. 2**, volume 1 of *Advanced Texts in Physics*. Springer. (1 citation located at page 114.)

[Rubiola, 2009] Rubiola, E. (2009). **Phase Noise and Frequency Stability in Oscillators**. The Cambridge RF and Microwave Engineering Series. Cambridge University Press, Cambridge. (1 citation located at page 9.)

[Sakamoto et al., 2008] Sakamoto, K., Kubo, K., et Ono, K. (2008). **Development of ultra low noise VHF OCXO with excellent temperature stability**. In *2008 IEEE International Frequency Control Symposium*, pages 565–568, Honolulu, HI. IEEE. (1 citation located at page 11.)

[Schröter, 2008] Schröter, A. (2008). **Mechanical Losses in Materials for Future Cryogenic Gravitational Wave Detectors**. PhD thesis, Friedrich-Schiller-Universität Jena, Jena. (3 citations located at pages 13, 19, and 19.)

[Sellitto et al., 2019] Sellitto, A., Sciacca, M., et Amendola, A. (2019). **Generalized heat equation and transitions between different heat-transport regimes in narrow stripes**. *Mechanics Research Communications*, 98:22–30. (1 citation located at page 84.)

[Shelby et al., 1985] Shelby, R. M., Levenson, M. D., et Bayer, P. W. (1985). **Guided acoustic-wave Brillouin scattering**. *Physical Review B*, 31(8):5244–5252. (1 citation located at page 107.)

[Shields et al., 1956] Shields, J. H., et Ellis, J. W. (1956). **Dispersion of Birefringence of Quartz in the Near Infrared**. *Journal of the Optical Society of America*, 46(4):263. (1 citation located at page 29.)

[Siciliani de Cumis et al., 2009] Siciliani de Cumis, M., Farsi, A., Marino, F., D'Arrigo, G., Marin, F., Cataliotti, F. S., et Rimini, E. (2009). **Radiation pressure excitation and cooling of a cryogenic micro-mechanical systems cavity**. *Journal of Applied Physics*, 106(1):013108. (3 citations located at pages 107, 109, and 109.)

[Smith et al., 1995] Smith, D., et Fickett, F. (1995). **Low-Temperature Properties of Silver**. *Journal of Research of the National Institute of Standards and Technology*, 100(2):119. (1 citation located at page 72.)

[Smith et al., 1999] Smith, D. D., Yoon, Y., Boyd, R. W., Campbell, J. K., Baker, L. A., Crooks, R. M., et George, M. (1999). **Scan measurement of the nonlinear absorption of a thin gold film**. *Journal of Applied Physics*, 86(11):6200–6205. (1 citation located at page 52.)

[Starunov et al., 1970] Starunov, V. S., et Fabelinskii, I. L. (1970). **Stimulated Mandel'shtam-Brillouin Scattering and Stimulated Entropy (Temperature) Scattering of light**. *Soviet Physics Uspekhi*, 12(4):28. (1 citation located at page 107.)

[Steck, 2020] Steck, D. A. (2020). **Classical and Modern Optics**. Technical Report, University of Oregon, Eugene, Oregon. (1 citation located at page 37.)

[Steinlechner et al., 2018] Steinlechner, J., Martin, I. W., Bell, A. S., Hough, J., Fletcher, M., Murray, P. G., Robie, R., Rowan, S., et Schnabel, R. (2018). **Silicon-Based Optical Mirror Coatings for Ultrahigh Precision Metrology and Sensing**. *Physical Review Letters*, 120(26). (1 citation located at page 130.)

[Stevens et al., 1986] Stevens, D. S., et Tiersten, H. F. (1986). **An analysis of doubly rotated quartz resonators utilizing essentially thickness modes with transverse variation**. *The Journal of the Acoustical Society of America*, 79(6):1811–1826. (1 citation located at page 24.)

[Tarumi et al., 2007] Tarumi, R., Nakamura, K., Ogi, H., et Hirao, M. (2007). **Complete set of elastic and piezoelectric coefficients of α-quartz at low temperatures**. *Journal of Applied Physics*, 102(11):113508. (3 citations located at pages 135, 136, and 136.)

[Tichý et al., 2010] Tichý, J., Erhart, J., Kittinger, E., et Přívratská, J. (2010). **Fundamentals of Piezoelectric Sensorics**. Springer Berlin Heidelberg, Berlin, Heidelberg. (3 citations located at pages 135, 135, and 136.)

[Tiersten, 1975] Tiersten, H. F. (1975). **Analysis of intermodulation in thickness-shear and trapped energy resonators**. *The Journal of the Acoustical Society of America*, 57(3):667–681. (1 citation located at page 142.)

[Tompkins et al., 2005] Tompkins, H. G., et Irene, E. A., editors (2005). **Handbook of Ellipsometry**. William Andrew Pub. ; Springer, Norwich, NY : Heidelberg, Germany. (1 citation located at page 80.)

[Tzou et al., 2010] Tzou, D., et Guo, Z.-Y. (2010). **Nonlocal behavior in thermal lagging**. *International Journal of Thermal Sciences*, 49(7):1133–1137. (1 citation located at page 84.)

[Uchiyama et al., 1999] Uchiyama, T., Tomaru, T., Tobar, M., Tatsumi, D., Miyoki, S., Ohashi, M., Kuroda, K., Suzuki, T., Sato, N., Haruyama, T., Yamamoto, A., et Shintomi, T. (1999). **Mechanical quality factor of a cryogenic sapphire test mass for gravitational wave detectors**. *Physics Letters A*, 261(1-2):5–11. (1 citation located at page 19.)

[Vahala, 2008] Vahala, K. J. (2008). **Back-action limit of linewidth in an optomechanical oscillator**. *Physical Review A*, 78(2). (1 citation located at page 109.)

[Vajente et al., 2021] Vajente, G., Yang, L., Davenport, A., Fazio, M., Ananyeva, A., Zhang, L., Billingsley, G., Prasai, K., Markosyan, A., Bassiri, R., Fejer, M. M., Chicoine, M., Schiettekatte, F., et Menoni, C. S. (2021). **Low Mechanical Loss TiO 2 : GeO 2 Coatings for Reduced Thermal Noise in Gravitational Wave Interferometers**. *Physical Review Letters*, 127(7):071101. (1 citation located at page 128.)

[Vallet, 2018] Vallet, G. (2018). **Cavity Non Destructive Detection on an Optical Lattice Clock**. PhD thesis, Université Paris-Sciences-et-Lettres, Paris. (2 citations located at pages 5 and 106.)

[Vicarini et al., 2019] Vicarini, R., Boudot, R., Abdel Hafiz, M., Maurice, V., Passilly, N., Kroemer, E., Ribetto, L., Gaff, V., Gorecki, C., et Galliou, S. (2019). **Mitigation of Temperature-Induced Light-Shift Effects in Miniaturized Atomic Clocks**. *IEEE Transactions on Ultrasonics, Ferroelectrics, and Frequency Control*, 66(12):1962–1967. (1 citation located at page 12.)

[Wall et al., 2015] Wall, B., Gruenwald, R., Klein, M., et Bruckner, G. (2015). **A 600℃ Wireless and Passive Temperature Sensor Based on Langasite SAW-Resonators**. In *Proceedings SENSOR 2015*, pages 6 Pages, 1.1 MB. AMA Service GmbH, P.O. Box 2352, 31506 Wunstorf, Germany. (1 citation located at page 10.)

[Wang et al., 2010] Wang, R. T., et Tjoelker, R. L. (2010). **High Q Miniature Sapphire Acoustic Resonator**. In *2010 IEEE International Frequency Control Symposium*, pages 155–157, Newport Beach, CA, USA. IEEE. (1 citation located at page 19.)

[Wang et al., 2016] Wang, S., Ng, J., Xiao, M., et Chan, C. T. (2016). **Electromagnetic stress at the boundary: Photon pressure or tension?** *Science Advances*, 2(3):e1501485. (1 citation located at page 107.)

[Waterhouse et al., 1968] Waterhouse, N., et Yates, B. (1968). **The interferometric measurement of the thermal expansion of silver and palladium at low temperatures**. *Cryogenics*, 8(5):267–271. (2 citations located at pages 77 and 78.)

[Weber et al., 2010] Weber, J. W., Calado, V. E., et van de Sanden, M. C. M. (2010). **Optical constants of graphene measured by spectroscopic ellipsometry**. *Applied Physics Letters*, 97(9):091904. (1 citation located at page 80.)

[White et al., 1972] White, G. K., et Collins, J. G. (1972). **Thermal expansion of copper, silver, and gold at low temperatures**. *Journal of Low Temperature Physics*, 7(1-2):43–75. (2 citations located at pages 77 and 78.)

[Wiederhecker et al., 2019] Wiederhecker, G. S., Dainese, P., et Mayer Alegre, T. P. (2019). **Brillouin optomechanics in nanophotonic structures**. *APL Photonics*, 4(7):071101. (1 citation located at page 107.)

[Wineland et al., 1975] Wineland, D., et Dehmelt, H. (1975). **Proposed 1014 $\Delta\nu/\nu$ laser fluorescence spectroscopy on Ti+ mono-ion oscillator III (side band cooling)**. In *Bulletin of the American Physical Society*, volume 20, pages 637–637. (1 citation located at page 106.)

[Wolff et al., 2015] Wolff, C., Steel, M. J., Eggleton, B. J., et Poulton, C. G. (2015). **Stimulated Brillouin scattering in integrated photonic waveguides: Forces, scattering mechanisms, and coupled-mode analysis**. *Physical Review A*, 92(1). (2 citations located at pages 107 and 119.)

[Yakubovsky et al., 2017] Yakubovsky, D. I., Arsenin, A. V., Stebunov, Y. V., Fedyanin, D. Y., et Volkov, V. S. (2017). **Optical constants and structural properties of thin gold films**. *Optics Express*, 25(21):25574. (1 citation located at page 59.)

[Yang et al., 2015] Yang, H. U., D'Archangel, J., Sundheimer, M. L., Tucker, E., Boreman, G. D., et Raschke, M. B. (2015). **Optical dielectric function of silver**. *Physical Review B*, 91(23):235137. (1 citation located at page 80.)

[Zhang et al., 2017] Zhang, M., Wang, C., Cheng, R., Shams-Ansari, A., et Lončar, M. (2017). **Monolithic ultra-high-Q lithium niobate microring resonator**. *Optica*, 4(12):1536. (1 citation located at page 10.)

Document generated with LaTeX and:
the LaTeX style for PhD Thesis created by S. Galland — http://www.multiagent.fr/ThesisStyle
the tex-upmethodology package suite — http://www.arakhne.org/tex-upmethodology/